

From Nuclei to Compact Stars

Contents

1	Topics	1033
2	Participants	1037
2.1	ICRANet	1037
2.2	External on going collaborations	1037
2.3	Postdocs	1038
2.4	Graduate Students	1039
3	Publications 2020	1041
3.1	Refereed Journals	1041
3.1.1	Printed	1041
3.1.2	Accepted for publication or in press	1044
3.1.3	Submitted for publication	1045
3.2	To be submitted	1047

1 Topics

The study of compact objects such as white dwarfs, neutron stars and black holes requires the interplay between nuclear and atomic physics together with relativistic field theories, e.g., general relativity, quantum electrodynamics, quantum chromodynamics, as well as particle physics. In addition to the theoretical physics aspects, the study of astrophysical scenarios characterized by the presence of at least one of the above compact object is focus of extensive research within our group. The research of our group can be divided into the following topics:

- **Nuclear and Atomic Astrophysics.** We study the properties and processes occurring in compact stars in which nuclear and atomic physics have to be necessarily applied. We focus on the properties of nuclear matter under extreme conditions of density, pressure and temperature in the compact star interiors. The matter equation of state is studied in detail taking into account all the interactions between the constituents within a full relativistic framework.
- **White Dwarfs Physics and Structure.** The aim of this part of our research is the construction of the white dwarf structure within a self-consistent description of the equation of state of the interior together with the solution of the hydrostatic equilibrium equations in general relativity. Non-magnetized, magnetized, non-rotating and rotating white dwarfs are studied. The interaction and evolution of a central white dwarf with a surrounding disk, as occurred in the aftermath of white dwarf binary mergers, is also a subject of study.
- **White Dwarfs Astrophysics.** We are interested in the astrophysics of white dwarfs both isolated and in binaries. Magnetized white dwarfs, soft gamma repeaters, anomalous X-ray pulsars, white dwarf pulsars, cataclysmic variables, binary white dwarf mergers, and type Ia supernovae are studied. The role of a realistic white dwarf interior structure is particularly emphasized.

- **Neutron Stars Physics and Structure.** We calculate the properties of the interior structure of neutron stars using realistic models of the nuclear matter equation of state within the general relativistic equations of equilibrium. Strong, weak, electromagnetic and gravitational interactions have to be jointly taken into due account within a self-consistent fully relativistic framework. Non-magnetized, magnetized, non-rotating and rotating neutron stars are studied.
- **Neutron Stars Astrophysics.** We study astrophysical systems harboring neutron stars such as isolated and binary pulsars, low and intermediate X-ray binaries, inspiraling and merging double neutron stars. Most extreme cataclysmic events involving neutron stars and their role in the explanation of extraordinarily energetic astrophysical events such as gamma-ray bursts are analyzed in detail.
- **Radiation Mechanisms of Compact Objects.** We here study the possible emission mechanisms of compact objects such as white dwarfs, neutron stars, and black holes. Therefore, we are interested in the electromagnetic, neutrino and gravitational-wave emission at work in astrophysical systems such as compact object magnetospheres, accretion disks surrounding them, as well as inspiraling and merging relativistic binaries, e.g. double neutron stars, neutron star-white dwarfs, white dwarf-white dwarf and neutron star-black holes.
- **Exact and Numerical Solutions of the Einstein and Einstein-Maxwell Equations in Astrophysics.** We analyze the ability of analytic exact solutions of the Einstein and Einstein-Maxwell equations to describe the exterior spacetime of compact stars such as white dwarfs and neutron stars. For this we compare and contrast exact analytic with numerical solutions of the stationary axisymmetric Einstein equations. The problem of matching between interior and exterior spacetime is addressed in detail. The effect of the quadrupole moment on the properties of the spacetime is also investigated. Particular attention is given to the application of exact solutions in astrophysics, e.g. the dynamics of particles around compact stars and its relevance in astrophysical systems such as X-ray binaries and gamma-ray bursts.
- **Critical Fields and Non-linear Electrodynamics Effects in Astrophysics.** We study the conditions under which ultrastrong electromagnetic fields

can develop in astrophysical systems such as neutron stars and in the process of gravitational collapse to a black hole. The effects of non-linear electrodynamics minimally coupled to gravity are investigated. New analytic and numeric solutions to the Einstein-Maxwell equations representing black holes or the exterior field of a compact star are obtained and analyzed. The consequences on extreme astrophysical systems, for instance gamma-ray bursts, are studied.

2 Participants

2.1 ICRANet

- C. L. Bianco (ICRANet, Italy)
- J. A. Rueda (ICRANet, Italy)
- R. Moradi (ICRANet, Italy)
- R. Ruffini (ICRANet, Italy)
- N. Sahakyan (ICRANet, Armenia)
- G. Vereschagin (ICRANet, Italy)
- S.-S. Xue (ICRANet, Italy)
- Y. Wang (ICRANet, Italy)

2.2 External on going collaborations

- K. Boshkayev (Al-Farabi Kazakh National University, Kazakhstan)
- R. Camargo (Universidade do Estado de Santa Catarina, Florianópolis, Brazil)
- C. Cherubini (Università Campus Biomedico, Rome, Italy)
- J. G. Coelho (Universidade Tecnológica Federal do Paraná, Brazil)
- S. Filippi (Università Campus Biomedico, Rome, Italy)
- C. L. Fryer (University of Arizona; Los Alamos National Laboratory, USA)

- G. A. González (Universidad Industrial de Santander, Colombia)
- M. M. Guzzo (Universidade Estadual de Campinas, Brazil)
- F. D. Lora-Clavijo (Universidad Industrial de Santander, Colombia)
- P. Lorén Aguilar (University of Exeter, United Kingdom)
- S. O. Kepler (Universidade Federal do Rio Grande do Sul, Brazil)
- M. Malheiro (Instituto Tecnológico de Aeronáutica, Brazil)
- R. M. Jr. Marinho (Instituto Tecnológico de Aeronáutica, Brazil)
- G. Mathews (University of Notre Dame, USA)
- L. A. Nuñez (Universidad Industrial de Santander, Colombia)
- R. Riahi (Department of Science, Shahrekord Branch, Islamic Azad University, Iran)
- C. V. Rodrigues (Instituto Nacional de Pesquisas Espaciais, Brazil)
- J. F. Rodriguez (Universidad Industrial de Santander, Colombia)
- F. Rossi-Torres (Universidade Estadual de Campinas, Brazil)
- C. A. Z. Vasconcellos (Universidade Federal do Rio Grande do Sul, Brazil)
- J. I. Zuluaga (Universidad de Antioquia, Colombia)

2.3 Postdocs

- L. Becerra (Universidad Pontificia Católica de Chile, Chile)
- C. L. Ellinger (Los Alamos National Laboratory, USA)
- J. P. Pereira (Nicolaus Copernicus Astronomical Center, Polish Academy of Sciences, Poland)

2.4 Graduate Students

- E. A. Becerra (ICRANet; Sapienza University of Rome, Italy)
- S. Campion (ICRANet; Sapienza University of Rome, Italy)
- G. A. Carvalho (Instituto Tecnológico de Aeronáutica, Brazil)
- R. V. Lobato (ICRANet; Sapienza University of Rome, Italy; Instituto Tecnológico de Aeronáutica, Brazil)
- G. Nurbakyt (ICRANet; Sapienza Al-Farabi Kazakh National University, Kazakhstan)
- J. D. Uribe (ICRANet; Sapienza University of Rome, Italy)
- G. Zhumakhanova (ICRANet; Sapienza Al-Farabi Kazakh National University, Kazakhstan)

3 Publications 2020

3.1 Refereed Journals

3.1.1 Printed

1. de Lima, Rafael C. R.; Coelho, Jaziel G.; Pereira, Jonas P.; Rodrigues, Claudia V.; Rueda, J. A., *Evidence for a Multipolar Magnetic Field in SGR J1745-2900 from X-Ray Light-curve Analysis*, *The Astrophysical Journal* 889, 165, 2020.

SGR J1745-2900 was detected from its outburst activity in 2013 April and it was the first soft gamma repeater (SGR) detected near the center of the Galaxy (Sagittarius A*). We use 3.5 yr Chandra X-ray light-curve data to constrain some neutron star (NS) geometric parameters. We assume that the flux modulation comes from hot spots on the stellar surface. Our model includes the NS mass, radius, a maximum of three spots of any size, temperature and positions, and general relativistic effects. We find that the light curve of SGR J1745-2900 could be described by either two or three hot spots. The ambiguity is due to the small amount of data, but our analysis suggests that one should not disregard the possibility of multi-spots (due to a multipolar magnetic field) in highly magnetized stars. For the case of three hot spots, we find that they should be large and have angular semiapertures ranging from 16° to 67° . The large size found for the spots points to a magnetic field with a nontrivial poloidal and toroidal structure (in accordance with magnetohydrodynamics investigations and Neutron Star Interior Composition Explorer's (NICER) recent findings for PSR J0030+0451) and is consistent with the small characteristic age of the star. Finally, we also discuss possible constraints on the mass and radius of SGR J1745-2900 and briefly envisage possible scenarios accounting for the 3.5 yr evolution of SGR J1745-290 hot spots.

2. Rueda, J. A.; Ruffini, Remo; Karlica, Mile; Moradi, Rahim; Wang, Yu,

Magnetic Fields and Afterglows of BdHNe: Inferences from GRB 130427A, GRB 160509A, GRB 160625B, GRB 180728A, and GRB 190114C, The Astrophysical Journal 893, 148, 2020.

GRB 190114C is the first binary-driven hypernova (BdHN) fully observed from initial supernova (SN) appearance to the final emergence of the optical SN signal. It offers an unprecedented testing ground for the BdHN theory, which is here determined and further extended to additional gamma-ray bursts (GRBs). BdHNe comprise two subclasses of long GRBs, with progenitors a binary system composed of a carbon-oxygen star (CO_{core}) and a neutron star (NS) companion. The CO_{core} explodes as an SN, leaving at its center a newborn NS (νNS). The SN ejecta hypercritically accretes on both the νNS and the NS companion. BdHNe I are very tight binaries, where the accretion leads the companion NS to gravitationally collapse into a black hole (BH). In BdHN II, the accretion rate onto the NS is lower, so there is no BH formation. We observe the same afterglow structure for GRB 190114C and other selected examples of BdHNe I (GRB 130427A, GRB 160509A, GRB 160625B) and for BdHN II (GRB 180728A). In all cases, the afterglows are explained via the synchrotron emission powered by the νNS , and their magnetic field structures and their spin are determined. For BdHNe I, we discuss the properties of the magnetic field embedding the newborn BH, which was inherited from the collapsed NS and amplified during the gravitational collapse process, and surrounded by the SN ejecta.

3. Rueda, J. A.; Ruffini, R., *The blackholic quantum*, The European Physical Journal C 80, 300, 2020.

We show that the high-energy emission of GRBs originates in the *inner engine*: a Kerr black hole (BH) surrounded by matter and a magnetic field B_0 . It radiates a sequence of discrete events of particle acceleration, each of energy $\mathcal{E} = \hbar \Omega_{\text{eff}}$, the *blackholic quantum*, where $\Omega_{\text{eff}} = 4(m_{\text{Pl}}/m_n)^8 (c a / G M) (B_0^2 / \rho_{\text{Pl}}) \Omega_+$. Here M , $a = J/M$, $\Omega_+ = c^2 \partial M / \partial J = (c^2 / G) a / (2Mr_+)$ and r_+ are the BH mass, angular momentum per unit mass, angular velocity and horizon; m_n is the neutron mass, m_{Pl} , $\lambda_{\text{Pl}} = \hbar / (m_{\text{Pl}} c)$ and $\rho_{\text{Pl}} = m_{\text{Pl}} c^2 / \lambda_{\text{Pl}}^3$, are the Planck mass, length and energy density. Here and in the following use CGS-Gaussian units. The timescale of each process is $\tau_{\text{el}} \sim \Omega_+^{-1}$, along the rotation axis, while it is much shorter off-axis owing to energy losses such as

synchrotron radiation. We show an analogy with the Zeeman and Stark effects, properly scaled from microphysics to macrophysics, that allows us to define the *BH magneton*, $\mu_{\text{BH}} = (m_{\text{Pl}}/m_n)^4 (c a / G M) e \hbar / (M c)$. We give quantitative estimates for GRB 130427A adopting $M = 2.3 M_{\odot}$, $c a / (G M) = 0.47$ and $B_0 = 3.5 \times 10^{10}$ G. Each emitted *quantum*, $\mathcal{E} \sim 10^{37}$ erg, extracts only 10^{-16} times the BH rotational energy, guaranteeing that the process can be repeated for thousands of years. The *inner engine* can also work in AGN as we here exemplified for the supermassive BH at the center of M87.

4. Uribe Suárez, J. D.; Rueda, J. A., *Some Recent Results on Neutrino Oscillations in Hypercritical Accretion*, *Astronomische Nachrichten* 340, 935, 2020.

The study of neutrino flavour oscillations in astrophysical sources has been boosted in the last two decades thanks to achievements in experimental neutrino physics and observational astronomy. We here discuss two cases of interest in the modelling of short and long gamma-ray bursts (GRBs): hypercritical, i.e. highly super-Eddington spherical/disk accretion onto a neutron star (NS)/black hole (BH). We show that in both systems the ambient conditions of density and temperature imply the occurrence of neutrino flavour oscillations, with a relevant role of neutrino self-interactions.

5. Uribe, J. D.; Becerra-Vergara, E. A.; Rueda, J. A., *Neutrino Oscillations in Neutrino-Dominated Accretion Around Rotating Black Holes*, *Universe* 7, 7, 2021.

In the binary-driven hypernova model of long gamma-ray bursts, a carbon-oxygen star explodes as a supernova in presence of a neutron star binary companion in close orbit. Hypercritical (i.e. highly super-Eddington) accretion of the ejecta matter onto the neutron star sets in, making it reach the critical mass with consequent formation of a Kerr black hole. We have recently shown that, during the accretion process onto the neutron star, fast neutrino flavour oscillations occur. Numerical simulations of the above system show that a part of the ejecta keeps bound to the newborn Kerr black hole, leading to a new process of hypercritical accretion. We here address, also for this phase of the binary-driven hypernova, the occurrence of neutrino flavour oscillations given

the extreme conditions of high density (up to 10^{12} g cm $^{-3}$) and temperatures (up to tens of MeV) inside this disk. We estimate the behaviour of the electronic and non-electronic neutrino content within the two-flavour formalism ($\nu_e\nu_x$) under the action of neutrino collective effects by neutrino self-interactions. We find that in the case of inverted mass hierarchy, neutrino oscillations inside the disk have frequencies between $\sim (10^5\text{--}10^9)$ s $^{-1}$, leading the disk to achieve flavour equipartition. This implies that the energy deposition rate by neutrino annihilation ($\nu + \bar{\nu} \rightarrow e^- + e^+$) in the vicinity of the Kerr black hole, is smaller than previous estimates in the literature not accounting by flavour oscillations inside the disk. The exact value of the reduction factor depends on the ν_e and ν_x optical depths but it can be as high as ~ 5 . The results of this work are a first step toward the analysis of neutrino oscillations in a novel astrophysical context and, as such, deserve further attention.

3.1.2 Accepted for publication or in press

1. Uribe, J. D.; Rueda, J. A., *Neutrino Flavour Oscillations in Gamma-Ray Bursts*, to be published as a chapter in the book “New phenomena and new states of matter in the Universe: from quarks to Cosmos”, Eds. Peter Hess, Thomas Boller and Cesar Zen Vasconcellos, World Scientific 2021.

In the binary-driven hypernova model of long gamma-ray bursts, a carbon-oxygen star explodes as a supernova in presence of a neutron star binary companion in close orbit. Hypercritical (i.e. highly super-Eddington) accretion of the ejecta matter onto the neutron star sets in, making it reach the critical mass with consequent formation of a Kerr black hole. We have recently shown that, during the accretion process onto the neutron star, fast neutrino flavour oscillations occur. Numerical simulations of the above system show that a part of the ejecta keeps bound to the newborn Kerr black hole, leading to a new process of hypercritical accretion. We address here the occurrence of neutrino flavour oscillations given the extreme conditions of high density (up to 10^{12} g cm $^{-3}$) and temperatures (up to tens of MeV) inside this disk. We estimate the evolution of the electronic and non-electronic neutrino content within the two-flavour formalism ($\nu_e\nu_x$) under the action of neutrino collective effects by neutrino self-interactions. We find that

neutrino oscillations inside the disk have frequencies between $\sim (10^5 - 10^9) \text{ s}^{-1}$, leading the disk to achieve flavour equipartition. This implies that the energy deposition rate by neutrino annihilation ($\nu + \bar{\nu} \rightarrow e^- + e^+$) in the vicinity of the Kerr black hole, is smaller than previous estimates in the literature not accounting by flavour oscillations inside the disk. The exact value of the reduction factor depends on the ν_e and ν_x optical depths but it can be as high as ~ 5 .

2. Rueda, J. A.; Ruffini, R., *An Inner Engine Based on Binary-Driven Hypernovae for the High-Energy Emission of Long Gamma-Ray Bursts*, to be published as a chapter in the book "New phenomena and new states of matter in the Universe: from quarks to Cosmos", Eds. Peter Hess, Thomas Boller and Cesar Zen Vasconcellos, World Scientific 2021.

A multi-decade theoretical effort has been devoted to finding an efficient mechanism to use the rotational and electromagnetic extractable energy of a Kerr-Newman black hole (BH) to power the most energetic astrophysical sources, gamma-ray bursts (GRBs) and active galactic nuclei (AGN). We show an efficient general relativistic electro-dynamical process which occurs in the "inner engine" of a binary driven hypernova (BdHN). The *inner engine* is composed of a rotating Kerr BH, surrounded by a magnetic field of strength B_0 , aligned and parallel to the rotation axis, and a very-low-density ionized plasma. The gravitomagnetic interaction between the Kerr BH and the magnetic field induces an electric field that accelerates charged particles from the environment. Along the BH rotation axis, the particles reach energies above 10^{18} eV hence contributing to ultrahigh-energy cosmic rays, and at other latitudes emit synchrotron radiation at GeV energies which explain the high-energy emission of long GRBs observed by Fermi-LAT.

3.1.3 Submitted for publication

1. Campion, S.; Melon Fuksman, J. D.; J. A. Rueda, *Neutrino production from proton-proton interactions in binary-driven hypernovae*, submitted for publication to Physical Review D.

We estimate the neutrino emission from the decay chain of the π -meson and μ -lepton, produced by proton-proton inelastic scattering in energetic ($E_{\text{iso}} \gtrsim 10^{52} \text{ erg}$) long gamma-ray bursts (GRBs), within the type

I binary-driven hypernova (BdHN) model. The BdHN I progenitor is binary system composed of a carbon-oxygen star (CO_{core}) and a neutron star (NS) companion. The CO_{core} explosion as supernova (SN) triggers a massive accretion process onto the NS. For short orbital periods of few minutes, the NS reaches the critical mass, hence forming a black hole (BH). Recent numerical simulations of the above scenario show that the SN ejecta becomes highly asymmetric, creating a *cavity* around the newborn BH site, due to the NS accretion and gravitational collapse. Therefore, the electron-positron (e^\pm) plasma created in the BH formation, during its isotropic and expanding self-acceleration, engulfs different amounts of ejecta baryons along different directions, leading to a direction-dependent Lorentz factor. The protons engulfed inside the high-density ($\sim 10^{23}$ particle/cm³) ejecta reach energies in the range $1.24 \lesssim E_p \lesssim 6.14$ GeV and interact with the unshocked protons in the ejecta. The protons engulfed from the low density region around the BH reach energies ~ 1 TeV and interact with the low-density (~ 1 particle/cm³) protons of the interstellar medium (ISM). The above interactions give rise, respectively, to neutrino energies $E_\nu \leq 2$ GeV and $10 \leq E_\nu \leq 10^3$ GeV, and for both cases we calculate the spectra and luminosity.

2. Moradi, R.; Rueda, J. A.; Ruffini, R., Wang, Y., *The newborn black hole in GRB 191014C manifests that is alive*, submitted for publication to Astronomy & Astrophysics.

A multi-decade theoretical effort has been devoted to finding an efficient mechanism to use the rotational and electro-dynamical extractable energy of a Kerr-Newman black hole (BH), to power the most energetic astrophysical sources such as gamma-ray bursts (GRBs) and active galactic nuclei (AGN). We show an efficient general relativistic electro-dynamical process which occurs in the “*inner engine*” of a binary driven hypernova (BdHN). The *inner engine* is composed of a rotating Kerr BH of mass M and dimensionless spin parameter α , a magnetic field of strength B_0 aligned and parallel to the rotation axis, and a very low density ionized plasma. Here, we show that the gravitomagnetic interaction between the BH and the magnetic field induces an electric field that accelerates electrons/protons from the environment to ultrarelativistic energies emitting synchrotron radiation. We show that in GRB 190114C the BH of mass $M = 4.4 M_\odot$, $\alpha = 0.4$ and $B_0 \approx 4 \times 10^{10}$ G, can

lead to a high-energy (\gtrsim GeV) luminosity of 10^{51} erg s $^{-1}$. The *inner engine* parameters are determined by requiring: 1) that the BH extractable energy explains the high-energy emission energetics, 2) that the emitted photons are not subjected to magnetic-pair production, and 3) that the synchrotron radiation timescale agrees with the observed high-energy timescale. We find for GRB 190114C a clear jetted emission of GeV energies with a semi-aperture angle of approximately 60° with respect to the BH rotation axis.

3.2 To be submitted

1. Rueda, J. A.; Ruffini, R.; Kerr, R. P., *Gravitomagnetic interaction of a Kerr black hole with a magnetic field as source of the jetted GeV radiation of gamma-ray bursts*, in preparation.
2. Rueda, J. A.; Ruffini, R., *On a gravitomagnetic source of ultrahigh-energy cosmic rays in gamma-ray bursts and active galactic nuclei*, in preparation.



Evidence for a Multipolar Magnetic Field in SGR J1745-2900 from X-Ray Light-curve Analysis

Rafael C. R. de Lima^{1,2}, Jaziel G. Coelho^{2,3,4}, Jonas P. Pereira^{5,6,7}, Claudia V. Rodrigues⁴, and Jorge A. Rueda^{2,8,9,10,11}

¹ Universidade do Estado de Santa Catarina, Av. Madre Benvenuta, 2007 Itacorubi, 88.035-901, Florianópolis, Brazil; rafael.lima@udesc.br

² ICRAANet, Piazza della Repubblica 10, I-65122, Pescara, Italy; jazielcoelho@utfpr.edu.br

³ Departamento de Física, Universidade Tecnológica Federal do Paraná, 85884-000 Medianeira, PR, Brazil

⁴ Divisão de Astrofísica, Instituto Nacional de Pesquisas Espaciais, Avenida dos Astronautas 1758, 12227-010, São José dos Campos, SP, Brazil

⁵ Universidade Federal do ABC, Centro de Ciências Naturais e Humanas, Avenida dos Estados, 5001-Bangú, CEP 09210-170, Santo André, SP, Brazil
jpereira@camk.edu.pl

⁶ Mathematical Sciences and STAG Research Centre, University of Southampton, Southampton, SO17 1BJ, UK

⁷ Nicolaus Copernicus Astronomical Center, Polish Academy of Sciences, Bartycka 18, 00-716, Warsaw, Poland

⁸ ICRAANet-Rio, Centro Brasileiro de Pesquisas Físicas, Rua Dr. Xavier Sigaud 150, 22290-180 Rio de Janeiro, Brazil

⁹ ICRAANet-Ferrara, Dipartimento di Fisica e Scienze della Terra, Università degli Studi di Ferrara, Via Saragat 1, I-44122 Ferrara, Italy

¹⁰ Dipartimento di Fisica e Scienze della Terra, Università degli Studi di Ferrara, Via Saragat 1, I-44122 Ferrara, Italy

¹¹ INAF, Istituto di Astrofisica e Planetologia Spaziali, Via Fosso del Cavaliere 100, I-00133 Rome, Italy

Received 2019 May 13; revised 2019 December 24; accepted 2019 December 27; published 2020 February 4

Abstract

SGR J1745-2900 was detected from its outburst activity in 2013 April and it was the first soft gamma repeater (SGR) detected near the center of the Galaxy (Sagittarius A*). We use 3.5 yr *Chandra* X-ray light-curve data to constrain some neutron star (NS) geometric parameters. We assume that the flux modulation comes from hot spots on the stellar surface. Our model includes the NS mass, radius, a maximum of three spots of any size, temperature and positions, and general relativistic effects. We find that the light curve of SGR J1745-2900 could be described by either two or three hot spots. The ambiguity is due to the small amount of data, but our analysis suggests that one should not disregard the possibility of multi-spots (due to a multipolar magnetic field) in highly magnetized stars. For the case of three hot spots, we find that they should be large and have angular semiapertures ranging from 16° to 67° . The large size found for the spots points to a magnetic field with a nontrivial poloidal and toroidal structure (in accordance with magnetohydrodynamics investigations and *Neutron Star Interior Composition Explorer's* (NICER) recent findings for PSR J0030+0451) and is consistent with the small characteristic age of the star. Finally, we also discuss possible constraints on the mass and radius of SGR J1745-2900 and briefly envisage possible scenarios accounting for the 3.5 yr evolution of SGR J1745-290 hot spots.

Key words: dense matter – pulsars: general – stars: neutron – starspots – X-rays: individual (SGR J1745-2900)

1. Introduction

Electromagnetic data-driven constraints to the mass and radius of NSs are very elusive. Radius measurements are mostly based on the observation of thermal emission and comparisons with theoretical models. The modeling, however, due to the complex and relativistic nature of NSs, suffers from a number of complications such as parameter degeneracy, the unknown NS equation of state (EOS), among other uncertainties, e.g., the distance to the object (see, e.g., Özel et al. 2016b; Özel & Freire 2016, and references therein). Notwithstanding, currently operating and future observatories, such as the *Neutron Star Interior Composition Explorer* (NICER; Gendreau et al. 2016), the enhanced X-ray Timing and Polarimetry mission (Zhang et al. 2019), and the Spectroscopic Time-Resolving Observatory for Broadband Energy X-rays (Ray et al. 2018), promise to greatly decrease the uncertainties of NS parameters. They are expected to provide masses and radii of NSs with an accuracy of a few percent (see Sieniawska et al. 2018, and references therein). In particular, one of the most significant developments in the measurement of the dense matter EOS is going to come from the NICER detector (see Özel et al. 2016a). The pulsed X-ray emission from hot spots on the surface of a rotating NS contains encoded information about its gravitational field and the properties of the spot emission pattern. NICER is using this approach to measure NS radii, based on the shape and amplitude of the pulsed emission observed from pulsar

surface in multiple wavebands. The data accuracy allows for precise comparison between measurements and models of NSs (Sieniawska et al. 2018), and will significantly improve our understanding of the physics of superdense matter in the universe. Indeed, NICER's X-ray data from PSR J0030+0451 has recently led to the first precise measurements (below 10% uncertainty) of the radius and mass of a pulsar (see Bilous et al. 2019; Bogdanov et al. 2019a, 2019b; Guillot et al. 2019; Miller et al. 2019; Raaijmakers et al. 2019; Riley et al. 2019). Besides, it has also allowed for the first map of the hot spots on the surface of a star. It provided the locations, shapes, sizes, and temperatures of the heated regions, which should give precise details of the magnetic field of a neutron star (NS). In this regard, it has already been found that the hot spots are far from antipodal, meaning that the magnetic field structure of a compact star is much more complex than previously thought.

In order to constrain uncertainties up to a few percent, stellar rotation should be large (>100 Hz), time resolution should be small ($\lesssim 10 \mu\text{s}$), and the number of photons should be large (at least $\sim 10^6$; Watts 2019). However, it is still possible to obtain interesting constraints on the properties of slowly rotating NSs, such as the Soft Gamma Repeaters (SGRs) and the Anomalous X-ray Pulsars (AXPs).

SGR 1745-2900 was the first SGR detected near the Milky Way center, Sagittarius A* (Kennea et al. 2013; Mori et al. 2013), and it is at distance of 8.3 kpc. It has a rotational period

$P = 3.76$ s and a changing spindown rate since the 2013 outburst. From its latest update, it is $\dot{P} \sim 3 \times 10^{-11}$ s/s (Coti Zelati et al. 2017). It is characterized by an X-ray luminosity $L_X \approx 10^{32} - 10^{36}$ erg s $^{-1}$. Owing to the flaring/outburst activity ($10^{38} - 10^{45}$ erg), SGR 1745-2900 has been classified within the SGR and AXP class (see, e.g., Olausen & Kaspi 2014). For a comprehensive review on observations of SGR 1745-2900, even the long-term ones, see Coti Zelati et al. (2015, 2017). For a systematic study of pulsed fractions of magnetars in quiescent state, including SGR 1745-2900, see Hu et al. (2019).

In this paper, we apply the approach of Turolla & Nobili (2013) for the emission of an NS with hot spots to two X-ray light curves of SGR 1745-2900 in different epochs. We use Genetic Algorithm (GA) techniques to constrain the mass and radius of SGR 1745-2900 with a minimum set of assumptions. This paper is organized as follows. In Section 2, we present the aspects of the model used for obtaining light curves from NS surfaces with hot spots. Section 3 explains the genetic algorithm techniques we use for fits of the SGR 1745-2900 light curves and how to obtain the NS parameters. In Sections 4 and 6 we present our results and discuss them.

2. Pulsed Profile Model

Here we show how the theoretical pulsed profiles are calculated for an NS with thermal spots on its surface. We follow the procedure of Turolla & Nobili (2013) to calculate the observed flux, which allows us to treat circular spots having arbitrary size and location on the stellar surface. The mass and radius of the star are denoted by M and R , respectively, and the spacetime outside the star is described by the Schwarzschild metric, i.e., we neglect rotational effects. This is an accurate approximation for SGR J1754-2900 given its slow rotational period of 3.76 s (clearly contrasting with millisecond pulsars, see, e.g., Belvedere et al. 2015; Cipolletta et al. 2015; Coelho et al. 2017). Let (r, θ, ϕ) be a spherical coordinate system with the origin at the stellar center and the polar axis along the line of sight (LOS; see Figure 1).

We consider an observer at $r \rightarrow \infty$ and a photon that arises from the stellar surface at $dS = R^2 \sin \theta d\theta d\phi$, making an angle α with the local normal to the surface ($0 \leq \alpha \leq \pi/2$). The photon path is then bended by an additional angle β owing to the spacetime curvature, and the effective emission angle as seen by the observer is $\psi = \alpha + \beta$ (see Figure 1). The geometry is symmetric relative to ϕ . Beloborodov (2002) has shown that the following simple approximate formula can be used to relate the emission angle α to the angle θ :

$$1 - \cos \alpha = (1 - \cos \theta) \left(1 - \frac{R_s}{R}\right), \quad (1)$$

where $R_s = 2GM/c^2$ is the Schwarzschild radius and G denotes the gravitational constant. We note that Equation (1) is a very good approximation for $R > 3R_s$ since it typically leads to very small errors ($\lesssim 1\%$). For the range of masses and corresponding radii of interest here, errors would be up to a few percent.

We assume that the spot emission follows a local Planck spectrum and that the observed flux comes mainly from hot spots. The intensity $B_\nu(T)$ is given by a blackbody with temperature T , where ν is the photon frequency. The flux is proportional to the visible area of the emitting region (S_ν) plus

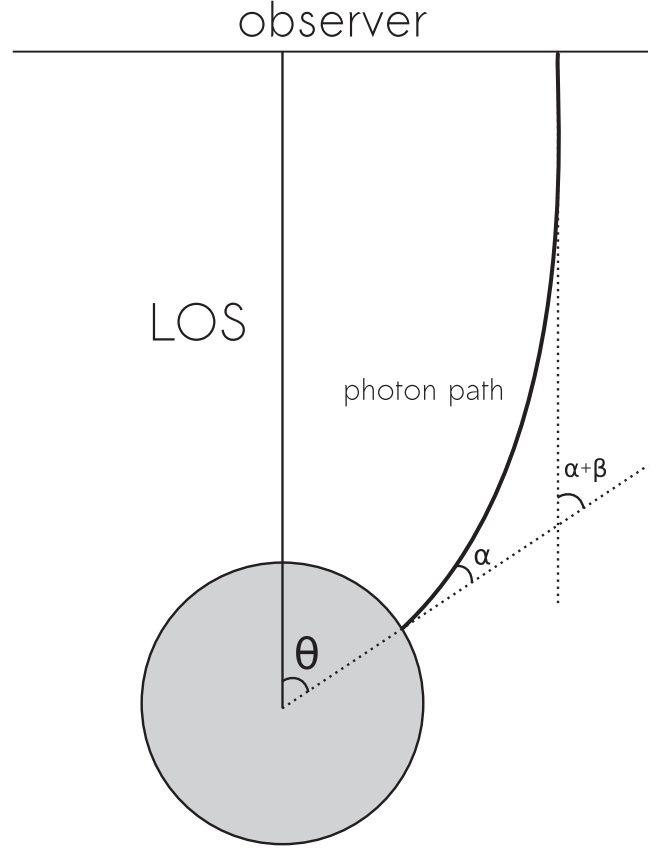


Figure 1. Illustration of the model geometry showing the photon trajectory and the angles θ , α , and β .

a relativistic correction, and it is given by (Beloborodov 2002; Turolla & Nobili 2013)

$$\begin{aligned} F_\nu &= \left(1 - \frac{R_s}{R}\right)^2 B_\nu(T) \int_{S_\nu} \cos \alpha \frac{d \cos \alpha}{d(\cos \theta)} ds \\ &= \left(1 - \frac{R_s}{R}\right)^2 B_\nu(T) (I_p + I_s), \end{aligned} \quad (2)$$

where

$$I_p = \int_{S_\nu} \cos \theta \sin \theta d\theta d\phi, \quad I_s = \int_{S_\nu} \sin \theta d\theta d\phi. \quad (3)$$

In polar coordinates, the circular hot spot has its center at θ_0 and a semiaperture θ_c . The spot is bounded by the function $\phi_b(\theta)$, where $0 \leq \phi_b \leq \pi$, and since we must consider just the visible part of the star, the spot must be also limited by a constant θ_F . It is defined by

$$\theta_F = \arccos \left(1 - \frac{c^2 R}{2GM}\right)^{-1}. \quad (4)$$

For a given bending angle β , θ_F occurs for the maximum emission α , i.e., $\alpha = \pi/2$. In Newtonian gravity, where $\beta = 0$, the maximum visible angle is $\theta_F = \pi/2$, meaning that half of the stellar surface is visible. However, for a relativistic star

$\theta_F > \pi/2$. Then

$$\begin{aligned} I_p &= 2 \int_{\theta_{\min}}^{\theta_{\max}} \cos \theta \sin \phi_b(\theta) d\theta, \\ I_s &= 2 \int_{\theta_{\min}}^{\theta_{\max}} \sin \theta \phi_b(\theta) d\theta, \end{aligned} \quad (5)$$

where θ_{\min} , θ_{\max} are the limiting values, to be determined to the spot considered. Turolla & Nobili (2013) show how to solve these integrals and how to carefully treat the limiting angles. Finally, the flux given by Equation (2) can be written as (Turolla & Nobili 2013)

$$F_\nu = \left(1 - \frac{R_s}{R}\right)^2 \frac{B_\nu(T)}{D^2} A_{\text{eff}}(\theta_c, \theta_0), \quad (6)$$

where D is the distance to the source, and it corrects the flux for an observer on Earth, and A_{eff} is the effective area, given by

$$A_{\text{eff}}(\theta_c, \theta_0) = R^2 \left[\frac{R_s}{R} I_s + \left(1 - \frac{R_s}{R}\right) I_p \right]. \quad (7)$$

The total flux produced by N_σ spots, where the σ th spot has a semiaperture $\theta_{c\sigma}$ and a temperature T_σ , can be calculated by adding up each contribution, and so we have

$$F_\nu^{\text{TOT}} = \left(1 - \frac{R_s}{R}\right)^2 \sum_{\sigma} \frac{B_\nu(T_\sigma)}{D^2} A_{\text{eff}}(\theta_{c\sigma}, \theta_{0\sigma}). \quad (8)$$

Besides, the pulse profile in a given energy band $[\nu_1, \nu_2]$ for a given spot σ is

$$F_\sigma(\nu_1, \nu_2) = \left(1 - \frac{R_s}{R}\right)^2 A_{\text{eff}}(\theta_{c\sigma}, \theta_{0\sigma}) \int_{\nu_1}^{\nu_2} \frac{B_\nu(T_\sigma)}{D^2} d\nu. \quad (9)$$

Therefore, one can rewrite Equation (8) for a given energy band, and it becomes

$$F^{\text{TOT}} = \sum_{\sigma} F_\sigma(\nu_1, \nu_2). \quad (10)$$

We define by \hat{r} the unit vector parallel to the rotation axis of the star, whose angular velocity is $\Omega = 2\pi/P$. It is also useful to introduce i , the angle between the LOS (unit vector \hat{l}) and the rotation axis, and j , the angle between the polar cap axis (unit vector \hat{c}) and the rotation axis ($\cos i = \hat{r} \cdot \hat{l}$ and $\cos j = \hat{r} \cdot \hat{c}$).

When the total flux, Equation (10), is calculated for a given configuration (i, j) for a time interval ($0 - P$), the typical result is a pulsed flux with a maximum (F_{\max}) and a minimum flux (F_{\min}). We shall use the normalized version of Equation (10), given by

$$\bar{F}^{\text{TOT}} = \frac{1}{\bar{N}} F^{\text{TOT}}, \quad (11)$$

where $\bar{N} = (F_{\max} + F_{\min})/2$. This normalization makes our model independent of the source distance, avoiding uncertainties linked to its precise determination. As SGR 1745-2900 is located near the Galactic center, its emission is heavily absorbed by the interstellar medium (ISM). However, we have verified that the ISM absorption can be neglected when using this normalization.

Table 1
List of Parameters and Ranges Used in Our Genetic Algorithm to Fit a Light-curve

Chromosome		
Gene	Definition	Range
$M(M_\odot)$	Star's mass	1.0–2.0
R (km)	Star's radius	8.9–13.7
N_σ	Number of hot spots	1–4
$\theta_{c\sigma}$	σ th spot's semiaperture	2°–180°
T_σ (keV)	σ th spot's temperature	0.0–0.9
θ_σ	σ th spot's colatitude	0°–180°
ϕ_σ	σ th spot's longitude	0°–360°
i	Angle between the LOS and the rotation axis	0°–90°
j	Angle between the polar cap and the rotation axis	0°–90°

We also define the pulsed fraction as

$$\text{PF} = \frac{F_{\max} - F_{\min}}{F_{\max} + F_{\min}}. \quad (12)$$

We have considered two main physical scenarios. (i) Two-spot configuration: the spots can have any size and temperature, but their centers are diametrically opposed (as the poles of a dipolar magnetic field). So, in this case, the spots are called polar caps and we can define a polar cap axis. (ii) Three-spot configuration: two-spot configuration plus a third spot of any size, location, and temperature.

As the star rotates, the polar coordinate of the spot's center, θ_0 , changes. Let $\gamma(t) = \Omega t$ be the star's rotational phase. Thus, from a geometrical reasoning we have that

$$\cos \theta_0(t) = \cos i \cos j - \sin i \sin j \cos \gamma(t), \quad (13)$$

where we have taken that i and j do not change with time.

3. Genetic Algorithms

A GA is a type of programming technique inspired in the modern understanding of natural selection, i.e., the best genetic code is the one whose phenotype manages to survive all natural vicissitudes. In our work, the chromosome is given by the set of all free parameters used to generate a theoretical pulse profile. In GA, the individual parameters of a chromosome are called genes. In our case, the mass and radius of the star (M and R) and the angles i and j are examples of genes. The entire set of genes is given in Table 1.

The desired phenotype is given by the observed pulse profile, and a chromosome fitness is calculated from it. A typical GA procedure comprises six steps:

- (1) Initialization: generation of a population of solutions (i.e., the chromosomes).
- (2) Phenotype evaluation—calculation of each model solution fitness.
- (3) Selection of the best solutions.
- (4) Reproduction—the genes of the best solutions are recombined.
- (5) Mutation—genes can be randomly selected and changed.
- (6) Population replacement.

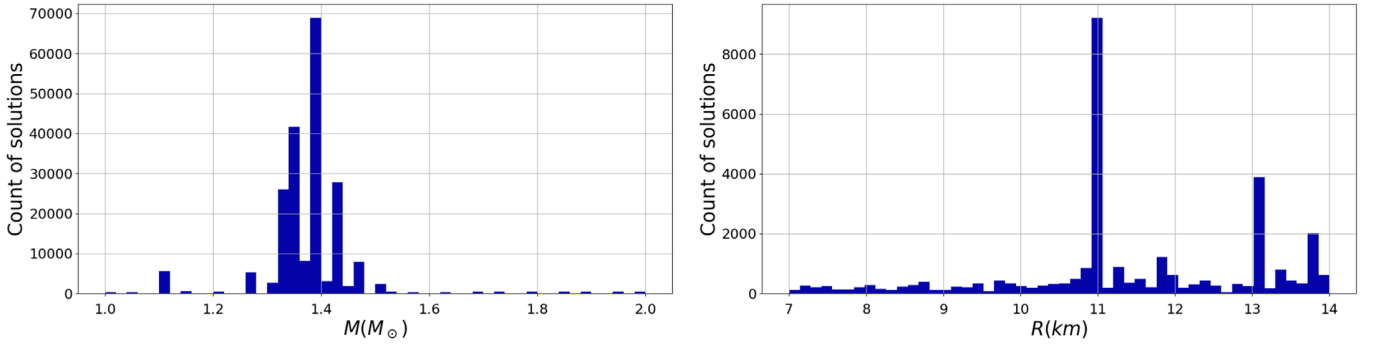


Figure 2. Histograms of all generations of solutions for D13 and D16. Left panel: from a normal distribution fit of the count of solutions one learns that the mean mass is $1.4M_{\odot}$ and the standard deviation is $0.1M_{\odot}$. Right panel: the histogram shows the count of solutions of different radii for $M = 1.4M_{\odot}$ (the mean mass). Also from a normal distribution fit, the mean radius in this case is given by $R = 10.9$ km and the standard deviation is 1.5 km.

Every iteration from step 2 to 6 is called a generation. In order to handle the genetic evolution and gene operations, we use the python library Pyevolve,¹² maintained by Christian S. Perone and modified by us.

3.1. Goodness-of-fit Calculation

The goodness-of-fit (GoF) of a given solution is calculated by the square of the difference between the model and the observed data. This is summed over the period of the pulsed profile, i.e.,

$$\text{GoF} = \sum_k [\bar{F}_k^{\text{TOT}} - \bar{F}_k^{\text{OBS}}]^2, \quad (14)$$

where \bar{F}_k^{TOT} is given by Equation (11). Note that the summation is discrete because of the data nature, but the temporal change in \bar{F}_k^{TOT} is controlled by Equation (13) over the star’s period. \bar{F}_k^{OBS} is the normalized observed flux and $k = 1-N$, where N is the number of observed points of the light curve. The optimal case would be $\text{GoF} = 0$. Therefore, the GA’s goal is to minimize GoF. We note that the data uncertainty σ of SGR 1745-2900 is a given constant for each data set, and hence GoF and the standard χ^2 ($\chi^2 \equiv \text{GoF}/\sigma^2$) carry the same statistical information. Since the definition given by Equation (14) is better suited for numerical computations, we use it for our fits. However, for statistical considerations we use χ^2 in order to be closer to standard analyses.

4. Results

Our aim is to find the set of parameters (see Table 1) that best fit the X-ray emission of SGR J1745-2900. We use the light curve from two epochs: 2013 (D13) and 2016 (D16)—presented by Coti Zelati et al. (2017). We let the parameters evolve as laid out in Section 3, and this is done independently for each data set. The final criterion to accept the best solutions is that both D13 and D16 result in the same most likely radius and inclination angles i and j , since these are expected to remain stable. For the determination of the mass and radius (based on the mean mass) ranges, global data analyses have been done, as explained below.

We have performed a “zeroth run” with all data points to find out which values of mass were the most likely to fit the SGR 1745-2900 light curve. This has been done in order to fix

one parameter and expedite the convergence time of subsequent (more precise) analyses. Our results are summarized in Figure 2 where one has the histogram of all generations of solutions fitting SGR 1745-2900 light curves. There one sees that, to one standard deviation, the majority of candidates have mass $1.4 \pm 0.1 M_{\odot}$. Thus, we take the SGR 1745-2900 mass as a fixed value in the subsequent fits and equal to the mean value of the normal distribution of Figure 2, the canonical NS ($1.4M_{\odot}$). However, as the large radius scattering of the zeroth run (when compared to the mass) already suggests ($R = 10.9 \pm 1.5$ km), we do not take the radius of SGR 1745-2900 as a fixed parameter in our subsequent investigations. Further details in this regard are given in Section 6.

As a first test, we have attempted to fit the light curve with only one hot spot, but the fits were very poor and are not discussed here. So we explore two spots, either having free positions or being antipodal. The two-spot fits can be seen in Figure 3 for the D13 data set, where the GoF per degree of freedom for the fits are in the range 0.041–0.044. In order to contemplate another geometry, we added a third hot spot with a free position relative to the other two, chosen to be antipodal. This choice of spots acts like a correction (which can be large) to the dipolar model, and, as shown below, it results in better fits to the light curves. A summary of the best-fit parameters for the D13 and D16 data sets in this case can be seen in Table 2. Figure 4 shows the best fits for the D13 and D16 sets using three spots. One can see that three spots fit reasonably well the main features of both data sets. For the D13 data set we find that GoF per degree of freedom is around 0.037, which is slightly better than the two-spot fits. We discuss further the quality of the fits and some subtleties of the D16 data set in Sections 4.1 and 6.

Figure 5 shows the hot spot positions on the stellar surface. The nonantipodal spot, in the southern hemisphere of the star, is responsible for the hottest blackbody temperature (0.87 keV) for both epochs, and its semiaperture increases from 2013 to 2016. This temperature is very close to 0.88 keV, as found by Coti Zelati et al. (2017) when fitting SGR 1745-2900 spectrum with a single hot spot.

4.1. Statistical Considerations

Given that some macroscopic aspects of the star should not change significantly from one period to the other, important conclusions could already be reached from one data set alone, for example D13. Clearly, three hot spots can fit better the data than two hot spots. This can be seen by their goodness-of-fit per degree

¹² <http://pyevolve.sourceforge.net/>

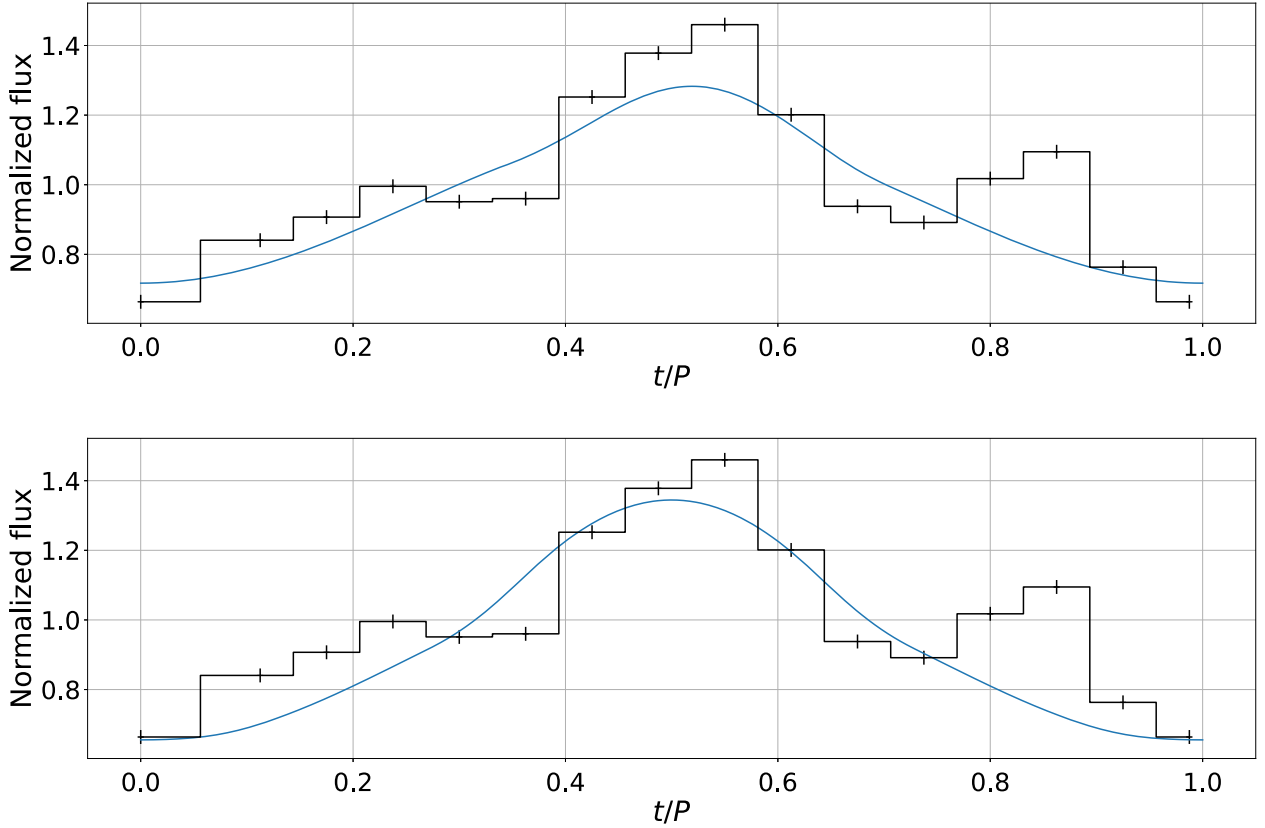


Figure 3. Upper panel: D13's fitting for two spots. The mass is $1.4 M_{\odot}$ and the two spots are free. The radius found is $R = 13.74$ km, and $\text{GoF} = 0.22$. In this case, the number of degrees of freedom (DoF) is 5 and hence $\text{GoF}/\text{DoF} = 0.044$. Bottom panel: D13's fitting for two antipodal spots. The mass is $1.4 M_{\odot}$, $R = 13.4$ km, and $\text{GoF} = 0.29$. Here, $\text{DoF} = 7$ and then $\text{GoF}/\text{DoF} = 0.041$. The normalization factor used in the plots is $\bar{N} = (F_{\max} + F_{\min})/2$.

Table 2
List of Solutions Found for D13 and D16

Best Solutions		
	D13	D16
GoF	0.11	0.27
$M (M_{\odot})$	1.40	1.40
R (km)	10.97	11.02
i	57°	58°
j	57°	56°
N_{σ}	3	3
PF	0.31	0.32
θ_{c1}	22°	40°
θ_1	0°	2°
ϕ_1	0°	351°
T_1 (keV)	0.6967	0.2857
θ_{c2}	16°	67°
θ_2	180°	178°
ϕ_2	0°	341°
T_2 (keV)	0.7858	0.0752
θ_{c3}	21°	26°
θ_3	102°	117°
ϕ_3	234°	225°
T_3 (keV)	0.8789	0.8798

Note. The positions of the spots can be visualized in Figure 5.

of freedom (GoF/DoF), as present in Figures 3 and 4 and in Table 3. However, for meaningful fit comparisons we calculate the standard reduced χ^2 , $\chi_{\text{red}}^2 := \text{GoF}/(\sigma^2 \text{DoF}) = \chi^2/\text{DoF}$ (σ is the

normalized error bar of the measurements). As is clear from Table 3, one can see that $\chi_{\text{red}}^2 = 2 - 6$ for both data sets. A possible interpretation of the large values of χ_{red}^2 is an overfitting due to the small number of data points (resulting in a small DoF). We have also performed the F-test between nested models. The p -values of these statistics suggest that there is not a preferred model. This is not surprising given the large number of parameters when compared to the data (small number of degrees of freedom).

In order to increase the number of degrees of freedom, we have also attempted to fit the data in other ways. We have assumed the case where the D13 and D16 data sets are fit simultaneously for certain parameters. Our results are summarized in Table 4 (for free fitting masses and radii) and 5 (free fitting radii and fixed mass at $1.4 M_{\odot}$). As one can clearly see, no case led to a preferred hot spot scenario. For instance, the χ_{red}^2 found are as large as before, which is yet a consequence of the very small number of observational data for SGR 1745-2900. One might wonder what is the minimum amount of data points needed to reach more stringent results. As the goodnesses of fit of Table 4 already suggests, assume that this hypothesized case still leads to $\text{GoF} \approx 0.6$ to the simultaneous fit. Then, it follows that $\chi_{\text{red}}^2 \approx 1.05$ would be reached when the degrees of freedom are approximately 70. This is much larger than our SGR 1745-2900 data. We come back to this issue in Section 6.

5. Additional Systematic Uncertainties to M and R

Care should be taken when extracting physical information from pure blackbody emission models. The processes

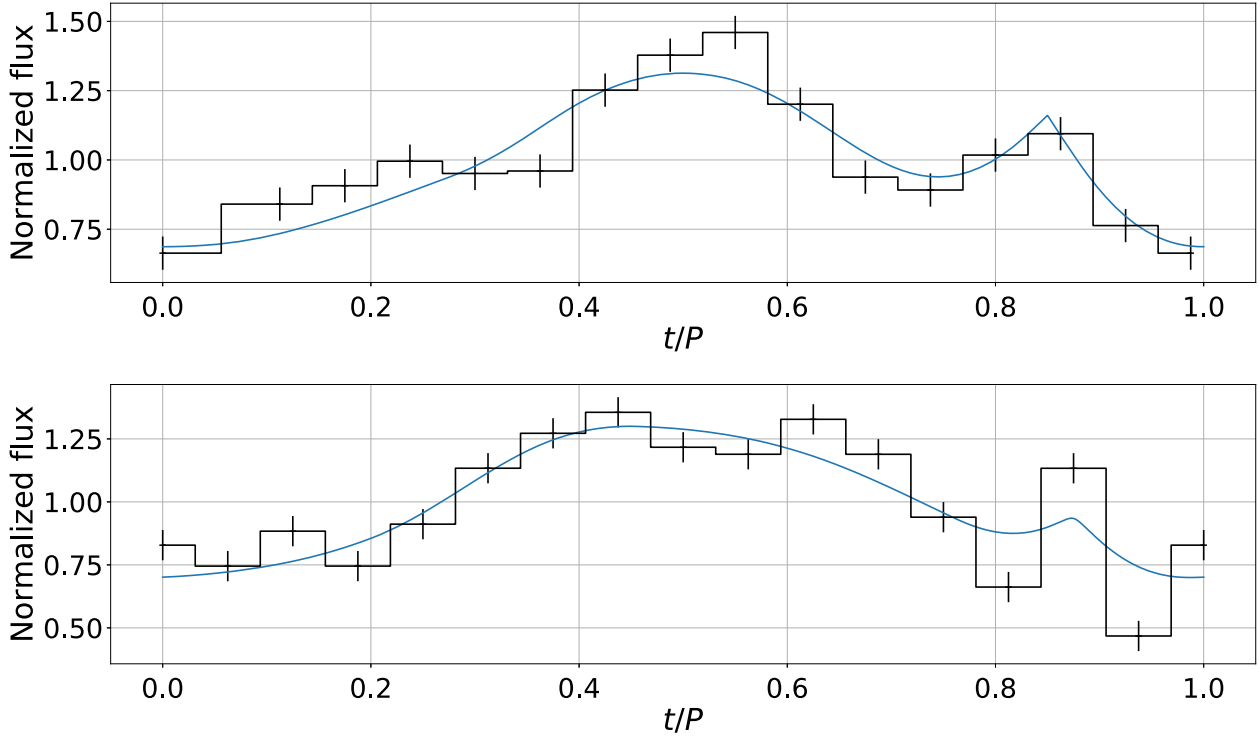


Figure 4. Upper panel: D13’s fitting for three spots. The mass is $1.4 M_{\odot}$ and two spots are antipodal, while the third one is free. The parameters found were $R = 10.97$ km, $j = 57^{\circ}$, $i = 57^{\circ}$, $T_1 = 0.6967$ keV, $T_2 = 0.7858$ keV, and $T_3 = 0.8789$ keV. $\text{GoF} = 0.11$ and the number of degrees of freedom here is 3 (the mass has been fixed by our zeroth run), which implies that $\text{GoF}/\text{DoF} = 0.037$. Bottom panel: D16’s fitting for three spots. Same mass and spot configurations as the D13 set. The parameters found were $R = 11.02$ km, $j = 58^{\circ}$, $i = 56^{\circ}$, $T_1 = 0.2857$ keV, $T_2 = 0.0752$ keV, and $T_3 = 0.8798$ keV. $\text{GoF} = 0.27$ ($\text{GoF}/\text{DoF} = 0.09$).

responsible for radiation emission in SGRs/AXPs are still largely unknown. They may be related to the presence of an atmosphere, although with properties quite different from those of standard atmospheres around passively cooling NSs, or even arise from a condensed surface. In both cases, the spectrum is expected to be thermal but not necessarily blackbody-like (see, e.g., Potekhin 2014, and references therein). In the case of NSs, one can expect that the emitting layers are comprised of just one, lightest available, chemical element because heavier elements sink into deeper layers due to the immense NS gravitational field.

Several works have addressed the problem of modeling the radiation transport in magnetized NS atmospheres. Shibano et al. (1992) were the first to perform detailed calculations of radiation spectra emerging from strongly magnetized NS photospheres, for the case of a fully ionized plasma. Besides, they have created a database of magnetic hydrogen spectra (see also Ho & Lai 2001; Ho et al. 2007, and references therein) and have shown that the spectra of magnetic hydrogen and helium atmospheres are softer than the nonmagnetic ones, but harder than the blackbody spectrum with the same temperature. Thus, if an amount of hydrogen is present in the outer layers (e.g., because of accretion of the interstellar matter), one can expect a pure hydrogen atmosphere. The latter can lead to much harder spectra in the Wien tail than the blackbody spectrum, because hotter deep layers are seen at high frequencies, where the spectral opacity is lower (Pavlov et al. 1996). In this case, the best-fit effective temperature of the atmosphere is considerably lower than the blackbody temperature, whereas the R/D ratio is larger than the one for the blackbody fit. Therefore, models that go beyond blackbody assumptions could have an important influence on SGR 1745-2900 mass and radius constraints.

A crude way of estimating further uncertainties to our M and R results due to the presence of atmospheres (e.g., hydrogen) could be as follows. One could average out the different hot spot temperatures in the D13 and D16 data sets and find a representative temperature and an uncertainty to them. With this uncertainty, one could estimate a range of wavelengths around the one for the maximum flux, λ_{max} (the most relevant wavelength for a given temperature), and then use known atmospheric models (Pons et al. 2007) to find the largest change of the flux (with respect to the blackbody) for this wavelength interval. Finally, by extrapolating these results, one gets the flux change estimates to our case. Using the spots’ temperatures from Table 2, one has that a representative value for them is 0.6 ± 0.3 keV ($7.0 \pm 0.3 \times 10^6$ K).¹³ For the above hot spot temperature uncertainty, one then expects the relevant wavelengths to range from $(2/3)\lambda_{\text{max}}$ to $2\lambda_{\text{max}}$. From Figure 6 of Ho et al. (2007; or Figure 1 of Suleimanov et al. 2009), it thus follows that hydrogen atmospheres of isolated magnetized stars should lead to a maximum difference in flux of approximately 20% when compared to blackbody results. If now one goes back to the expression of the flux and takes it as a function of M and R , it follows that a 20% change of it leads to a maximum uncertainty of approximately 7% to the radius and a 5% uncertainty to the mass with respect to blackbody outcomes. In order to reach these differences, we have taken

¹³ If one assumes that the flux of the hot spots is around 10 times larger than the one from the star’s surface (DeDeo et al. 2001), then the mean hot spot temperature should be around twice as large as the star’s surface. This allows us to conclude that our fit parameters are in good agreement with independent fits of surface temperatures and magnetic fields of stars (Pons et al. 2007) since the surface dipolar magnetic field of SGR 1745-2900 would be around 2×10^{14} G (Coti Zelati et al. 2015).

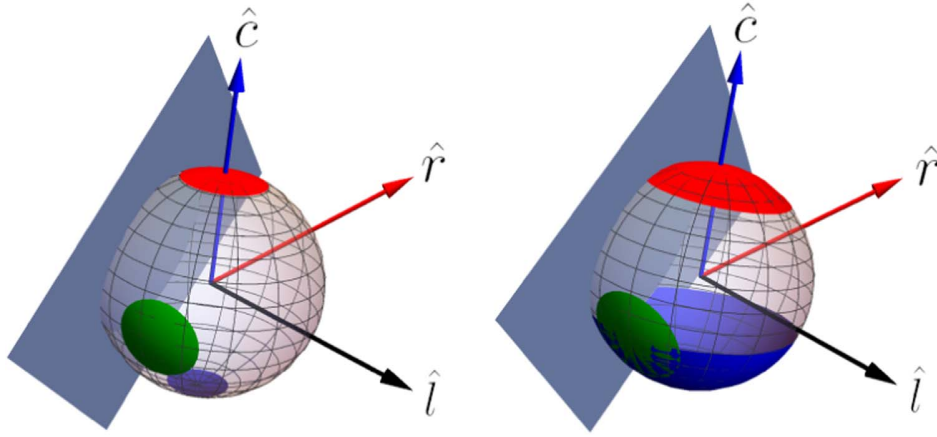


Figure 5. Left panel: D13’s three-spot positions. $T_1 = 0.6967$ keV (north pole spot), $T_2 = 0.7858$ keV (south pole spot), and $T_3 = 0.8789$ keV (nonantipodal—or southern hemisphere—spot). Right panel: D16’s three-spot positions. $T_1 = 0.2857$ keV (north pole spot), $T_2 = 0.0752$ keV (south pole spot), and $T_3 = 0.8798$ keV (nonantipodal spot). The arrows shown are the \hat{l} (LOS), around the star’s equatorial plane, \hat{c} (polar cap axis), crossing the north pole, and \hat{r} (rotation axis), the remaining arrow in the northern hemisphere. A plane is drawn as a reference to the maximum angle θ_F from which the observer cannot receive signals anymore.

Table 3

Acronym Meanings: Number of Fitting Parameters (NFP), Number of Data Points (NDP), and Degrees of Freedom (DoF)

Separated Fits of D13 and D16 Epochs						
Model	A1	B1	C1	A2	B2	C2
Data	D13	D13	D13	D16	D16	D16
N_σ	2	2	3	2	2	3
Antipodal	y	n	y	y	n	y
GoF	0.29	0.22	0.11	0.33	0.35	0.27
σ	0.09	0.09	0.09	0.15	0.15	0.15
$\chi^2 (D_i)$	35.80	27.16	13.58	14.67	15.56	12.00
χ^2_{red}	5.11	5.43	4.53	2.10	3.11	4.00
NFP	9	11	13	9	11	13
NDP	16	16	16	16	16	16
DoF	7	5	3	7	5	3
Models	A1/B1	B1/C1	B2/C2			
F-statistics	0.7954	1.4999	0.4444			
p -value	0.5012	0.3535	0.6775			

Note. σ stands for the data uncertainty. The row “antipodal” specifies whether models have (y) or do not have (n) two antipodal spots. The F-statistics and p -value are calculated by comparing two models as indicated by (X1)/(X2). The mean value of the mass has been fixed by the zeroth run, while the radii have been kept free for both epoch fits (see Section 4 for details).

$I_p = I_s \approx 0.015$ as a representative value. We note that the above changes could either increase or decrease the mean mass and radius of SGR 1745-2900.

Another source of uncertainty to our blackbody-based results is light beaming. This is specially the case for systems with high magnetic fields (DeDeo et al. 2001; Suleimanov et al. 2009), as is very likely the case of SGR 1745-2900 (Coti Zelati et al. 2015). Besides the plasma present in the magnetosphere, the presence of an accretion column itself could lead the emission from hot spots to be beamed (DeDeo et al. 2001). When compared to isotropic emission models, beaming could change pulsed fractions substantially (DeDeo et al. 2001). One could crudely estimate additional uncertainties to our model in the following way. The averaged semiaperture angle from our hot spots is $\theta_c \approx 32^\circ$ (see Table 2). From our model, the SGR 1745-2900 pulsed fraction is approximately 0.3.

Assuming that the hot spots could have a flux around 10 times larger than the star’s surface (DeDeo et al. 2001), from Figure 4 of DeDeo et al. (2001), one sees that the most appropriate beaming index in this case should be $n = 1$ ($I \propto \cos^n \alpha$) and changes in the maximum to minimum flux ratio could be 65% (pulsed fraction going from 0.1, the maximum in the isotropic case (DeDeo et al. 2001), to 0.3, the inferred one from our analysis of SGR 1745-2900). This means, crudely speaking, that the flux could change around 30% from a pure blackbody. In terms of differences to macroscopic parameters, following the procedure laid out before for atmospheres, we find that beaming leads to a maximum difference of 6% to the mass and 10% to the radius. We stress that this is very model and parameter dependent and it is not excluded larger or smaller corrections to blackbody outcomes. We comment further on beaming in the discussion section.

All the above systematic uncertainties indicate that, so far, it is not possible to make predictions for the mass and radius of SGR 1745-2900 as precise as one would wish. Combining the above models, systematic modeling uncertainties could lead the radius and the mass to change by up to 20% and 10%, respectively. However, a clear aspect from our simple analysis is that fits with three hot spots resulted in smaller GoF, meaning that they are more statistically relevant than two hot spots. We discuss possible interpretations of that in the next section.

6. Discussions and Conclusions

Chandra X-ray data have been used to constrain SGR J1745-2900 properties by means of genetic algorithm techniques. From SGR 1745-2900 X-ray light curve and pulsed fraction and the assumption that they come from stellar hot spots of any size, temperature, and stellar position, fits have been made attempting to reproduce as best as possible the data. We took into account relativistic effects such as light bending and we have ignored the effects of stellar rotation, well supported by the SGR 1745-2900 long rotation period (3.76 s). In this first approach, we have also ignored atmospheric effects and beaming on the fits. Global and split into two epochs data have been investigated for uncertainty estimations and precise parameter extractions.

Although fits with three hot spots lead to better-than-two GoFs, statistical considerations have shown that both models

Table 4
The Mass and Radius Were Free to Vary and Have Been Simultaneously Adjusted for the D13 and D16 Epochs

Simultaneous Fits of D13 and D16 with Free Masses and Radii								
Model	D		E		F		G	
Data	D13 + D16		D13+D16		D13+D16		D13+D16	
N_σ	2		2		3		3	
Antipodal	y		n		y		n	
GoF	0.5882		0.5589		0.5203		0.3761	
χ^2 (D13+D16)	45.21		42.71		39.28		19.05	
χ^2_{red}	2.83		3.56		4.91		4.76	
NFP	16		20		24		28	
NDP	32		32		32		32	
DoF	16		12		8		4	
D_i	D13	D16	D13	D16	D13	D16	D13	D16
GoF	0.2413	0.3469	0.2260	0.3329	0.2044	0.3159	0.0294	0.3467
σ	0.09	0.15	0.09	0.15	0.09	0.15	0.09	0.15
χ^2 (D_i)	29.79	15.42	27.91	14.80	25.24	14.04	3.64	15.41
Models	D/E	E/F	F/G					
F-statistics	0.1760	0.1746	1.0619					
p -value	0.9470	0.9452	0.4774					

Note. The intermediate GoF and χ^2 (D13 and D16) for the simultaneous fits are shown in the midpart of the table. The meaning of the acronyms and statistics are the same as in Table 3.

Table 5
The Meaning of the Acronyms Are the Same As in Table 3

Simultaneous Fittings for D13 and D16. Stellar Mass Is Fixed at $1.4M_\odot$				
Model	H		I	
Data	D13 + D16		D13 + D16	
N_σ	2		3	
Antipodal	y		y	
GoF	0.5976		0.5272	
χ^2 (D13+D16)	46.40		40.20	
χ^2_{red}	2.73		4.47	
NFP	15		23	
NDP	32		32	
DoF	17		9	
D_i	D13	D16	D13	D16
GoF	0.2511	0.3465	0.2122	0.3150
σ	0.09	0.15	0.09	0.15
χ^2 (D_i)	31.00	15.40	26.20	14.00
Models	H/I			
F-statistics	0.1735			
p -value	0.9891			

Note. The middle part refers to the intermediate GoF and χ^2 for the simultaneous fits, as in Table 4.

are equivalent. This is due to the limitation of the observational data itself, which severely decreases the degrees of freedom of the system for the models. Even though the resultant statistics is poor in any case, one could interpret the above-mentioned ambiguity as a suggestion that a multipolar structure in SGR 1745-2900 should not be excluded. This comes from the fact that at least one model we have analyzed is a reasonable first-order description to NSs. Indeed, this should be the case for dipolar models since braking index measurements for pulsars are not too far from three (see, e.g., Coelho et al. 2016; de Araujo et al. 2016a, 2016b, 2016c, 2017) and some

properties of SGRs/AXPs would need strong dipolar fields (Coelho et al. 2017). Thus, if two hot spots are reasonable at the surfaces of stars and they are statistically equivalent to three hot spots, one should not disregard the latter (or other situations with more hot spots) in modeling NS light curves. This has indeed been shown to be the case of pulsar PSR J0030+0451, which strengthens even further the suggestions of our statistical analysis for SGR 1745-2900. We leave for future work investigations of light curves of NSs with more data points using the GA techniques developed here. In particular, we plan to investigate PSR J0030+0451, given that the hot spot configuration found for it is very different from what is expected in the dipolar case (see Bilous et al. 2019; Bogdanov et al. 2019a, 2019b; Guillot et al. 2019; Miller et al. 2019; Raaijmakers et al. 2019; Riley et al. 2019).

Regarding the normalized flux fits, some words are in order. First, we have not fitted both data sets entirely independently. We have taken the mean mass from our zeroth run (with all data sets run simultaneously; see Figure 2) in order to minimize the computation time of other parameters. This is reasonable because SGR 1745-2900 is an isolated NS. We have not taken the mean value of the radius from our zeroth run, but we have treated it as a free parameter in the D13 and D16 fits. However, we expect them, as well as the inclination angles i and j , to remain almost the same, as indeed happened to many populations, and that has been used as our criterion for selecting “the best” solution (see Table 2).¹⁴ This shows consistency in our simple model. Nonetheless, the fit of the last points of the D16 data set indicates that the model is not entirely appropriate. This could be due to several reasons, one

¹⁴ The GA we have made use of has a mutation parameter to prevent solutions from getting stuck in a false minimum. We have taken it to be 0.1, meaning that in every generation 10% of the population suffers mutation. Besides that, we have used many initial populations and have stopped running generations when the best solution (minimum of χ^2) had been the same for many successive generations (around 1000). Not all populations converged to the same solution, but we selected the physical one as the best of those with the same macroscopic parameters for both data sets.

of them being the small amount of data itself (see Coti Zelati et al. 2017). Another reason would be that we have modeled the data in a very simple way, forcing both epochs to be described equally, and important effects might have been left out. An example of that could be significant changes of SGR 1745-2900 atmospheric conditions from one epoch to the other. A sharp change of the beaming might also take place, meaning that accretion columns could change their properties due to an outburst. Indeed, it could rearrange or disturb the atmosphere of the magnetized NS, and as a result the flux could change non-negligibly. Thus, better fits could raise if different atmospheric models are taken for the epochs analyzed, which we have not done in this first analysis. We plan to elaborate on the above in future works.

The uncertainties to M and R , coming from our zeroth run, should be taken just as indicative. Systematic uncertainties due to different models could also be relevant. We have investigated some of them and it seems that atmospheric models and beaming could play an important role in more realistic uncertainties to the parameters. Rough estimates suggest that variations of the flux with respect to our model are around 50%, meaning an additional 20% (10%) radius (mass) uncertainty to SGR 1745-2900's mean blackbody outcomes. However, it is important to bear in mind that models for NS atmospheres are still debatable and blackbody results could give us interesting insights for testing them more precisely.

We now make a few comments regarding the case the surface of SGR 1745-2900 has three hot spots. The hot spots in Figure 5, in the light of the Gourgouliatos & Hollerbach (2017) results, could be interpreted as follows. First of all, the magnetic field at the stellar surface in both data sets seems to be far from axially symmetric because of the better fits coming from three hot spots. For the D13 set, the presence of the nonantipodal spot (southern hemisphere), whose size is comparable to the antipodal spots (north and south poles), suggests that the toroidal field should be relevant. Indeed, purely dipolar models would lead to spot areas of the order of the polar cap area $A_{pc} = \pi R_{pc}^2$, where $R_{pc} = \sqrt{2\pi R^3 / (cP)}$ (see, e.g., Ruderman & Sutherland 1975; Cheng & Ruderman 1977; Chen & Ruderman 1993), and, for an NS with $R = 11$ km and $P = 3.76$ s, $A_{pc} \approx 0.023$ km², much smaller than the areas of the spots in Figure 5. This clearly indicates that the magnetic field of SGR J1745-2900 is very different from a dipolar configuration. According to Gourgouliatos & Hollerbach (2017), a very localized spot (≈ 1 km) implies a very specific configuration where 99% of the energy is in the toroidal field. However, smaller toroidal energy budgets lead to more extended magnetic zones at the stellar surface and, as a consequence, an extended hot region (Gourgouliatos & Hollerbach 2017). Therefore, our results suggest that SGR J1745-2900 has a complex multipolar magnetic field structure, with a relevant toroidal component for both D13 and D16 data sets (not overwhelmingly dominant, though, because the hot spots are not small). Indeed, the variability of the spindown rate of SGR J1745-2900 implies that its characteristic age (≈ 4.3 kyr) is accurate to its real age up to one order of magnitude, meaning it would be a young source and hence it might have a quite complex magnetic field structure. In addition, the association of some SGRs/AXPs with supernova remnants suggests that the ages of these sources are typically $\leq 10^4$ – 10^5 yr (see, e.g., Kaspi & Beloborodov 2017).

The variation of the spots' temperatures and sizes from one epoch to the other is pronounced. One might interpret these results as due to thermal conduction and temperature gradients on the stellar surface. This seems reasonable given the very large electric conductivity of the star, which would also imply a very large thermal conductivity, and so very small timescales for temperature variations. The temperature change of the spot at the north pole might be associated with its expansion, triggered by temperature gradients, and standard cooling processes. The significant temperature decrease of the south pole hot spot might also be due to its large increase, possibly triggered by similar reasons as to what happened to the north pole hot spot. However, the temperature change in the nonantipodal spot has been practically zero, and that might be related to its partial overlap with the south pole hot spot.

Apart from temperature values of some of the hot spots of SGR 1745-2900, our results contrast with those of Coti Zelati et al. (2017) for the same source and data. First, we have taken two and three hot spots, while they assume just a single one. Second, we have found that the sizes of the spots increase from 2013 to 2016, while the opposite happens to their single spot. In their case, the spot shrinking was important to explain the increase of the pulsed fraction. In our case, the increase of the pulsed fraction might be explained with the large temperature changes of some spots from one epoch to the other. Due to the relevance of hot spot size evolution to physical processes taking place in stars (Coti Zelati et al. 2017), we leave precise analyses thereof in light of our results to be carried out elsewhere.

We stress an important point of our analysis. One can see from the bottom panel of Figure 4 that our best fit to the normalized flux has not been so good for the last 2016 data points. This means that our pulsed fraction increase is not as pronounced (see Table 2) as the observed one (from approximately 0.35 to 0.58; Coti Zelati et al. 2017). We have tried to enhance the 2016 fit with three free hot spots on the stellar surface, but no better results have been found. Since in this case the number of free parameters is the same as the data points for each set, we have kept analyses with three hot spots where two of them are antipodal, which naturally have less parameters than data. Thus, it is still pending ways to enhance the fit of the last data points of the 2016 light curve of SGR 1745-2900.

We have performed a light curve and pulsed fraction X-ray data analysis of SGR 1745-2900 without assuming any specific nuclear EOS. The data analysis based on the blackbody model alone indicates that SGR J1745-2900 has as the most likely mass the canonical NS mass $M = 1.4 M_{\odot}$, and it should have a corresponding radius $R_{1.4} \approx 9.4$ – 12.3 km. This result obtained from electromagnetic data agrees with recent constraints obtained from gravitational wave observations that lead to $R_{1.4} \lesssim 13.5$ km for hadronic stars (Abbott et al. 2018; Annala et al. 2018; De et al. 2018; Most et al. 2018). The above values would disfavor relativistic mean-field theory models, which usually lead to $R_{1.4}$ larger than 13.5 km (Fortin et al. 2016). Some Skyrme models (see, for instance, Figure 7 of Fortin et al. 2016, where models should have $R_{1.4}$ in the range of 11.5–13.5 km), as well as the MPA1, APR, and WFF parameterizations (see their $R_{1.4}$ in Read et al. 2009), among other EOS, especially stiffer, seem to be favored by our analysis. However, the systematic modeling uncertainties that we have pointed out before significantly weaken the above

EOS constraints, and no definite conclusion can be reached so far; this might be mitigated just when precise emissions models are analyzed or when more data is collected. Finally, the question of whether SGR J1745-2900 could be a hybrid star remains open since many of the hybrid EOS would lead to a third family of NSs which would satisfy our light-curve constraints (see, for instance, Paschalidis et al. 2018; Sieniawska et al. 2019 and references therein).

Summing up, we have carried out fits of the light curve of SGR 1745-2900 using the genetic algorithm techniques. Although the observational data of SGR 1745-2900 is not enough to achieve stringent statistical conclusions, our analysis gave us important hints on magnetic fields of SGRs/AXPs. The fact that two or three hot spots could equally describe the data of SGR 1745-2900 suggests that in NS cases with more observations one should not disregard a multipolar structure of their magnetic fields.

We thank the anonymous referee for important suggestions which have improved our work. We would like to thank F. C. Zelati for providing us with the light-curve data. We are grateful to Professor John Boguta for insightful discussions on the nuclear EOS and relativistic mean-field theory models. R.C. R.L. acknowledges the support of Fundação de Amparo à Pesquisa e Inovação do Estado de Santa Catarina (FAPESC) under grant No. 2017TR1761. J.G.C. is likewise grateful to the support of Conselho Nacional de Desenvolvimento Científico e Tecnológico—CNPq (421265/2018-3 and 305369/2018-0). J.P.P. acknowledges the financial support given by Fundação de Amparo à Pesquisa do Estado de São Paulo (FAPESP) (2015/04174-9 and 2017/21384-2), and the Polish National Science Centre under grant No. 2016/22/E/ST9/00037. C.V.R. is grateful for grants from CNPq (303444/2018-5) and FAPESP (2013/26258-4).

ORCID iDs

Rafael C. R. de Lima  <https://orcid.org/0000-0003-1718-3838>

Jaziel G. Coelho  <https://orcid.org/0000-0001-9386-1042>

Jonas P. Pereira  <https://orcid.org/0000-0002-9385-5176>

Claudia V. Rodrigues  <https://orcid.org/0000-0002-9459-043X>

Jorge A. Rueda  <https://orcid.org/0000-0002-3455-3063>

References

Abbott, B. P., Abbott, R., Abbott, T. D., et al. 2018, *PhRvL*, **121**, 161101
 Annala, E., Gorda, T., Kurkela, A., & Vuorinen, A. 2018, *PhRvL*, **120**, 172703
 Beloborodov, A. M. 2002, *ApJL*, **566**, L85
 Belvedere, R., Rueda, J. A., & Ruffini, R. 2015, *ApJ*, **799**, 23
 Bilous, A. V., Watts, A. L., Harding, A. K., et al. 2019, *ApJL*, **887**, L23

Bogdanov, S., Guillot, S., Ray, P. S., et al. 2019a, *ApJL*, **887**, L25
 Bogdanov, S., Lamb, F. K., Mahmoodifar, S., et al. 2019b, *ApJL*, **887**, L26
 Chen, K., & Ruderman, M. 1993, *ApJ*, **402**, 264
 Cheng, A. F., & Ruderman, M. A. 1977, *ApJ*, **214**, 598
 Cipolletta, F., Cherubini, C., Filippi, S., Rueda, J. A., & Ruffini, R. 2015, *PhRvD*, **92**, 023007
 Coelho, J. G., Cáceres, D. L., de Lima, R. C. R., et al. 2017, *A&A*, **599**, A87
 Coelho, J. G., Pereira, J. P., & de Araujo, J. C. N. 2016, *ApJ*, **823**, 97
 Coti Zelati, F., Rea, N., Papitto, A., et al. 2015, *MNRAS*, **449**, 2685
 Coti Zelati, F., Rea, N., Turolla, R., et al. 2017, *MNRAS*, **471**, 1819
 de Araujo, J. C. N., Coelho, J. G., & Costa, C. A. 2016a, *JCAP*, **2016**, 023
 de Araujo, J. C. N., Coelho, J. G., & Costa, C. A. 2016b, *ApJ*, **831**, 35
 de Araujo, J. C. N., Coelho, J. G., & Costa, C. A. 2016c, *EPJC*, **76**, 481
 de Araujo, J. C. N., Coelho, J. G., & Costa, C. A. 2017, *EPJC*, **77**, 350
 DeDeo, S., Psaltis, D., & Narayan, R. 2001, *ApJ*, **559**, 346
 De, S., Finstad, D., Lattimer, J. M., et al. 2018, *PhRvL*, **121**, 091102
 Fortin, M., Providencia, C., Raduta, A. R., et al. 2016, *PhRvC*, **94**, 035804
 Gendreau, K. C., Arzoumanian, Z., Adkins, P. W., et al. 2016, *Proc. SPIE*, **9905**, 99051H
 Gourgouliatos, K. N., & Hollerbach, R. 2017, *ApJ*, **852**, 21
 Guillot, S., Kerr, M., Ray, P. S., et al. 2019, *ApJL*, **887**, L27
 Ho, W. C. G., Kaplan, D. L., Chang, P., van Adelsberg, M., & Potekhin, A. Y. 2007, *MNRAS*, **375**, 821
 Ho, W. C. G., & Lai, D. 2001, *MNRAS*, **327**, 1081
 Hu, C.-P., Ng, C. Y., & Ho, W. C. G. 2019, *MNRAS*, **485**, 4274
 Kaspi, V. M., & Beloborodov, A. M. 2017, *ARA&A*, **55**, 261
 Kennea, J. A., Burrows, D. N., Kouveliotou, C., et al. 2013, *ApJL*, **770**, L24
 Miller, M. C., Lamb, F. K., Dittmann, A. J., et al. 2019, *ApJL*, **887**, L24
 Mori, K., Gotthelf, E. V., Zhang, S., et al. 2013, *ApJL*, **770**, L23
 Most, E. R., Weih, L. R., Rezzolla, L., & Schaffner-Bielich, J. 2018, *PhRvL*, **120**, 261103
 Olausen, S. A., & Kaspi, V. M. 2014, *ApJS*, **212**, 6
 Özel, F., & Freire, P. 2016, *ARA&A*, **54**, 401
 Özel, F., Psaltis, D., Arzoumanian, Z., Morsink, S., & Bauböck, M. 2016a, *ApJ*, **832**, 92
 Özel, F., Psaltis, D., Güver, T., et al. 2016b, *ApJ*, **820**, 28
 Paschalidis, V., Yagi, K., Alvarez-Castillo, D., Blaschke, D. B., & Sedrakian, A. 2018, *PhRvD*, **97**, 084038
 Pavlov, G. G., Zavlin, V. E., Truemper, J., & Neuhäuser, R. 1996, *ApJL*, **472**, L33
 Pons, J. A., Link, B., Miralles, J. A., & Geppert, U. 2007, *PhRvL*, **98**, 071101
 Potekhin, A. Y. 2014, *PhyU*, **57**, 735
 Raaijmakers, G., Riley, T. E., Watts, A. L., et al. 2019, *ApJL*, **887**, L22
 Ray, P. S., Arzoumanian, Z., Brandt, S., et al. 2018, *Proc. SPIE*, **10699**, 1069919
 Read, J. S., Lackey, B. D., Owen, B. J., & Friedman, J. L. 2009, *PhRvD*, **79**, 124032
 Riley, T. E., Watts, A. L., Bogdanov, S., et al. 2019, *ApJL*, **887**, L21
 Ruderman, M. A., & Sutherland, P. G. 1975, *ApJ*, **196**, 51
 Shibano, I. A., Zavlin, V. E., Pavlov, G. G., & Ventura, J. 1992, *A&A*, **266**, 313
 Sieniawska, M., Bejger, M., & Haskell, B. 2018, *A&A*, **616**, A105
 Sieniawska, M., Turczański, W., Bejger, M., & Zdunik, J. L. 2019, *A&A*, **622**, A174
 Suleimanov, V., Potekhin, A. Y., & Werner, K. 2009, *A&A*, **500**, 891
 Turolla, R., & Nobili, L. 2013, *ApJ*, **768**, 147
 Watts, A. L. 2019, in AIP Conf. Proc. 2127, Xiamen-CUSTIPEN Workshop on the EOS of Dense Neutron-Rich Matter in the Era of Gravitational Wave Astronomy, ed. A. Li, B.-A. Li, & F. Xu (Melville, NY: AIP), 020008
 Zhang, S., Santangelo, A., Feroci, M., et al. 2019, *SCPMA*, **62**, 29502



Magnetic Fields and Afterglows of BdHNe: Inferences from GRB 130427A, GRB 160509A, GRB 160625B, GRB 180728A, and GRB 190114C

J. A. Rueda^{1,2,3,4,5,6}, Remo Ruffini^{1,2,3,7,8}, Mile Karlica^{1,2,7}, Rahim Moradi^{1,2,9}, and Yu Wang^{1,2,9}

¹ICRA, Dipartimento di Fisica, Sapienza Università di Roma, P.le Aldo Moro 5, I-00185 Rome, Italy

²ICRANet, Piazza della Repubblica 10, I-65122 Pescara, Italy; yu.wang@icranet.org

³ICRANet-Rio, Centro Brasileiro de Pesquisas Físicas, Rua Dr. Xavier Sigaud 150, 22290-180 Rio de Janeiro, Brazil

⁴ICRANet-Ferrara, Dipartimento di Fisica e Scienze della Terra, Università degli Studi di Ferrara, Via Saragat 1, I-44122 Ferrara, Italy

⁵Dipartimento di Fisica e Scienze della Terra, Università degli Studi di Ferrara, Via Saragat 1, I-44122 Ferrara, Italy

⁶INAF, Istituto di Astrofisica e Planetologia Spaziali, Via Fosso del Cavaliere 100, I-00133 Rome, Italy

⁷Université de Nice Sophia Antipolis, CEDEX 2, Grand Château Parc Valrose, Nice, France

⁸INAF, Viale del Parco Mellini 84, I-00136 Rome, Italy

⁹INAF—Osservatorio Astronomico d’Abruzzo, Via M. Maggini snc, I-64100 Teramo, Italy; rahim.moradi@inaf.it

Received 2019 May 22; revised 2020 March 14; accepted 2020 March 16; published 2020 April 24

Abstract

GRB 190114C is the first binary-driven hypernova (BdHN) fully observed from initial supernova (SN) appearance to the final emergence of the optical SN signal. It offers an unprecedented testing ground for the BdHN theory, which is here determined and further extended to additional gamma-ray bursts (GRBs). BdHNe comprise two subclasses of long GRBs, with progenitors a binary system composed of a carbon–oxygen star (CO_{core}) and a neutron star (NS) companion. The CO_{core} explodes as an SN, leaving at its center a newborn NS (νNS). The SN ejecta hypercritically accretes on both the νNS and the NS companion. BdHNe I are very tight binaries, where the accretion leads the companion NS to gravitationally collapse into a black hole (BH). In BdHN II, the accretion rate onto the NS is lower, so there is no BH formation. We observe the same afterglow structure for GRB 190114C and other selected examples of BdHNe I (GRB 130427A, GRB 160509A, GRB 160625B) and for BdHN II (GRB 180728A). In all cases, the afterglows are explained via the synchrotron emission powered by the νNS , and their magnetic field structures and their spin are determined. For BdHNe I, we discuss the properties of the magnetic field embedding the newborn BH, which was inherited from the collapsed NS and amplified during the gravitational collapse process, and surrounded by the SN ejecta.

Unified Astronomy Thesaurus concepts: High energy astrophysics (739); Gamma-ray bursts (629); Black hole physics (159)

1. Introduction

We first briefly review the traditional afterglow models and the possible alternatives. This task has been facilitated by the publication of the comprehensive book by Zhang (2018). We focus on additional results introduced since then by the understanding of the X-ray flare (Ruffini et al. 2018e) and afterglow of GRB 130427A (Ruffini et al. 2018b) and GRB 190114C (Ruffini et al. 2019b, 2019a).

We first recall the well-known discoveries by the Beppo-SAX satellite:

1. The discovery of the first afterglow in GRB 970228 (Costa et al. 1997);
2. The consequent identification of the cosmological redshift of GRBs (GRB 970508; Metzger et al. 1997), which proved the cosmological nature of GRBs and their outstanding energetics; and
3. The first clear coincidence of a long GRB with the onset of a supernova (GRB 980425/SN 1998bw, Galama et al. 1998).

Even before these discoveries, three contributors, based on first principles, formulated models for long GRBs by assuming their cosmological nature and their origination from black hole (BH) formation. At the time, these works expressed the point of view of a small minority. A parallel successful move was done by Paczynski and collaborators for short GRBs

(Paczynski 1991, 1992; Narayan et al. 1992). The aforementioned three contributors are the following:

1. Damour & Ruffini (1975) predicted that a vacuum polarization process occurring around an overcritical Kerr–Newman BH leads toward GRB energetics of up to 10^{54} erg, linking their activities as well to the emergence of ultra-high-energy cosmic rays;
2. Rees & Meszaros (1992) and Mészáros & Rees (1997) also proposed a BH as the origin of GRBs, but there, an ultrarelativistic blast wave, whose expansion follows the Blandford–McKee self-similar solution, was used to explain the prompt emission phase (Blandford & McKee 1976);
3. Woosley (1993) linked the GRB’s origin to a Kerr BH emitting an ultrarelativistic jet originating from the accretion of toroidal material onto the BH. There, the idea was presented that for long GRBs, the BH would be likely produced from the direct collapse of a massive star—a “failed” SN leading to a large BH of approximately $5M_{\odot}$, possibly as high as $10M_{\odot}$, a “collapsar.”

1.1. Traditional Afterglow Model Originating from BH

The paper by Damour & Ruffini (1975) has only recently started to attract attention for binary-driven hypernovae (BdHNe) in the context of the exact solution of the Einstein–Maxwell

equations by Wald (1974); see Section 2 for further details. The papers by Rees & Meszaros (1992), Mészáros & Rees (1997), and Woosley (1993), on the contrary, have led to the traditional GRB model. There, the afterglow is explained by the synchrotron/synchrotron self-Compton (SSC) emission from accelerated electrons when an ultrarelativistic blast wave of $\Gamma \sim 1000$ is slowed down by the circumburst medium (Waxman & Piran 1994; Sari & Piran 1995; Sari 1997; Wijers et al. 1997; Sari et al. 1998). This has become known as the ultrarelativistic shock-wave model. As pointed out by Zhang (2018), this ultrarelativistic blast-wave model has been traditionally adopted in order to explain a vast number of observations:

1. The X-ray afterglow, including the steep and the shallow decay phases all the way to the X-ray flares (see Section 2.2.2 in Zhang 2018);
2. The optical and the radio afterglow (see Sections 2.2.3 and 2.2.4 in Zhang 2018); and
3. The high-energy afterglow in the GeV emission (see Sections 2.2.5 in Zhang 2018).

Related to the above traditional approach are the papers by Ruffini & Wilson (1975) and Blandford & Znajek (1977), which addressed the gravitational accretion of magnetized plasma of infinite conductivity into a Kerr BH. Such a gravitation-dominated accretion theory implies the need for a large magnetic field ($\sim 10^{15}$ G) and high density ($\sim 10^{12} - 10^{13}$ g cm $^{-3}$) near the last stable orbit around a $\sim 3 M_{\odot}$ BH. This gravitation-dominated accretion has been commonly adopted as input for the above-mentioned ultrarelativistic jetted emission from the accretion (at a rate $\sim 1 M_{\odot}$ s $^{-1}$) onto a Kerr BH to power a GRB of luminosity $\sim 10^{52}$ erg s $^{-1}$.

Since 2018, it has become clear that the three above processes do not share a common origin, and they are not related to an ultrarelativistic blast wave.

An electrodynamic accretion process of ionized plasma as an alternative to the gravitation-dominated accretion theory has been announced (see companion paper Ruffini et al. 2019b), operating at a density of $\sim 10^{-14}$ g cm $^{-3}$ (see Section 8).

1.2. Role of Magnetars and Spinning Neutron Stars

In parallel, a variety of models have been developed, adopting, instead of a BH, energy injection from various combinations of NSs and “magnetars.” Dai & Lu (1998a, 1998b) and Zhang & Mészáros (2001) adopted energy injection from a long-lasting spinning-down millisecond pulsar or a magnetar (magnetic dipole strength $\sim 10^{15}$ G). Within this approach, the shallow decay or the plateau observed at times $\sim 10^2 - 10^4$ s is attributed to the energy injection by the magnetic dipole radiation (see, e.g., Fan & Xu 2006; de Pasquale et al. 2007; Fan et al. 2013). The magnetar model is consistent with so-called “internal plateaus,” namely the ones that end with a very steep decay slope, which cannot be explained solely by external shock waves. The steep drop is thus explained by the sudden decrease in the energy injection by the pulsar/magnetar engine at the characteristic lifetime of magneto-dipole emission (Troja et al. 2007; Rowlinson et al. 2010, 2013; Lü & Zhang 2014; Li et al. 2018b; Lü et al. 2015). All these alternative models converge finally to the ultrarelativistic shock-wave model. We show below how from 2018 the observations sharply constrain this model.

As we will show below, in the BdHN scenario, the GRB afterglow originates from mildly relativistic expanding SN ejecta with energy injection from the newly born neutron star (hereafter ν NS) at its center and from the ν NS pulsar emission itself.

1.3. The Role of Binary Progenitors in GRBs

Alternatively to the above models, in addressing the GRB within a single-progenitor scenario, fundamental papers have presented a vast number of possible binary progenitors for GRBs (Fryer et al. 1999; Heger et al. 2003). Following this seminal paper, we have developed the concept of BdHNE, which is recalled in Section 2. This model includes three different components: (1) a CO $_{\text{core}}$ undergoing an SN explosion in the presence of a binary NS companion; (2) an additional NS, indicated as a ν NS, which is the newborn NS originating at the center of the SN, accreting the SN ejecta and giving rise to the afterglow; and (3) the formation of the BH by the hypercritical accretion of the SN ejecta onto the preexisting NS companion, giving rise to the GeV emission.

Since the beginning of 2018, there have been considerable advances in the time-resolved spectral analysis of GRBs through state-of-the-art algorithms and tools (Skilling 2004; Vianello et al. 2015). Thanks to this methodology, which is conceptually different from the Band function approach (see, e.g., Ruffini et al. 2019a), together with improved feedback from three-dimensional smoothed-particle-hydrodynamics (SPH) simulations (Becerra et al. 2019), three new results have followed from the BdHN analysis which question the traditional approach.

(1) The explanation of X-ray flares in the “flare–plateau–afterglow” (FPA) phase (Ruffini et al. 2018e) as originating from a BdHN observed in the orbital plane of the binary progenitor system. In particular, the observational data of soft X-ray flares in the early ($t \sim 100$ s rest-frame) FPA phase indicate that the emission arises from a mildly relativistic system with Lorentz factor $\Gamma \sim 2-5$ (Ruffini et al. 2018e).

(2) We investigated the FPA phase of GRB 130427A using time-resolved spectral analysis of the early X-ray data (Ruffini et al. 2015, 2019d; Wang et al. 2019b). There, from the thermal emission in the FPA phase (see Figure 7 in Ruffini et al. 2015), an upper limit of $\sim 0.9 c$ to the expansion velocity was established. Such a mildly relativistic expansion of the FPA phase emitter was further confirmed in GRB 151027A (Ruffini et al. 2018a) by soft and hard X-ray observations, and in GRB 171205A by the optical emission lines (Izzo et al. 2019). It motivated the first detailed model, applied to GRB 130427A, of the plateau–afterglow emission of the FPA phase (Ruffini et al. 2018b; Wang et al. 2019b) as arising from the synchrotron radiation by relativistic electrons within the mildly relativistic expanding SN ejecta magnetized by the ν NS.

(3) One of the newest results on GRB 190114C infers the GeV emission, originating in the traditional model at distances $10^{12} - 10^{16}$ cm, to originate instead from the electrodynamic process of BH rotational energy extraction very close to the BH horizon (Ruffini et al. 2019d). This electrodynamic process occurs in a very low-density environment of $\sim 10^{-14}$ g cm $^{-3}$ and leads to an energy per particle of up to 10^{18} eV. This is confirmed by simulations in the accompanying cavity generated by the BH accretion (Ruffini et al. 2019b).

All of the above shows the different roles in a BdHN I of three main components: the SN, the ν NS, and the newborn BH.

In this article, we aim to further clarify, confirm, and extend the explanation of the plateau–afterglow emission of the FPA phase, as powered by the SN and ν NS interaction within the BdHN scenario, following the treatment presented in Ruffini et al. (2018b) and Wang et al. (2019b). We analyze the cases of GRB 130427A, GRB 180728A, GRB 160509A, GRB 160625B, and GRB 190114C.

This article is organized as follows. In Section 2, we recall the physical and astrophysical properties of the BdHN model. In Section 3, we recall the observational properties of the GRBs analyzed in this work. In Section 4, we simulate the X-ray afterglow of the above-mentioned sources using the mild-relativistic synchrotron model and infer the magnetic field of the ν NS based on the framework presented in Wang et al. (2019b). The nature of the obtained magnetic field of the ν NS is discussed in Section 6. In Section 7, we discuss the possible nature of the magnetic field around the newborn BH in a BdHN. Finally, in Section 8, we outline our conclusions.

2. The BdHN Scenario

The BdHN model has been introduced to explain long-duration gamma-ray bursts (GRBs), and it is based on the induced gravitational collapse (IGC) paradigm (Rueda & Ruffini 2012) occurring in a specific binary system following a specific evolutionary path (see Figure 1 and Fryer et al. 2014; Becerra et al. 2015; Fryer et al. 2015; Rueda et al. 2019 for details).

As Figure 1 shows, the system starts with a binary composed of two main-sequence stars, say of 15 and 12 M_{\odot} , respectively. At a given time, at the end of its thermonuclear evolution, the more massive star undergoes core-collapse SN and forms an NS. The system then enters the X-ray binary phase. After possibly multiple common-envelope phases and binary interactions (see Fryer et al. 2014, 2015, and references therein), the hydrogen and helium envelopes of the other main-sequence star are stripped, leaving exposed its core that is rich in carbon and oxygen. For short, we refer to it as the carbon–oxygen core (CO_{core}) following the literature on the subject (see e.g., Nomoto et al. 1994; Filippenko et al. 1995; Iwamoto et al. 2000; Pian et al. 2006; Yoshida & Umeda 2011). The system at this stage is a CO_{core} –NS binary in tight orbit (period of the order of a few minutes), which is taken as the initial configuration of the BdHN scenario in which the IGC phenomenon occurs (Fryer et al. 2014; Becerra et al. 2015, 2016, 2019).

We now proceed to describe the BdHN scenario. At the end of its thermonuclear evolution the CO_{core} undergoes a core-collapse SN (of type Ic in view of the hydrogen and helium absence). Matter is ejected but also at the center of the SN, a newborn NS is formed, for short referred to as ν NS, to differentiate it from the accreting NS binary companion. As we shall see, this differentiation is necessary in light of the physical phenomena and corresponding observables in a BdHN associated with each of them. Owing to the short orbital period, the SN ejecta produce a hypercritical (i.e., highly super-Eddington) accretion process onto the NS companion. The material hits the NS surface developing and outward shock which creates an accretion “atmosphere” of very high density and temperature on top the NS. These conditions turn out to be appropriate for the thermal production of positron–electron (e^+e^-) pairs which, when annihilating, leads to a copious production of neutrino–antineutrino pairs ($\nu\bar{\nu}$), which turn out

to be the most important carriers of the gravitational energy gain of the accreting matter, allowing the rapid and massive accretion to continue. We refer to Fryer et al. (2014) and Becerra et al. (2016, 2018) for details on the hypercritical accretion and the involved neutrino physics.

Depending on the specific system parameters, i.e., mass of the binary components, orbital period, SN explosion energy, etc., two possible fates for the NS are possible (see Becerra et al. 2015, 2016, 2019 for details on the relative influence of each parameter in the system). For short binary periods, i.e., ~ 5 minutes, the NS reaches the critical mass for gravitational collapse and forms a BH (see, e.g., Becerra et al. 2015, 2016, 2019; Fryer et al. 2015). We have called this kind of system a BdHN type I (Wang et al. 2019b). A BdHN I emits an isotropic energy $E_{\text{iso}} \gtrsim 10^{52}$ erg and gives rise to a new binary composed of the NS formed at the center of the SN, hereafter ν NS, and the BH formed by the collapse of the NS. For longer binary periods, the hypercritical accretion onto the NS is not sufficient to bring it to the critical mass, and a more massive NS (MNS) is formed. We have called these systems BdHNe of type II (Wang et al. 2019b), and they emit energies $E_{\text{iso}} \lesssim 10^{52}$ erg. A BdHN II gives origin to a new binary composed of the ν NS and the MNS.

The BdHNe I represent, in our binary classification of GRBs, the totality of long GRBs with energy larger than 10^{52} erg, while BdHNe II, with their energy smaller than 10^{52} erg, are far from unique, and there is a variety of long GRBs in addition to them that can have similar energetics, e.g., double white dwarf (WD–WD) mergers and NS–WD mergers (see Ruffini et al. 2016, 2018c; Wang et al. 2019b, for details).

Three-dimensional numerical SPH simulations of BdHNe have been recently presented in Becerra et al. (2019). These simulations improve and extend the previous ones by Becerra et al. (2016). A fundamental contribution of these simulations has been to provide a visualization of the morphology of the SN ejecta, which is modified from the initial spherical symmetry. A low-density cavity is carved initially by the NS companion and, once it collapses, further by the BH formation process (see also Ruffini et al. 2019a). Such an asymmetric density distribution leads to a dependence of the GRB description on the observer viewing angle—in the orbital/equatorial plane or in the plane orthogonal to it (Becerra et al. 2016; Ruffini et al. 2018e, 2018a; Becerra et al. 2019)—and on the orbital period of the binary, in the simulation of Figure 2 at about 300 s (Ruffini et al. 2018a).

The SN transforms into a hypernova (HN) as a result of the energy and momentum transfer of the e^+e^- plasma (Ruffini et al. 2018a; Becerra et al. 2019). The SN shock breakout and the hypercritical accretion can be observed as X-ray precursors (Becerra et al. 2016; Wang et al. 2019b). The e^+e^- feedback also produces the gamma- and X-ray flares observed in the early afterglow (Ruffini et al. 2018e). There is then the most interesting emission episode, which is related to the ν NS that originated from the SN explosion, that is, the synchrotron emission by relativistic electrons, injected from the ν NS pulsar emission into the HN ejecta in the presence of the ν NS magnetic field, explains the X-ray afterglow and its power-law luminosity (Ruffini et al. 2018b; Wang et al. 2019b). Finally, the HN is observed in the optical bands a few days after the GRB trigger, powered by the energy release of the nickel decay.

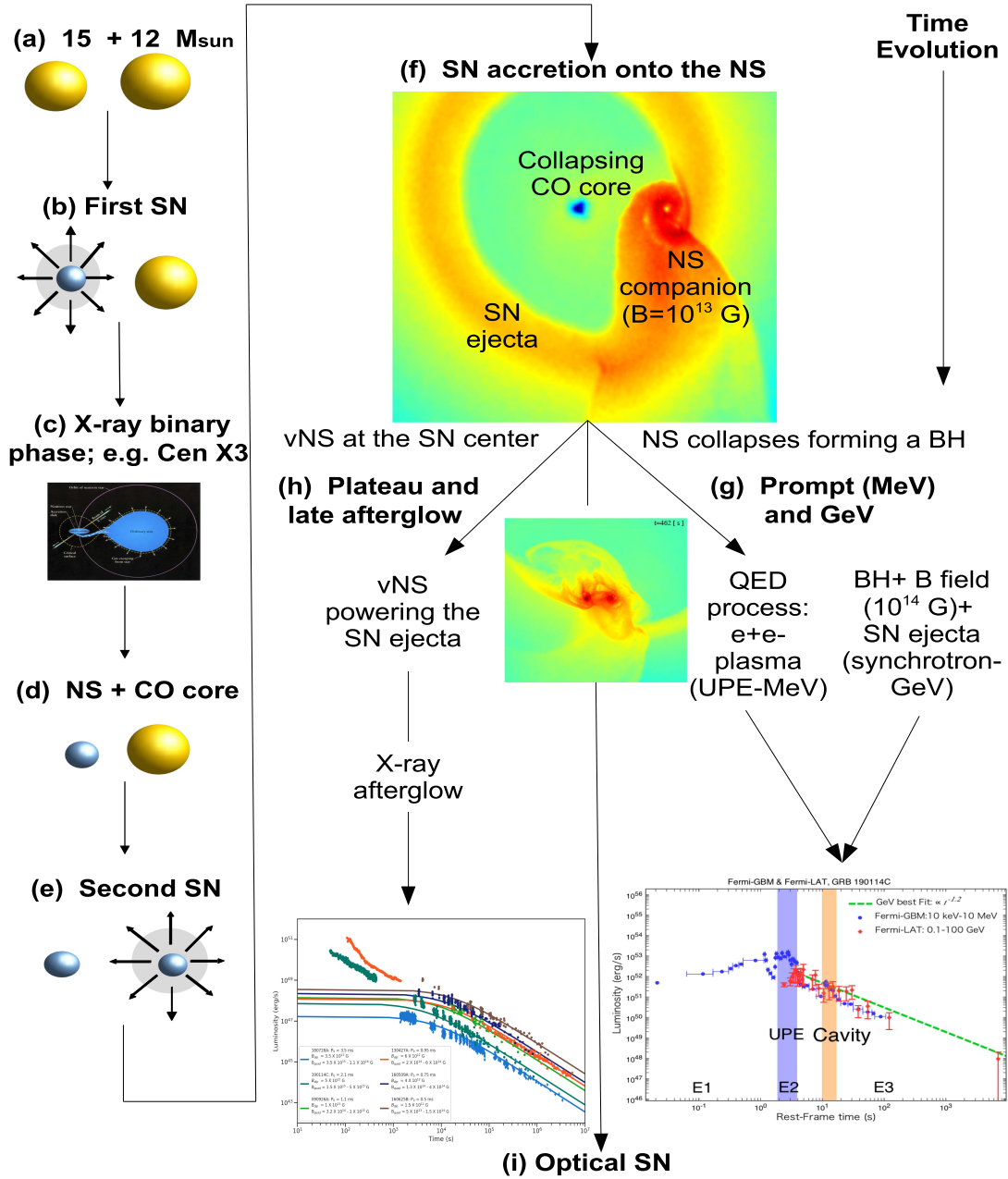


Figure 1. Schematic evolutionary path of a massive binary up to the emission of a BdHN. (a) Binary system composed of two main-sequence stars of 15 and 12 M_{\odot} , respectively. (b) At a given time, the more massive star undergoes a core-collapse SN and forms an NS (which might have a magnetic field $B \sim 10^{13}$ G). (c) The system enters the X-ray binary phase. (d) The core of the remaining evolved star, rich in carbon and oxygen, CO_{core} for short, is left exposed as the hydrogen and helium envelopes have been stripped by binary interactions and possibly multiple common-envelope phases (not shown in this diagram). The system is, at this stage, a CO_{core} -NS binary, which is taken as the initial configuration of the BdHN model (Fryer et al. 2014; Becerra et al. 2015, 2016, 2019). (e) The CO_{core} explodes as an SN when the binary period is of the order of a few minutes, the SN ejecta of a few solar masses start to expand, and a fast-rotating, newborn NS, ν NS for short, is left in the center. (f) The SN ejecta accrete onto the NS companion, forming a massive NS (BdHN II) or a BH (BdHN I; this example), depending on the initial NS mass and the binary separation. Conservation of magnetic flux and possibly additional MHD processes amplify the magnetic field from the NS value to $B \sim 10^{14}$ G around the newborn BH. At this stage, the system is a ν NS-BH binary surrounded by ionized matter of the expanding ejecta. (g) The accretion, the formation, and the activities of the BH contribute to the GRB prompt gamma-ray emission and GeV emission (not the topic of this work).

Figure 1 and Table 1 summarize the above correspondence between the BdHN physical process and each GRB observable, emphasizing the role of each component of the binary system. We also refer the reader to Rueda et al. (2019), and references therein, for a recent review on the physical processes at work and related observables in BdHNe I and II.

3. GRBs (BdHNe I) of the Present Work

GRB 130427A is one of the best-observed GRBs; it is located at redshift $z \sim 0.34$ (Levan et al. 2013), and more than 50 observatories participated in the observation. It hits the record for brightness in gamma-ray emission, so that Fermi-GBM was saturated. It also hits the record for GeV observation,

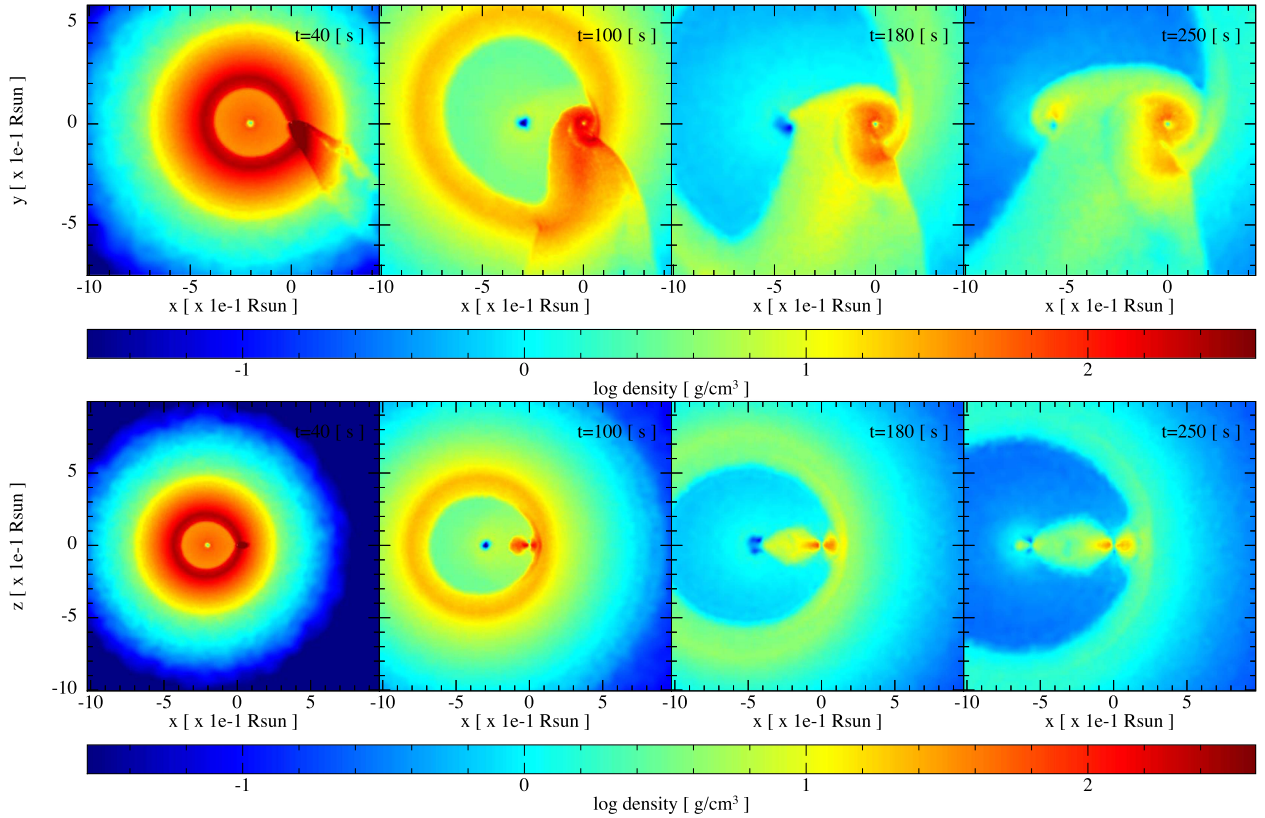


Figure 2. SPH simulation of a BdHN I: model “25M1p1e” of Table 2 in Becerra et al. (2019). The binary progenitor is composed of a CO_{core} of $\approx 7 M_{\odot}$, produced by a zero-age main-sequence star of $25 M_{\odot}$ (see Table 1 in Becerra et al. 2019), and a $2 M_{\odot}$ NS companion. The orbital period is ≈ 5 minutes. Each frame, from left to right, corresponds to selected increasing times with $t = 0$ s the instant of the SN shock breakout. The upper panel shows the mass density on the equatorial plane and the lower panel the plane orthogonal to the equatorial one. The reference system is rotated and translated to align the x -axis with the line joining the binary components. The origin of the reference system is located at the NS companion position. The first frame corresponds to $t = 40$ s, and it shows that the particles entering the NS capture region form a tail behind them. These particles then circularize around the NS, forming a thick disk that is already visible in the second frame at $t = 100$ s. Part of the SN ejecta is also attracted by the νNS accreting onto it; this is appreciable in the third frame at $t = 180$ s. At $t = 250$ s (about one orbital period), a disk structure has been formed around the νNS and the NS companion. To guide the eye, the νNS is at the x coordinates -2.02 , -2.92 , -3.73 , and -5.64 for $t = 40$ s, 100 s, 180 s, and 250 s, respectively. This figure has been produced with the SNsplash visualization program (Price 2011). The figure has been taken from Becerra et al. (2019) with the permission of the authors.

with more than 500 photons above 100 MeV received, and GeV emission observed until $\sim 10^4$ s (Ackermann et al. 2014).

The shape of its prompt emission consists of a ~ 3 s precursor, followed by a multi-peaked pulse lasting ~ 10 s. At time ~ 120 s, an additional flare appears, then it enters the afterglow (Maselli et al. 2014). The X-ray afterglow is observed by Swift and NuStar. Swift covers discretely from ~ 150 to $\sim 10^7$ s (Li et al. 2015), and NuStar observes three epochs, starting approximately at 1.2, 4.8, and 5.4 days, for observational durations of 30.5, 21.2, and 12.3 ks (Kouveliotou et al. 2013). The power-law decay index of the late-time afterglow after ~ 2000 s gives ~ -1.32 (Ruffini et al. 2015).

The optical spectrum reveals that 16.7 days after the GRB trigger, a typical SN Ic emerges (Xu et al. 2013; Li et al. 2018a), as predicted by Ruffini et al. (2013).

GRB 160509A, at redshift $z \sim 1.17$ (Tanvir et al. 2016), is a strong source of GeV emission, including a 52 GeV photon arriving at 77 s, and a 29 GeV photon arriving ~ 70 ks (Laskar et al. 2016).

GRB 160509A consists of two emission periods, 0–40 s and 280–420 s (Tam et al. 2017). The first period exhibits a single-pulse structure for sub-MeV emission, and a double-pulse structure for ~ 100 MeV emission. The second period is in the sub-MeV energy range with a double-pulse structure.

Swift–XRT started the observation ~ 7000 s after the burst, with a shallow power-law decay of index ~ -0.6 , followed by a normal decay of power-law index ~ -1.45 after 5×10^4 s (Tam et al. 2017; Li et al. 2018b).

There is no SN association reported; the optical signal of SNe can hardly be confirmed for GRBs with redshift > 1 as the absorption is intense (Woosley & Bloom 2006).

GRB 160625B, at redshift 1.406 (Xu et al. 2016), is a bright GRB with the special quality that its polarization has been detected. Fermi-LAT has detected more than 300 photons with energy > 100 MeV (Lü et al. 2017).

The gamma-ray light curve has three distinct pulses (Zhang et al. 2018; Li 2019). The first short pulse is totally thermal and lasts ~ 2 s, the second bright pulse starts from ~ 180 s and ends at ~ 240 s, and the last weak pulse emerges at ~ 330 s and lasts ~ 300 s. The total isotropic energy reaches $\sim 3 \times 10^{54}$ erg (Alexander et al. 2017; Lü et al. 2017).

Swift–XRT starts the observation at a late time ($> 10^4$ s), finding a power-law behavior with decaying index ~ -1.25 .

There is no SN confirmation, possibly due to the redshift being > 1 (Woosley & Bloom 2006).

GRB 190114C, at redshift $z \sim 0.42$ (Selsing et al. 2019), is the first GRB with TeV photon detection by MAGIC (Mirzoyan et al. 2019; MAGIC Collaboration et al. 2019). It

Table 1
Summary of the GRB Observables Associated with Each BdHN I Component and Physical Phenomena

BdHN Component/Phenomena	GRB Observable				
	X-Ray Precursor	Prompt (MeV)	GeV–TeV Emission	X-Ray Flares Early Afterglow	X-Ray Plateau and Late Afterglow
SN breakout ^a	⊗				
Hypercritical accretion onto the NS ^b	⊗				
e^+e^- from BH formation: transparency in the low baryon load region ^c		⊗			
<i>Inner engine</i> : newborn BH + B -field+SN ejecta ^d			⊗		
e^+e^- from BH formation: transparency in the high baryon load region (SN ejecta) ^e				⊗	
Synchrotron emission by ν NS-injected particles on SN ejecta ^f					⊗
ν NS pulsar-like emission ^f					⊗

Notes.

^a Wang et al. (2019b).

^b Fryer et al. (2014), Becerra et al. (2016), Rueda et al. (2019).

^c Bianco et al. (2001).

^d Ruffini et al. (2018d, 2019d, 2019a, 2019b).

^e Ruffini et al. (2018e).

^f Ruffini et al. (2018b), Wang et al. (2019b), and this work.

has similar features to GRB 130427A (Wang et al. 2019a), and it has caught great attention as well.

The prompt emission of GRB 190114C starts with a multi-peaked pulse, its initial ~ 1.5 s is nonthermal, which is then followed by a possible thermal emission until ~ 1.8 s. A confident thermal emission exists during the peak of the pulse, from 2.7 to 5.5 s. The GeV emission starts from 2.7 s, initiated by a spiky structure, then follows a power-law decay with index ~ -1.2 (Ruffini et al. 2019a). The GeV emission is very luminous; more than 200 photons with energy > 100 MeV are received. The X-ray afterglow observed by Swift–XRT shows a persistent power-law decay behavior, with decaying index ~ 1.35 (Wang et al. 2019a).

An continuous observational campaign lasting ~ 50 days unveiled the SN emergence ~ 15 days after the GRB (Melandri et al. 2019), which is consistent with the prediction of 18.8 ± 3.7 days after the GRB by Ruffini et al. (2019c).

4. X-Ray Afterglow of the GRB and Magnetic Field of the ν NS

The newborn NS at the center of the SN, i.e., the ν NS, ejects high-energy particles as in traditional pulsar models. This means that these particles escape from the ν NS magnetosphere through so-called “open” magnetic field lines, namely, the field lines that do not close within the light cylinder radius that determines the size of the corotating magnetosphere. These particles interact with the SN ejecta, which, by expanding in the ν NS magnetic field, produce synchrotron radiation, which we discuss below. Hence, the acceleration mechanism is similar to the one occurring in traditional SN remnants but with two main differences in our case: (1) we have a ~ 1 ms ν NS pulsar powering the SN ejecta and (2) the SN ejecta are at a radius of $\sim 10^{12}$ cm at the beginning of the afterglow, at the rest-frame time $t \sim 100$ s, as the SN expands with velocity $\sim 0.1c$.

The above distance is well beyond the light cylinder radius, so it is expected that only the toroidal component of the magnetic field, which decreases as $1/r$ (see Equations (4) and (12)), survives (see, e.g., Goldreich & Julian 1969 for details).

Therefore, the relevant magnetic field for synchrotron radiation in the afterglow is that of the ν NS, which is stronger (as shown below, at that distance it is of the order of 10^5 G) than the one possibly produced inside the remnant by dilute plasma currents, unlike the traditional models for the emission of old ($\gtrsim 1$ kyr) SN remnants.

In Ruffini et al. (2018b) and Wang et al. (2019b), we simulated the afterglow by the synchrotron emission of electrons from the optically thin region of the SN ejecta, which expand mildly relativistically in the ν NS magnetic field. The FPA emission at times $t \gtrsim 10^2$ s has two origins: the emission before the plateau phase ($\sim 5 \times 10^3$ s) is mainly contributed by the remaining kinetic energy of the SN ejecta, and at later times, the continuous energy injection from the ν NS dominates. We extend the same approach in this paper to the GRBs of Section 3.

To fully follow the temporal behavior of radiation spectra, it is necessary to solve the kinetic equation for electron distribution in the transparent region of the SN ejecta:

$$\frac{\partial N(\gamma, t)}{\partial t} = \frac{\partial}{\partial \gamma}(\dot{\gamma}(\gamma, t)N(\gamma, t)) + Q(\gamma, t), \quad (1)$$

where $N(\gamma, t)$ is the electron number distribution as a function of electron energy $\gamma = E/m_e c^2$, $\dot{\gamma}(\gamma, t)$ is the electron energy-loss rate normalized to the electron rest mass, and $Q(\gamma, t) = Q_0(t)\gamma^{-p}$ is the particle injection rate, assumed to be a power law of index p , so the electrons injected are within the energy range of γ_{\min} to γ_{\max} . The total injection luminosity $L_{\text{inj}}(t)$ is provided by the kinetic energy of the SN and the rotational energy of the ν NS, here parameterized via the power-law injection power,

$$L_{\text{inj}}(t) = \int_{\gamma_{\min}}^{\gamma_{\max}} Q(\gamma, t) d\gamma \simeq L_0 \left(1 + \frac{t}{\tau_0}\right)^{-k}, \quad (2)$$

where L_0 , k , and τ_0 are assessed by fitting the light-curve data. The majority of energy loss is considered to be the adiabatic

energy loss and the synchrotron energy loss,

$$\dot{\gamma}(\gamma, t) = \frac{\dot{R}(t)}{R(t)}\gamma + \frac{4}{3} \frac{\sigma_T}{m_e c} \frac{B(t)^2}{8\pi} \gamma^2, \quad (3)$$

where $R(t)$ is the size of the emitter, σ_T is the Thomson cross section, and $B(t)$ is the magnetic field strength expected to have a toroidal configuration given by

$$B(t) = B_0 \left(\frac{R(t)}{R_0} \right)^{-1}, \quad (4)$$

where B_0 is the magnetic field strength at the distance R_0 . The final bolometric synchrotron luminosity from this system gives

$$L_{\text{syn}}(\nu, t) = \int_1^{\gamma_{\text{max}}} N(\gamma, t) P_{\text{syn}}(\nu, \gamma, B(t)) d\gamma. \quad (5)$$

As we have introduced in Section 1, the thermal emission during the FPA phase indicates a mildly relativistic velocity, $\sim 0.5\text{--}0.9c$, at time ~ 100 s (Ruffini et al. 2015, 2018e, 2019d; Wang et al. 2019b). We adopt this value as the initial velocity and radius of the transparent part of the SN ejecta.

For later stages at around 10^6 s, when a sizable front shell of SN ejecta becomes transparent, we adopt the velocity of $\sim 0.1c$ obtained through observations of Fe II emission lines (see, e.g., Xu et al. 2013). We make the simplest assumption of a uniformly decelerating expansion during the time interval $10^2 \lesssim t \lesssim 10^6$ s. The SN ejecta remain in the coasting phase for hundreds of years (see e.g., Sturmer et al. 1997); therefore, we adopt a constant velocity from 10^6 s until 10^7 s.

Following the above discussion and our data analysis, we describe the expansion velocity as

$$\dot{R}(t) = \begin{cases} v_0 - a_0 t & 10^2 < t < 10^6 \text{ s} \\ v_f & 10^7 > t > 10^6 \text{ s} \end{cases} \quad (6)$$

with typical value $v_0 = 2.4 \times 10^{10} \text{ cm s}^{-1}$, $a_0 = 2.1 \times 10^4 \text{ cm s}^{-2}$, and $v_f = 3 \times 10^9 \text{ cm s}^{-1}$.

It is appropriate to clarify how the model parameters presented in this table are obtained: R_0 and τ_0 are fixed by the observed thermal component at around 10^2 s, from which we obtain the radius and expansion velocity of the SN front. The minimum and maximum energies of the injected electrons, γ_{min} and γ_{max} , are fixed once B is given. L_0 is fixed by a normalization of the observed source luminosity. The power-law index of the energy injection rate, p , is fixed to the value $p = 3/2$. The parameter k is fixed to produce the power-law decay of the late-time X-ray data. Therefore, the ‘‘free parameter’’ to be obtained is B_0 .

In Ruffini et al. (2018b), we have given detailed fitting parameters and figures of GRB 130427A. In this article, we additionally fit GRB 160625B and confirm that the mildly relativistic model is capable of producing the GRB afterglow. As shown in Table 2 and Figure 3, our model fits very well the optical and the X-ray spectrum but not the GeV data. This is in agreement with the BdHN paradigm because the GeV emission is expected to be explained by the newborn BH activity and not by the νNS one (Ruffini et al. 2019d). On the other hand, radio data show a lack of expected flux, which comes from synchrotron self-absorption processes that are rather complicated to model in the current numerical framework but can be thoroughly ignored at frequencies above 10^{14} Hz.

Comparing their fitting parameters, GRB 130427A and GRB 160625B are similar except for the constant of injection power

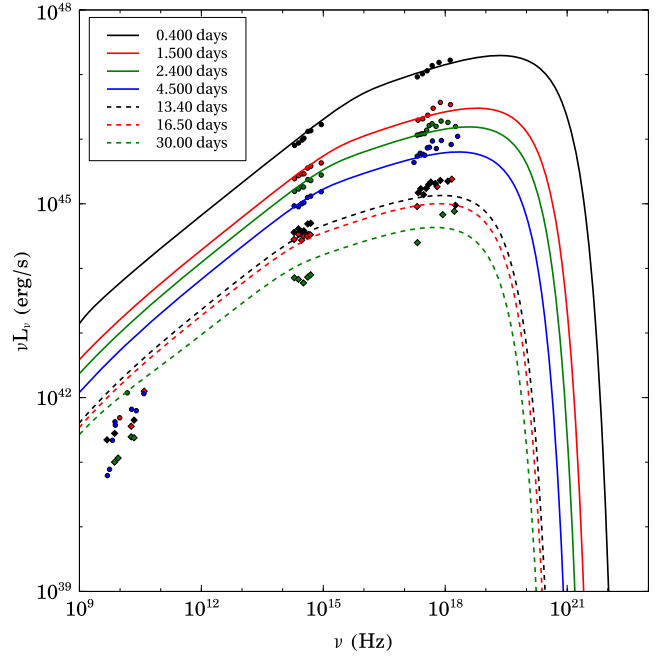


Figure 3. Model evolution of synchrotron spectral luminosity at various times compared with measurements in various spectral bands for GRB 160625B.

Table 2
Parameters Used for the Simulation of GRB 160625B

Parameter	Value
B_0	$1.0 \times 10^6 \text{ G}$
R_0	$1.2 \times 10^{11} \text{ cm}$
L_0	$8.44 \times 10^{52} \text{ erg s}^{-1}$
k	1.42
τ_0	$5.0 \times 10^0 \text{ s}$
p	1.5
γ_{min}	4.0×10^3
γ_{max}	1.0×10^6

L_0 (see Equation (2)). Such similarities can be extended to others. It can be seen from Figure 4 that taking everything else as similar, from the magnetic field strength and structure to expansion evolution, simulated light curve of GRB 190114C at the relevant times can be obtained from that of GRB 130427A by scaling L_0 by a factor of $1/5$.

The injection power index $k \sim 1.5$ from the fitting suggests that the quadrupole emission from a pulsar dominates the late-time afterglow. As we will see below, the complementary analysis allows the initial rotation period of the νNS as well as an independent estimate of its magnetic field structure to be inferred.

Being just born, the νNS must be rapidly rotating, and as such it contains abundant rotational energy:

$$E = \frac{1}{2} I \Omega^2, \quad (7)$$

where I is the moment of inertia and $\Omega = 2\pi/P_{\nu\text{NS}}$ is the angular velocity. For a millisecond νNS and $I \sim 10^{45} \text{ g cm}^2$, the total rotational energy $E \sim 2 \times 10^{52} \text{ erg}$. Assuming that the rotational energy loss is driven by magnetic dipole and

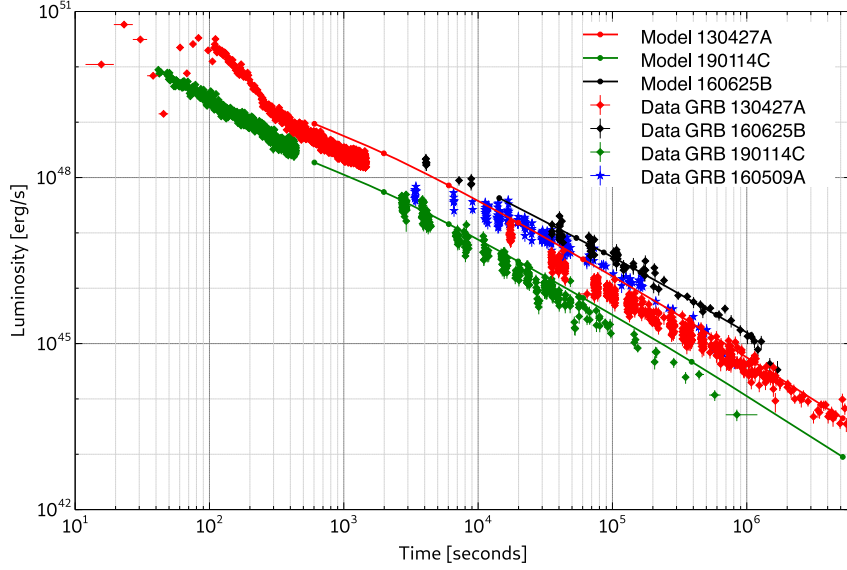


Figure 4. X-ray light curve of GRB 160625B, GRB 130427A, GRB 190114C, and GRB 160509A (black, red and green diamonds, and blue stars with error bars respectively). Simulated synchrotron light curves in the Swift X-ray band are shown for GRB 160625B (black line) and GRB 130427A (red line). It is also shown how, by scaling the injection power by a factor 1/5, the light curve of GRB 130427A scales down (from the red line to the green one), fitting the data of GRB 190114C.

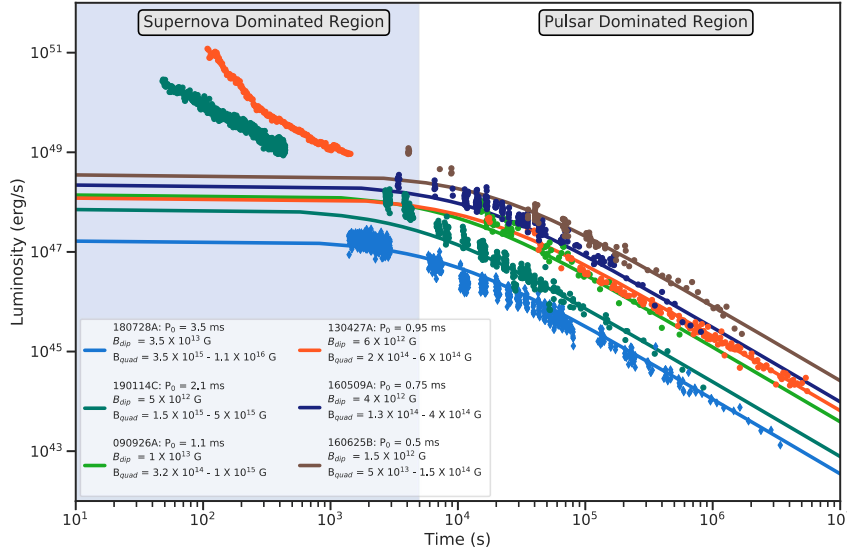


Figure 5. The brown, deep blue, orange, green, and bright blue points correspond to the bolometric (about ~ 5 times brighter than the soft X-ray observed by Swift–XRT inferred from the fitted synchrotron spectrum) light curves of GRBs 160625B, 160509A, 130427A, 190114C, and 180728A, respectively. The lines are the fits to the energy injection from the rotational energy of the pulsar. The pulsar powers the late afterglow ($t \gtrsim 5 \times 10^3$ s, white background), while at earlier times ($t \lesssim 5 \times 10^3$ s, dusty blue background), the remaining kinetic energy of the SN ejecta plays the leading role. The fitted parameters are shown in the legend and in Table 3. The quadrupole field is given in a range; its upper value is three times the lower value due to the oscillation angle χ_2 , which is a free parameter. The fits to GRB 130427A and 180728A are reproduced from Wang et al. (2019b).

quadrupole radiation, we have

$$L_{\text{NS}}(t) = \frac{dE}{dt} = -I\Omega\dot{\Omega} = -\frac{2}{3c^3}\Omega^4 B_{\text{dip}}^2 R_{\nu\text{NS}}^6 \sin^2 \chi_1 \left(1 + \eta^2 \frac{16}{45} \frac{R_{\nu\text{NS}}^2 \Omega^2}{c^2} \right), \quad (8)$$

where

$$\eta^2 = (\cos^2 \chi_2 + 10 \sin^2 \chi_2) \frac{B_{\text{quad}}^2}{B_{\text{dip}}^2}, \quad (9)$$

with χ_1 and χ_2 the inclination angles of the magnetic moment, and B_{dip} and B_{quad} are the dipole and quadrupole magnetic fields, respectively. The parameter η measures the quadrupole to dipole magnetic field strength ratio.

Figure 5 shows the bolometric light curves (~ 5 times brighter than the Swift–XRT light curves inferred from the fitting) of GRBs 160625B, 160509A, 130427A, 190114C, and 180728A, respectively. We show that the νNS luminosities $L_{\text{NS}}(t)$ fit the light curves. We report the fitting νNS parameters—the dipole (B_{dip}) and quadrupole (B_{quad}) magnetic field components, the initial rotation period ($P_{\nu\text{NS}}$)—and assume a

Table 3
Observational Properties of the GRB and Inferred Physical Quantities of the ν NS of the Corresponding BdHN Model that Fits the GRB Data

GRB	Type	Redshift	E_{iso} (erg)	$P_{\nu\text{NS}}$ (ms)	E_{rot} (erg)	B_{dip} (G)	B_{quad} (G)
130427A	BdHN I	0.34	1.40×10^{54}	0.95	3.50×10^{52}	6.0×10^{12}	$2.0 \times 10^{13} \sim 6.0 \times 10^{14}$
160509A	BdHN I	1.17	1.06×10^{54}	0.75	5.61×10^{52}	4.0×10^{12}	$1.3 \times 10^{14} \sim 4.0 \times 10^{14}$
160625B	BdHN I	1.406	3.00×10^{54}	0.5	1.26×10^{53}	1.5×10^{12}	$5.0 \times 10^{13} \sim 1.6 \times 10^{14}$
190114C	BdHN I	0.42	2.47×10^{53}	2.1	7.16×10^{51}	5.0×10^{12}	$1.5 \times 10^{15} \sim 5.0 \times 10^{15}$
180728A	BdHN II	0.117	2.73×10^{51}	3.5	2.58×10^{51}	1.0×10^{13}	$3.5 \times 10^{15} \sim 1.1 \times 10^{16}$

Note. Column 1: GRB name; column 2: identified BdHN type; column 3: the isotropic energy released (E_{iso}) in gamma-rays; column 4: cosmological redshift (z); column 5: ν NS rotation period ($P_{\nu\text{NS}}$); column 6: ν NS rotational energy (E_{rot}); columns 7 and 8: strength of the dipole (B_{dip}) and quadrupole (B_{quad}) magnetic field components of the ν NS. The quadrupole magnetic field component is given in the range where the upper limit is three times the lower limit; this is brought about by the freedom of the inclination angles of the magnetic moment. During the fitting, we consistently assume the NS mass of $1.4M_{\odot}$ and the NS radius of 10^6 cm for all three cases. The fitted light curves are shown in Figure 5; the parameters of GRB 1340427A and 180728A are taken from Wang et al. (2019b).

ν NS of mass and radius of $1.4M_{\odot}$ and 10^6 cm, respectively. The results are also summarized in Table 3. It also becomes clear from this analysis that the ν NS emission alone is not able to explain the emission of the FPA phase at early times 10^2 – 10^3 s. As we have shown, that emission is mainly powered by the mildly relativistic SN kinetic energy.

5. A Self-consistency Check

Having estimated the magnetic field structure and the rotation period of the ν NS from the fit of the data of the FPA phase at times 10^2 – 10^7 s, we can now assess their self-consistency with the expected values within the BdHN scenario.

First, let us adopt the binary as tidally locked, i.e., the rotation period of the binary components is synchronized with the orbital period. This implies that the rotation period of the CO_{core} is $P_{\text{CO}} = P$, where P denotes the orbital period. From the Kepler law, the value of P is connected to the orbital separation a_{orb} and to the binary mass as

$$P_{\text{CO}} = P = 2\pi \sqrt{\frac{a_{\text{orb}}^3}{GM_{\text{tot}}}}, \quad (10)$$

where G is the gravitational constant and $M_{\text{tot}} = M_{\text{CO}} + M_{\text{NS}}$ is the total mass of the binary, where M_{CO} and M_{NS} are the masses of the CO_{core} and the NS companion, respectively. Thus, $M_{\text{CO}} = M_{\text{Fe}} + M_{\text{ej}}$, with M_{Fe} and M_{ej} the masses of the iron core (which collapses and forms the ν NS) and the ejected mass in the SN event, respectively.

The mass of the ν NS is $M_{\nu\text{NS}} \approx M_{\text{Fe}}$. The rotation period, $P_{\nu\text{NS}}$, is estimated from that of the iron core, P_{Fe} , by applying angular momentum conservation in the collapse process, i.e.,

$$P_{\nu\text{NS}} = \left(\frac{R_{\nu\text{NS}}}{R_{\text{Fe}}} \right)^2 P, \quad (11)$$

where $R_{\nu\text{NS}}$ and R_{Fe} are the radius of the ν NS and of the iron core, respectively, and we have assumed that the pre-SN star has uniform rotation; so, $P_{\text{Fe}} = P_{\text{CO}} = P$.

Without loss of generality, in our estimates we can adopt a ν NS order-of-magnitude radius of 10^6 cm. As we shall see below, a more careful estimate is that for the CO_{core} progenitor (which tells us the radius of the iron core) and the orbital period/binary separation, which affect additional observables of a BdHN.

It is instructive to appreciate the above statement with specific examples; for these we use the results of Wang et al. (2019b) for two BdHN archetypes: GRB 130427A for BdHN I and GRB 180827A for BdHN II. Table 3 shows, for the above GRBs, as well as for GRB 190114C, GRB 160625B, and GRB 160509A, some observational quantities (the isotropic energy released E_{iso} and the cosmological redshift), the inferred BdHN type, and the properties of the ν NS (rotation period $P_{\nu\text{NS}}$, rotational energy, and the strength of the dipole and quadrupole magnetic field components).

By examining the BdHN models simulated in Becerra et al. (2019) (see, e.g., Table 2 there), we have shown in Wang et al. (2019b) that the Model “25m1p08e” fits the observational requirements of GRB 130427A, and the Model “25m3p1e” those of GRB 180827A. These models have the same binary progenitor components: the $\approx 6.8M_{\odot}$ CO_{core} ($R_{\text{Fe}} \sim 2 \times 10^8$ cm) developed by a $25M_{\odot}$ zero-age main-sequence star (see Table 1 in Becerra et al. 2019) and a $2M_{\odot}$ NS companion. For GRB 130427A, the orbital period is $P = 4.8$ minutes (binary separation $a_{\text{orb}} \approx 1.3 \times 10^{10}$ cm), resulting in $P_{\nu\text{NS}} \approx 1.0$ ms while, for GRB 180827A, the orbital period is $P = 11.8$ minutes ($a_{\text{orb}} \approx 2.6 \times 10^{10}$ cm), so a less compact binary, which leads to $P_{\nu\text{NS}} \approx 2.5$ ms.

We turn now to perform a further self-consistency check of our picture. Namely, we make a cross-check of the estimated ν NS parameters obtained first from the early afterglow via synchrotron emission, and then from the late X-ray afterglow via the pulsar luminosity, with respect to expectations from NS theory.

Up to factors of order unity, the surface dipole B_s and the toroidal component B_t at a distance r from the surface are approximately related as (see, e.g., Goldreich & Julian 1969)

$$B_t \approx \left(\frac{2\pi R_{\nu\text{NS}}}{cP_{\nu\text{NS}}} \right)^2 \left(\frac{R_{\nu\text{NS}}}{r} \right) B_s. \quad (12)$$

Let us analyze the case of GRB 130427A. By equating Equations (4) and (12), and using the values of $B_0 = 5 \times 10^5$ G and $R_0 = 2.4 \times 10^{12}$ cm obtained from synchrotron analysis by Ruffini et al. (2018b), and $P_{\nu\text{NS}} = P_0 \approx 1$ ms from the pulsar activity in the late-afterglow analysis, we obtain $B_s \approx 2 \times 10^{13}$ G. This value has to be compared with that obtained from the constraint that the pulsar luminosity power the late afterglow, $B_{\text{dip}} = 6 \times 10^{12}$ G (see Table 3). If we use the parameters $B_0 = 1.0 \times 10^6$ G and $R_0 = 1.2 \times 10^{11}$ cm from Table 2 for GRB 160625B, and the corresponding $P_{\nu\text{NS}} = P_0 \approx 0.5$ ms, we obtain $B_s \approx 6.8 \times 10^{11}$ G, compared with $B_{\text{dip}} \approx 10^{12}$ G (see

Table 3). An even better agreement can be obtained by using a more accurate value of the ν NS radius, which is surely bigger than the fiducial value $R_{\nu\text{NS}} = 10^6$ cm we have used in these estimates.

6. Nature of the Dipole + Quadrupole Magnetic Field Structure of the ν NS

We attribute the spin-down energy of the ν NS to the energy injection of the late-time afterglow. By fitting the observed emission through the synchrotron model, the spin period and the magnetic field of the ν NS can be inferred. In Wang et al. (2019b), we have applied this approach to GRB 130427A and GRB 180728A; here we apply the same method to the recent GRB 190114C and to other two, GRB 160509A and GRB 160625B, for comparison. In Figure 5, we plot the energy injection from the dipole and quadrupole emission of ν NS; the fitting results indicate 190114C leaves a ν NS of spin period 2.1 ms, with dipole magnetic field $B_{\text{dip}} = 5 \times 10^{12}$ G, and a quadrupole magnetic field $>10^{15}$ G. The fitting parameters of all the GRBs are listed in table 3. Generally, the NS in the BdHN I system spins faster, of period $\lesssim 2$ ms, and contains more rotational energy $\gtrsim 10^{52}$ erg. We notice that GRB 160625B has the shortest initial spin period of $P = 0.5$ ms, which is exactly on the margin of the rotational period of an NS at the Keplerian sequence. For an NS of mass $1.4 M_{\odot}$ and radius 12 km, its Keplerian frequency $f_{\text{K}} \simeq 1900$ (Lattimer & Prakash 2004; Riahi et al. 2019), corresponding to the spin period of $P \simeq 0.5$ ms.

From Equations (10) and (11), the orbital separation of the binary system relates to the spin of ν NS as $a_{\text{orb}} \propto P_{\nu\text{NS}}^{2/3}$. Therefore, with the knowledge of the binary separation of GRB 130427A, $\sim 1.35 \times 10^{10}$ cm, the spin period of ~ 1 ms, and the newly inferred spin of GRB 190114C of ~ 1.2 ms, assuming these two systems have the same mass and radius as the CO_{core} and the ν NS, we obtain the orbital separation of GRB 190114C as $\sim 1.52 \times 10^{10}$ cm.

The self-consistent value obtained for the orbital period/separation gives a strong support to our basic assumptions: (1) owing to the system compactness, the binary components are tidally locked, and (2) the angular momentum is conserved in the core-collapse SN process.

We would like to recall that it has been shown that purely poloidal field configurations are unstable against adiabatic perturbations; for nonrotating stars, it has been first demonstrated by Wright (1973), Markey & Tayler (1973; see also Flowers & Ruderman 1977). For rotating stars, similar results have been obtained, e.g., by Pitts & Tayler (1985). In addition, Tayler (1973) has shown that purely toroidal configurations are also unstable. We refer the reader to Spruit (1999) for a review of the different possible instabilities that may be active in magnetic stars. In this vein, the dipole–quadrupole magnetic field configuration found in our analyses with a quadrupole component dominating in the early life of the ν NS is particularly relevant. They also give support to theoretical expectations pointing to the possible stability of poloidal–toroidal magnetic field configurations on timescales longer than the collapsing time of the pre-SN star; for details, see, e.g., Tayler (1980) and Mestel (1984).

It remains the question of how, during the process of gravitational collapse, the magnetic field increases its strength to the observed NS values. This is still one of the most relevant open questions in astrophysics, which at this stage is out of the

scope of the present work. We shall mention here only one important case, which is the traditional explanation for the NS magnetic field strength based on the amplification of the field by magnetic flux conservation. The flux conservation implies $\Phi_i = \pi B_i R_i^2 = \Phi_f = \pi B_f R_f^2$, where i and f stand for the initial and final configurations and $R_{i,f}$ the corresponding radii. The radius of the collapsing iron core is of the order of 10^8 – 10^9 cm, while the radius of the ν NS is of the order of 10^6 cm; therefore, the magnetic flux conservation implies an amplification of 10^4 – 10^6 times the initial field during the ν NS formation. Therefore, a seed magnetic field of 10^7 – 10^9 G is necessary to be present in the iron core of the pre-SN star to explain a ν NS magnetic field of 10^{13} G. The highest magnetic fields observed in main-sequence stars leading to the pre-SN stars of interest are of the order of 10^4 G (Spruit 2009). If the magnetic field is uniform inside the star, then the value of the magnetic field observed in these stars poses a serious issue to the magnetic flux conservation hypothesis for the NS magnetic field genesis. A summary of the theoretical efforts to understand the possible sources of the magnetic field of an NS can be found in Spruit (2009).

7. Nature of the Magnetic Field around the Newborn BH

The BH in a BdHN I is formed from the gravitational collapse of the NS companion of the CO_{core} , which reaches critical mass by the hypercritical accretion of the ejecta of the SN explosion of the CO_{core} . Hence, the magnetic field surrounding the BH derived in the previous section to explain the GeV emission should originate from the collapsed NS. In fact, the magnetic field of the ν NS evaluated at the BH position is too low to be relevant in this discussion. As we shall see, the magnetic field inherited from the collapsed NS can easily reach values of the order of 10^{14} G. Instead, the magnetic field of the ν NS at the BH site is $B_{\text{dip}}(R_{\nu\text{NS}}/a_{\text{orb}})^3 = 10$ G, adopting fiducial parameters according to the results of Table 3: a dipole magnetic field at the ν NS surface $B_{\text{dip}} = 10^{13}$ G, a binary separation of $a_{\text{orb}} = 10^{10}$ cm, and a ν NS radius of $R_{\nu\text{NS}} = 10^6$ cm.

Having clarified this issue, we proceed now to discuss the nature of the field. Both the ν NS and the NS follow an analogous formation channel, namely, they are born from core-collapse SNe. In fact, to reach the BdHN stage, the massive binary has to survive two SN events: the first SN which forms the NS and the second one which forms the ν NS (core collapse of the CO_{core}). Figure 1 shows the evolutionary path of a massive binary leading to a BdHN I. It is then clear that the NS companion of the CO_{core} will have magnetic field properties analogous to those of the ν NS, which were discussed in the previous section. Therefore, we can conclude that the BH forms from the collapse of a magnetized and fast-rotating NS.

In this scenario, the magnetic field of the collapsing NS companion should then be responsible for the magnetic field surrounding the BH. Only a modest amplification of the initial field from the NS, which is $\sim 10^{13}$ G, is needed to reach the value of 10^{14} G around the newborn BH. Then, even the single action of magnetic flux conservation can suffice to explain the magnetic field amplification. The BH horizon is $r_+ \sim GM/c^2$, where M can be assumed to be equal to the NS critical mass, say, $3 M_{\odot}$, so $r_+ \approx 4.4$ km. The NS at the collapse point, owing to high rotation, will have a radius in excess of the typically adopted 10 km (Cipolletta et al. 2015); let us assume a conservative range of 12–15 km. These conditions suggest that

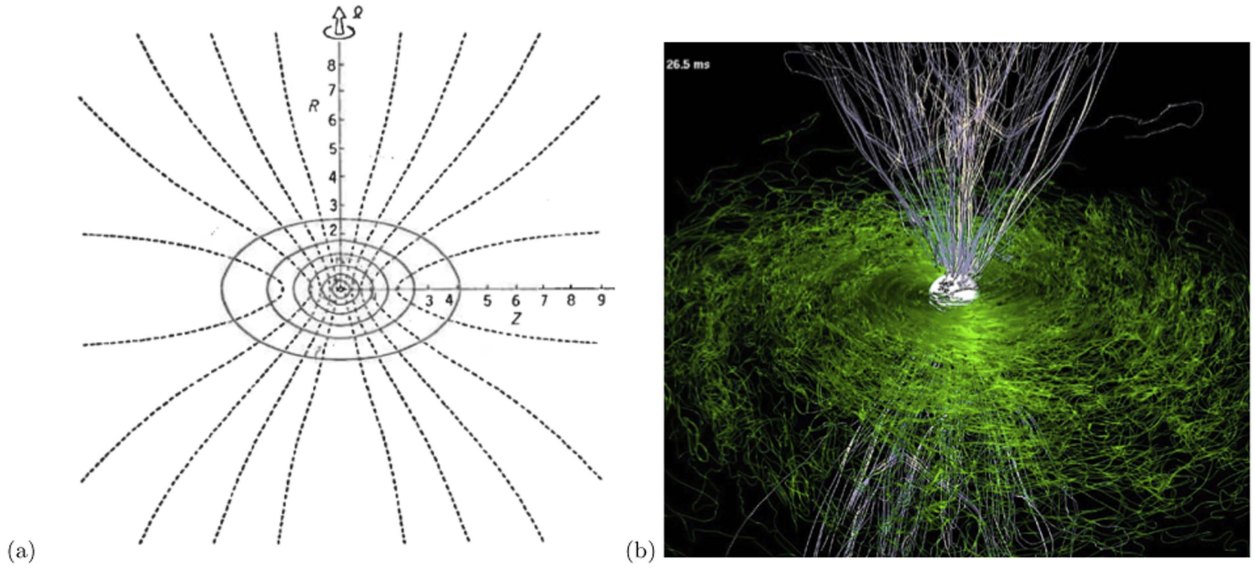


Figure 6. (a) Figure reproduced from Wilson (1978): numerical simulation of the gravitational collapse of a star accounting for the magnetic field presence. Isodensity surfaces are indicated by the solid lines and poloidal field lines are indicated by the dashed lines. The time is the end of the numerical simulation. (b) Figure taken from Rezzolla et al. (2011) with the author’s permission. Magnetic-field structure after the collapse to a BH. Green refers to magnetic-field lines inside the torus and on the equatorial plane, while white refers to magnetic-field lines outside the torus and near the axis.

magnetic flux conservation magnifies the magnetic field in the BH formation by a factor of 7–12. Therefore, a seed field of 10^{13} G present in the collapsing NS is enough to explain the magnetic field of 10^{14} G near the newborn BH.

It is worth clarifying a crucial point: the magnetic field has to remain anchored to some NS material, which guarantees its existence. It is therefore expected that some part of the NS does not take part in the BH formation. Assuming that magnetic flux is conserved during the collapse, then the magnetic energy is a constant fraction of the gravitational energy during the entire process, so only high rotation (see, e.g., Becerra et al. 2016) and some degree of differential rotation (see, e.g., Shibata et al. 2006) of the NS at the critical mass point are responsible for some fraction of the NS matter to avoid remaining outside with sufficient angular momentum to orbit the newborn BH (see, e.g., Figure 6).

The three-dimensional simulations of BdHNe presented in Becerra et al. (2019) show that the part of the SN ejecta surrounding the BH forms a torus-like structure around it. The aforementioned matter from the NS with high angular momentum will add to this orbiting matter around the BH. In the off-equatorial directions, the density is much smaller (Ruffini et al. 2018b; Becerra et al. 2019; see also Ruffini et al. 2019a). This implies that on the equatorial plane, the field is compressed, while in the axial direction, the matter accretion flows in along the field lines.

Our inner engine, the BH + magnetic field configuration powering the high-energy emission in a BdHN I, finds additional support in numerical simulations of magnetic and rotational collapse into a BH. The first numerical computer treatment of the gravitational collapse to a BH in the presence of magnetic fields starts with the pioneering two-dimensional simulations by Wilson (1975; see Figure 6(a), reproduced from Wilson 1978). These works already showed the amplification of the magnetic field in the gravitational collapse process. Rotating magnetized gravitational collapse into a BH has been more recently treated in greater detail by three-dimensional simulations, which have confirmed this picture and the

crucial role of the combined presence of magnetic field and rotation (Dionysopoulou et al. 2013; Nathanail et al. 2017; Most et al. 2018).

Additional support can be also found in the context of binary NS mergers. Numerical simulations have indeed shown that the collapse of the unstable massive NS formed in the merger into a BH leads to a configuration composed of a BH surrounded by a nearly collimated magnetic field and an accretion disk (see Duez et al. 2006a, 2006b; Shibata et al. 2006; Stephens et al. 2007, 2008 for details). Three-dimensional numerical simulations have also been performed and confirm this scenario (Rezzolla et al. 2011). In particular, it is appropriate to underline the strong analogy between Figure 6(a) taken from Wilson (1978) with Figure 6(b) reproduced in this paper from Rezzolla et al. (2011). It is also interesting that the value of the magnetic field close to the BH estimated in Rezzolla et al. (2011) along the BH spin axis, 8×10^{14} G, is similar to the value of 3×10^{14} G needed for the operation of the “inner engine” of GRB 130427A (Ruffini et al. 2018d). What is also conceptually important is that the uniform magnetic field assumed by the Wald solution should be expected to reach a poloidal configuration already relatively close to the BH. This already occurs in the original Wilson (1978) solution confirmed by the recent and most detailed calculation by Rezzolla et al. (2011); see Figures 6(a) and (b).

Although the above simulations refer to the remnant configuration of a binary NS merger, the post-merger configuration is analogous to the one developed for BdHNe I related to the newborn BH, which we have applied in our recent works (see, e.g., Ruffini et al. 2018b, 2018d, 2019d, 2019a; Wang et al. 2019b, and references therein), and which is supported by the recently presented three-dimensional simulations of BdHNe (see Becerra et al. 2019 for details).

Before closing, let us indicate the difference between the NS merger and the BdHN. In the case of the BdHN, the gravitational collapse leading to the BH with the formation of a horizon creates a very-low-density cavity of 10^{-14} g cm $^{-3}$ with a radius of $\sim 10^{11}$ cm in the SN ejecta; see Figure 1 and

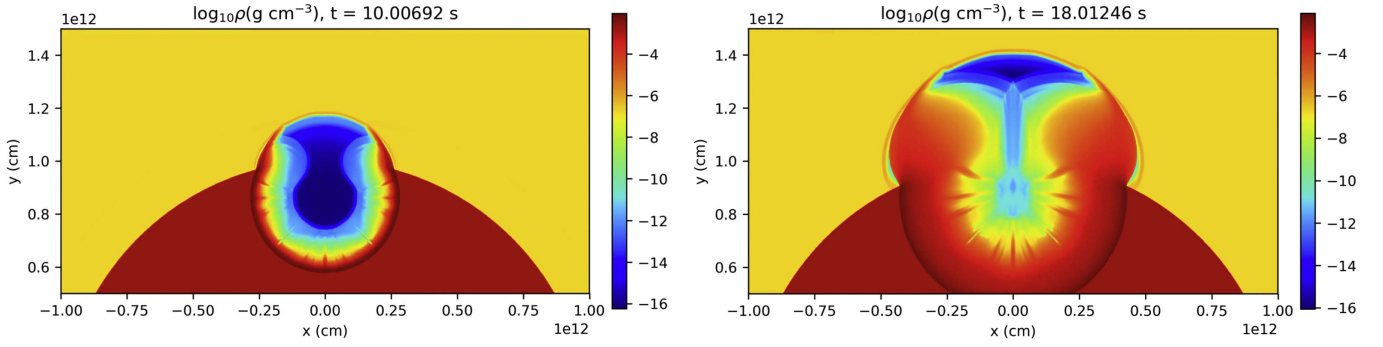


Figure 7. Spatial distribution of matter density at different times of impact of the $e^+e^- \gamma$ plasma onto the cavity walls at $t_{\text{imp}} = 10$ s (left) and $t_{\text{imp}} = 18$ s (right) for GRB 190114C; more information in Ruffini et al. (2019b).

Figure 7, reproduced from Ruffini et al. (2019b). The presence of such a low-density environment is indeed essential for the successful operation of the “inner engine.”

Reaching a poloidal configuration already close to the BH in the Wald solution and the existence of the cavity are crucial factors in the analysis of the propagation of the photons produced by synchrotron radiation and in reaching the transparency condition of the “inner engine” of the BdHN (Ruffini et al. 2019d).

8. Conclusions

Our general conclusions were reached by comparing and contrasting the observations of GRB 130427A, GRB 160509A, GRB 160625B, GRB 180728A, and GRB 190114C:

1. From the analysis of GRB 130427A (Ruffini et al. 2018a) and GRB 190114C presented here (see Figures 4 and 5), we conclude that the early ($t \sim 10^2$ – 10^4 s) X-ray emission during the FPA phase is explained by the injection of ultrarelativistic electrons from the ν NS into the magnetized expanding ejecta, producing synchrotron radiation. The magnetic field inferred in this part of the analysis is found to be consistent with the toroidal/longitudinal magnetic field component of the ν NS. The dominance of this component is expected at distances much larger ($\sim 10^{12}$ cm) than the light cylinder radius in which this synchrotron emission occurs. No data on the other GRBs considered in this paper are available in this time interval.
2. Using the data of all present GRBs, we concluded that at times $t \gtrsim 10^3$ – 10^4 s of the FPA phase, the power-law decaying luminosity is dominated by the pulsar magnetic-braking radiation. We have inferred a dipole+quadrupole structure of the ν NS magnetic field, with the quadrupole component initially dominant. The strength of the dipole component is about 10^{12} – 10^{13} G while that of the quadrupole can be of order 10^{15} G (see Figure 4 and Table 3). As clearly shown in Figures 4 and 5, ν NS solely with the dipole + quadrupole magnetic field structure cannot explain the emission of the early FPA phase, which is dominated by SN emission.
3. We have checked that the magnetic field of the ν NS, inferred independently in the two above regimes of the FPA phase, give values in very good agreement. The ν NS magnetic fields obtained from the explanation of the FPA phase, at times 10^2 – 10^3 s, by synchrotron radiation, and at times $t \gtrsim 10^4$ s by pulsar magnetic braking, are in close agreement (see Section 4, Table 3 and Figure 5).

4. In Section 5, we have shown the consistency of the inferred ν NS parameters with the expectations in the BdHN scenario. In particular, we have used the rotation period of the ν NS inferred from the FPA phase at times $t \gtrsim 10^3$ – 10^4 s, we have inferred the orbital period/separation assuming tidal synchronization of the binary and angular momentum conservation in the gravitational collapse of the iron core leading to the ν NS. This inferred binary separation is shown to be in excellent agreement with the numerical simulations of the binary progenitor in Wang et al. (2019b).

Before concluding, in view of the recent understanding gained on the “inner engine” of the high-energy emission of the GRB (Ruffini et al. 2019d), we can also conclude the following:

1. The magnetic field along the rotational axis of the BH is rooted in the magnetosphere left by the binary companion NS prior to the collapse.
2. While in the equatorial plane the field is magnified by magnetic flux conservation, in the axial direction, the matter accretion flows in along the field lines; see Figure 2 and Becerra et al. (2019). Indeed, three-dimensional numerical simulations of the gravitational collapse into a BH in the presence of rotation and a magnetic field confirm our picture; see Figure 6 and Rezzolla et al. (2011), Dionysopoulou et al. (2013), Nathanail et al. (2017), and Most et al. (2018).
3. The clarification reached regarding the role of SN accretion both in the NS and in the ν NS, the stringent limits imposed on the Lorentz factor of the FPA phase, and the energetic requirement of the “inner engine” inferred from recent publications clearly point to an electro-dynamical nature of the “inner engine” of the GRB, occurring close to the BH horizon, as opposed to the traditional, gravitational massive blast-wave model.

We acknowledge the public data from the Swift and Fermi satellites. We appreciate the discussion with Prof. She-sheng Xue and the suggestions from the referee.

References

- Ackermann, M., Ajello, M., Asano, K., et al. 2014, *Sci*, 343, 42
 Alexander, K. D., Laskar, T., Berger, E., et al. 2017, *ApJ*, 848, 69
 Becerra, L., Bianco, C. L., Fryer, C. L., Rueda, J. A., & Ruffini, R. 2016, *ApJ*, 833, 107

- Becerra, L., Cipolletta, F., Fryer, C. L., Rueda, J. A., & Ruffini, R. 2015, *ApJ*, 812, 100
- Becerra, L., Ellinger, C. L., Fryer, C. L., Rueda, J. A., & Ruffini, R. 2019, *ApJ*, 871, 14
- Becerra, L., Guzzo, M. M., Rossi-Torres, F., et al. 2018, *ApJ*, 852, 120
- Bianco, C. L., Ruffini, R., & Xue, S.-S. 2001, *A&A*, 368, 377
- Blandford, R. D., & McKee, C. F. 1976, *PhFl*, 19, 1130
- Blandford, R. D., & Znajek, R. L. 1977, *MNRAS*, 179, 433
- Cipolletta, F., Cherubini, C., Filippi, S., Rueda, J. A., & Ruffini, R. 2015, *PhRvD*, 92, 023007
- Costa, E., Frontera, F., Heise, J., et al. 1997, *Natur*, 387, 783
- Dai, Z. G., & Lu, T. 1998a, *A&A*, 333, L87
- Dai, Z. G., & Lu, T. 1998b, *PhRvL*, 81, 4301
- Damour, T., & Ruffini, R. 1975, *PhRvL*, 35, 463
- de Pasquale, M., Oates, S. R., Page, M. J., et al. 2007, *MNRAS*, 377, 1638
- Dionysopoulou, K., Alic, D., Palenzuela, C., Rezzolla, L., & Giacomazzo, B. 2013, *PhRvD*, 88, 044020
- Duez, M. D., Liu, Y. T., Shapiro, S. L., Shibata, M., & Stephens, B. C. 2006a, *PhRvL*, 96, 031101
- Duez, M. D., Liu, Y. T., Shapiro, S. L., Shibata, M., & Stephens, B. C. 2006b, *PhRvD*, 73, 104015
- Fan, Y.-Z., & Xu, D. 2006, *MNRAS*, 372, L19
- Fan, Y.-Z., Yu, Y.-W., Xu, D., et al. 2013, *ApJL*, 779, L25
- Filippenko, A. V., Barth, A. J., Matheson, T., et al. 1995, *ApJL*, 450, L11
- Flowers, E., & Ruderman, M. A. 1977, *ApJ*, 215, 302
- Fryer, C. L., Oliveira, F. G., Rueda, J. A., & Ruffini, R. 2015, *PhRvL*, 115, 231102
- Fryer, C. L., Rueda, J. A., & Ruffini, R. 2014, *ApJL*, 793, L36
- Fryer, C. L., Woosley, S. E., & Hartmann, D. H. 1999, *ApJ*, 526, 152
- Galama, T. J., Vreeswijk, P. M., van Paradijs, J., et al. 1998, *Natur*, 395, 670
- Goldreich, P., & Julian, W. H. 1969, *ApJ*, 157, 869
- Heger, A., Fryer, C. L., Woosley, S. E., Langer, N., & Hartmann, D. H. 2003, *ApJ*, 591, 288
- Iwamoto, K., Nakamura, T., Nomoto, K., et al. 2000, *ApJ*, 534, 660
- Izzo, L., de Ugarte Postigo, A., Maeda, K., et al. 2019, *Natur*, 565, 324
- Kouveliotou, C., Granot, J., Racusin, J. L., et al. 2013, *ApJL*, 779, L1
- Laskar, T., Alexander, K. D., Berger, E., et al. 2016, *ApJ*, 833, 88
- Lattimer, J. M., & Prakash, M. 2004, *Sci*, 304, 536
- Levan, A. J., Cenko, S. B., Perley, D. A., & Tanvir, N. R. 2013, *GCN*, 14455, 1
- Li, L. 2019, *ApJS*, 242, 16
- Li, L., Wang, Y., Shao, L., et al. 2018a, *ApJS*, 234, 26
- Li, L., Wu, X.-F., Huang, Y.-F., et al. 2015, *ApJ*, 805, 13
- Li, L., Wu, X.-F., Lei, W.-H., et al. 2018b, *ApJS*, 236, 26
- Lü, H.-J., Lü, J., Zhong, S.-Q., et al. 2017, *ApJ*, 849, 71
- Lü, H.-J., & Zhang, B. 2014, *ApJ*, 785, 74
- Lü, H.-J., Zhang, B., Lei, W.-H., Li, Y., & Lasky, P. D. 2015, *ApJ*, 805, 89
- MAGIC Collaboration, Acciari, V. A., Ansoldi, S., et al. 2019, *Natur*, 575, 455
- Markey, P., & Tayler, R. J. 1973, *MNRAS*, 163, 77
- Maselli, A., Melandri, A., Nava, L., et al. 2014, *Sci*, 343, 48
- Melandri, A., Izzo, L., D'Avanzo, P., et al. 2019, *GCN*, 23983, 1
- Mestel, L. 1984, *AN*, 305, 301
- Mészáros, P., & Rees, M. J. 1997, *ApJL*, 482, L29
- Metzger, M. R., Djorgovski, S. G., Kulkarni, S. R., et al. 1997, *Natur*, 387, 878
- Mirzoyan, R., Noda, K., Moretti, E., et al. 2019, *GCN*, 23701, 1
- Most, E. R., Nathanail, A., & Rezzolla, L. 2018, *ApJ*, 864, 117
- Narayan, R., Paczynski, B., & Piran, T. 1992, *ApJL*, 395, L83
- Nathanail, A., Most, E. R., & Rezzolla, L. 2017, *MNRAS*, 469, L31
- Nomoto, K., Yamaoka, H., Pols, O. R., et al. 1994, *Natur*, 371, 227
- Paczynski, B. 1991, *AcA*, 41, 257
- Paczynski, B. 1992, in *Gamma-Ray Bursts from Colliding Neutron Stars*, ed. C. Ho, R. I. Epstein, & E. E. Fenimore (Cambridge: Cambridge Univ. Press), 67
- Pian, E., Mazzali, P. A., Masetti, N., et al. 2006, *Natur*, 442, 1011
- Pitts, E., & Tayler, R. J. 1985, *MNRAS*, 216, 139
- Price, D. J. 2011, *SPLASH: An Interactive Visualization Tool for Smoothed Particle Hydrodynamics Simulations*, Astrophysics Source Code Library, ascl:1103.004
- Rees, M. J., & Meszaros, P. 1992, *MNRAS*, 258, 41P
- Rezzolla, L., Giacomazzo, B., Baiotti, L., et al. 2011, *ApJL*, 732, L6
- Riahi, R., Kalantari, S. Z., & Rueda, J. A. 2019, *PhRvD*, 99, 043004
- Rowlinson, A., O'Brien, P. T., Metzger, B. D., Tanvir, N. R., & Levan, A. J. 2013, *MNRAS*, 430, 1061
- Rowlinson, A., O'Brien, P. T., Tanvir, N. R., et al. 2010, *MNRAS*, 409, 531
- Rueda, J. A., & Ruffini, R. 2012, *ApJL*, 758, L7
- Rueda, J. A., Ruffini, R., & Wang, Y. 2019, *Univ*, 5, 110
- Ruffini, R., Becerra, L., Bianco, C. L., et al. 2018a, *ApJ*, 869, 151
- Ruffini, R., Bianco, C. L., Enderli, M., et al. 2013, *GCN*, 14526, 1
- Ruffini, R., Karlica, M., Sahakyan, N., et al. 2018b, *ApJ*, 869, 101
- Ruffini, R., Li, L., Moradi, R., et al. 2019a, *arXiv:1904.04162*
- Ruffini, R., Melon Fuksman, J. D., & Vereshchagin, G. V. 2019b, *ApJ*, 883, 191
- Ruffini, R., Moradi, R., Aimuratov, Y., et al. 2019c, *GCN*, 23715, 1
- Ruffini, R., Moradi, R., Rueda, J. A., et al. 2019d, *ApJ*, 886, 82
- Ruffini, R., Rodriguez, J., Muccino, M., et al. 2018c, *ApJ*, 859, 30
- Ruffini, R., Rueda, J. A., Moradi, R., et al. 2018d, *arXiv:1811.01839*
- Ruffini, R., Rueda, J. A., Muccino, M., et al. 2016, *ApJ*, 832, 136
- Ruffini, R., Wang, Y., Aimuratov, Y., et al. 2018e, *ApJ*, 852, 53
- Ruffini, R., Wang, Y., Enderli, M., et al. 2015, *ApJ*, 798, 10
- Ruffini, R., & Wilson, J. R. 1975, *PhRvD*, 12, 2959
- Sari, R. 1997, *ApJL*, 489, L37
- Sari, R., & Piran, T. 1995, *ApJL*, 455, L143
- Sari, R., Piran, T., & Narayan, R. 1998, *ApJL*, 497, L17
- Selsing, J., Fynbo, J. P. U., Heintz, K. E., Watson, D., & Dyrbye, N. 2019, *GCN*, 23695, 1
- Shibata, M., Duez, M. D., Liu, Y. T., Shapiro, S. L., & Stephens, B. C. 2006, *PhRvL*, 96, 031102
- Skilling, J. 2004, in *AIP Conf. Proc. 735, Cosmic Magnetic Fields: From Planets, to Stars and Galaxies*, ed. R. Fischer, R. Preuss, & U. V. Toussaint (Melville, NY: AIP), 395
- Spruit, H. C. 1999, *A&A*, 349, 189
- Spruit, H. C. 2009, in *IAU Symp. 259, Cosmic Magnetic Fields: From Planets, to Stars and Galaxies*, ed. K. G. Strassmeier, A. G. Kosovichev, & J. E. Beckman (Cambridge: Cambridge Univ. Press), 61
- Stephens, B. C., Duez, M. D., Liu, Y. T., Shapiro, S. L., & Shibata, M. 2007, *CQGra*, 24, S207
- Stephens, B. C., Shapiro, S. L., & Liu, Y. T. 2008, *PhRvD*, 77, 044001
- Sturmer, S. J., Skibo, J. G., Dermer, C. D., & Mattox, J. R. 1997, *ApJ*, 490, 619
- Tam, P.-H. T., He, X.-B., Tang, Q.-W., & Wang, X.-Y. 2017, *ApJL*, 844, L7
- Tanvir, N. R., Levan, A. J., Cenko, S. B., et al. 2016, *GCN*, 19419, 1
- Tayler, R. J. 1973, *MNRAS*, 161, 365
- Tayler, R. J. 1980, *MNRAS*, 191, 151
- Troja, E., Cusumano, G., O'Brien, P. T., et al. 2007, *ApJ*, 665, 599
- Vianello, G., Lauer, R. J., Burgess, J. M., et al. 2015, *arXiv:1507.08343*
- Wald, R. M. 1974, *PhRvD*, 10, 1680
- Wang, Y., Li, L., Moradi, R., & Ruffini, R. 2019a, *arXiv:1901.07505*
- Wang, Y., Rueda, J. A., Ruffini, R., et al. 2019b, *ApJ*, 874, 39
- Waxman, E., & Piran, T. 1994, *ApJL*, 433, L85
- Wijers, R. A. M. J., Rees, M. J., & Meszaros, P. 1997, *MNRAS*, 288, L51
- Wilson, J. R. 1975, *NYASA*, 262, 123
- Wilson, J. R. 1978, in *Physics and Astrophysics of Neutron Stars and Black Holes*, ed. R. Giacconi & R. Ruffini (Amsterdam: North-Holland), 644
- Woosley, S. E. 1993, *ApJ*, 405, 273
- Woosley, S. E., & Bloom, J. S. 2006, *ARA&A*, 44, 507
- Wright, G. A. E. 1973, *MNRAS*, 162, 339
- Xu, D., de Ugarte Postigo, A., Leloudas, G., et al. 2013, *ApJ*, 776, 98
- Xu, D., Malesani, D., Fynbo, J. P. U., et al. 2016, *GCN*, 1, 19600
- Yoshida, T., & Umeda, H. 2011, *MNRAS*, 412, L78
- Zhang, B. 2018, *The Physics of Gamma-Ray Bursts* (Cambridge: Cambridge Univ. Press)
- Zhang, B., & Mészáros, P. 2001, *ApJL*, 552, L35
- Zhang, B.-B., Zhang, B., Castro-Tirado, A. J., et al. 2018, *NatAs*, 2, 69



The blackholic quantum

J. A. Rueda^{1,2,3,4,5,a}, R. Ruffini^{1,2,6,b}

¹ ICRA Net, Piazza della Repubblica 10, 65122 Pescara, Italy

² ICRA, Dipartimento di Fisica, Sapienza Università di Roma, P.le Aldo Moro 5, 00185 Rome, Italy

³ ICRA Net-Ferrara, Dipartimento di Fisica e Scienze della Terra, Università degli Studi di Ferrara, Via Saragat 1, 44122 Ferrara, Italy

⁴ Dipartimento di Fisica e Scienze della Terra, Università degli Studi di Ferrara, Via Saragat 1, 44122 Ferrara, Italy

⁵ INAF, Istituto de Astrofisica e Planetologia Spaziali, Via Fosso del Cavaliere 100, 00133 Rome, Italy

⁶ INAF, Viale del Parco Mellini 84, 00136 Rome, Italy

Received: 12 July 2019 / Accepted: 3 March 2020

© The Author(s) 2020

Abstract We show that the high-energy emission of GRBs originates in the *inner engine*: a Kerr black hole (BH) surrounded by matter and a magnetic field B_0 . It radiates a sequence of discrete events of particle acceleration, each of energy $\mathcal{E} = \hbar \Omega_{\text{eff}}$, the *blackholic quantum*, where $\Omega_{\text{eff}} = 4(m_{\text{Pl}}/m_n)^8 (c a/G M)(B_0^2/\rho_{\text{Pl}})\Omega_+$. Here M , $a = J/M$, $\Omega_+ = c^2 \partial M/\partial J = (c^2/G)a/(2Mr_+)$ and r_+ are the BH mass, angular momentum per unit mass, angular velocity and horizon; m_n is the neutron mass, m_{Pl} , $\lambda_{\text{Pl}} = \hbar/(m_{\text{Pl}}c)$ and $\rho_{\text{Pl}} = m_{\text{Pl}}c^2/\lambda_{\text{Pl}}^3$, are the Planck mass, length and energy density. Here and in the following use CGS-Gaussian units. The timescale of each process is $\tau_{\text{el}} \sim \Omega_+^{-1}$, along the rotation axis, while it is much shorter off-axis owing to energy losses such as synchrotron radiation. We show an analogy with the Zeeman and Stark effects, properly scaled from microphysics to macrophysics, that allows us to define the *BH magneton*, $\mu_{\text{BH}} = (m_{\text{Pl}}/m_n)^4 (c a/G M)e \hbar/(Mc)$. We give quantitative estimates for GRB 130427A adopting $M = 2.3 M_\odot$, $c a/(GM) = 0.47$ and $B_0 = 3.5 \times 10^{10}$ G. Each emitted *quantum*, $\mathcal{E} \sim 10^{37}$ erg, extracts only 10^{-16} times the BH rotational energy, guaranteeing that the process can be repeated for thousands of years. The *inner engine* can also work in AGN as we here exemplified for the supermassive BH at the center of M87.

1 Introduction

The GeV radiation in long GRBs is observed as a continuous, *macroscopic* emission with a luminosity that, in the source rest-frame, follows a specific power-law behavior: for instance the 0.1–100 GeV rest-frame luminosity

of GRB 130427A observed by Fermi-LAT is well fitted by $L = A t^{-\alpha}$, $A = (2.05 \pm 0.23) \times 10^{52}$ erg s^{-1} and $\alpha = 1.2 \pm 0.04$ [1]. We have there shown that the rotational energy of a Kerr BH is indeed sufficient to power the GeV emission. From the global energetics we have determined the BH parameters, namely its mass M and angular momentum per unit mass $a = J/M$ and, from the change of the luminosity with time, we have obtained the slowing-down rate of the Kerr BH. We have applied this procedure to the GeV-emission data of 21 sources. For GRB 130427A, we obtained that the BH initial parameters are $M \approx 2.3 M_\odot$ and $c a/(GM) \approx 0.47$ [2].

One of the most extended multi-messenger campaign of observation in the field of science, ranging from ultra high-energy photons GeV/TeV (MAGIC) and MeV radiation (Swift, Fermi, Integral, Konus/WIND and UHXRT satellites) and to fifty optical observatories including the VLT, has given unprecedented details data on GRB 190114C. An in-depth time-resolved spectral analysis of its prompt emission, obtaining the best fit of the spectrum, and repeating it in successive time iterations with increasingly shorter time bins has been presented in [3]. It turns out that the spectra are self-similar and that the gamma-ray luminosity, expressed in the rest-frame, follows a power-law dependence with an index -1.20 ± 0.26 , similar to the one of the GeV luminosity.

These data have offered us the first observational evidence of the moment of BH formation and, indeed, it clearly appears that the high-energy radiation is emitted in a sequence of elementary events, each of 10^{37} erg, and with an ever increasing repetition time from 10^{-14} to 10^{-12} s [2].

We have shown that this emission can be powered by what we have called the *inner engine* [2–4]: a Kerr BH immersed in a magnetic field B_0 and surrounded by matter. This *inner engine* naturally forms in the binary-driven hypernova (BdHN) scenario of GRBs [5–8]. The BdHN starts with

^a e-mail: jorge.rueda@icra.it (corresponding author)

^b e-mail: ruffini@icra.it

the supernova explosion of a carbon-oxygen star that forms a tight binary system with a neutron star companion. The supernova ejecta produces a hypercritical accretion process onto the neutron star bringing it to the critical mass point for gravitational collapse, hence forming a rotating BH. The Kerr BH, in presence of the magnetic field inherited from the neutron star, induces an electromagnetic field that is described by the Wald solution [9]. The BH is surrounded by matter from the supernova ejecta that supply ionized matter that is accelerated to ultrarelativistic energies at expenses of the BH rotational energy. This model has been applied to specific GRB sources in [2,3,10].

We here show that the GRB high-energy (GeV/TeV) radiation is indeed better understood within this scenario and that in particular: (1) it originates near the BH and (2) it is extracted from the BH rotational energy by *packets, quanta* of energy, in a number of finite discrete processes. We show that it is indeed possible to obtain the *quantum of energy* of this elementary process: $\mathcal{E} = \hbar\Omega_{\text{eff}}$, where Ω_{eff} is proportional to the BH angular velocity, Ω_+ , and the proportionality constant depends only on fundamental constants. The timescale of the elementary process is shown to be $\tau_{\text{el}} \sim \Omega_+^{-1}$. Quantitatively speaking, initially $\mathcal{E} \approx 10^{37}$ erg and τ_{el} is shorter than microseconds.

This elementary process is not only finite in energy but it uses in each iteration only a small fraction of the BH rotational energy which can be as large as $E_{\text{rot}} \sim 10^{53}$ erg. As we shall see, this implies that the repetitive process, in view of the slowing-down of the BH, can lasts thousands of years. The considerations on the *inner engine* apply as well to the case of AGN and we give a specific example for the case of M87*, the supermassive BH at the center of the M87.

2 The inner engine electromagnetic field structure

The axisymmetric Kerr metric for the exterior field of a rotating BH, in Boyer-Lindquist coordinates (t, r, θ, ϕ) , can be written as [11]:

$$ds^2 = - \left(1 - \frac{2\hat{M}r}{\Sigma} \right) (cdt)^2 - \frac{4\hat{a}\hat{M}r \sin^2\theta}{\Sigma} cdt d\phi + \frac{\Sigma}{\Delta} dr^2 + \Sigma d\theta^2 + \left[r^2 + \hat{a}^2 + \frac{2r\hat{M}\hat{a}^2 \sin^2\theta}{\Sigma} \right] \sin^2\theta d\phi^2, \tag{1}$$

where $\Sigma = r^2 + \hat{a}^2 \cos^2\theta$ and $\Delta = r^2 - 2\hat{M}r + \hat{a}^2$. The (outer) event horizon is located at $r_+ = \hat{M} + \sqrt{\hat{M}^2 - \hat{a}^2}$, where $\hat{M} = GM/c^2$ and $\hat{a} = a/c$, being M and $a = J/M$, respectively, the BH mass and the angular momentum per unit mass. Quantities with the hat on top are in geometric units.

Denoting by η_μ and ψ_μ , respectively, the timelike and spacelike Killing vectors, the electromagnetic four-potential of the Wald solution is $A_\mu = \frac{1}{2}B_0 \psi_\mu + \hat{a} B_0 \eta_\mu$, where B_0 is the test magnetic field value [9]. The associated electromagnetic field (in the Carter's orthonormal tetrad), for parallel magnetic field and BH spin, is:

$$E_{\hat{r}} = \frac{\hat{a}B_0}{\Sigma} \left[r \sin^2\theta - \frac{\hat{M}(\cos^2\theta + 1)(r^2 - \hat{a}^2 \cos^2\theta)}{\Sigma} \right], \tag{2}$$

$$E_{\hat{\theta}} = \frac{\hat{a}B_0}{\Sigma} \sin\theta \cos\theta \sqrt{\Delta}, \tag{3}$$

$$B_{\hat{r}} = -\frac{B_0}{\Sigma} \cos\theta \left(-\frac{2\hat{a}^2 \hat{a}r (\cos^2\theta + 1)}{\Sigma} + \hat{a}^2 + r^2 \right), \tag{4}$$

$$B_{\hat{\theta}} = \frac{B_0 r}{\Sigma} \sin\theta \sqrt{\Delta}. \tag{5}$$

3 Energetics and timescale of the elementary process

The electrostatic energy gained by an electron (or proton for the antiparallel case) when accelerated from the horizon to infinity, along the rotation axis, is

$$\varepsilon_e = -eA_\mu \eta^\mu|_\infty + eA_\mu \eta^\mu|_{r_+} = e\hat{a} B_0 = \frac{1}{c} e a B_0, \tag{6}$$

where we have used that $\psi_\mu \eta^\mu = 0$ and $\eta_\mu \eta^\mu \rightarrow -1$ along the rotation axis, and $\eta_\mu \eta^\mu = 0$ on the horizon [9].

The electric field for $\theta = 0$, and at the horizon, E_+ , is [2]:

$$|E_+| = \frac{1}{2} \frac{\hat{a}}{\hat{M}} B_0 = \frac{1}{2} \frac{cJ}{GM^2} B_0 \approx \frac{1}{c} \Omega_+ r_+ B_0, \tag{7}$$

where the last expression is accurate for $\hat{a}/\hat{M} \lesssim 0.5$ [2], and it evidences the *inducting* role of the BH angular velocity

$$\Omega_+ = \frac{\partial M c^2}{\partial J} = c \frac{1}{2} \frac{\hat{a}/\hat{M}}{r_+}. \tag{8}$$

Using Eq. (7), Eq. (6) can be written as

$$\varepsilon_e \approx e |E_+| r_+ \approx \frac{1}{c} e r_+^2 \Omega_+ B_0. \tag{9}$$

It is worth to note that this angular frequency can be related to the energy gained timescale of the elementary process:

$$\tau_{\text{el}} = \frac{\varepsilon_e}{e|E_+|c} \approx \frac{r_+}{c} = \frac{\hat{a}/\hat{M}}{2\Omega_+}, \tag{10}$$

that is the characteristic acceleration time of the particle along the BH rotation axis. Thus, this is the longest timescale for the elementary process and it happens on the rotation axis where no (or negligible) radiation losses occur. This is relevant for the emitting power of ultrahigh-energy charged particles leading to ultrahigh-energy cosmic rays. Off-polar axis,

the charged particles emit e.g. synchrotron radiation at GeV energies, in a much shorter timescale of the order of 10^{-14} s (see [2] for details).

The total electric energy available for the *inner engine* elementary process is [2]:

$$\mathcal{E} \approx \frac{1}{2}|E_+|^2 r_+^3 = \frac{1}{4} \frac{\hat{a}}{\hat{M}} \frac{r_+ \Omega_+}{c} r_+^3 B_0^2, \tag{11}$$

where in the last equality we have used Eqs. (7) and (8).

4 The quantum of energy for GRBs

We recall that in a BdHN the BH is formed from the collapse of a neutron star when it reaches the critical mass, M_{crit} , by accreting the ejected matter in the supernova explosion of a companion carbon-oxygen star [5–8, 12–14]. Thus, for the GRB case we can adopt $r_+ \sim 2GM/c^2$ and $M = M_{\text{crit}} \sim m_{\text{pl}}^3/m_n^2$, where M_{crit} is accurate within a factor of order unity; $m_{\text{pl}} = \sqrt{\hbar c/G}$ and m_n are the Planck and neutron mass. With this, the energy per proton (9) can be written in the *quantized* form:

$$\varepsilon_e = \hbar \omega_p, \quad \omega_p \equiv \frac{4G}{c^4} \left(\frac{m_{\text{pl}}}{m_n}\right)^4 e B_0 \Omega_+. \tag{12}$$

Following the above steps for ε_e , we can also write Eq. (11) in the *quantized* form:

$$\mathcal{E} = \hbar \Omega_{\text{eff}}, \quad \Omega_{\text{eff}} \equiv 4 \left(\frac{m_{\text{pl}}}{m_n}\right)^8 \left(\frac{\hat{a}}{\hat{M}}\right) \left(\frac{B_0^2}{\rho_{\text{pl}}}\right) \Omega_+, \tag{13}$$

where $\rho_{\text{pl}} \equiv m_{\text{pl}} c^2 / \lambda_{\text{pl}}^3$ and $\lambda_{\text{pl}} = \hbar / (m_{\text{pl}} c)$ are the Planck energy-density and length. The quantities in parenthesis are dimensionless; e.g. B_0^2 is an energy density as it is ρ_{pl} . Each discrete process extracts a specific amount of the BH rotational energy set by the *blackholic quantum* (13).

5 Specific quantitative examples

Concerning quantitative estimates, let us compute the main physical quantities of the *inner engine* for the case of GRB 130427A [2]. We have there estimated that, an *inner engine* composed of a newborn BH of $M \approx 2.3 M_\odot$, $\hat{a}/\hat{M} = 0.47$ and $B_0 = 3.5 \times 10^{10}$ G, can explain the observed GeV emission. We recall that the *inner engine* parameters in [2] were determined at the end of the prompt emission (at 37 s rest-frame time). At that time, the observed GeV luminosity is $L_{\text{GeV}} \approx 10^{51}$ erg s $^{-1}$. The timescale of synchrotron radiation expected to power this emission was found to be $t_c \sim 10^{-14}$ s (to not be confused with τ_{el}), which implies an energy $\mathcal{E} \sim L_{\text{GeV}} \times t_c = 10^{37}$ erg, consistent with the

Table 1 *Inner engine* astrophysical quantities for GRBs and AGN. The power reported in the last row is the one to accelerate ultrahigh-energy particles, i.e. $\dot{\mathcal{E}} = \mathcal{E}/\tau_{\text{el}}$. In both cases the parameters (mass, spin and magnetic field) have been fixed to explain the observed high-energy (\gtrsim GeV) luminosity

	GRB (130427-like)	AGN (M87*-like)
τ_{el}	2.21×10^{-5} s	0.49 day
ε_e (eV)	1.68×10^{18}	1.19×10^{19}
\mathcal{E} (erg)	4.73×10^{36}	5.19×10^{47}
$\dot{\mathcal{E}}$ (erg/s)	2.21×10^{41}	1.22×10^{43}

blackholic quantum estimated here for the above *inner engine* parameters (see Table 1).

The elementary, discrete process introduced here can also be at work in AGN where the time variability of the high-energy GeV–TeV radiation appears to be emitted on sub-horizon scales (see [15] for the case of M87*). Thus, we also show in Table 1 the physical quantities for an AGN, which can be obtained from the expressions in Sect. 3. We adopt as a proxy M87*, so $M \approx 6 \times 10^9 M_\odot$ (e.g. [16]), and we assume respectively for the BH spin and the external magnetic field, $\hat{a}/\hat{M} = 0.9$ and $B_0 = 50$ G. The magnetic field has been fixed to explain the observed high-energy luminosity which is $\text{few} \times 10^{42}$ erg s $^{-1}$ (e.g. [17, 18]).

This shows that the energy of the *blackholic quantum* is finite and is a very small fraction of the BH rotational energy: for GRBs we have $E_{\text{rot}} \sim 10^{53}$ erg and $\mathcal{E}/E_{\text{rot}} \approx 10^{-16}$ and for AGN $\mathcal{E}/E_{\text{rot}} \approx 10^{-13}$. This guarantees that the emission process has to occur following a sequence of the elementary processes. Under these conditions, the duration of the repetitive sequence, $\Delta t \sim (E_{\text{rot}}/\mathcal{E})\tau_{\text{el}}$, can be of thousands of years, in view of the slowing-down of the BH leading to an ever increasing value of τ_{el} [2] (while \mathcal{E} holds nearly constant).

6 The black hole magneton

It is interesting to show the analogy of the above result with the case of an atom placed in an external electric or magnetic field for which its energy levels suffer a shift, respectively, from the Stark or Zeeman effect (see e.g. [19]).

In the case of the Zeeman effect, the energy shift is:

$$\Delta\varepsilon_Z = \mu_B B_0, \quad \mu_B \equiv e \frac{\hbar}{2m_e c}, \tag{14}$$

where μ_B is the Bohr magneton. Indeed, by using $\Omega_+ \approx c(\hat{a}/\hat{M})/(4GM/c^2)$, and introducing μ_{BH} , the *BH magneton*,

$$\mu_{\text{BH}} \equiv \left(\frac{m_{\text{pl}}}{m_n}\right)^4 \left(\frac{\hat{a}}{\hat{M}}\right) e \frac{\hbar}{Mc}, \tag{15}$$

the particle energy (12) can be written as

$$\varepsilon_e = \mu_{BH} B_0, \tag{16}$$

which adds an unexpected deeper meaning to ε_e .

In the Stark effect, the energy shift is given by

$$\Delta\varepsilon_S = e |E_+| r_B, \tag{17}$$

where $r_B = \hbar^2/(m_e e^2)$ is the Bohr radius. This expression can be directly compared with the first equality in Eq. (9).

7 A direct application to the electron

The use of the Wald solution overcomes the conceptual difficulty of explaining the origin of the charge in BH electrodynamics. Indeed, an effective charge of the system can be expressed as [2,9]

$$Q_{\text{eff}} = \frac{G}{c^3} 2 J B_0, \tag{18}$$

which is not an independent parameter but, instead, it is a derived quantity from the BH angular momentum and the magnetic field B_0 . These quantities become the free parameters of the electrodynamical process and therefore the concept of the BH charge is not anymore a primary concept.

The effective charge (18) can be also expressed in terms of M , J and the magnetic moment μ as:

$$Q_{\text{eff}} = \frac{Mc}{J} \mu, \tag{19}$$

where we have used the computation of the Geroch–Hansen multipole moments [20,21] performed in [9]. Assuming the electron spin $J_e = \hbar/2$ and $Q_{\text{eff}} = e$, the magnetic moment becomes the Bohr magneton. But more interestingly, if we adopt the angular momentum and magnetic moment of the electron, then we obtain that the derived effective charge (19) becomes indeed the electron charge:

$$Q_{\text{eff}} = \frac{m_e c}{J_e} \mu_B = \frac{2m_e c}{\hbar} \frac{\hbar}{2m_e c} e = e. \tag{20}$$

8 Conclusions

We recall:

1. That in addition of being exact mathematical solutions of the Einstein equations, BHs are objects relevant for theoretical physics and astrophysics as it was clearly indicated in “Introducing the BH” [22].
2. That the mass-energy of a Kerr–Newman BH, established over a few months period ranging from September 17, 1970, to March 11, 1971 in [23–25], can be simply expressed by

$$M^2 = \frac{c^2 J^2}{4G^2 M_{\text{irr}}^2} + \left(\frac{Q^2}{4G M_{\text{irr}}} + M_{\text{irr}} \right)^2, \tag{21}$$

$$S = 16\pi G^2 M_{\text{irr}}^2 / c^4,$$

$$\delta S = 32\pi G^2 M_{\text{irr}} \delta M_{\text{irr}} / c^4 \geq 0, \tag{22}$$

where Q , J and M are the three independent parameters of the Kerr–Newman geometry: charge, angular momentum and mass. M_{irr} and S are, respectively, the derived quantities representing the irreducible mass and the horizon surface area.

3. That for extracting the Kerr BH rotational energy the existence of the Wald solution [9] was essential [2,3,10].

From the observational point of view, the time-resolved spectral analysis of GRB 130427A [1,2] and GRB 190114C [3] clearly points to the existence of self-similarities in the Fermi-GBM spectra, to the power-law in the GeV luminosity of the Fermi-LAT and to a discrete emission of elementary impulsive events of 10^{37} erg. The timescale of the emission is, on the rotation axis $\sim 10^{-6}$ s, leading to ultrahigh-energy particles contributing to cosmic rays, and off-axis of $\sim 10^{-14}$ s, leading to GeV–TeV radiation [2].

Extrapolating these considerations from a BH to an electron, we showed that the electron charge turns out to be a derived quantity, a function of the electron’s angular momentum and magnetic moment, with the electron’s mass and the speed of light considered as fundamental constants.

The definition, the formulation of the equation and the identification of the mechanism of the process of emission of the *blackholic quantum* has become a necessity and it is presented in this article.

Data Availability Statement This manuscript has no associated data or the data will not be deposited. [Authors’ comment: This is theoretical work in which no experimental data are generated and/or analyzed.]

Open Access This article is licensed under a Creative Commons Attribution 4.0 International License, which permits use, sharing, adaptation, distribution and reproduction in any medium or format, as long as you give appropriate credit to the original author(s) and the source, provide a link to the Creative Commons licence, and indicate if changes were made. The images or other third party material in this article are included in the article’s Creative Commons licence, unless indicated otherwise in a credit line to the material. If material is not included in the article’s Creative Commons licence and your intended use is not permitted by statutory regulation or exceeds the permitted use, you will need to obtain permission directly from the copyright holder. To view a copy of this licence, visit <http://creativecommons.org/licenses/by/4.0/>.

Funded by SCOAP³.

References

1. R. Ruffini, R. Moradi, J.A. Rueda, Y. Wang, Y. Aimuratov, L. Becerra, C.L. Bianco, Y.C. Chen, C. Cherubini, S. Filippi, M. Kar-

- lica, G.J. Mathews, M. Muccino, G.B. Pisani, D. Primorac, S.S. Xue, (2018). [arXiv:1803.05476](https://arxiv.org/abs/1803.05476)
2. R. Ruffini, R. Moradi, J.A. Rueda, L. Becerra, C.L. Bianco, C. Cherubini, S. Filippi, Y.C. Chen, M. Karlica, N. Sahakyan, Y. Wang, S.S. Xue, *Astrophys. J.* **886**(2), 82 (2019). <https://doi.org/10.3847/1538-4357/ab4ce6>
 3. R. Ruffini, L. Li, R. Moradi, J.A. Rueda, Y. Wang, S.S. Xue, C.L. Bianco, S. Campion, J.D. Melon Fuksman, C. Cherubini, S. Filippi, M. Karlica, N. Sahakyan, (2019). [arXiv:1904.04162](https://arxiv.org/abs/1904.04162)
 4. J.A. Rueda, R. Ruffini, M. Karlica, R. Moradi, Y. Wang, (2019). [arXiv:1905.11339](https://arxiv.org/abs/1905.11339)
 5. J.A. Rueda, R. Ruffini, *Astrophys. J.* **758**, L7 (2012). <https://doi.org/10.1088/2041-8205/758/1/L7>
 6. C.L. Fryer, J.A. Rueda, R. Ruffini, *Astrophys. J.* **793**, L36 (2014). <https://doi.org/10.1088/2041-8205/793/2/L36>
 7. L. Becerra, C.L. Bianco, C.L. Fryer, J.A. Rueda, R. Ruffini, *Astrophys. J.* **833**, 107 (2016). <https://doi.org/10.3847/1538-4357/833/1/107>
 8. L. Becerra, M.M. Guzzo, F. Rossi-Torres, J.A. Rueda, R. Ruffini, J.D. Uribe, *Astrophys. J.* **852**, 120 (2018). <https://doi.org/10.3847/1538-4357/aaa296>
 9. R.M. Wald, *Phys. Rev. D* **10**, 1680 (1974). <https://doi.org/10.1103/PhysRevD.10.1680>
 10. R. Ruffini, J.D. Melon Fuksman, G.V. Vereshchagin, *Astrophys. J.* **883**(2), 191 (2019). <https://doi.org/10.3847/1538-4357/ab3c51>
 11. B. Carter, *Phys. Rev.* **174**(5), 1559 (1968). <https://doi.org/10.1103/PhysRev.174.1559>
 12. L. Becerra, F. Cipolletta, C.L. Fryer, J.A. Rueda, R. Ruffini, *Astrophys. J.* **812**, 100 (2015). <https://doi.org/10.1088/0004-637X/812/2/100>
 13. C.L. Fryer, F.G. Oliveira, J.A. Rueda, R. Ruffini, *Phys. Rev. Lett.* **115**(23), 231102 (2015). <https://doi.org/10.1103/PhysRevLett.115.231102>
 14. L. Becerra, C.L. Ellinger, C.L. Fryer, J.A. Rueda, R. Ruffini, *Astrophys. J.* **871**, 14 (2019). <https://doi.org/10.3847/1538-4357/aaf6b3>
 15. J. Aleksić, S. Ansoldi, L.A. Antonelli, P. Antoranz, A. Babic, P. Bangale, J.A. Barrio, J.B. González, W. Bednarek, E. Bernardini, *Science* **346**(6213), 1080 (2014). <https://doi.org/10.1126/science.1256183>
 16. J.L. Walsh, A.J. Barth, L.C. Ho, M. Sarzi, *Astrophys. J.* **770**, 86 (2013). <https://doi.org/10.1088/0004-637X/770/2/86>
 17. A.A. Abdo, M. Ackermann, M. Ajello, W.B. Atwood, M. Axelsson, L. Baldini, J. Ballet, G. Barbiellini, D. Bastieri, K. Bechtol, *Astrophys. J.* **707**(1), 55 (2009). <https://doi.org/10.1088/0004-637X/707/1/55>
 18. S. de Jong, V. Beckmann, S. Soldi, A. Tramacere, A. Gros, *Mon. Not. R. Astron. Soc.* **450**, 4333 (2015). <https://doi.org/10.1093/mnras/stv927>
 19. L.D. Landau, E.M. Lifshitz, *Quantum Mechanics* (Pergamon Press, Oxford, 1965)
 20. R. Geroch, *J. Math. Phys.* **11**(8), 2580 (1970). <https://doi.org/10.1063/1.1665427>
 21. R.O. Hansen, *J. Math. Phys.* **15**(1), 46 (1974). <https://doi.org/10.1063/1.1666501>
 22. R. Ruffini, J.A. Wheeler, *Phys. Today* **24**(1), 30 (1971). <https://doi.org/10.1063/1.3022513>
 23. D. Christodoulou, *Phys. Rev. Lett.* **25**, 1596 (1970). <https://doi.org/10.1103/PhysRevLett.25.1596>
 24. D. Christodoulou, R. Ruffini, *Phys. Rev. D* **4**, 3552 (1971). <https://doi.org/10.1103/PhysRevD.4.3552>
 25. S.W. Hawking, *Phys. Rev. Lett.* **26**, 1344 (1971). <https://doi.org/10.1103/PhysRevLett.26.1344>

ORIGINAL ARTICLE

Some recent results on neutrino oscillations in hypercritical accretion

Juan David Uribe¹ | Jorge Armando Rueda^{1,2,3,4}

¹International Center for Relativistic Astrophysics Network (ICRANet), Pescara, Italy

²ICRANet-Ferrara, Dipartimento di Fisica e Scienze della Terra, Università degli Studi di Ferrara, Ferrara, Italy

³Dipartimento di Fisica e Scienze della Terra, Università degli Studi di Ferrara, Ferrara, Italy

⁴INAF, Istituto di Astrofisica e Planetologia Spaziali, Rome, Italy

Correspondence

J.A. Rueda, ICRANet, P.zza della Repubblica 10, I-65122 Pescara, Italy.
Email: jorge.rueda@icra.it

Abstract

The study of neutrino flavor oscillations in astrophysical sources has been boosted in the last two decades thanks to achievements in experimental neutrino physics and in observational astronomy. We here discuss two cases of interest in the modeling of short and long gamma-ray bursts: hypercritical, that is, highly super-Eddington spherical/disk accretion onto a neutron star/black hole. We show that in both systems, the ambient conditions of density and temperature imply the occurrence of neutrino flavor oscillations, with a relevant role of neutrino self-interactions.

KEYWORDS

black hole, gamma-ray bursts, neutrino flavor oscillations, neutron star

1 | INTRODUCTION

The occurrence of neutrino flavor oscillations has been, undoubtedly, experimentally demonstrated (de Salas et al. 2018). Of special interest here is, it has become clear in recent years that for the analysis of neutrino oscillations in matter, for example, the Mikheyev-Smirnov-Wolfenstein (MSW) effect (Mikheyev & Smirnov 1986; Wolfenstein 1978), refractive effects of neutrinos on themselves, due to the neutrino self-interaction potential, are essential.

Over the last two decades, the achievements of experimental neutrino physics and the constant development of observational astronomy, have caused an increasing interest in the study of the occurrence of neutrino flavor oscillations in astrophysical sources. Although the bulk of astrophysical analyses has been limited to supernova (SN) neutrinos, flavor oscillations may also occur in other relativistic astrophysics sources. In particular, as we are showing here, this phenomenon is expected to occur in known scenarios of short- and long-duration gamma ray bursts (GRBs).

The emergent picture of GRBs is that both, short-duration and long-duration GRBs, originate in binary systems (Ruffini et al. 2016). Short bursts are associated with mergers of NS-NS and/or NS-BH binaries. For this case, the role of neutrino-antineutrino ($\nu\bar{\nu}$) annihilation leading to the formation of an electron-positron plasma (e^-e^+) has been introduced (Narayan et al. 1992) (for general relativistic effects, see [Salmonson & Wilson 2002]). For long bursts, it has been introduced binary progenitor composed of a carbon-oxygen star (CO_{core}) and a companion neutron star (NS) (Fryer et al. 2014; Rueda & Ruffini 2012). These binaries can form in an evolutionary path, including a first SN explosion, common-envelope phases, tidal interactions, and mass loss (Fryer et al. 2015). The GRB is expected to occur when the binary experiences the second SN, that is, the one of the CO_{core} . Part of the ejected matter produces a hypercritical accretion (i.e., highly super-Eddington) process onto the NS companion. The NS then reaches its critical mass for gravitational collapse, hence forming a rotating black hole (BH) (Becerra et al. 2015; Becerra et al. 2016). These systems have been

called binary-driven hypernovae (BdHNe), and they lead to a variety of observable emissions from the X-rays all the way to high-energy gamma rays (see e.g., [Rueda et al. 2019; Ruffini et al. 2019] for details).

As we are showing below, a key ingredient in the above systems is a copious emission of neutrinos during the hypercritical accretion. The high neutrino and matter density involved suggests that a study of neutrino oscillations may lead to new neutrino physics in these sources. Our aim here is to compile the main results of neutrino oscillations in the physical conditions expected in the above scenarios of GRBs.

2 | NEUTRINO OSCILLATIONS

To study the flavor evolution of neutrinos within a particular system, a Hamiltonian governing neutrino oscillation must be set up. The relative strength of the potentials appearing in such Hamiltonian depends on four elements: geometry, mass content, neutrino content, and neutrino mass hierarchy. Geometry refers to the nature of net neutrino fluxes and possible gravitational effects. Mass and neutrino content refers to the distribution of leptons of each flavor (e, μ, τ) present in the medium. Finally, mass hierarchy refers to the relative values of the masses m_1, m_2 , and m_3 for each neutrino mass eigen states. The equations that govern the evolution of an ensemble of mixed neutrinos are the quantum Liouville equations

$$i\dot{\rho}_{\mathbf{p}} = [H_{\mathbf{p}}, \rho_{\mathbf{p}}]; \quad i\dot{\bar{\rho}}_{\mathbf{p}} = [\bar{H}_{\mathbf{p}}, \bar{\rho}_{\mathbf{p}}]. \quad (1)$$

The Hamiltonian is (see, e.g., [Becerra et al. 2018; Uribe Suárez & Rueda Hernandez 2019] and references therein)

$$H_{\mathbf{p},t} = \Omega_{\mathbf{p},t} + \sqrt{2}G_F \int (l_{\mathbf{q},t} - \bar{l}_{\mathbf{q},t})(1 - \mathbf{v}_{\mathbf{q},t} \cdot \mathbf{v}_{\mathbf{p},t}) \frac{d^3\mathbf{q}}{(2\pi)^3} + \sqrt{2}G_F \int (\rho_{\mathbf{q},t} - \bar{\rho}_{\mathbf{q},t})(1 - \mathbf{v}_{\mathbf{q},t} \cdot \mathbf{v}_{\mathbf{p},t}) \frac{d^3\mathbf{q}}{(2\pi)^3}; \quad (2)$$

$$\bar{H}_{\mathbf{p},t} = -\Omega_{\mathbf{p},t} + \sqrt{2}G_F \int (l_{\mathbf{q},t} - \bar{l}_{\mathbf{q},t})(1 - \mathbf{v}_{\mathbf{q},t} \cdot \mathbf{v}_{\mathbf{p},t}) \frac{d^3\mathbf{q}}{(2\pi)^3} + \sqrt{2}G_F \int (\rho_{\mathbf{q},t} - \bar{\rho}_{\mathbf{q},t})(1 - \mathbf{v}_{\mathbf{q},t} \cdot \mathbf{v}_{\mathbf{p},t}) \frac{d^3\mathbf{q}}{(2\pi)^3}. \quad (3)$$

In these equations, $\rho_{\mathbf{p}}$ ($\bar{\rho}_{\mathbf{p}}$) is the matrix of occupation numbers $(\rho_{\mathbf{p}})_{ij} = \langle a_j^\dagger a_i \rangle_{\mathbf{p}}$ for neutrinos ($(\bar{\rho}_{\mathbf{p}})_{ij} = \langle \bar{a}_i^\dagger \bar{a}_j \rangle_{\mathbf{p}}$ for antineutrinos), for each momentum \mathbf{p} and flavors i, j . The diagonal elements are the distribution functions $f_{\nu_i(\bar{\nu}_i)}(\mathbf{p})$ such that their integration over the momentum space gives the neutrino number density n_{ν_i} of a determined flavor i . The off-diagonal elements provide information about the

overlapping between the two neutrino flavors. $\Omega_{\mathbf{p}}$ is the matrix of vacuum oscillation frequencies, $l_{\mathbf{p}}$ and $\bar{l}_{\mathbf{p}}$ are matrices of occupation numbers for charged leptons built in a similar way to the neutrino matrices, and $\mathbf{v}_{\mathbf{p}} = \mathbf{p}/p$ is the velocity of a particle with momentum \mathbf{p} (either neutrino or charged lepton). Since the matter in the accretion zone is composed of protons, neutrons, electrons, and positrons, ν_e and $\bar{\nu}_e$ interact with matter by both charged and neutral currents, while $\nu_\mu, \nu_\tau, \bar{\nu}_\mu$, and $\bar{\nu}_\tau$ interact only by neutral currents. Therefore, the behavior of these states can be clearly divided into electronic and nonelectronic allowing us to use the two-flavor approximation. Within this approximation, ρ in Equation (1) can be written in terms of Pauli matrices and the polarization vector $\mathbf{P}_{\mathbf{p}}$ as:

$$\rho_{\mathbf{p}} = \begin{pmatrix} \rho_{ee} & \rho_{ex} \\ \rho_{xe} & \rho_{xx} \end{pmatrix}_{\mathbf{p}} = \frac{1}{2}(f_{\mathbf{p}} \mathbb{1} + \mathbf{P}_{\mathbf{p}} \cdot \vec{\sigma}), \quad (4)$$

where $f_{\mathbf{p}} = \text{Tr}[\rho_{\mathbf{p}}] = f_{\nu_e}(\mathbf{p}) + f_{\nu_x}(\mathbf{p})$ is the sum of the distribution functions for ν_e and ν_x . Note that the z component of the polarization vector obeys

$$P_{\mathbf{p}}^z = f_{\nu_e}(\mathbf{p}) - f_{\nu_x}(\mathbf{p}). \quad (5)$$

Hence, this component tracks the fractional flavor composition of the system and appropriately normalizing $\rho_{\mathbf{p}}$ allows defining a survival and mixing probability

$$P_{\nu_e \leftrightarrow \nu_e} = \frac{1}{2}(1 + P_{\mathbf{p}}^z), \quad (6a)$$

$$P_{\nu_e \leftrightarrow \nu_x} = \frac{1}{2}(1 - P_{\mathbf{p}}^z). \quad (6b)$$

On the other hand, the Hamiltonian can be written as a sum of three interaction terms:

$$H = H_{\text{vac}} + H_{\text{m}} + H_{\text{vv}}, \quad (7)$$

where H is the two-flavor Hamiltonian. The first term is the Hamiltonian in vacuum (Qian & Fuller 1995):

$$H_{\text{vac}} = \frac{\omega_{\mathbf{p}}}{2} \begin{pmatrix} -\cos 2\theta & \sin 2\theta \\ \sin 2\theta & \cos 2\theta \end{pmatrix} = \frac{\omega_{\mathbf{p}}}{2} \mathbf{B} \cdot \vec{\sigma}, \quad (8)$$

where $\omega_{\mathbf{p}} = \Delta m^2/2p$, $\mathbf{B} = (\sin 2\theta, 0, -\cos 2\theta)$ and θ is the smallest neutrino mixing angle in vacuum.

The other two terms in Equation (3) are special since they make the evolution equations nonlinear. Even though they are very similar, we are considering that the electrons during the accretion form an isotropic gas; hence, the vector $\mathbf{v}_{\mathbf{q}}$ in the first integral is distributed uniformly on the unit sphere and the factor $\mathbf{v}_{\mathbf{q}} \cdot \mathbf{v}_{\mathbf{p}}$ averages to zero. After

integrating the matter Hamiltonian is given by:

$$H_m = \frac{\lambda}{2} \begin{pmatrix} 1 & 0 \\ 0 & -1 \end{pmatrix} = \frac{\lambda}{2} \mathbf{L} \cdot \vec{\sigma}, \quad (9)$$

where $\lambda = \sqrt{2}G_F(n_{e^-} - n_{e^+})$ is the charged current matter potential and $\mathbf{L} = (0, 0, 1)$.

Such simplification cannot be made with the final term. Since neutrinos are responsible for the energy loss of the infalling material during accretion, they must be escaping the accretion zone and the net neutrino and antineutrino flux is nonzero. In this case, the factor $\mathbf{v}_q \cdot \mathbf{v}_p$ cannot be averaged to zero. At any rate, we can still use Equation (4) and obtain (Malkus et al. 2016; Pantaleone 1992; Zhu et al. 2016):

$$H_{\nu\nu} = \sqrt{2}G_F \left[\int (1 - \mathbf{v}_q \cdot \mathbf{v}_p) (P_q - \bar{P}_q) \frac{d^3\mathbf{q}}{(2\pi)^3} \right] \cdot \vec{\sigma}. \quad (10)$$

Introducing every Hamiltonian term in Equation (1), and using the commutation relations of the Pauli matrices, we find the equations of oscillation for neutrinos and antineutrinos for each momentum mode \mathbf{p} :

$$P_p = \left[\omega_p \mathbf{B} + \lambda \mathbf{L} + \sqrt{2}G_F \int (1 - \mathbf{v}_q \cdot \mathbf{v}_p) \times (P_q - \bar{P}_q) \frac{d^3\mathbf{q}}{(2\pi)^3} \right] \cdot P_p; \quad (11a)$$

$$\bar{P}_p = \left[-\omega_p \mathbf{B} + \lambda \mathbf{L} + \sqrt{2}G_F \int (1 - \mathbf{v}_q \cdot \mathbf{v}_p) \times (P_q - \bar{P}_q) \frac{d^3\mathbf{q}}{(2\pi)^3} \right] \cdot \bar{P}_p. \quad (11b)$$

This set of equations is the starting point of any analysis of neutrino oscillation in an astrophysical system.

2.1 | Neutrino oscillation in spherical accretion

In the BdHN scenario of GRBs, the SN material first reaches the gravitational capture region of the NS companion, namely, the Bondi-Hoyle region. The infalling material shocks as it piles up onto the NS surface forming an accretion zone where it compresses and eventually becomes sufficiently hot to trigger a highly efficient neutrino emission process. Neutrinos take away most of the infalling matter's gravitational energy gain, letting it reduce its entropy and be incorporated into the NS. It was shown in (Becerra et al. 2016) that the matter in the accretion zone near the NS surface develops conditions of temperature and density such that it is in a nondegenerate, relativistic, hot plasma state. The most efficient neutrino

emission channel under those conditions becomes the electron positron pair annihilation process. The neutrino emissivity can be approximated with a very good accuracy by (Yakovlev et al. 2001).

$$\varepsilon_i^m \approx \frac{2G_F^2(T)^{8+m}}{9\pi^5} C_{+,i}^2 [\mathcal{F}_{m+1,0}(\eta_{e^+}) \mathcal{F}_{1,0}(\eta_{e^-}) + \mathcal{F}_{m+1,0}(\eta_{e^-}) \mathcal{F}_{1,0}(\eta_{e^+})], \quad (12)$$

where $\mathcal{F}_{k,\ell}(y, \eta)$ are the generalized Fermi functions (see [Becerra et al. 2018] for details) and $\mathcal{F}_{k,\ell}(\eta) = \mathcal{F}_{k,\ell}(y=0, \eta)$. For $m=0$ and $m=1$ Equation (12) gives the neutrino and antineutrino number emissivity (neutrino production rate), and the neutrino and antineutrino energy emissivity (energy per unit volume per unit time) for a certain flavor i , respectively. Using Equation (12), we find that the ratio of emission rates between electronic and nonelectronic neutrino flavors obey the relation

$$\frac{\varepsilon_e^0}{\varepsilon_x^0} \approx \frac{7}{3}. \quad (13)$$

and because of the symmetry of the annihilation process, the neutrinos and antineutrinos are produced in equal quantities. We can also find an expression for the average neutrino energy

$$\langle E_\nu \rangle = \langle E_{\bar{\nu}} \rangle \approx 4.1 T, \quad (14)$$

for all neutrino flavors. The neutrino energy emissivity in Equation (12) can be written as

$$\varepsilon_{e^-e^+} \approx 8.69 \times 10^{30} \left(\frac{T}{1 \text{ MeV}} \right)^9 \text{ MeV cm}^{-3} \text{ s}^{-1}, \quad (15)$$

which allows us to define an effective neutrino emission region (Becerra et al. 2018)

$$\Delta r_\nu = \frac{\varepsilon_{e^-e^+}}{\nabla \varepsilon_{e^-e^+}} \approx 0.08 R_{\text{NS}}, \quad (16)$$

with R_{NS} the radius of the NS. Recollecting results, we can make another simplifying assumption (Becerra et al. 2018): Since the neutrino emission region is thin, we will consider it as a spherical shell. This allows us to use the single-angle approximation (Dasgupta & Dighe 2008; Duan et al. 2006) and simplify the last term in Equations (11a) and (11b). Precisely, the *multi-angle* term and the one responsible for kinematic decoherence (Fogli et al. 2007; Hannestad et al. 2006; Raffelt & Sigl 2007). With the single-angle approximation and the inverse square law of flux dilution, it is possible to find the explicit dependence in r of each of the potentials in Equations (11a) and

(11b), namely,

$$\omega_{p,r} = \frac{\Delta m^2}{2p\langle v_r \rangle}, \quad \lambda_r = \sqrt{2}G_F(n_{e^-} - n_{e^+})\frac{1}{\langle v_r \rangle};$$

$$\mu_r = \frac{\sqrt{2}G_F}{2} \left(\sum_{i \in \{e,x\}} n_{\nu_i}^C \right) \left(\frac{R_{NS}}{r} \right)^2 \left(\frac{1 - \langle v_r \rangle^2}{\langle v_r \rangle} \right), \quad (17)$$

where

$$\langle v_r \rangle = \frac{1}{2} \left[1 + \sqrt{1 - \left(\frac{R_{NS}}{r} \right)^2} \right]. \quad (18)$$

Using Equation (12) and the hydrodynamic simulations in (Becerra et al. 2016), we can obtain the thermodynamic properties of the accreting matter at the NS surface (Table 1), which in turn are the initial condition to solve Equations (11a) and (11b) and obtain an approximate behavior of oscillations. In Figures 1 and 2, we show the solution of Equations (11a) and (11b) for both normal and inverted hierarchies using a monochromatic spectrum dominated by the average neutrino energy for $\dot{M} = 10^{-2}, 10^{-3}, 10^{-4}$ and $5 \times 10^{-5} M_\odot \text{s}^{-1}$. For the inverted hierarchy, there is no difference between the neutrino and antineutrino survival probabilities. This should be expected since for these values of r , the matter and self-interaction potentials are much larger than the vacuum potential, and there is virtually no difference between Equations (11a) and (11b). Also, note that the antineutrino flavor proportions in Table 1 remain virtually unchanged for normal hierarchy while the neutrino flavor proportions change drastically around the point $\lambda_r \sim \omega_r$. From these solutions, we can calculate the oscillation length to be

$$l_{\text{osc}} \approx (0.05 - 1) \text{ km}, \quad (19)$$

which agree with the algebraic estimations in (Hannestad et al. 2006; Raffelt & Sigl 2007). Clearly, the full equations of oscillations are highly nonlinear so the solution may not reflect the real neutrino flavor evolution. Concerning the single-angle approximation, it is discussed in (Fogli et al. 2007; Hannestad et al. 2006; Raffelt & Sigl 2007) that in the more realistic multi-angle approach, kinematic decoherence happens for both mass hierarchies, and in (Esteban-Pretel et al. 2007) the conditions for decoherence as a function of the neutrino flavor asymmetry have been discussed. It is concluded that if the symmetry of neutrinos and antineutrinos is broken beyond the limit of $O(25\%)$, that is, if the difference between emitted neutrinos and antineutrinos is roughly larger than 25% of the total number of neutrinos in the medium, decoherence becomes a sub-dominant effect. As a direct consequence of the peculiar symmetric situation, we are dealing with, in which neutrinos and antineutrinos are produced in

similar numbers, bipolar oscillations happen and, as we have already discussed, they present very small oscillation length as shown in Equation (19). Note also that the bipolar oscillation length depends on the neutrino energy. Therefore, the resulting process is equivalent to an averaging over the neutrino energy spectrum and an equipartition among different neutrino flavors is expected (Raffelt & Sigl 2007). Although, for simplicity, we are dealing with the two neutrino hypothesis, this behavior is easily extended to the more realistic three-neutrino situation. We assume, therefore, that at few kilometers from the emission region, neutrino flavor equipartition is a reality:

$$\nu_e : \nu_\mu : \nu_\tau = 1 : 1 : 1. \quad (20)$$

After leaving the emission region, beyond $r \approx R_{NS} + \Delta r_\nu$, where Δr_ν is the width defined in Equation (16), the effective neutrino density quickly falls in a asymptotic behavior $\mu_r \approx 1/r^4$. The decay of λ_r is slower. Hence, very soon the neutrino flavor evolution is determined by the matter potential. Matter suppresses neutrino oscillations and we do not expect significant changes in the neutrino flavor content along a large region. Nevertheless, the matter potential can be so small that there will be a region along the neutrino trajectory in which it can be compared with the neutrino vacuum frequencies and the higher and lower resonant density conditions will be satisfied. Using the results in (Becerra et al. 2018; Fogli et al. 2003), we can include the matter effects and compare in Table 2 the flavor content at the emission region and after decoherence and the MSW resonance.

Finally, we note that for accretion rates $\dot{M} < 5 \times 10^{-5} M_\odot \text{s}^{-1}$, either the matter potential is close enough to the vacuum potential and the MSW condition is satisfied, or both the self-interaction and matter potentials are so low that the flavor oscillations are only due to the vacuum potential. In both cases, bipolar oscillations are not present (Becerra et al. 2018). Without bipolar oscillations, it is not possible to guarantee that decoherence will be complete and Equation (20) is no longer valid.

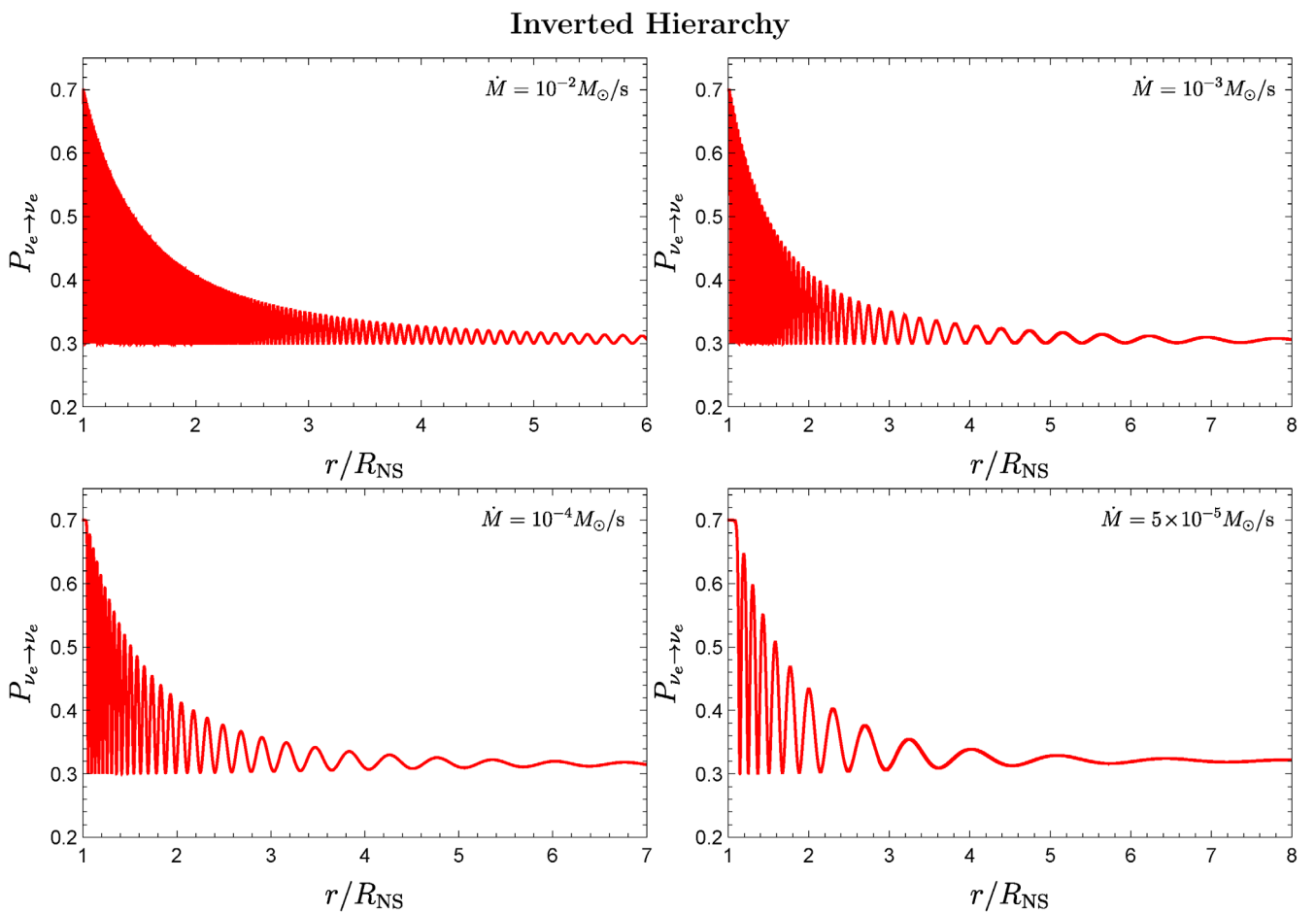
2.2 | Neutrino oscillations in accretion disks

In the same BdHN scenario of Section 2, part of the SN ejecta keeps bound to the newborn Kerr BH, forming an accretion disk (Becerra et al. 2019). In order to study analytically the properties of accretion disks, different models make approximations that allow casting the physics of an accretion disk as a two- or even one-dimensional problem. Here, we will consider neutrino-cooled accretion disks, which are steady-state (Page & Thorne 1974;

TABLE 1 Characteristics inside the neutrino emission zone for selected values of the accretion rate \dot{M}

\dot{M} ($M_{\odot} \text{ s}^{-1}$)	ρ (g cm^{-3})	T (MeV)	$\eta_{e\pm}$	$n_{e^-} - n_{e^+}$ (cm^{-3})	$T_{\nu\bar{\nu}}$ (MeV)	$\langle E_{\nu} \rangle$ (MeV)	$F_{\nu_e, \bar{\nu}_e}^C$ ($\text{cm}^{-2} \text{ s}^{-1}$)	$F_{\nu_x, \bar{\nu}_x}^C$ ($\text{cm}^{-2} \text{ s}^{-1}$)	$n_{\nu_e, \bar{\nu}_e}^C$ (cm^{-3})	$n_{\nu_x, \bar{\nu}_x}^C$ (cm^{-3})	$\sum_i n_{\nu_i, \bar{\nu}_i}^C$ (cm^{-3})
10^{-6}	1.12×10^7	2.59	± 0.193	3.38×10^{30}	2.93	10.61	2.40×10^{38}	1.03×10^{38}	1.60×10^{28}	6.90×10^{27}	2.29×10^{28}
10^{-5}	3.10×10^7	3.34	± 0.147	9.56×10^{30}	3.78	13.69	1.84×10^{39}	7.87×10^{39}	1.23×10^{29}	5.20×10^{28}	1.75×10^{29}
10^{-4}	8.66×10^7	4.30	± 0.111	2.61×10^{31}	4.87	17.62	1.39×10^{40}	5.94×10^{39}	9.24×10^{29}	3.96×10^{29}	1.32×10^{30}
10^{-3}	2.48×10^8	5.54	± 0.082	7.65×10^{31}	6.28	22.70	1.04×10^{41}	4.51×10^{41}	7.00×10^{30}	3.00×10^{30}	1.00×10^{31}
10^{-2}	7.54×10^8	7.13	± 0.057	2.27×10^{32}	8.08	29.22	7.92×10^{41}	3.39×10^{41}	5.28×10^{31}	2.26×10^{31}	7.54×10^{31}

Note: The symbols F^C and n^C refer to the neutrino flux and neutrino density at the emission region. The electron fraction is $Y_e = 0.5$ and the pinching parameter for the neutrino spectrum is $\eta_{\nu\bar{\nu}} = 2.04$.

**FIGURE 1** Neutrino flavor evolution for inverted hierarchy. Electron neutrino survival probability is shown as a function of the radial distance from the neutron star surface. The curves for the electron antineutrino match the ones for electron neutrinos

Uribe Suárez & Rueda Hernandez 2019), axisymmetric, thin, alpha-disk models with the following parameters: \dot{M} the accretion rate, α the alpha-viscosity, and a the spin of the BH (Abramowicz et al. 1999; Chen & Beloborodov 2007; Krolik 1999; Liu et al. 2017; Novikov & Thorne 1973; Page & Thorne 1974; Shakura & Sunyaev 1973; Uribe Suárez & Rueda Hernandez 2019). The procedure

to analyze the dynamics of oscillations is similar to the one in Section 2.1. The first step is to find the neutrino flavor distributions to establish the initial conditions for Equations (11a) and (11b), and then we have to find each of the potentials and finally solve the equation. To do this, we first solve the hydrodynamic model in the absence of oscillations.

Normal Hierarchy

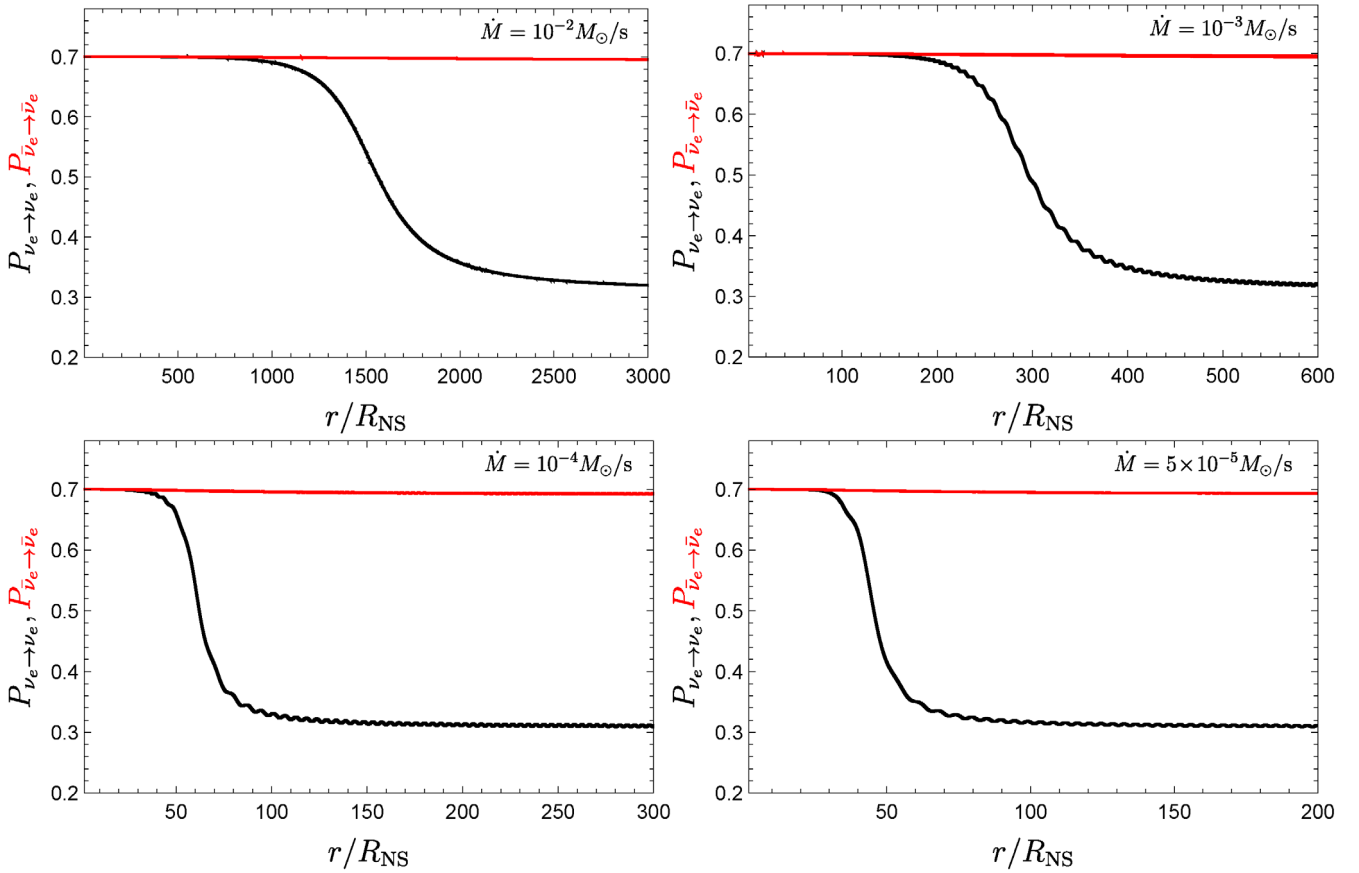


FIGURE 2 Electron neutrino and antineutrino flavor evolution for normal hierarchy. The survival probability is shown as a function of the radial distance from the neutron star surface

TABLE 2 Fraction of neutrinos and antineutrinos for each flavor after decoherence and matter effects, $n = 2 \sum_i n_{\nu_i}$

	$n_{\nu_e}^0/n$	$n_{\bar{\nu}_e}^0/n$	$n_{\nu_x}^0/n$	$n_{\bar{\nu}_x}^0/n$	n_{ν_e}/n	$n_{\bar{\nu}_e}/n$	n_{ν_x}/n	$n_{\bar{\nu}_x}/n$
Normal hierarchy	$\frac{1}{6}$	$\frac{1}{6}$	$\frac{1}{3}$	$\frac{1}{3}$	$\frac{1}{6} + \frac{1}{6} \sin^2 \theta_{12}$	$\frac{1}{6} - \frac{1}{6} \sin^2 \theta_{12}$	$\frac{1}{3}$	$\frac{1}{3}$
Inverted hierarchy	$\frac{1}{6}$	$\frac{1}{6}$	$\frac{1}{3}$	$\frac{1}{3}$	$\frac{1}{6} - \frac{1}{6} \cos^2 \theta_{12}$	$\frac{1}{6} + \frac{1}{6} \cos^2 \theta_{12}$	$\frac{1}{3}$	$\frac{1}{3}$

In Figure 3, we find the neutrino number densities and energies inside the disk. Note that, as in Section 2.1, the energies of neutrinos are comparable to the ones in spherical accretion and the number of neutrinos and antineutrinos are equal. There is also a significant excess of electron neutrinos over nonelectron neutrinos. However, there are several key differences that make the analysis in accretion disks more complex. First, an accretion disk has an effective thickness H and neutrinos can be produced at any point inside the disk. This means that it is not possible to set a *surface of emission* as before and due to the lack of spherical symmetry does not allow using the single-angle approximation. Second, close to the BH the

effects of curvature may not be negligible, implying that in Equation (1), when applying the Liouville operator, a term proportional rate of change of the energy of neutrinos \mathbf{p} may be present. To simplify the equations of oscillation, we consider the local rest frame of the disk (see [Bardeen et al. 1972; Thorne 1974] for details) and make a set of assumptions:

1. Due to axial symmetry, the neutrino density is constant along the \mathbf{z} direction. Moreover, since neutrinos follow null geodesics, we can set $\dot{p}_z \approx \dot{p}_\phi = 0$. Also, within the thin disk approximation, the neutrino and matter densities are constant along the \mathbf{y} direction and the

momentum change due to curvature along this direction can be neglected, that is, $\dot{p}_y \approx 0$.

2. In the local rest frame of the disk, the normalized radial momentum of a neutrino can be written as

$$p_x = \pm \frac{r}{\sqrt{r^2 - 2Mr + M^2a^2}},$$

(see [Uribe Suárez & Rueda Hernandez 2019] for details). Hence, the typical scale of the change of momentum with radius is

$$\Delta r_{p_x, \text{eff}} = \left| \frac{d \ln p_x}{dr} \right|^{-1} = \frac{r(r^2 - 2Mr + M^2a^2)}{M(Ma^2 - r)},$$

which obeys

$$\Delta r_{p_x, \text{eff}} > r_s \quad \text{for } r > 2r_{\text{in}}.$$

This means we can assume $\dot{p}_x \approx 0$ up to regions very close to the inner edge of the disk.

3. We define an effective distance

$$\Delta r_{\rho, \text{eff}} = \left| \frac{d \ln(n_{e^-} - n_{e^+})}{dr} \right|^{-1}.$$

For all the systems we evaluated, we found that is comparable to the height of the disk ($\Delta r_{\rho, \text{eff}} \sim 2 - 5r_s$). This means that at any point of the disk, we can calculate neutrino oscillations in small regions assuming that both the electron density and neutrino densities are constant.

4. We neglect energy and momentum transport between different regions of the disk by neutrinos that are recaptured by the disk due to curvature. This assumption is reasonable except for regions very close to the BH but is consistent with the thin disk model (Page & Thorne 1974). We also assume initially that the neutrino content of neighboring regions of the disk (different values of r) do not affect each other. As a consequence of the results discussed above, we assume that at any point inside the disk and at any instant of time, an observer in the local rest frame can describe both the charged leptons and neutrinos as isotropic gases around small enough regions of the disk.

All assumptions are sensible except 4, which is considerably restrictive. However, we can build our analysis on top of it and use the same results of Section 2.1 to generalize the model. Note that with our assumptions, the last term in Equations (11a) and (11b) is again simplified. When we calculate the oscillation in different point of the disk (Figure 4) we obtain fast flavor transformations with oscillation lengths of the order

$$t_{\text{osc}} \approx 10^{-6} \text{ s}. \quad (21)$$

Keeping this in mind and given the symmetry between neutrinos and antineutrinos in Figure 3, we note that in (Esteban-Pretel et al. 2007), it was shown that if the symmetry between neutrinos and antineutrinos is not broken beyond the limit of 25%, kinematic decoherence is still the main effect of neutrino oscillations. Additionally, in (Raffelt & Sigl 2007) it is shown that for asymmetric $\nu\bar{\nu}$ gas, even an infinitesimal anisotropy triggers an exponential evolution toward equipartition. Decoherence happens within a few oscillation cycles of oscillation so we can expect a steady-state, thin disk model to achieve flavor equipartition and is the result of a nonvanishing flux term (which is present in accretion disks due to the increasing density towards the BH) such that at any point, (anti)-neutrinos traveling in different directions, do not experience the same self-interaction potential due to the multiangle term in the integral of Equation (3). This effect is of the neutrino mass hierarchy and neutrino flavor equipartition is achieved for both hierarchies. Within the disk dynamic, this is equivalent to imposing the condition

$$\langle P_{\nu_e \rightarrow \nu_e} \rangle = \langle P_{\bar{\nu}_e \rightarrow \bar{\nu}_e} \rangle = 0.5. \quad (22)$$

Within this condition, we can compare the behavior of disks with and without flavor equipartition. Figure 5 shows that equipartition increases the disk density and reduces the temperature where the neutrino emission is important. The effect is mild for low accretion rates while very pronounced for high ones. Thus, result can be explained as follows: for low accretion rates, the neutrino optical depth for all flavors is $\tau_{\nu\bar{\nu}} \lesssim 1$ (Figure 6), hence neutrinos, regardless of their flavor, are free to leave the disk. When the initial (mainly electron flavor) is redistributed among both flavors, the total neutrino cooling remains virtually unchanged and the disk evolves as if equipartition had never occurred, save the new emission flavor content. On the other hand, when accretion rates are high, the optical depth obeys $\tau_{\nu_x} \approx \tau_{\bar{\nu}_x} \lesssim \tau_{\bar{\nu}_e} < \tau_{\nu_e} \sim 10^3$. The ν_e cooling is more heavily suppressed than the others. When flavors are redistributed, the new ν_x particles are free to escape, enhancing the total cooling with a consequent reduction of the temperature. As the temperature decreases, a lower internal energy allows for a higher matter density. The net impact of flavor equipartition is to make the disk evolution less sensitive to ν_e opacity. It can be shown (see [Uribe Suárez & Rueda Hernandez 2019] for details) that it increases the total cooling efficiency by the precise factor

$$\frac{1}{2} \left(1 + \frac{\langle E_{\nu_x} \rangle (1 + \tau_{\nu_e})}{\langle E_{\nu_e} \rangle (1 + \tau_{\nu_x})} \right). \quad (23)$$

The main difference with the previous system is that, for similar accretion rates, the density of the accretion

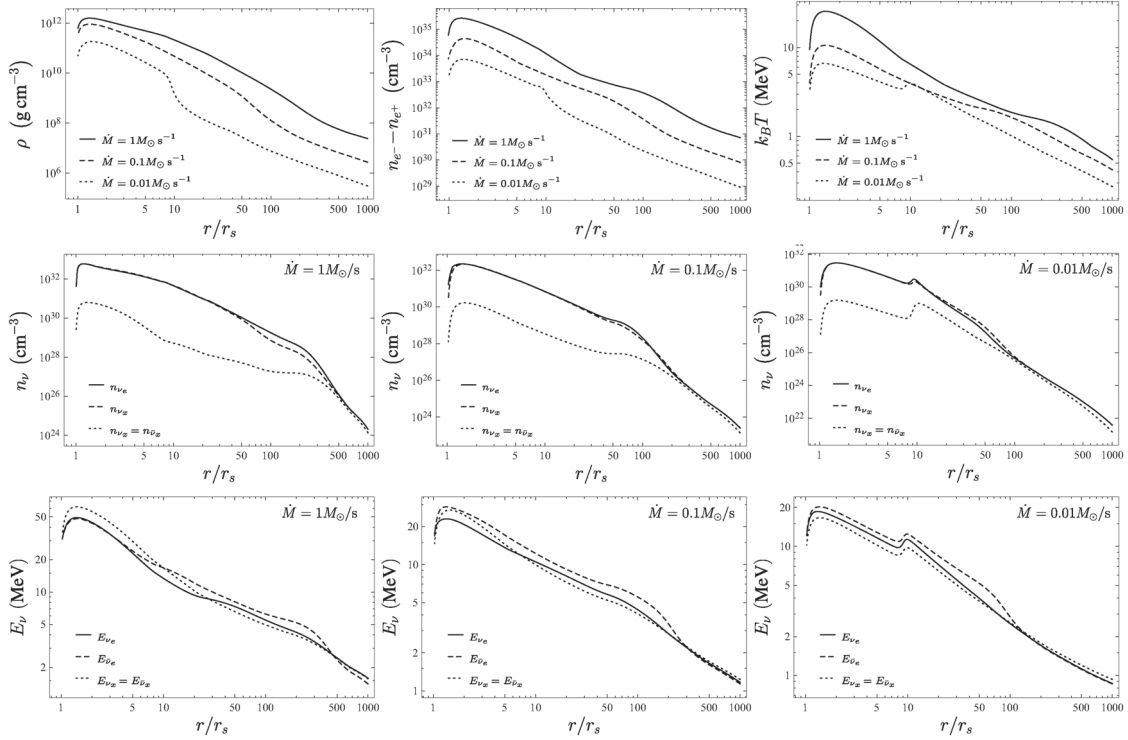


FIGURE 3 Properties of accretion disks in the absence of oscillations with $M = 3 M_{\odot}$, $\alpha = 0.01$, $a = 0.95$ for accretion rates $\dot{M} = 1 M_{\odot} \text{ s}^{-1}$, $\dot{M} = 0.1 M_{\odot} \text{ s}^{-1}$, and $\dot{M} = 0.01 M_{\odot} \text{ s}^{-1}$, respectively

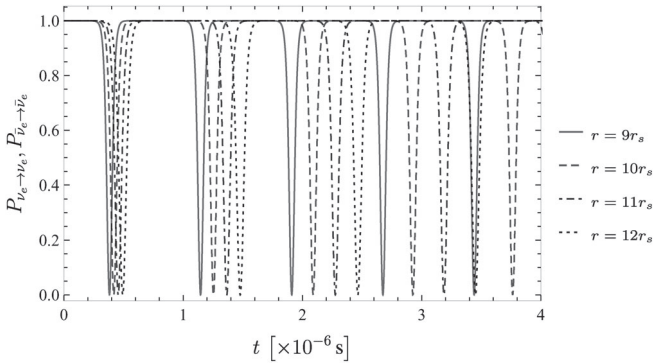


FIGURE 4 Survival probability for electron neutrinos and antineutrinos for the accretion disk with $\dot{M} = 0.1 M_{\odot} \text{ s}^{-1}$ at $r = 9r_s, 10r_s, 11r_s, 12r_s$

disk can be highly dense to impede, or even trap neutrinos within it. However, since electron and nonelectron neutrinos have different cross sections, the flavor transformations affect not only the dynamics of the disk but also the neutrino flavor content emerging from the disk. This, in turn, affects the energy deposition rate of the process $\nu + \bar{\nu} \mapsto e^- + e^+$. In particular, it leads to a deficit of electron neutrinos and a smaller energy deposition rate with respect to previous estimates not accounting by flavor oscillations inside the disk. The exact value of the reduction factor depends on the ν_e and ν_x optical depths but it

can be as high as ~ 5 . We refer the reader to Uribe Suárez & Rueda Hernandez (2019) for further details on this subject.

3 | CONCLUDING REMARKS

We have outlined the implications of neutrino oscillations in two different accreting systems within the BdHN scenario of GRBs. In both, spherical accretion and disk accretion, the emission of neutrinos is a crucial ingredient since they act as the main cooling process that allows the accretion onto the NS (or onto the BH) to proceed at very high rates of up to $1 M_{\odot} \text{ s}^{-1}$. Also, the ambient conditions of density and temperature imply the occurrence of neutrino flavor oscillations, with a relevant role of neutrino self-interactions.

We have seen that in spherical accretion, the density of neutrinos on the surface of the NS implies that neutrino self-interactions dominate the flavor evolution, leading to collective effects. The latter induce quick flavor conversions with an oscillation length as small as (0.05–1) km. Far from the NS surface, the neutrino density decreases and so the matter potential and MSW resonances dominate the flavor oscillations. Owing to the above, the neutrino flavor content emerging from the system is completely different with respect to the one created at the bottom of it, namely, on the NS accreting surface.

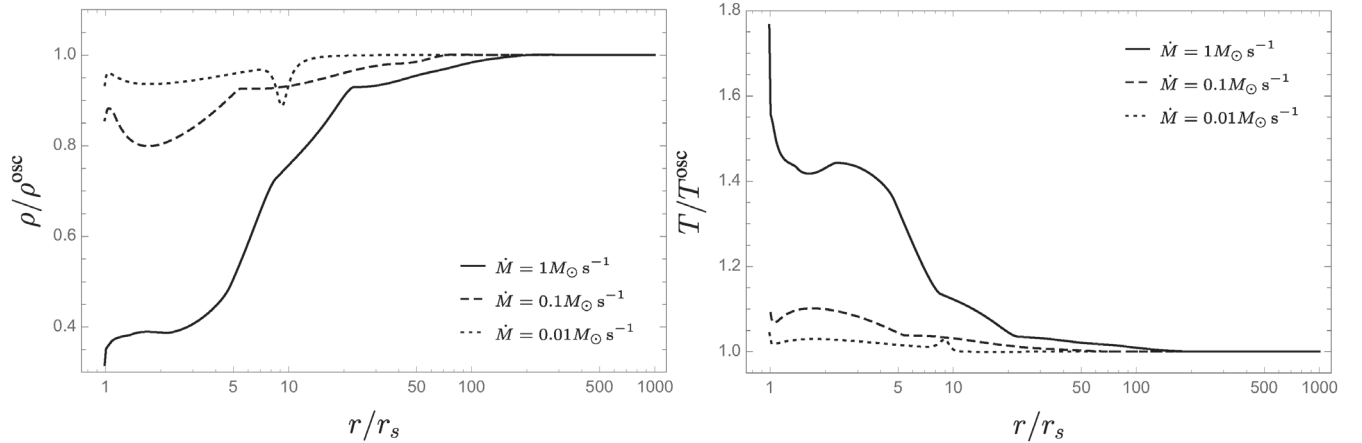


FIGURE 5 Comparison of density and temperature between thin disks with and without neutrino flavor equipartition for selected accretion rates

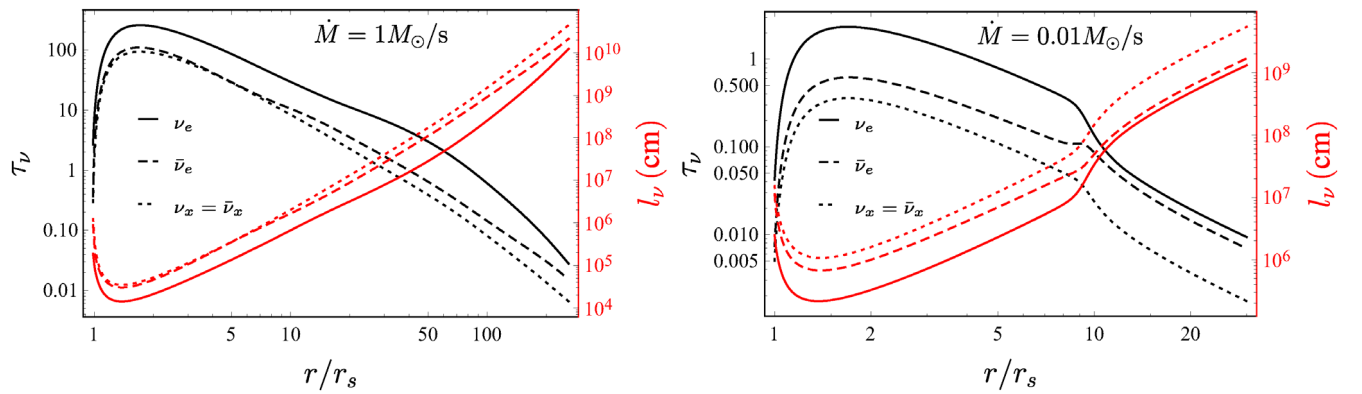


FIGURE 6 Total optical depth (left scale) and mean free path (right scale) for neutrinos and antineutrinos of both flavors for accretion disks with $\dot{M} = 1 M_\odot \text{s}^{-1}$ and $0.01 M_\odot \text{s}^{-1}$, between the inner radius and the ignition radius

Concerning disk accretion onto a BH, we saw that the number densities of electron neutrinos and antineutrinos are very similar. As a consequence of this particular environment, very fast pair conversions, $\nu_e \bar{\nu}_e \rightleftharpoons \nu_x \bar{\nu}_x$, induced by bipolar oscillations, are obtained for the inverted mass hierarchy case with high oscillation frequencies. However, due to the interaction between neighboring regions of the disk, the onset of kinematic decoherence with a timescale comparable to the oscillation length induces flavor equipartition among electronic and non-electronic neutrinos throughout the disk. Therefore, the neutrino content emerging from the disk is very different from the one that is usually assumed (see e.g., [Liu et al. 2016; Malkus et al. 2012]).

Flavor equipartition, while leaving antineutrino cooling practically unchanged, it enhances neutrino cooling by allowing the energy contained (and partially trapped inside the disk due to high opacity) within the ν_e gas to escape in the form of ν_x , rendering the disk insensible to the electron neutrino opacity. The variation of the

flavor content in the emission flux implies a loss in the electron neutrino luminosity and an increase in nonelectron neutrino luminosity and $L_{\bar{\nu}_e}$. As a consequence, the total energy deposition rate of the process $\nu + \bar{\nu} \rightarrow e^- + e^+$ is reduced.

These results are only a first step toward the analysis of neutrino oscillations in a novel relativistic astrophysics context that can have an impact on a wide range of astrophysical phenomena: from $e^- e^+$ plasma production above BHs in GRB models, to r-process nucleosynthesis in disk winds and possible MeV neutrino detectability.

REFERENCES

- Abramowicz, M. A., Björnsson, G., & Pringle, J. E. 1999, *Theory of Black Hole Accretion Discs*, Cambridge University Press (Cambridge).
- Bardeen, J. M., Press, W. H., & Teukolsky, S. A. 1972, *ApJ*, 178, 347.
- Becerra, L., Bianco, C. L., Fryer, C. L., Rueda, J. A., & Ruffini, R. 2016, *ApJ*, 833, 107.
- Becerra, L., Cipolletta, F., Fryer, C. L., Rueda, J. A., & Ruffini, R. 2015, *ApJ*, 812, 100.

- Becerra, L., Ellinger, C. L., Fryer, C. L., Rueda, J. A., & Ruffini, R. 2019, *ApJ*, 871, 14.
- Becerra, L., Guzzo, M. M., Rossi-Torres, F., Rueda, J. A., Ruffini, R., & Uribe, J. D. 2018, *ApJ*, 852, 120.
- Chen, W.-X., & Beloborodov, A. M. 2007, *ApJ*, 657, 383.
- Dasgupta, B., & Dighe, A. 2008, *Phys. Rev.*, D77, 113002.
- de Salas, P. F., Forero, D. V., Ternes, C. A., Tortola, M., & Valle, J. W. F. 2018, *Phys. Lett.*, B782, 633.
- Duan, H., Fuller, G. M., Carlson, J., & Qian, Y.-Z. 2006, *Phys. Rev.*, D74, 105014.
- Esteban-Pretel, A., Pastor, S., Tomas, R., Raffelt, G. G., & Sigl, G. 2007, *Phys. Rev.*, D76, 125018.
- Fogli, G. L., Lisi, E., Marrone, A., & Mirizzi, A. 2007, *JCAP*, 0712, 010.
- Fogli, G. L., Lisi, E., Montanino, D., & Mirizzi, A. 2003, *Phys. Rev.*, D68, 033005.
- Fryer, C. L., Oliveira, F. G., Rueda, J. A., & Ruffini, R. 2015, *Phys. Rev. Lett.*, 115(23), 231102.
- Fryer, C. L., Rueda, J. A., & Ruffini, R. 2014, *Astrophys. J.*, 793(2), L36.
- Hannestad, S., Raffelt, G. G., Sigl, G., & Wong, Y. Y. Y. 2006, *Phys. Rev.*, D74, 105010.
- Krolik, J. H. 1999, *Active Galactic Nuclei: From the Central Black Hole to the Galactic Environment*, Princeton University Press (Princeton, NJ).
- Liu, T., Gu, W.-M., & Zhang, B. 2017, *New Astron. Rev.*, 79, 1.
- Liu, T., Zhang, B., Li, Y., Ma, R.-Y., & Xue, L. 2016, *Phys. Rev. D*, 93(12), 123004.
- Malkus, A., Kneller, J. P., McLaughlin, G. C., & Surman, R. 2012, *Phys. Rev. D*, 86(8), 085015.
- Malkus, A., McLaughlin, G. C., & Surman, R. 2016, *Phys. Rev. D*, 93(4), 045021.
- Mikheyev, S. P., & Smirnov, A. Y. 1986, *Il Nuovo Cimento C*, 9(1), 17.
- Narayan, R., Paczynski, B., & Piran, T. 1992, *ApJ*, 395, L83.
- Novikov, I. D., & Thorne, K. S. 1973, in: *Black Holes (Les Astres Occlus)*, eds. C. Dewitt & B. S. Dewitt, 343. Gordon and Breach Science Publishers (New York, NY).
- Page, D. N., & Thorne, K. S. 1974, *ApJ*, 191, 499.
- Pantaleone, J. 1992, *Phys. Lett. B*, 287, 128.
- Qian, Y. Z., & Fuller, G. M. 1995, *Phys. Rev.*, D51, 1479.
- Raffelt, G. G., & Sigl, G. 2007, *Phys. Rev.*, D75, 083002.
- Rueda, J. A., & Ruffini, R. 2012, *ApJ*, 758, L7.
- Rueda, J. A., Ruffini, R., & Wang, Y. 2019, *Universe*, 5, 110.
- Ruffini, R., Moradi, R., Rueda, J. A., et al. 2019, *ApJ*, 886(2), 82.
- Ruffini, R., Rueda, J. A., Muccino, M., et al. 2016, *ApJ*, 832, 136.
- Salmonson, J. D., & Wilson, J. R. 2002, *ApJ*, 578, 310.
- Shakura, N. I., & Sunyaev, R. A. 1973, *Astron. Astrophys.*, 24, 337.
- Thorne, K. S. 1974, *ApJ*, 191, 507.
- Uribe Suárez, J. D., & Rueda Hernandez, J. A. 2019, *Sep*, *arXiv e-prints*.
- Wolfenstein, L. 1978, *Phys. Rev. D*, 17, 2369.
- Yakovlev, D. G., Kaminker, A. D., Gnedin, O. Y., & Haensel, P. 2001, *Phys. Rep.*, 354, 1.
- Zhu, Y.-L., Perego, A., & McLaughlin, G. C. 2016, *ArXiv e-prints*.

How to cite this article: Uribe JD, Rueda JA. Some recent results on neutrino oscillations in hypercritical accretion. *Astron. Nachr.* 2019;340:935–944. <https://doi.org/10.1002/asna.201913749>

Article

Neutrino Oscillations in Neutrino-Dominated Accretion Around Rotating Black Holes

Juan David Uribe ^{1,2,†} , Eduar Antonio Becerra-Vergara ^{1,2,3,†}  and Jorge Armando Rueda ^{2,4,5,6,*,†} 

¹ Dipartimento di Fisica, Sapienza Università di Roma, P.le Aldo Moro 5, 00185 Rome, Italy; juandavid.uribe@uniroma1.it (J.D.U.); eduar.becerra@icranet.org (E.A.B.-V.)

² ICRANet, Piazza della Repubblica 10, 65122 Pescara, Italy

³ Grupo de Investigación en Relatividad y Gravitación, Escuela de Física, Universidad Industrial de Santander, A. A. 678, Bucaramanga 680002, Colombia

⁴ ICRANet-Ferrara, Dipartimento di Fisica e Scienze della Terra, Università degli Studi di Ferrara, Via Saragat 1, 44122 Ferrara, Italy

⁵ Dipartimento di Fisica e Scienze della Terra, Università degli Studi di Ferrara, Via Saragat 1, 44122 Ferrara, Italy

⁶ INAF, Istituto di Astrofisica e Planetologia Spaziali, Via Fosso del Cavaliere 100, 00133 Rome, Italy

* Correspondence: jorge.rueda@icra.it

† These authors contributed equally to this work.

Abstract: In the binary-driven hypernova model of long gamma-ray bursts, a carbon–oxygen star explodes as a supernova in the presence of a neutron star binary companion in close orbit. Hypercritical (i.e., highly super-Eddington) accretion of the ejecta matter onto the neutron star sets in, making it reach the critical mass with consequent formation of a Kerr black hole. We have recently shown that, during the accretion process onto the neutron star, fast neutrino flavor oscillations occur. Numerical simulations of the above system show that a part of the ejecta stays bound to the newborn Kerr black hole, leading to a new process of hypercritical accretion. We address herein, also for this phase of the binary-driven hypernova, the occurrence of neutrino flavor oscillations given the extreme conditions of high density (up to 10^{12} g cm⁻³) and temperatures (up to tens of MeV) inside this disk. We estimate the behavior of the electronic and non-electronic neutrino content within the two-flavor formalism ($\nu_e\nu_x$) under the action of neutrino collective effects by neutrino self-interactions. We find that in the case of inverted mass hierarchy, neutrino oscillations inside the disk have frequencies between $\sim(10^5\text{--}10^9)$ s⁻¹, leading the disk to achieve flavor equipartition. This implies that the energy deposition rate by neutrino annihilation ($\nu + \bar{\nu} \rightarrow e^- + e^+$) in the vicinity of the Kerr black hole is smaller than previous estimates in the literature not accounting for flavor oscillations inside the disk. The exact value of the reduction factor depends on the ν_e and ν_x optical depths but it can be as high as ~ 5 . The results of this work are a first step toward the analysis of neutrino oscillations in a novel astrophysical context, and as such, deserve further attention.

Keywords: accretion disk; neutrino physics; gamma-ray bursts; black hole physics



Citation: Uribe, J.D.; Becerra-Vergara, E.A.; Rueda, J.A. Neutrino Oscillations in Neutrino-Dominated Accretion Around Rotating Black Holes. *Universe* **2021**, *7*, 7. <https://doi.org/10.3390/universe7010007>

Received: 28 October 2020
Accepted: 25 December 2020
Published: 4 January 2021

Publisher's Note: MDPI stays neutral with regard to jurisdictional claims in published maps and institutional affiliations.



Copyright: © 2021 by the authors. Licensee MDPI, Basel, Switzerland. This article is an open access article distributed under the terms and conditions of the Creative Commons Attribution (CC BY) license (<https://creativecommons.org/licenses/by/4.0/>).

1. Introduction

Neutrino flavor oscillations are now an experimental fact [1], and in recent years, their study based only on Mikheyev–Smirnov–Wolfenstein (MSW) effects [2,3] has been transformed by the insight that refractive effects of neutrinos on themselves due to the neutrino self-interaction potential are essential. Their behavior in a vacuum, in matter or by neutrino self-interactions has been studied in the context of early universe evolution [4–15], solar and atmospheric neutrino anomalies [16–24] and core-collapse supernovae (SN) ([25–51] and references therein). We are interested in astrophysical situations when neutrino self-interactions become more relevant than the matter potential. This implies systems in which a high density of neutrinos is present and in fact most of the literature on neutrino self-interaction dominance is concentrated on supernova neutrinos. It has

been shown how collective effects, such as synchronized and bipolar oscillations, change the flavor content of the emitted neutrinos when compared with the original content deep inside the exploding star.

This article aims to explore the problem of neutrino flavor oscillations in the case of long gamma-ray bursts (GRBs), in particular in the context of the binary-driven hypernova (BdHN) scenario. Long GRBs are the most energetic and powerful cosmological transients so far observed, releasing energies of up to a few 10^{54} erg in just a few seconds. Most of the energy is emitted in the prompt gamma-ray emission and in the X-ray afterglow. We refer the reader to [52] for an excellent review on GRBs and its observational properties.

The GRB progenitor in the BdHN model is a binary system composed of a carbon-oxygen star (CO_{core}) and a companion neutron star (NS) in tight orbit with orbital periods in the order of a few minutes [53–58]. These binaries are expected to occur in the final stages of the evolutionary path of a binary system of two main-sequence stars of masses in the order of $10\text{--}15 M_{\odot}$, after passing from X-ray binary phase and possibly multiple common-envelope phases (see [57,59] and references therein).

The CO_{core} explodes as SN, creating at its center a newborn NS (νNS), and ejecting the matter from its outermost layers. Part of the ejected matter falls back and accretes onto the νNS , while the rest continues its expansion leading to a hypercritical accretion (i.e., highly super-Eddington) process onto the NS companion. The NS companion reaches the critical mass for gravitational collapse, hence forming a rotating black hole (BH). The class of BdHN in which a BH is formed has been called type I, i.e., BdHN I [60].

One of the most important aspects of the BdHN model of long GRBs is that different GRB observables in different energy bands of the electromagnetic spectrum are explained by different components and physical ingredients of the system. This is summarized in Table 1, taken from [61]. For a review on the BdHN model and all the physical phenomena at work, we refer the reader to [62].

Table 1. Summary of the gamma-ray burst (GRB) observables associated with each BdHN I component and physical phenomenon. Adapted from Table 1 in [61] with the permission of the authors. References in the table: ^a [60], ^b [57,62,63], ^c [64], ^d [65,66], ^e [67], ^f [60,68].

BdHN Component/Phenomena	GRB Observable				
	X-Ray Precursor	Prompt (MeV)	GeV-TeV Emission	X-Ray Flares Early Afterglow	X-Ray Plateau and Late Afterglow
SN breakout ^a	⊗				
Hypercrit. acc. onto the NS ^b	⊗				
e^+e^- : transparency in low baryon load region ^c		⊗			
Inner engine: BH + B + matter ^d			⊗		
e^+e^- : transparency in high baryon load region ^e				⊗	
Synchrotron by νNS injected particles on SN ejecta ^f					⊗
νNS pulsar-like emission ^f					⊗

The emission of neutrinos is a crucial ingredient, since they act as the main cooling process that allows the accretion onto the NS to proceed at very high rates of up to $1 M_{\odot} s^{-1}$ [57,59,63,69,70]. In [71], we studied the neutrino flavor oscillations in this hypercritical accretion process onto the NS, all the way to BH formation. We showed that the density of neutrinos on top the NS in the accreting "atmosphere" is such that neutrino self-interactions dominate the flavor evolution, leading to collective effects. The latter induce in this system quick flavor conversions with short oscillation lengths as small as

(0.05–1) km. Far from the NS surface, the neutrino density decreases, and so the matter potential and MSW resonances dominate the flavor oscillations. The main result has been that the neutrino flavor content emerging on top of the accretion zone was completely different compared to the one created at the bottom of it. In the BdHN scenario, part of the SN ejecta stays bound to the newborn Kerr BH, forming an accretion disk onto it. In this context, the study of accretion disks and their nuances related to neutrinos is of paramount importance to shed light on this aspect of the GRB central engine. In most cases, the mass that is exchanged in close binaries has enough angular momentum so that it cannot fall radially. As a consequence, the gas will start rotating around the star or BH, forming a disk. At this point, it is worth digressing to mention the case of short GRBs. They are widely thought to be the product of mergers of compact-object binaries, e.g., NS–NS and/or NS–BH binaries (see, e.g., the pioneering works [72–75]). It is then clear that, especially in NS–NS mergers, matter can be kept bound and circularize around the new central remnant. Additionally, in such a case, an accretion disk will form around the more massive NS or the newborn BH (if the new central object overcomes the critical mass), and therefore the results of this work become relevant for such physical systems.

The magneto-hydrodynamics that describe the behavior of accretion disks are too complex to be solved analytically and full numerical analysis is time-consuming and costly. To bypass this difficulty, different models make approximations that allow casting the physics of an accretion disk as a two-dimensional or even one-dimensional problem. These approximations can be pigeonholed into four categories: symmetry, temporal evolution, viscosity and dynamics. Almost all analytic models are axially symmetric. This is a sensible assumption for any physical system that rotates. Similarly, most models are time-independent, although this is a more complicated matter. A disk can evolve in time in several ways. For example, the accretion rate \dot{M} depends on the external source of material which need not be constant, and at the same time, the infalling material increases the mass and angular momentum of the central object, constantly changing the gravitational potential. Additionally, strong winds and outflows can continually change the mass of the disk. Nonetheless, $\dot{M}(x, t) = \dot{M} = \text{constant}$ is assumed. Viscosity is another problematic approximation. For the gas to spiral down, its angular momentum needs to be reduced by shear stresses. These come from the turbulence driven by differential rotation and the electromagnetic properties of the disk [76–79], but again, to avoid magneto-hydrodynamical calculations, the turbulence is accounted for using a phenomenological viscosity $\alpha = \text{constant}$, such that the kinematical viscosity takes the form $\nu \approx \alpha H c_s$, where c_s is the local isothermal sound speed of the gas and H is the height of the disk measured from the plane of rotation (or half-thickness). This idea was first put forward by [80] and even though there is disagreement about the value and behavior of the viscosity constant, and it has been criticized as inadequate [81–84], several thriving models use this prescription. Finally, the assumptions concerning the dynamics of the disk are related to what terms are dominant in the energy conservation equation and the Navier–Stokes equation that describe the fluid (apart from the ones related to symmetry and time independence). In particular, it amounts to deciding what cooling mechanisms are important, what external potentials should be considered and what are the characteristics of the internal forces in the fluid. The specific tuning of these terms breeds one of the known models: thin disks, slim disks, advection-dominated accretion flows (ADAFs), thick disks, neutrino-dominated accretion flows (NDAFs), convection-dominated accretion flows (CDAFs), luminous hot accretion flows (LHAFs), advection-dominated inflow-outflow solutions (ADIOS) and magnetized tori. The options are numerous and each model is full of subtleties, making accretion flows around a given object an extremely rich area of research. For useful reviews and important articles with a wide range of subjects related to accretion disks, see [85–99] and references therein.

NDAFs are of special interest for GRBs. They are hyperaccreting slim disks, optically thick to radiation that can reach high densities $\rho \approx 10^{10}–10^{13} \text{ g cm}^{-3}$ and high temperatures $T \approx 10^{10}–10^{11} \text{ K}$ around the inner edge. Under these conditions, the main cooling

mechanism is neutrino emission since copious amounts of (mainly electron) neutrinos and antineutrinos are created by electron–positron pair annihilation, URCA and nucleon–nucleon bremsstrahlung processes, and later emitted from the disk surface. These $\nu\bar{\nu}$ pairs might then annihilate above the disk producing an e^-e^+ dominated outflow. NDAFs were proposed as a feasible central engine for GRBs in [100] and have been studied extensively since [101–112]. In [103] and later in [107], it was found that the inner regions of the disk can be optically thick to $\nu_e\bar{\nu}_e$, trapping them inside the disk, hinting that NDAFs may be unable to power GRBs. However, the system involves neutrinos propagating through dense media, and consequently, an analysis of neutrino oscillations, missing in the above literature, must be performed. Figure 1 represents the standard situation of the physical system of interest. The dominance of the self-interaction potential induces collective effects or decoherence. In either case, the neutrino flavor content of the disk changes. Some recent articles are starting to recognize their role in accretion disks and spherical accretion [71,113–117]. In particular, refs. [113,117] calculated the flavor evolution of neutrinos once they are emitted from the disk, but did not take into account the oscillation behavior inside the disk. The energy deposition rate above a disk by neutrino-pair annihilation as a powering mechanism of GRBs in NDAFs can be affected by neutrino oscillation in two ways. The neutrino spectrum emitted at the disk surface depends not only on the disk temperature and density but also on the neutrino flavor transformations inside the disk. Additionally, once the neutrinos are emitted, they undergo flavor transformations before being annihilated.

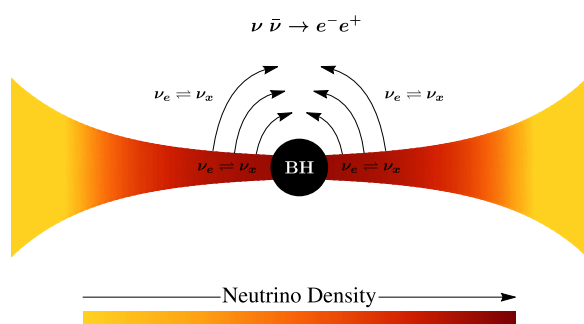


Figure 1. Schematic representation of the physical system. Due to conditions of high temperature and density, neutrinos are produced in copious amounts inside the disk. Since they have very low cross-sectional areas, neutrinos are free to escape but not before experiencing collective effects due to the several oscillation potentials. The energy deposition rate of the process $\nu + \bar{\nu} \rightarrow e^- + e^+$ depends on the local distribution of electronic and non-electronic (anti)neutrinos, which is affected by the flavor oscillation dynamics.

Our main objective is to propose a simple model to study neutrino oscillations inside an accretion disk and analyze its consequences. Applying the formalism of neutrino oscillations to non-symmetrical systems is difficult, so we chose a steady-state, α -disk as a first step in the development of such a model. The generalizations to more sophisticated accretion disks (see, e.g., [118–121]) can be subjects of future research.

This article is organized as follows. We outline the features of NDAFs and discuss in detail the assumptions needed to derive the disk equations in Section 2. Then, in Section 3, we discuss the general characteristics of the equation that drive the evolution of neutrino oscillations. We use the comprehensive exposition of the accretion disk of the previous section to build a simple model that adds neutrino oscillations to NDAFs, while emphasizing how the thin disk approximation can simplify the equations of flavor evolution. In Section 4 we set the parameters of the physical system and give some details on the initial conditions needed to solve the equations of accretion disks and neutrino oscillations. In Section 5 we discuss the main results of our calculations and analyze the phenomenology of neutrino oscillations in accretion disks. Finally, we present in Section 6 the conclusions of this work. Additional technical details are presented in a series of appendices at the end.

2. Hydrodynamics

2.1. Units, Velocities and Averaging

Throughout this article, we use Planck units $c = G = \hbar = k_B = k_e = 1$. To describe the spacetime around a Kerr BH of mass M , we use the metric $g_{\mu\nu}$ in Boyer–Lindquist coordinates, with a space-like signature, and with a dimensionless spin parameter $a = J/M^2$, which can be written as:

$$ds^2 = (g_{tt} - \omega^2 g_{\phi\phi}) dt^2 + g_{\phi\phi} (d\phi - \omega dt)^2 + g_{rr} dr^2 + g_{\theta\theta} d\theta^2, \tag{1}$$

in coordinates (t, r, θ, ϕ) . The covariant components $(g)_{\mu\nu}$ of the metric are

$$\begin{aligned} g_{tt} &= -\left(1 - \frac{2Mr}{\Sigma}\right), & g_{rr} &= \frac{\Sigma}{\Delta}, & g_{\theta\theta} &= \Sigma, \\ g_{\phi\phi} &= \left(r^2 + M^2 a^2 + \frac{2M^3 a^2 r}{\Sigma} \sin^2 \theta\right) \sin^2 \theta, & g_{t\phi} &= -\frac{2M^2 a r}{\Sigma} \sin^2 \theta, \end{aligned} \tag{2}$$

and its determinant is $g = -\Sigma^2 \sin^2 \theta$, with the well known functions $\Sigma = r^2 + M^2 a^2 \cos^2 \theta$ and $\Delta = r^2 - 2Mr + M^2 a^2$. We denote the coordinate frame by CF. Note that these coordinates can be used by an observer on an asymptotic rest frame. The angular velocity of the locally non-rotating frame (LNRF) is

$$\omega = -\frac{g_{t\phi}}{g_{\phi\phi}} = \frac{2 a M^2}{(r^3 + M^2 a^2 r + 2M^3 a^2)}, \tag{3}$$

and in Equation (2) it can be seen explicitly that if an observer has an angular velocity $\omega = d\phi/dt$, it would not measure any differences between the $\pm\phi$ directions. The LNRF is defined by orthonormality and the coordinate change $\phi_{\text{LNRF}} = \tilde{\phi} = \phi - \omega t$ [122,123]. We assume that the disk lies on the equatorial plane of the BH ($\theta = \pi/2$). This way we represent the average movement of the fluid by geodesic circular orbits with angular velocity $\Omega = d\phi/dt = u^\phi/u^t$ plus a radial velocity so that the local rest frame (LRF) of the fluid is obtained by performing, first, an azimuthal Lorentz boost with velocity $\beta^{\hat{\phi}}$ to a co-rotating frame (CRF) [124], and then a radial Lorentz boost with velocity $\beta^{\hat{r}}$. Clearly, the metric on the LNRF, CRF and LRF is $\text{diag}(-1, 1, 1, 1)$. The expression for the angular velocity of circular orbits is obtained by setting $\dot{r} = \ddot{r} = 0$ in the r -component of the geodesic equation

$$\Omega^\pm = \pm \frac{\sqrt{M}}{(r^{3/2} \pm M^{3/2} a)}, \tag{4}$$

where (+) is for prograde orbits and (−) is for retrograde orbits. We will limit our calculations to prograde movement with $0 \leq a \leq 1$, but extension to retrograde orbits is straightforward. Finally, we can get the components of the 4-velocity of the fluid by transforming $u_{\text{LRF}} = (1, 0, 0, 0)$ back to the CF

$$u^\mu = \left(\frac{\gamma_{\tilde{r}} \gamma_{\hat{\phi}}}{\sqrt{\omega^2 g_{\phi\phi} - g_{tt}}}, \frac{\gamma_{\tilde{r}} \beta^{\hat{r}}}{\sqrt{g_{rr}}}, 0, \frac{\gamma_{\tilde{r}} \gamma_{\hat{\phi}} \Omega}{\sqrt{\omega^2 g_{\phi\phi} - g_{tt}}} \right), \tag{5}$$

leaving $\beta^{\hat{r}}$ to be determined by the conservation laws. In Equation (5) we have replaced $\beta^{\hat{\phi}}$ with Equation (A3). A discussion on the explicit form of the transformations and some miscellaneous results are given in Appendix A. We will also assume that the disk is in a steady-state. This statement requires some analysis. There are two main ways in which it can be false:

First, as matter falls into the BH, its values M and a change [125,126], effectively changing the spacetime around it. For the spacetime to remain the same (i.e., for M and a to stay constant) we require $\Omega^{-1} \ll t_{\text{acc}} = \Delta M_0 / \dot{M}_{\text{acc}}$, where ΔM_0 is the total mass of the disk and \dot{M}_{acc} is the accretion rate. The characteristic accretion time must be bigger than the dynamical time of the disk so that flow changes due to flow dynamics are more important than flow changes due to spacetime changes. Equivalent versions of this condition that appear throughout disk accretion articles are $t_{\text{dym}} \ll t_{\text{visc}}$ and

$$\beta^r \ll \beta^\phi < 1, \tag{6}$$

where it is understood that the accretion rate obeys $\dot{M}_{\text{acc}} \approx \Delta M_0 / t_{\text{acc}}$. To put these numbers into perspective, consider a solar mass BH ($M = 1M_\odot$) and a disk with mass between $\Delta M_0 = (1 - 10)M_\odot$. For accretion rates up to $\dot{M}_{\text{acc}} = 1M_\odot/\text{s}$ the characteristic accretion time is $t_{\text{acc}} \lesssim (1 - 10)$ s, while $\Omega^{-1} \sim (10^{-5} - 10^{-1})$ s between $r = r_{\text{ISCO}}$ and $r = 2000M_\odot$. Consequently, a wide range of astrophysical systems satisfy this condition, and it is equivalent to claiming that both ∂_t and ∂_ϕ are killing fields.

Second, at any point inside the disk, any field $\psi(t, r, \theta, \phi)$ that reports a property of the gas may vary in time due to the turbulent motion of the flow. Thus, to assume that any field is time-independent and smooth enough in r for its flow to be described by Equation (5) means replacing such field by its average over an appropriate spacetime volume. The same process allows one to choose a natural set of variables that split the hydrodynamics into r -component equations and θ -component equations. The averaging process has been explained in [124,127,128]. We include the analysis here and try to explain it in a self-consistent manner. The turbulent motion is characterized by the eddies. The azimuthal extension of the largest eddies can be 2π , like waves crashing around an island, but their linear measure cannot be larger than the thickness of the disk, and as measured by an observer on the CRF, their velocity is in the order of $\beta^{\tilde{r}}$ so that their period along the r component is $\Delta \tilde{t} \approx (\text{Thickness}) / \beta^{\tilde{r}}$ (e.g., §33, [129]). If we denote by H the average half-thickness of the disk as measured by this observer at r over the time $\Delta \tilde{t}$, then the appropriate volume \mathcal{V} is composed by the points (t, r, θ, ϕ) such that $t \in [t^* - \Delta t/2, t^* + \Delta t/2]$, $\theta \in [\theta_{\text{min}}, \theta_{\text{max}}]$ and $\phi \in [0, 2\pi)$, where we have transformed $\Delta \tilde{t}$ and $\Delta \tilde{r}$ back to the CF using Equation (A4) as approximations. The values θ_{min} and θ_{max} correspond to the upper and lower faces of the disk, respectively. Then, the average takes the form

$$\psi(t, r, \theta, \phi) \mapsto \psi(r, \theta) = \langle \psi(t, r, \theta, \phi) \rangle = \frac{\int_{t^* - \Delta t/2}^{t^* + \Delta t/2} \int_0^{2\pi} \psi(r, t, \theta, \phi) \sqrt{\frac{-g}{g_{rr}g_{\theta\theta}}} dt d\phi}{\int_{t^* - \Delta t/2}^{t^* + \Delta t/2} \int_0^{2\pi} \sqrt{\frac{-g}{g_{rr}g_{\theta\theta}}} dt d\phi}. \tag{7}$$

The steady-state condition is achieved by requiring that the Lie derivative of the averaged quantity along the killing field ∂_t vanishes: $\mathcal{L}_{\partial_t} \langle \psi \rangle = 0$. Note that the thickness measurement performed by the observer already has an error $\sim M^2 a^2 H^3 / 6r^4$ since it extends the Lorentz frame beyond the local neighborhood, but if we assume that the disk is thin ($H/r \ll 1$), and we do, this error remains small. At the same time, we can take all metric components evaluated at the equator and use Equation (5) as the representative average velocity. Under these conditions, we have $\theta_{\text{max}} - \theta_{\text{min}} \approx 2H/r$, and the term $\sqrt{-g/g_{rr}}$ in Equation (7) cancels out. It becomes clear that an extra θ integral is what separates the radial and polar variables. In other words, the r -component variables are the vertically integrated fields

$$\psi(r, \theta) \mapsto \psi(r) = \int_{\theta_{\text{min}}}^{\theta_{\text{max}}} \psi(r, \theta) \sqrt{g_{\theta\theta}} d\theta. \tag{8}$$

The vertical equations of motion can be obtained by setting up Newtonian (with relativistic corrections) equations for the field $\psi(r, \theta)$ at each value of r (see, e.g., [99,127,130,131]).

2.2. Conservation Laws

The equations of evolution of the fluid are contained in the conservation laws $\nabla_\mu T^{\mu\nu} = 0$ and $\nabla_\mu(\rho u^\mu) = 0$. The most general stress–energy tensor for a Navier–Stokes viscous fluid with heat transfer is [132,133]

$$T = \overbrace{(\rho + U + P)\mathbf{u} \otimes \mathbf{u} + P\mathbf{g}}^{\text{Ideal Fluid}} + \overbrace{(-2\eta\sigma - \zeta(\nabla \cdot \mathbf{u})\mathbf{P})}^{\text{Viscous Stress}} + \overbrace{\mathbf{q} \otimes \mathbf{u} + \mathbf{u} \otimes \mathbf{q}}^{\text{Heat flux}}, \tag{9}$$

where $\rho, P, U, \zeta, \eta, \mathbf{q}, \mathbf{P}$ and σ are the rest-mass energy density, pressure, internal energy density, dynamic viscosity, bulk viscosity, heat-flux 4-vector, projection tensor and shear tensor, respectively, and thermodynamic quantities are measured on the LRF. We do not consider electromagnetic contributions and ignore the causality problems associated with the equations derived from this stress–energy tensor, since we are not interested in phenomena close to the horizon [124]. Before deriving the equations of motion and to add a simple model of neutrino oscillations to the dynamics of disk accretion, we must make some extra assumptions. We will assume that the θ integral in Equation (8) can be approximated by

$$\int_{\theta_{\min}}^{\theta_{\max}} \psi \sqrt{g_{\theta\theta}} d\theta \approx \psi r (\theta_{\max} - \theta_{\min}) \approx 2H\psi, \tag{10}$$

for any field ψ . Additionally, we use Stokes’ hypothesis ($\zeta = 0$). Since we are treating the disk as a thin fluid in differential rotation, we will assume that, on average, the only non-zero component of the shearing stress on the CRF is $\sigma_{\hat{r}\hat{\phi}}$ (there are torques only on the ϕ direction), and $q_{\hat{\theta}}$ is the only non-zero component of the energy flux (on average the flux is vertical). By $u^\mu \sigma_{\mu\nu} = 0$ and Equation (A7) we have

$$\sigma_{r\phi} = \frac{\gamma_{\hat{\phi}}^3}{2} \frac{g_{\phi\phi}}{\sqrt{\omega^2 g_{\phi\phi} - g_{tt}}} \partial_r \Omega, \quad \sigma_{rt} = -\Omega \sigma_{r\phi}. \tag{11}$$

Finally, the turbulent viscosity is estimated to be $\sim l\Delta u$ where l is the size of the turbulent eddies and Δu is the average velocity difference between points in the disk separated by a distance l . By the same arguments in (§33, [129]) and in Section 2.2, l can be at most equal to $2H$ and Δu can be at most equal to the isothermal sound speed $c_s = \sqrt{\partial P / \partial \rho}$ or else the flow would develop shocks [89]. The particular form of c_s can be calculated from Equation (15). This way we get

$$\eta = \Pi \nu_{\text{turb}} = 2\alpha \Pi H c_s, \tag{12}$$

with $\alpha \leq 1$ and $\Pi = \rho + U + P$. In a nutshell, this is the popular α -prescription put forward by [80]. As we mentioned at the end of Section 2.1, on the CRF for a fixed value of r , the polar equation takes the form of Euler’s equation for a fluid at rest where the acceleration is given by the tidal gravitational acceleration. Namely, the θ component of the fluid’s path-lines relative acceleration in the θ direction is

$$\frac{1}{r} \partial_\theta P \approx \rho r \cos \theta [\mathbf{R}(\mathbf{u}, \partial_{\hat{\theta}}, \mathbf{u}) \cdot \partial_{\hat{\theta}}]_{\theta=\pi/2}, \tag{13}$$

with \mathbf{R} being the Riemann curvature tensor. With $u^{\hat{i}} \approx (1, 0, 0, 0)$, Equations (10) and (A8) and assuming that there is no significant compression of the fluid under the action of the tidal force, integration of this equation yields the relation up to second order in $\pi/2 - \theta$:

$$P = \frac{1}{2} \rho R^{\hat{\theta}}_{\hat{i}\hat{\theta}\hat{i}} \Big|_{\theta=\pi/2} \left(H^2 - r^2 \left(\frac{\pi}{2} - \theta \right)^2 \right), \tag{14}$$

where we used the condition $P = 0$ at the disk’s surface. Hence, the average pressure inside the disk is (cf. [99,107,131])

$$P = \frac{1}{3} \rho H^2 R \bar{\theta}_{i\bar{t}\bar{t}} \Big|_{\theta=\pi/2}. \tag{15}$$

The equation of mass conservation is obtained by directly inserting into Equation (A13) the averaged density and integrating vertically to obtain

$$2Hr\rho u^r = \text{constant} = -\frac{\dot{M}}{2\pi}, \tag{16}$$

where the term $2Hr\rho u^r$ is identified as the average inward mass flux through a cylindrical surface of radius r per unit of azimuthal angle, and thus must be equal to the accretion rate divided by 2π . The same process applied to Equation (A12) yields the energy conservation equation:

$$u^r \left[\partial_r(HU) - \frac{U+P}{\rho} \partial_r(H\rho) \right] = 2\eta H \sigma^r \phi \sigma_{r\phi} - H\epsilon, \tag{17}$$

where factors proportional to H/r are ignored and we assume $\Pi \approx \rho$ to integrate the second term on the left-hand side. ϵ is the average energy density measured on the LRF (see the discussion around Equation (A16)). The first term on the right-hand side is the viscous heating rate F_{heat} and the second term is the cooling rate F_{cool} . The last constitutive equation is obtained by applying the zero torque at the last stable orbit condition. These relations are calculated in Appendix A. We just replace the density in Equation (16) using Equation (A21), obtaining

$$u^r = -\frac{4\alpha H c_s \sigma_{\phi}^r}{M f(x, x^*)}. \tag{18}$$

2.3. Equations of State

We consider that the main contribution to the rest-mass energy density of the disk is made up of neutrons, protons and ions. This way $\rho = \rho_B = n_B m_B$ with baryon number density n_B and baryon mass m_B equal to the atomic unit mass. The disk’s baryonic mass obeys Maxwell–Boltzmann statistics, and its precise composition is determined by the nuclear statistical equilibrium (NSE). We denote the mass fraction of an ion i by $X_i = \rho_i / \rho_B$ (if $i = p$ or n then we are referring to proton or neutrons) and it can be calculated by the Saha equation [134,135]

$$X_i = \frac{A_i m_B}{\rho} G_i \left(\frac{T A_i m_B}{2\pi} \right)^{3/2} \exp \left(\frac{Z_i (\mu_p + \mu_p^C) + N_i \mu_n - \mu_i^C + B_i}{T} \right), \tag{19}$$

with the constraints:

$$\sum_i X_i = 1, \quad \sum_i Z_i Y_i = Y_e. \tag{20}$$

In these equations, T , A_i , N_i , Z_i , Y_e , Y_i , G_i , μ_i and B_i are the temperature, atomic number, neutron number, proton number, electron fraction (electron abundance per baryon), ion abundance per baryon, nuclear partition function, chemical potential (including the nuclear rest-mass energy) and ion binding energy. The μ_i^C are the Coulomb corrections for the NSE state in a dense plasma (see Appendix C). The binding energy data for a large collection of nuclei can be found in [136] and the temperature-dependent partition functions are found in [137,138]. Even though we take into account Coulomb corrections in NSE, we assume that the baryonic mass can be described by an ideal gas^{1,2} and

$$P_B = \sum_i P_i = n_B T \sum_i \frac{X_i}{A_i}, \quad U_B = \frac{3}{2} P_B. \tag{21}$$

¹ Since bulk viscosity effects appear as a consequence of correlations between ion velocities due to Coulomb interactions and of large relaxation times to reach local equilibrium, the NSE and ideal gas assumptions imply that imposing Stokes’ hypothesis becomes de rigueur [133,139,140]

² We will consider accretion rates of up to $1M_{\odot} \text{ s}^{-1}$. These disks reach densities of $10^{13} \text{ g cm}^{-3}$. Baryons can be lightly degenerate at these densities but we will still assume that the baryonic mass can be described by an ideal gas.

The disk also contains photons, electrons, positrons, neutrinos and antineutrinos. As is usual in neutrino oscillations analysis, we distinguish only between electron (anti)neutrinos $\nu_e, (\bar{\nu}_e)$ and x (anti)neutrinos $\nu_x, (\bar{\nu}_x)$, where $x = \mu + \tau$ is the superposition of muon neutrinos and tau neutrinos. Photons obey the usual relations

$$P_\gamma = \frac{\pi^2 T^4}{45}, \quad U_\gamma = 3P_\gamma, \tag{22}$$

while, for electrons and positrons we have

$$n_{e^\pm} = \frac{\sqrt{2}}{\pi^2} \zeta^{3/2} [\mathcal{F}_{1/2,0}(\zeta, \eta_{e^\pm}) + \zeta \mathcal{F}_{3/2,0}(\zeta, \eta_{e^\pm})], \tag{23a}$$

$$U_{e^\pm} = \frac{\sqrt{2}}{\pi^2} \zeta^{5/2} [\mathcal{F}_{3/2,0}(\zeta, \eta_{e^\pm}) + \zeta \mathcal{F}_{5/2,0}(\zeta, \eta_{e^\pm})], \tag{23b}$$

$$P_{e^\pm} = \frac{2\sqrt{2}}{3\pi^2} \zeta^{5/2} \left[\mathcal{F}_{3/2,0}(\zeta, \eta_{e^\pm}) + \frac{\zeta}{2} \mathcal{F}_{5/2,0}(\zeta, \eta_{e^\pm}) \right], \tag{23c}$$

with $\zeta = T/m_e$ and written in terms of the generalized Fermi functions

$$\mathcal{F}_{k,\ell}(y, \eta) = \int_\ell^\infty \frac{x^k \sqrt{1+xy/2}}{\exp(x-\eta)+1} dx. \tag{24}$$

In these equations $\eta_{e^\pm} = (\mu_{e^\pm} - m_e)/T$ is the electron (positron) degeneracy parameter without rest-mass contributions (not to be confused with η in Section 2.2). Since electrons and positrons are in equilibrium with photons due to the pair creation and annihilation processes ($e^- + e^+ \rightarrow 2\gamma$), we know that their chemical potentials are related by $\mu_{e^+} = -\mu_{e^-}$, which implies $\eta_{e^+} = -\eta_{e^-} - 2/\zeta$ from the charge neutrality condition, and we obtain

$$n_B Y_e = n_{e^-} - n_{e^+}. \tag{25}$$

For neutrinos, the story is more complicated. In the absence of oscillations and if the disk is hot and dense enough for neutrinos to be trapped within it and in thermal equilibrium, n_ν, U_ν, P_ν can be calculated with Fermi–Dirac statistics using the same temperature T

$$n_{\nu(\bar{\nu})}^{\text{trapped}} = \frac{T^3}{\pi^2} \mathcal{F}_{2,0}(\eta_{\nu(\bar{\nu})}), \tag{26a}$$

$$U_{\nu(\bar{\nu})}^{\text{trapped}} = \frac{T^4}{\pi^2} \mathcal{F}_{3,0}(\eta_{\nu(\bar{\nu})}), \tag{26b}$$

$$P_{\nu(\bar{\nu})}^{\text{trapped}} = \frac{U_{\nu(\bar{\nu})}^{\text{trapped}}}{3}, \tag{26c}$$

where it is understood that $\mathcal{F}(\eta) = \mathcal{F}(y = 0, \eta)$ with $\eta_{\nu(\bar{\nu})} = \mu_{\nu(\bar{\nu})}/T$ and the ultra-relativistic approximation $m_\nu \ll 1$ for any neutrino flavor is used. If thermal equilibrium is has not been achieved, Equation (26) cannot be used. Nevertheless, at any point in the disk and for given values of T and ρ , (anti)neutrinos are being created through several processes. The processes we take into account are pair annihilation $e^- + e^+ \rightarrow \nu + \bar{\nu}$, electron or positron capture by nucleons $p + e^- \rightarrow n + \nu_e$ or $n + e^+ \rightarrow p + \bar{\nu}_e$, electron capture by ions $A + e^- \rightarrow A' + \nu_e$, plasmon decay $\tilde{\gamma} \rightarrow \nu + \bar{\nu}$ and nucleon-nucleon bremsstrahlung $n_1 + n_2 \rightarrow n_3 + n_4 + \nu + \bar{\nu}$. The emission rates can be found in Appendix D. The chemical equilibria for these processes determine the values of $\eta_{\nu(\bar{\nu})}$. In particular,

$$\eta_{\nu_e} = \eta_{e^-} + \ln\left(\frac{X_p}{X_n}\right) + \frac{1 - \mathbb{Q}}{\xi}, \tag{27a}$$

$$\eta_{\bar{\nu}_e} = -\eta_{\nu_e}, \tag{27b}$$

$$\eta_{\nu_x} = \eta_{\bar{\nu}_x} = 0, \tag{27c}$$

satisfy all equations. Here, $\mathbb{Q} = (m_n - m_p)/m_e \approx 2.531$. Once the (anti)neutrino number and energy emission rates (R_i, Q_i) are calculated for each process i , the (anti)neutrino thermodynamic quantities are given by

$$n_{\nu(\bar{\nu})}^{\text{free}} = H \sum_i R_{i,\nu(\bar{\nu})}, \tag{28a}$$

$$U_{\nu(\bar{\nu})}^{\text{free}} = H \sum_i Q_{i,\nu(\bar{\nu})}, \tag{28b}$$

$$P_{\nu(\bar{\nu})}^{\text{free}} = \frac{U_{\nu(\bar{\nu})}^{\text{free}}}{3}. \tag{28c}$$

Remember we are using Planck units, so in these expressions there should be an H/c instead of just an H . The transition for each (anti)neutrino flavor between both regimes occurs when Equations (26b) and (28b) are equal, and it can be simulated by defining the parameter

$$w_{\nu(\bar{\nu})} = \frac{U_{\nu(\bar{\nu})}^{\text{free}}}{U_{\nu(\bar{\nu})}^{\text{free}} + U_{\nu(\bar{\nu})}^{\text{trapped}}}. \tag{29}$$

With this equation, the (anti)neutrino average energy can be defined as

$$\langle E_{\nu(\bar{\nu})} \rangle = \left(1 - w_{\nu(\bar{\nu})}\right) \frac{U_{\nu(\bar{\nu})}^{\text{free}}}{n_{\nu(\bar{\nu})}^{\text{free}}} + w_{\nu(\bar{\nu})} \frac{U_{\nu(\bar{\nu})}^{\text{trapped}}}{n_{\nu(\bar{\nu})}^{\text{trapped}}}. \tag{30}$$

and the approximated number and energy density are

$$n_{\nu(\bar{\nu})} = \begin{cases} n_{\nu(\bar{\nu})}^{\text{free}}, & \text{if } w_{\nu(\bar{\nu})} < 1/2. \\ n_{\nu(\bar{\nu})}^{\text{trapped}}, & \text{if } w_{\nu(\bar{\nu})} \geq 1/2. \end{cases} \tag{31a}$$

$$U_{\nu(\bar{\nu})} = \begin{cases} U_{\nu(\bar{\nu})}^{\text{free}}, & \text{if } w_{\nu(\bar{\nu})} < 1/2. \\ U_{\nu(\bar{\nu})}^{\text{trapped}}, & \text{if } w_{\nu(\bar{\nu})} \geq 1/2. \end{cases} \tag{31b}$$

$$P_{\nu(\bar{\nu})} = \frac{U_{\nu(\bar{\nu})}}{3}. \tag{31c}$$

Note that both Equations (28c) and (31c) are approximations since they are derived from equilibrium distributions, but they help make the transition smooth. Besides, the neutrino pressure before thermal equilibrium is negligible. This method was presented in [107] where it was used only for electron (anti)neutrinos. The total (anti)neutrino number and energy flux through one the disk's faces can be approximated by

$$\dot{n}_{\nu_j(\bar{\nu}_j)} = \sum_{j \in \{e,x\}} \frac{n_{\nu_j(\bar{\nu}_j)}}{1 + \tau_{\nu_j(\bar{\nu}_j)}}, \tag{32a}$$

$$F_{\nu_j(\bar{\nu}_j)} = \sum_{j \in \{e,x\}} \frac{U_{\nu_j(\bar{\nu}_j)}}{1 + \tau_{\nu_j(\bar{\nu}_j)}}, \tag{32b}$$

where τ_{ν_i} is the total optical depth for the (anti)neutrino $\nu_i(\bar{\nu}_i)$. By collecting all the expressions, we write the total internal energy and total pressure as

$$U = \sum_{j \in \{e,x\}} (U_{\nu_j} + U_{\bar{\nu}_j}) + U_B + U_{e^-} + U_{e^+} + U_\gamma, \tag{33a}$$

$$P = \sum_{j \in \{e,x\}} (P_{\nu_j} + P_{\bar{\nu}_j}) + P_B + P_{e^-} + P_{e^+} + P_\gamma. \tag{33b}$$

The (anti)neutrino energy flux through the disk faces contributes to the cooling term in the energy conservation equation, but it is not the only one. Another important energy sink is photodisintegration of ions. To calculate it we proceed as follows. The energy spent to knocking off a nucleon of an ion i is equal to the binding energy per nucleon B_i/A_i . Now, consider a fluid element of volume V whose moving walls are attached to the fluid so that no baryons flow in or out. The total energy of photodisintegration contained within this volume is the sum over i of (energy per nucleon of ion i) \times (# of freed nucleons of ion i inside V). This can be written as $\sum_i (B_i/A_i) n_{f,i} V$, or, alternatively, $n_B V \sum_i (B_i/A_i) X_{f,i}$. If we approximate B_i/A_i by the average binding energy per nucleon \bar{B} (which is a good approximation save for a couple of light ions) the expression becomes $n_B V \bar{B} \sum_i X_{f,i} = n_B V \bar{B} X_f = n_B V \bar{B} (X_p + X_n)$. We place the value of \bar{B} in Section 4.

The rate of change of this energy on the LRF, denoting the proper time by λ , is

$$\frac{d}{d\lambda} [n_B V \bar{B} (X_p + X_n)] = n_B V \bar{B} \frac{d}{d\lambda} (X_p + X_n). \tag{34}$$

The derivative of $n_B V$ vanishes by baryon conservation. Transforming back to CF and taking the average we find the energy density per unit time used in disintegration of ions

$$\epsilon_{\text{ions}} = n_B \bar{B} u^r H \partial_r (X_p + X_n). \tag{35}$$

The average energy density measured on the LRF ϵ appearing in Equation (17) is

$$\epsilon = \epsilon_{\text{ions}} + \frac{1}{H} \sum_{i \in \{e,x\}} (F_{\nu_i} + F_{\bar{\nu}_i}). \tag{36}$$

Finally, a similar argument allows us to obtain the equation of lepton number conservation. For any lepton ℓ , the total lepton number density is $\sum_{\ell \in \{e,\mu,\tau\}} (n_\ell - n_{\bar{\ell}} + n_{\nu_\ell} - n_{\bar{\nu}_\ell})$. Thus, with Equation (25), calculating the rate of change as before, using Gauss's theorem and taking the average, we get

$$u^r H \left[n_B \partial_r Y_e + \partial_r \sum_{\ell \in \{e,x\}} (n_{\nu_\ell} - n_{\bar{\nu}_\ell}) \right] = \sum_{\ell \in \{e,x\}} (\dot{n}_{\bar{\nu}_\ell} - \dot{n}_{\nu_\ell}), \tag{37}$$

where the right-hand side represents the flux of lepton number through the disk's surface.

3. Neutrino Oscillations

To study the flavor evolution of neutrinos within a particular system, a Hamiltonian governing neutrino oscillation must be set up. The relative strengths of the potentials appearing in such a Hamiltonian depend on four elements: geometry, mass content, neutrino content and neutrino mass hierarchy. Geometry refers to the nature of net neutrino fluxes and possible gravitational effects. Mass and neutrino contents refer to respective distributions of leptons of each flavor (e, μ, τ) present in the medium. Finally, mass hierarchy refers to the relative values of the masses m_1, m_2, m_3 for each neutrino mass eigenstates (see Table 2). We dedicate this section to a detailed derivation of the equations of flavor evolution for a neutrino dominated accretion disk. To maintain consistency with the traditional literature of neutrino oscillations, we will reuse some symbols appearing in

previous sections. To avoid confusion, we point out that the symbols in this section are independent of the previous sections unless we explicitly draw a comparison.

Table 2. Mixing and squared mass differences as they appear in [141]. Error values in parentheses are shown in 3σ interval. The squared mass difference is defined as $\Delta m^2 = m_3^2 - (m_2^2 + m_1^2)/2$ and its sign depends on the hierarchy $m_1 < m_2 < m_3$ or $m_3 < m_1 < m_2$.

$\Delta m_{21}^2 = 7.37 (6.93 - 7.96) \times 10^{-5} \text{ eV}^2$
$ \Delta m^2 = 2.56 (2.45 - 2.69) \times 10^{-3} \text{ eV}^2$ Normal Hierarchy
$ \Delta m^2 = 2.54 (2.42 - 2.66) \times 10^{-3} \text{ eV}^2$ Inverted Hierarchy
$\sin^2 \theta_{12} = 0.297 (0.250 - 0.354)$
$\sin^2 \theta_{23} (\Delta m^2 > 0) = 0.425 (0.381 - 0.615)$
$\sin^2 \theta_{23} (\Delta m^2 < 0) = 0.589 (0.383 - 0.637)$
$\sin^2 \theta_{13} (\Delta m^2 > 0) = 0.0215 (0.0190 - 0.0240)$
$\sin^2 \theta_{13} (\Delta m^2 < 0) = 0.0216 (0.0190 - 0.0242)$

3.1. Equations of Oscillation

The equations that govern the evolution of an ensemble of mixed neutrinos are the Boltzmann collision equations

$$i\dot{\rho}_{\mathbf{p},t} = C(\rho_{\mathbf{p},t}), \tag{38a}$$

$$i\dot{\bar{\rho}}_{\mathbf{p},t} = C(\bar{\rho}_{\mathbf{p},t}). \tag{38b}$$

The collision terms should include the vacuum oscillation plus all possible scattering interactions that neutrinos undergo through their propagation. For free streaming neutrinos, only the vacuum term and the forward-scattering interactions are taken into account so that the equations become

$$i\dot{\rho}_{\mathbf{p},t} = [H_{\mathbf{p},t}, \rho_{\mathbf{p},t}], \tag{39a}$$

$$i\dot{\bar{\rho}}_{\mathbf{p},t} = [\bar{H}_{\mathbf{p},t}, \bar{\rho}_{\mathbf{p},t}]. \tag{39b}$$

Here, $H_{\mathbf{p},t}$ ($\bar{H}_{\mathbf{p},t}$) is the oscillation Hamiltonian for (anti)neutrinos and $\rho_{\mathbf{p},t}$ ($\bar{\rho}_{\mathbf{p},t}$) is the matrix of occupation numbers: $(\rho_{\mathbf{p},t})_{ij} = \langle a_i^\dagger a_j \rangle_{\mathbf{p},t}$ for neutrinos and $(\bar{\rho}_{\mathbf{p},t})_{ij} = \langle \bar{a}_i^\dagger \bar{a}_j \rangle_{\mathbf{p},t}$ for antineutrinos, for each momentum \mathbf{p} and flavors i, j . The diagonal elements are the distribution functions $f_{\nu_i}(\mathbf{p})$ such that their integration over the momentum space gives the neutrino number density n_{ν_i} of a determined flavor i at time t . The off-diagonal elements provide information about the overlapping between the two neutrino flavors. Taking into account the current-current nature of the weak interaction in the standard model, the Hamiltonian for each equation is [142–144]

$$H_{\mathbf{p},t} = \Omega_{\mathbf{p},t} + \sqrt{2}G_F \int (l_{\mathbf{q},t} - \bar{l}_{\mathbf{q},t})(1 - \mathbf{v}_{\mathbf{q},t} \cdot \mathbf{v}_{\mathbf{p},t}) \frac{d^3 \mathbf{q}}{(2\pi)^3} + \sqrt{2}G_F \int (\rho_{\mathbf{q},t} - \bar{\rho}_{\mathbf{q},t})(1 - \mathbf{v}_{\mathbf{q},t} \cdot \mathbf{v}_{\mathbf{p},t}) \frac{d^3 \mathbf{q}}{(2\pi)^3}, \tag{40a}$$

$$\bar{H}_{\mathbf{p},t} = -\Omega_{\mathbf{p},t} + \sqrt{2}G_F \int (l_{\mathbf{q},t} - \bar{l}_{\mathbf{q},t})(1 - \mathbf{v}_{\mathbf{q},t} \cdot \mathbf{v}_{\mathbf{p},t}) \frac{d^3 \mathbf{q}}{(2\pi)^3} + \sqrt{2}G_F \int (\rho_{\mathbf{q},t} - \bar{\rho}_{\mathbf{q},t})(1 - \mathbf{v}_{\mathbf{q},t} \cdot \mathbf{v}_{\mathbf{p},t}) \frac{d^3 \mathbf{q}}{(2\pi)^3}. \tag{40b}$$

where G_F is the Fermi coupling constant, $\Omega_{\mathbf{p},t}$ is the matrix of vacuum oscillation frequencies, $l_{\mathbf{p},t}$ and $\bar{l}_{\mathbf{p},t}$ are matrices of occupation numbers for charged leptons built in a similar way to the neutrino matrices, and $\mathbf{v}_{\mathbf{p},t} = \mathbf{p}/p$ is the velocity of a particle with momentum \mathbf{p} (either neutrino or charged lepton). As stated before, we will only consider two neutrino flavors: e and $x = \mu + \tau$. Three-flavor oscillations can be approximated by two-flavor oscillations as a result of the strong hierarchy of the squared mass differences $|\Delta m_{13}^2| \approx |\Delta m_{23}^2| \gg |\Delta m_{12}^2|$. In this case, only the smallest mixing angle θ_{13} is considered. We will drop the suffix for the rest of the discussion. Consequently, the relevant oscillations

are $v_e \rightleftharpoons v_x$ and $\bar{v}_e \rightleftharpoons \bar{v}_x$, and each term in the Hamiltonian governing oscillations becomes a 2×2 Hermitian matrix. Now, consider an observer on the LRF (which is almost identical to the CRF due to Equation (6) at a point r . In its spatial local frame, the unit vectors $\hat{x}, \hat{y}, \hat{z}$ are parallel to the unit vectors $\hat{r}, \hat{\theta}, \hat{\phi}$ of the CF, respectively. Solving Equation (39) in this coordinate system would yield matrices $\rho, \bar{\rho}$ as functions of time t . However, in our specific physical system, both the matter density and the neutrino density vary with the radial distance from the BH. This means that the equations of oscillations must be written in a way that makes explicit the spatial dependence, i.e., in terms of the coordinates x, y, z . For a collimated ray of neutrinos, the expression $dt = dr$ would be good enough, but for radiating extended sources or neutrino gases the situation is more complicated.

In Equation (39) we must replace the matrices of occupation numbers by the space-dependent Wigner functions $\rho_{\mathbf{p},\mathbf{x},t}$ (and $\bar{\rho}_{\mathbf{p},\mathbf{x},t}$) and the total time derivative by the Liouville operator [145,146]:

$$\dot{\rho}_{\mathbf{p},\mathbf{x},t} = \overbrace{\frac{\partial \rho_{\mathbf{p},\mathbf{x},t}}{\partial t}}^{\text{Explicit Time}} + \overbrace{\mathbf{v}_{\mathbf{p}} \cdot \nabla_{\mathbf{x}} \rho_{\mathbf{p},\mathbf{x},t}}^{\text{Drift}} + \overbrace{\dot{\mathbf{p}} \cdot \nabla_{\mathbf{p}} \rho_{\mathbf{p},\mathbf{x},t}}^{\text{External Forces}} \quad (41)$$

In this context, \mathbf{x} represents a vector in the LRF. In the most general case, finding $\rho_{\mathbf{p},\mathbf{x},t}$ and $\bar{\rho}_{\mathbf{p},\mathbf{x},t}$ means solving a 7D neutrino transport problem in the variables $x, y, z, p_x, p_y, p_z, t$. Since our objective is to construct a simple model of neutrino oscillations inside the disk, to obtain the specific form of Equation (39) we must simplify the equations by imposing on it conditions that are consistent with the assumptions made in Section 2.

- Due to axial symmetry, the neutrino density is constant along the z direction. Moreover, since neutrinos follow null geodesics, we can set $\dot{p}_z \approx \dot{p}_\phi = 0$.
- Within the thin disk approximation (as represented by Equation (10)) the neutrino and matter densities are constant along the y direction and the momentum change due to curvature along this direction can be neglected, that is, $\dot{p}_y \approx 0$.
- In the LRF, the normalized radial momentum of a neutrino can be written as $p_x = \pm r / \sqrt{r^2 - 2Mr + M^2a^2}$. Hence, the typical scale of the change of momentum with radius is $\Delta r_{p_x, \text{eff}} = |d \ln p_x / dr|^{-1} = (r/M)(r^2 - 2Mr + M^2a^2) / (Ma^2 - r)$, which obeys $\Delta r_{p_x, \text{eff}} > r_s$ for $r > 2r_{\text{in}}$. This means we can assume $\dot{p}_x \approx 0$ up to regions very close to the inner edge of the disk.
- We define an effective distance $\Delta r_{\rho, \text{eff}} = |d \ln(Y_e n_B) / dr|^{-1}$. For all the systems we evaluated, we found that it is comparable to the height of the disk ($\Delta r_{\rho, \text{eff}} \sim 2 - 5 r_s$). This means that at any point of the disk we can calculate neutrino oscillations in a small regions assuming that both the electron density and neutrino densities are constant.
- We neglect energy and momentum transport between different regions of the disk by neutrinos that are recaptured by the disk due to curvature. This assumption is reasonable except for regions very close to the BH but is consistent with the thin disk model (see, e.g., [128]). We also assume initially that the neutrino content of neighboring regions of the disk (different values of r) do not affect each other. As a consequence of the results discussed above, we assume that at any point inside the disk and at any instant of time an observer can describe both the charged leptons and neutrinos as isotropic gases around small enough regions of the disk. This assumption is considerably restrictive but we will generalize it in Section 5.

The purpose of these approximations is twofold. On one hand, we can reduce the problem considerably, since they allow us to add the neutrino oscillations to a steady-state disk model by simply studying the behavior of neutrinos at each point of the disk using the constant values of density and temperature at that point. We will see in Section 5, that this assumption would correspond to a transient state of an accretion disk, since very fast neighboring regions of the disk start interacting. On the other hand, the approximations allow us to simplify the equations of oscillation considering that all but the first term in Equation (41) vanish, leaving only a time derivative. In addition, both terms of the form

$\mathbf{v}_{\mathbf{q},t} \cdot \mathbf{v}_{\mathbf{p},t}$ in Equation (40) average to zero so that $\rho_{\mathbf{p},\mathbf{x},t} = \rho_{p,t}$ and $\bar{\rho}_{\mathbf{p},\mathbf{x},t} = \bar{\rho}_{p,t}$. We are now in a position to derive the simplified equations of oscillation for this particular model. Let us first present the relevant equations for neutrinos. Due to the similarity between $H_{p,t}$ and $\bar{H}_{p,t}$, the corresponding equations for antineutrinos can be obtained analogously. For simplicity, we will drop the suffix t since the time dependence is now obvious. In the two-flavor approximation, ρ_p is a 2×2 Hermitian matrix and can be expanded in terms of the Pauli matrices σ_i and a polarization vector $\mathbf{P}_p = (P^x, P^y, P^z)$ in the neutrino flavor space, such that

$$\rho_p = \begin{pmatrix} \rho_{ee} & \rho_{ex} \\ \rho_{xe} & \rho_{xx} \end{pmatrix} = \frac{1}{2}(f_p \mathbf{1} + \mathbf{P}_p \cdot \vec{\sigma}), \tag{42}$$

where $f_p = \text{Tr}[\rho_p] = f_{\nu_e}(p) + f_{\nu_x}(p)$ is the sum of the distribution functions for ν_e and ν_x . Note that the z component of the polarization vector obeys

$$P_p^z = f_{\nu_e}(p) - f_{\nu_x}(p). \tag{43}$$

Hence, this component tracks the fractional flavor composition of the system. Appropriately normalizing ρ_p allows one to define a survival and mixing probability

$$P_{p,\nu_e \rightarrow \nu_e} = \frac{1}{2}(1 + P_p^z), \tag{44a}$$

$$P_{p,\nu_e \rightarrow \nu_x} = \frac{1}{2}(1 - P_p^z). \tag{44b}$$

The Hamiltonian can be written as a sum of three interaction terms:

$$H = H_{\text{vacuum}} + H_{\text{matter}} + H_{\nu\nu}. \tag{45}$$

The first term is the Hamiltonian in vacuum [27]:

$$H_{\text{vacuum}} = \frac{\omega_p}{2} \begin{pmatrix} -\cos 2\theta & \sin 2\theta \\ \sin 2\theta & \cos 2\theta \end{pmatrix} = \frac{\omega_p}{2} \mathbf{B} \cdot \vec{\sigma}, \tag{46}$$

where $\omega_p = \Delta m^2/2p$, $\mathbf{B} = (\sin 2\theta, 0, -\cos 2\theta)$ and θ is the smallest neutrino mixing angle in vacuum. The other two terms in Equation (40) are special since they make the evolution equations non-linear. Since we are considering that the electrons inside the form an isotropic gas, the vector $\mathbf{v}_{\mathbf{q}}$ in the first integral is distributed uniformly on the unit sphere and the factor $\mathbf{v}_{\mathbf{q}} \cdot \mathbf{v}_{\mathbf{p}}$ averages to zero. After integrating the matter Hamiltonian is given by

$$H_{\text{matter}} = \frac{\lambda}{2} \begin{pmatrix} 1 & 0 \\ 0 & -1 \end{pmatrix} = \frac{\lambda}{2} \mathbf{L} \cdot \vec{\sigma}, \tag{47}$$

where $\lambda = \sqrt{2}G_F(n_{e^-} - n_{e^+})$ is the charged current matter potential and $\mathbf{L} = (0, 0, 1)$. Similarly, the same product disappears in the last term and after integrating we get

$$H_{\nu\nu} = \sqrt{2}G_F[\mathbf{P} - \bar{\mathbf{P}}] \cdot \vec{\sigma}. \tag{48}$$

Clearly, $\mathbf{P} = \int \mathbf{P}_p d\mathbf{p}/(2\pi)^3$. Introducing every Hamiltonian term in Equation (39), and using the commutation relations of the Pauli matrices, we find the equations of oscillation for neutrinos and antineutrinos for each momentum mode p :

$$\dot{\mathbf{P}}_p = \left[\omega_p \mathbf{B} + \lambda \mathbf{L} + \sqrt{2}G_F(\mathbf{P} - \bar{\mathbf{P}}) \right] \times \mathbf{P}_p, \tag{49a}$$

$$\dot{\bar{\mathbf{P}}}_p = \left[-\omega_p \mathbf{B} + \lambda \mathbf{L} + \sqrt{2}G_F(\mathbf{P} - \bar{\mathbf{P}}) \right] \times \bar{\mathbf{P}}_p, \tag{49b}$$

where we have assumed that the total neutrino distribution remains constant, $\dot{f}_p = 0$. This shows how the polarization vectors can be normalized. By performing the transformations $P_p/f_p \mapsto P_p$ and $\bar{P}_p/\bar{f}_p \mapsto \bar{P}_p$, and multiplying and dividing the last term by the total neutrino density Equation (49), we get

$$\dot{P}_p = [\omega_p \mathbf{B} + \lambda \mathbf{L} + \mu \mathbf{D}] \times P_p, \tag{50a}$$

$$\dot{\bar{P}}_p = [-\omega_p \mathbf{B} + \lambda \mathbf{L} + \mu \mathbf{D}] \times \bar{P}_p, \tag{50b}$$

$$\mathbf{D} = \frac{1}{n_{\nu_e} + n_{\nu_x}} \int (f_q P_q - \bar{f}_q \bar{P}_q) \frac{d\mathbf{q}}{(2\pi)^3}. \tag{50c}$$

These are the traditional forms of the equations in terms of the vacuum, matter and self-interaction potentials ω_p , λ and μ with

$$\mu = \sqrt{2} G_F \sum_{i \in \{e,x\}} n_{\nu_i}. \tag{51}$$

Different normalization schemes are possible (see, e.g., [36,49,144,147]). Assuming that we can solve the equations of oscillation with constant potentials λ and μ simplifies the problem even further. Following [29], with the vector transformation (a rotation around the z axis of flavor space)

$$R_z = \begin{pmatrix} \cos(\lambda t) & \sin(\lambda t) & 0 \\ -\sin(\lambda t) & \cos(\lambda t) & 0 \\ 0 & 0 & 1 \end{pmatrix}, \tag{52}$$

Equation (50) becomes

$$\dot{P}_p = [\omega_p \mathbf{B} + \mu \mathbf{D}] \times P_p, \tag{53a}$$

$$\dot{\bar{P}}_p = [-\omega_p \mathbf{B} + \mu \mathbf{D}] \times \bar{P}_p, \tag{53b}$$

eliminating the λ potential, but making \mathbf{B} time dependent. By defining the vector $\mathbf{S}_p = P_p + \bar{P}_p$, and adding and subtracting Equations (53a) and (53b) we get

$$\dot{\mathbf{S}}_p = \omega_p \mathbf{B} \times \mathbf{D}_p + \mu \mathbf{D} \times \mathbf{S}_p \approx \mu \mathbf{D} \times \mathbf{S}_p, \tag{54a}$$

$$\dot{\mathbf{D}}_p = \omega_p \mathbf{B} \times \mathbf{S}_p + \mu \mathbf{D} \times \mathbf{D}_p \approx \mu \mathbf{D} \times \mathbf{D}_p. \tag{54b}$$

The last approximation is true if we assume that the self-interaction potential is larger than the vacuum potential $\omega_p/\mu \ll 1$. We will show in Section 5 that this is the case for thin disks. The first equation implies that all the vectors \mathbf{S}_p and their integral \mathbf{S} evolve in the same way, suggesting the relation $\mathbf{S}_p = (f_p + \bar{f}_p) \mathbf{S}$. By replacing in Equation (54b) and integrating

$$\dot{\mathbf{S}} = \mu \mathbf{D} \times \mathbf{S}, \tag{55a}$$

$$\dot{\mathbf{D}} = \langle \omega \rangle \mathbf{B} \times \mathbf{S}. \tag{55b}$$

where $\langle \omega \rangle = \int \omega_p (f_p + \bar{f}_p) d\mathbf{p} / (2\pi)^3$ is the average vacuum oscillation potential. The fact that in our model the equations of oscillations can be written in this way has an important consequence. Usually, as it is done in supernovae neutrino oscillations, to solve Equation (50) we would need the neutrino distributions throughout the disk. If neutrinos are trapped, their distribution is given by Equation (26). If neutrinos are free, their temperature is not the same as the disk's temperature. Nonetheless, we can approximate the neutrino distribution in this regime by a Fermi–Dirac distribution with the same chemical potential as defined by Equation (27) but with an effective temperature T_ν^{eff} . This tempera-

ture can be obtained by solving the equation $\langle E_\nu \rangle = U(T_\nu^{\text{eff}}, \eta_\nu) / n(T_\nu^{\text{eff}}, \eta_\nu)$ which gives

$$T_{\nu_x, \bar{\nu}_x}^{\text{eff}} = \langle E_{\nu_x, \bar{\nu}_x} \rangle \frac{180 \zeta(3)}{7\pi^4}, \tag{56a}$$

$$T_{\nu_e, \bar{\nu}_e}^{\text{eff}} = \frac{\langle E_{\nu_e, \bar{\nu}_e} \rangle}{3} \frac{\text{Li}_3(-\exp(\eta_{\nu_e, \bar{\nu}_e}))}{\text{Li}_4(-\exp(\eta_{\nu_e, \bar{\nu}_e}))}, \tag{56b}$$

where $\zeta(3)$ is Apéry’s constant (ζ is the Riemann zeta function) and $\text{Li}_s(z)$ is Jonquière’s function. For convenience and considering the range of values that the degeneracy parameter reaches (see Section 6), we approximate the effective temperature of electron neutrinos and antineutrinos with the expressions

$$T_{\nu_e}^{\text{eff}} = \frac{\langle E_{\nu_e} \rangle}{3} (a\eta_{\nu_e}^2 + b\eta_{\nu_e} + c), \tag{57a}$$

$$T_{\bar{\nu}_e}^{\text{eff}} = \frac{\langle E_{\bar{\nu}_e} \rangle}{3}. \tag{57b}$$

with constants $a = 0.0024$, $b = -0.085$, $c = 0.97$. However, Equation (55) allows us to consider just one momentum mode, and the rest of the spectrum behaves in the same way.

4. Initial Conditions and Integration

In the absence of oscillations, we can use Equations (15), (17) and (37) to solve for the set of functions $\eta_{e^-}(r)$, $\zeta(r)$ and $Y_e(r)$ using as input parameters the accretion rate \dot{M} , the dimensionless spin parameter a , the viscosity parameter α and the BH mass M . From [99,107] we learn that neutrino dominated disks require accretion between $0.01 M_\odot \text{ s}^{-1}$ and $1 M_\odot \text{ s}^{-1}$ (this accretion rate range varies depending on the value of α). For accretion rates smaller than the lower value, the neutrino cooling is not efficient, and for rates larger than the upper value, the neutrinos are trapped within the flow. We also limit ourselves to the above accretion rate range, since it is consistent with the one expected to occur in a BdHN (see, e.g., [57,63,70]). We also know that a high spin parameter, high accretion rate, high BH mass and low viscosity parameter produce disks with higher density and higher temperature. This can be explained using the fact that several variables of the disk, such as pressure, density and height, are proportional to a positive power of M and a positive power of the quotient \dot{M}/α . To avoid this semi-degeneracy in the system, we reduce the parameter space, and considering that we want to focus on the study of the oscillation dynamics inside the disk, we fix the BH mass at $M = 3M_\odot$, the viscosity parameter at $\alpha = 0.01$ and the spin parameter at $a = 0.95$ while changing the accretion rate. These values also allow us to compare our results with earlier disk models. Equations (17) and (37) are first-order ordinary differential equations, and since we perform the integration from an external (far away) radius r_{out} up to the innermost stable circular orbit r_{in} , we must provide two boundary conditions at r_{out} . Following the induced gravitational collapse (IGC) paradigm of GRBs associated with type Ib/c supernovae we assume that at the external edge of the disk, the infalling matter is composed mainly by the ions present in the material ejected from an explosion of a carbon–oxygen core, that is, mainly oxygen and electrons. This fixes the electron fraction $Y_e(r_{\text{out}}) = 0.5$. We can also calculate the average binding energy per nucleon that appears in Equation (34) using the data in [136]. To establish the NSE we consider H2, H3, HE3, HE4, LI6, LI7, BE7, BE9, BE10, B10, B11, C11, C12, C13, C14, N13, N14, N15, O14, O15, O16, O17 and O18, and obtain the value of the average binding energy per nucleon $\bar{B} = 6.35 \text{ MeV}$. The second boundary condition can be obtained by the relation $(T\eta + m_B)\sqrt{g_{tt}} = \text{constant}$ [148–150], with η being the degeneracy parameter of the fluid. If we require the potentials to vanish at infinity and invoke Euler’s theorem, we arrive at the relation in the weak field limit

$$\frac{M}{r_{\text{out}}} = \left. \frac{\rho + U + P - TS}{\rho} \right|_{r=r_{\text{out}}}. \tag{58}$$

For a classical gas composed of ions and electrons, this relation becomes

$$\frac{M}{r_{\text{out}}} \lesssim \left. \frac{U}{\rho} \right|_{r=r_{\text{out}}} . \tag{59}$$

That is, the virial specific energy must be smaller or comparable to the energy per baryon. Equation (59) can be used together with Equations (15) and (33) to solve for $\eta_e(r_{\text{out}}), \xi(r_{\text{out}})$. The value of r_{out} is chosen to be at most the circularization radius of the accreting material as described in [63,69]. We can estimate this radius by solving for r in the expression of the angular momentum per unit mass for a equatorial circular orbits. Hence, using Equation (5) we need to solve

$$u_\phi = M \frac{x^2 - 2x + a^2}{x^{3/2} \sqrt{x^3 - 3x + 2a}} \sim 3 \times 10^7 \text{ cm}, \tag{60}$$

where $x = \sqrt{r/M}$ which yields $r_{\text{out}} \sim 1800r_s$ and the expression is in geometric units. Finally, for the initial conditions to be accepted, they are evaluated by the gravitational instability condition [151]:

$$\sqrt{R \left. \frac{\partial}{\partial \tilde{t}} \right|_{\theta=\pi/2}} \Omega \geq 2\sqrt{3}\pi\rho. \tag{61}$$

Integration of the equations proceeds as follows: With the initial conditions we solve Equation (37) to obtain the electron fraction in the next integration point. With the new value of the electron fraction we solve the differential algebraic system of Equations (15) and (17) at this new point. This process continues until the innermost stable circular orbit r_{in} is reached.

To add the dynamics of neutrino oscillations we proceed the same as before, but at each point of integration, once the values of Y_e, η and ξ are found, we solve Equation (50) for the average momentum mode to obtain the survival probabilities as a function of time. We then calculate the new neutrino and antineutrino distributions with the conservation of total number density and the relations

$$n_{\nu_e}^{\text{new}}(t) = P_{\nu_e \rightarrow \nu_e}(t)n_{\nu_e} + [1 - P_{\nu_e \rightarrow \nu_e}(t)]n_{\nu_x}, \tag{62a}$$

$$n_{\nu_x}^{\text{new}}(t) = P_{\nu_x \rightarrow \nu_x}(t)n_{\nu_x} + [1 - P_{\nu_x \rightarrow \nu_x}(t)]n_{\nu_e}. \tag{62b}$$

Since the disk is assumed to be in a steady-state, we then perform a time average of Equation (62) as discussed in Section 2. With the new distributions, we can calculate the new neutrino and antineutrino average energies and use them to re-integrate the disk equations.

Neutrino emission within neutrino-cooled disks is dominated by electron and positron capture, which only produces electron (anti)neutrinos. The second most important process is electron–positron annihilation, but it is several orders of magnitude smaller. In Figure 2 we show the total number emissivity for these two processes for an accretion rate of $\dot{M} = 0.1M_\odot \text{ s}^{-1}$. Other cases behave similarly. Moreover, although the degeneracy parameter suppresses the positron density, a high degeneracy limit does not occur in the disk and the degeneracy is kept low at values between about 0.2 and 3, as shown in Figure 3. The reason for this is the effect of high degeneracy on neutrino cooling. Higher degeneracy leads to a lower density of positrons, which suppresses the neutrino production and emission, which in turn leads to a lower cooling rate, higher temperature, lower degeneracy and higher positron density. This equilibrium leads, via the lepton number conservation Equation (37), to a balance between electronic and non-electronic neutrino densities within the inner regions of the disk. Given this fact, to solve the equations of oscillations, we can approximate the initial conditions of the polarization vectors with

$$P = \bar{P} \approx (0, 0, 1). \tag{63}$$

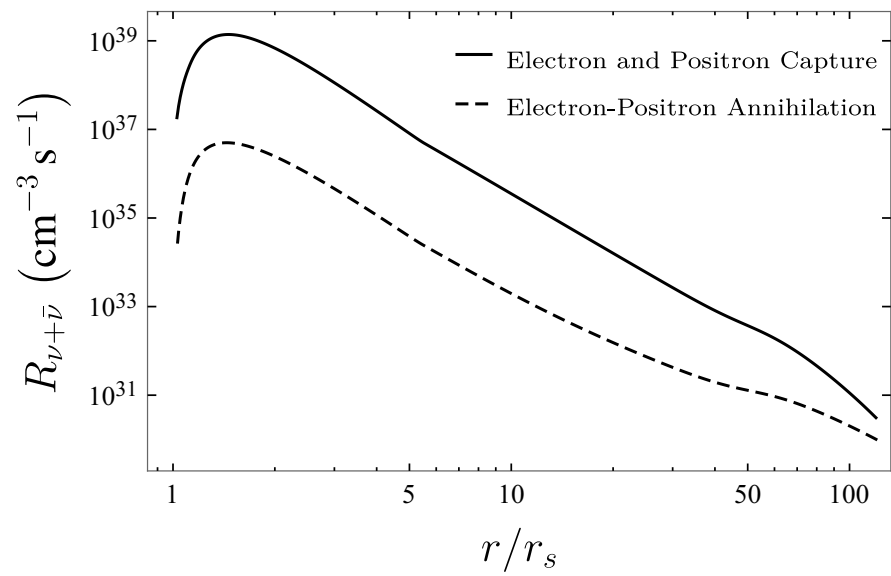


Figure 2. Total number emissivity for electron and positron capture ($p + e^- \rightarrow n + \nu_e, n + e^+ \rightarrow p + \bar{\nu}_e$) and electron–positron annihilation ($e^- + e^+ \rightarrow \nu + \bar{\nu}$) for accretion disks with $\dot{M} = 0.1M_\odot \text{ s}^{-1}$ between the inner radius and the ignition radius.

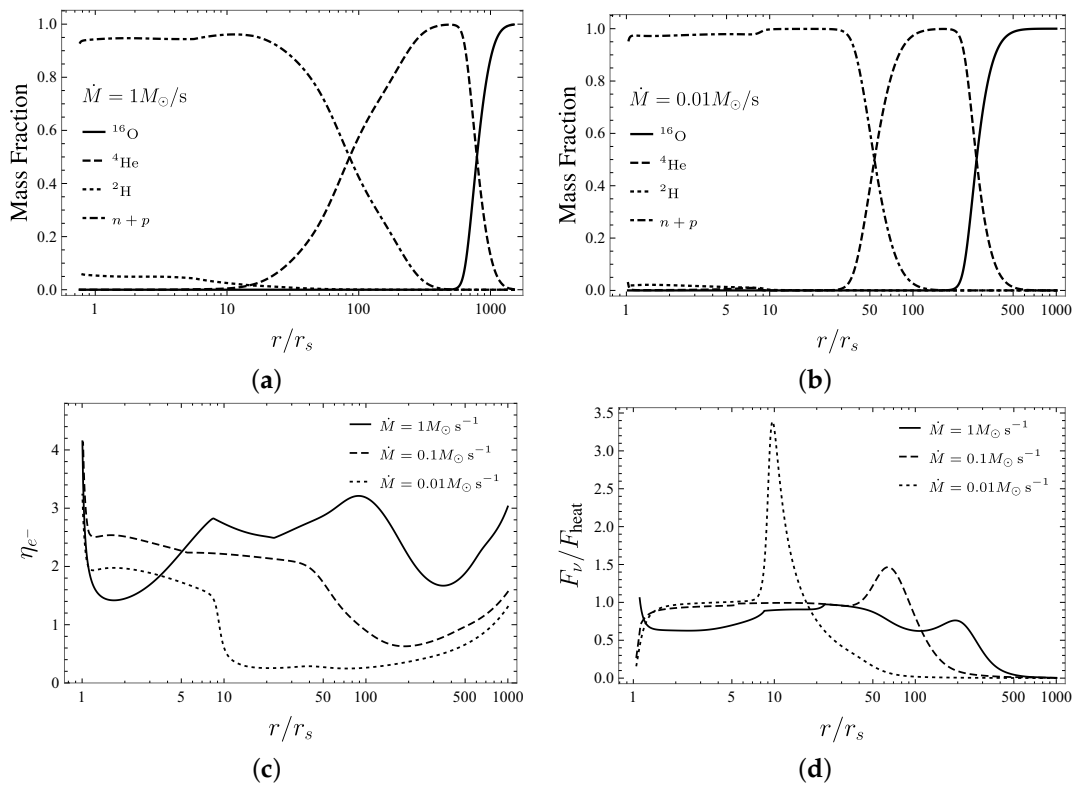


Figure 3. Cont.

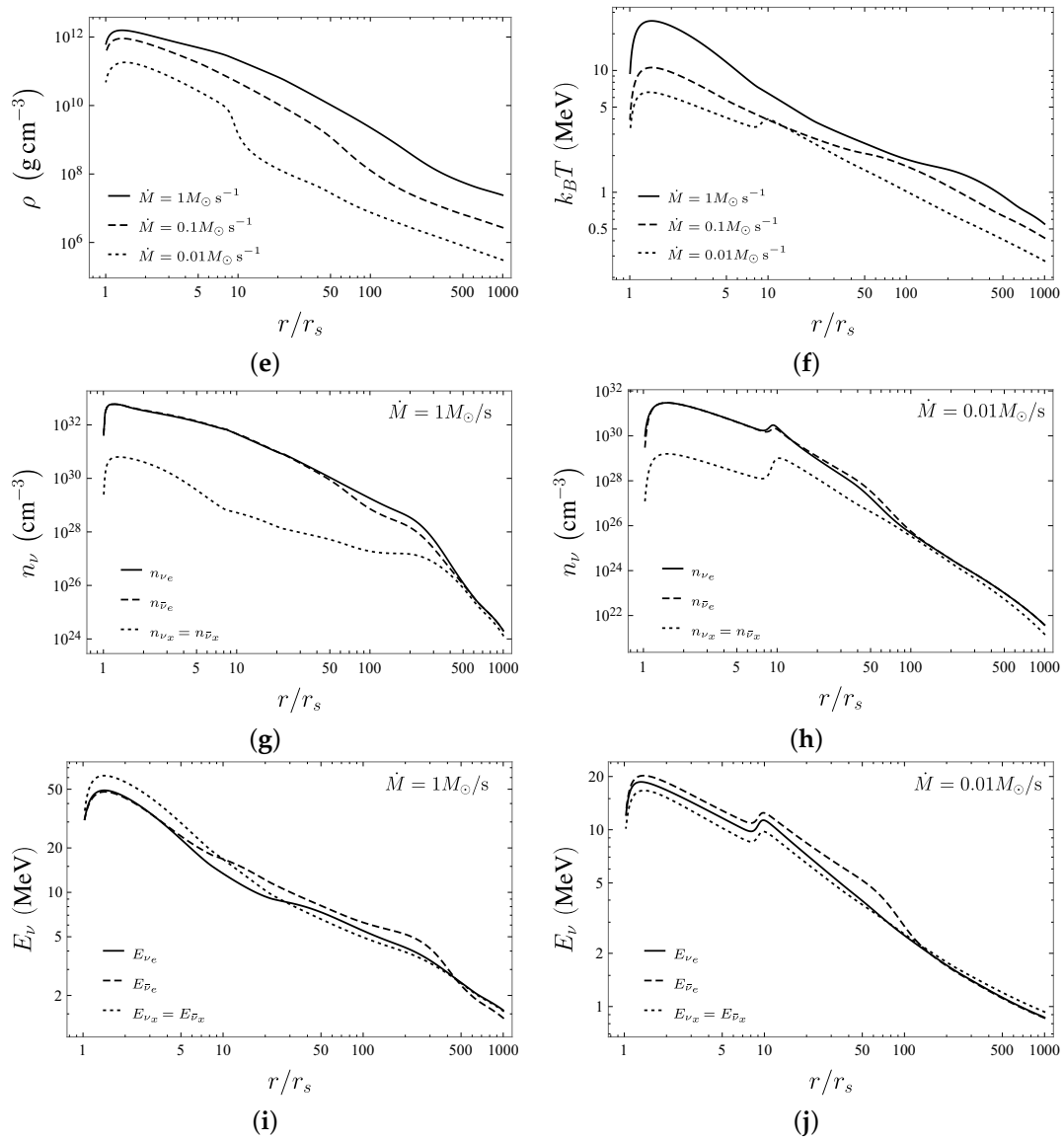


Figure 3. Properties of accretion disks in the absence of oscillations with $M = 3M_{\odot}$, $\alpha = 0.01$, $a = 0.95$. (a,b) The mass fraction inside the disk. We have plotted only the ones that appreciably change. (c) The electron degeneracy parameter. (d) The comparison between the neutrino cooling flux F_{ν} and the viscous heating F_{heat} . (e) The baryon density. (f) The temperature. (g,h) The neutrino number density. (i,j) The average neutrino energies.

5. Results and Analysis

In Figures 3 and 4, we present the main features of accretion disks for the parameters $M = 3M_{\odot}$; $\alpha = 0.01$; $a = 0.95$; and two selected accretion rates, $\dot{M} = 1M_{\odot} \text{ s}^{-1}$ and $\dot{M} = 0.01M_{\odot} \text{ s}^{-1}$. It exhibits the usual properties of thin accretion disks. High accretion rate disks have higher density, temperature and electron degeneracy. Additionally, for high accretion rates, the cooling due to photodisintegration and neutrino emission kicks in at larger radii. For all cases, as the disk heats up, the number of free nucleons starts to increase enabling the photodisintegration cooling at $r \sim (100\text{--}300)r_s$. Only the disintegration of alpha particles is important, and the nucleon content of the infalling matter is of little consequence for the dynamics of the disk. When the disk reaches temperatures ~ 1.3 MeV, the electron capture switches on, the neutrino emission becomes significant and the physics of the disk is dictated by the energy equilibrium between F_{heat} and F_{ν} . The radius at which neutrino cooling becomes significant (called ignition radius r_{ign}) is defined by the condition $F_{\nu} \sim F_{\text{heat}}/2$. For the low accretion rate $\dot{M} = 0.01M_{\odot} \text{ s}^{-1}$, the photodisintegration cooling finishes before the neutrino cooling becomes significant; this leads to fast heating of the

disk. Then the increase in temperature triggers a strong neutrino emission that carries away the excess heat generating a sharp spike in F_ν surpassing F_{heat} by a factor of ~ 3.5 . This behavior is also present in the systems studied in [107], but there it appears for fixed accretion rates and high viscosity ($\alpha = 0.1$). This demonstrates the semi-degeneracy mentioned in Section 5. The evolution of the fluid can be tracked accurately through the degeneracy parameter. At the outer radius, η_{e^-} starts to decrease as the temperature of the fluid rises. Once neutrino cooling becomes significant, it starts to increase until the disk reaches the local balance between heating and cooling. At this point, η_{e^-} stops rising and is maintained (approximately) at a constant value. Very close to r_{in} , the zero torque condition of the disk becomes important and the viscous heating is reduced drastically. This is reflected in a sharp decrease in the fluid's temperature and increase in the degeneracy parameter. For the high accretion rate, an additional effect has to be taken into account. Due to high ν_e optical depth, neutrino cooling is less efficient, leading to an increase in temperature and a second dip in the degeneracy parameter. This dip is not observed in low accretion rates because τ_{ν_e} does not reach significant values.

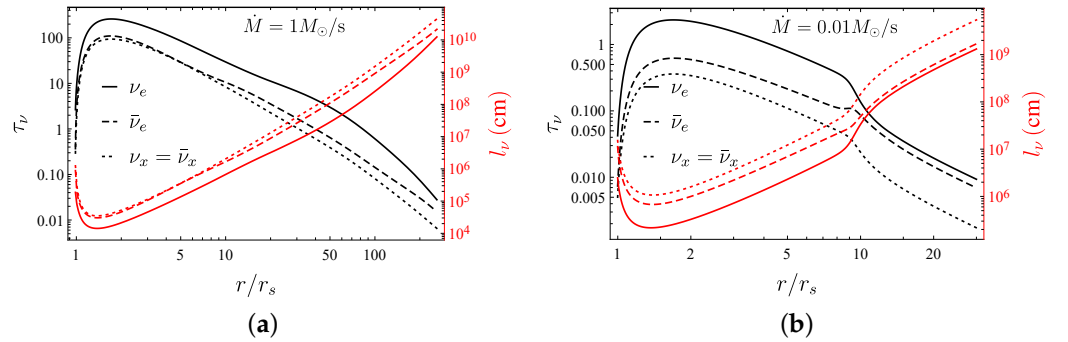


Figure 4. Total optical depth (left scale) and mean free path (right scale) for neutrinos and antineutrinos of both flavors between the inner radius and the ignition radius for accretion disks with (a) $\dot{M} = 1M_\odot \text{ s}^{-1}$ and (b) $0.01M_\odot \text{ s}^{-1}$.

With the information in Figure 3 we can obtain the oscillation potentials which we plot in Figure 5. Since the physics of the disk for $r < r_{\text{ign}}$ are independent of the initial conditions at the external radius and for $r > r_{\text{ign}}$ the neutrino emission is negligible, the impact of neutrino oscillations is important only inside r_{ign} .

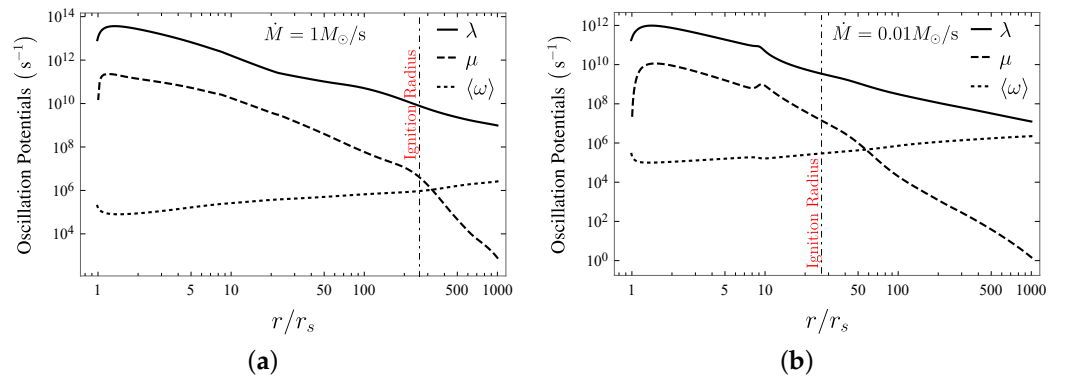


Figure 5. Oscillation potentials as functions of r with $M = 3M_\odot$, $\alpha = 0.01$, $a = 0.95$ for accretion rates (a) $\dot{M} = 1M_\odot \text{ s}^{-1}$ and (b) $\dot{M} = 0.01M_\odot \text{ s}^{-1}$, respectively. The vertical line represents the position of the ignition radius.

We can see that the discussion at the end of Section 3.1 is justified since, for $r_{\text{in}} < r < r_{\text{ign}}$, the potentials obey the relation

$$\langle \omega \rangle \ll \mu \ll \lambda. \quad (64)$$

Generally, the full dynamics of neutrino oscillations are a rather complex interplay between the three potentials, yet it is possible to understand the neutrino response in the disk using some numerical and algebraic results obtained in [33,36,144] and references therein. Specifically, we know that if $\mu \gg \langle \omega \rangle$, as long as the MSW condition $\lambda \simeq \langle \omega \rangle$ is not met (precisely our case), collective effects should dominate the neutrino evolution even if $\lambda \gg \mu$. On the other hand, if $\mu \lesssim \langle \omega \rangle$, the neutrino evolution is driven by the relative values between the matter and vacuum potentials (not our case). With Equation (55) we can build a very useful analogy. These equations are analogous to the equations of motion of a simple mechanical pendulum with a vector position given by \mathbf{S} , precessing around with angular momentum \mathbf{D} , subjected to a gravitational force $\langle \omega \rangle \mu \mathbf{B}$ with mass μ^{-1} . Using Equation (63) obtains the expression $|\mathbf{S}| = S \approx 2 + O(\langle \omega \rangle / \mu)$. Calculating $\partial_t(\mathbf{S} \cdot \mathbf{S})$, it can be checked that this value is conserved up to fluctuations of order $\langle \omega \rangle / \mu$. The analogous angular momentum is $\mathbf{D} = \mathbf{P} - \bar{\mathbf{P}} = 0$. Thus, the pendulum moves initially in a plane defined by \mathbf{B} and the z-axis, i.e., the plane xz . Then, it is possible to define an angle φ between \mathbf{S} and the z-axis such that

$$\mathbf{S} = S(\sin \varphi, 0, \cos \varphi). \tag{65}$$

The only non-zero component of \mathbf{D} is the y -component. From Equation (55) we find

$$\dot{\varphi} = \mu D, \tag{66a}$$

$$\dot{D} = -\langle \omega \rangle S \cos(\varphi + 2\theta). \tag{66b}$$

These equations can be equivalently written as

$$\ddot{\varphi} = -k^2 \sin(2\theta + \varphi), \tag{67}$$

where we have introduced the inverse characteristic time k by

$$k^2 = \langle \omega \rangle \mu S, \tag{68}$$

which is related to the anharmonic oscillations of the pendulum. The role of the matter potential λ is to logarithmically extend the oscillation length by the relation [144]

$$\tau = -k^{-1} \ln \left[\frac{k}{\theta(k^2 + \lambda^2)^{1/2}} \left(1 + \frac{\langle \omega \rangle}{S\mu} \right) \right]. \tag{69}$$

The total oscillation time can then be approximated by the period of an harmonic pendulum plus the logarithmic extension

$$t_{\text{osc}} = \frac{2\pi}{k} + \tau. \tag{70}$$

The initial conditions of Equation (63) imply

$$\varphi(t = 0) = \arcsin \left(\frac{\langle \omega \rangle}{S\mu} \sin 2\theta \right), \tag{71}$$

so that φ is a small angle. The potential energy for a simple pendulum is

$$V(\varphi) = k^2 [1 - \cos(\varphi + 2\theta)] \approx k^2 (\varphi + 2\theta)^2. \tag{72}$$

If $k^2 > 0$, which is true for the normal hierarchy $\Delta m^2 > 0$, we expect small oscillations around the initial position since the system begins in a stable position of the potential. The magnitude of flavor conversions is in the order $\sim \langle \omega \rangle / S\mu \ll 1$. We stress that normal hierarchy does not mean an absence of oscillations but rather imperceptible oscillations in P_z . No strong flavor oscillations are expected. On the contrary, for the inverted hierarchy $\Delta m^2 < 0, k^2 < 0$ and the initial φ indicates that the system begins in an unstable position and we expect very large anharmonic oscillations. P^z (and \bar{P}^z) oscillates between two

different maxima, passing through a minimum $-P^z$ ($-\bar{P}^z$) several times. This implies total flavor conversion: all electronic neutrinos (antineutrinos) are converted into non-electronic neutrinos (antineutrinos) and vice versa. This has been called bipolar oscillation in the literature [44]. If the initial conditions are not symmetric as in Equation (63), the asymmetry is measured by a constant $\zeta = \bar{P}^z/P^z$ if $\bar{P}^z < P^z$ or $\zeta = P^z/\bar{P}^z$ if $\bar{P}^z > P^z$ so that $0 < \zeta < 1$. Bipolar oscillations are present in an asymmetric system as long as the relation

$$\frac{\mu}{|\langle \omega \rangle|} < 4 \frac{1 + \zeta}{(1 - \zeta)^2}, \quad (73)$$

is obeyed [144]. If this condition is not met, instead of bipolar oscillation we get synchronized oscillations. Since we are considering constant potentials, synchronized oscillations are equivalent to the normal hierarchy case. From Figure 5 we can conclude that in the normal hierarchy case, neutrino oscillations have no effects on neutrino-cooled disks under the assumptions we have made. On the other hand, in the inverted hierarchy case, we expect extremely fast flavor conversions with periods of order $t_{\text{osc}} \sim (10^{-9}-10^{-5})$ s for high accretion rates and $t_{\text{osc}} \sim (10^{-8}-10^{-5})$ s for low accretion rates, between the respective r_{in} and r_{ign} .

For the purpose of illustration we solve the equations of oscillations for the $\dot{M} = 0.1M_{\odot} \text{ s}^{-1}$ case at $r = 10r_s$. The electronic (anti)neutrino survival probability at this point is shown in Figure 6 for inverted hierarchy and normal hierarchy, respectively. On both plots, there is no difference between the neutrino and antineutrino survival probabilities. This should be expected, since for these values of r , the matter and self-interaction potentials are much larger than the vacuum potential, and there is virtually no difference between Equations (50a) and (50b). Additionally, as mentioned before, note that the (anti)neutrino flavor proportions remain virtually unchanged for normal hierarchy, while the neutrino flavor proportions change drastically for the inverted hierarchy case. The characteristic oscillation time of the survival probability in inverted hierarchy found on the plot is

$$t_{\text{osc}} \approx 8.4 \times 10^{-7} \text{ s}, \quad (74)$$

which agrees with the ones given by Equation (70) up to a factor of order one. Such a small value suggests extremely quick $\nu_e \bar{\nu}_e \rightarrow \nu_x \bar{\nu}_x$ oscillations. A similar effect occurs for regions of the disk inside the ignition radius for all three accretion rates. In this example, the time average of the survival probabilities yields the values $\langle P_{\nu_e \rightarrow \nu_e} \rangle = \langle P_{\bar{\nu}_e \rightarrow \bar{\nu}_e} \rangle = 0.92$. With this number and Equations (62) and (57), the (anti)neutrino spectrum for both flavors can be constructed. However, more importantly, this means that the local observer at that point in the disk measures, on average, an electron (anti)neutrino loss of around 8%, which is represented by an excess of non-electronic (anti)neutrinos.

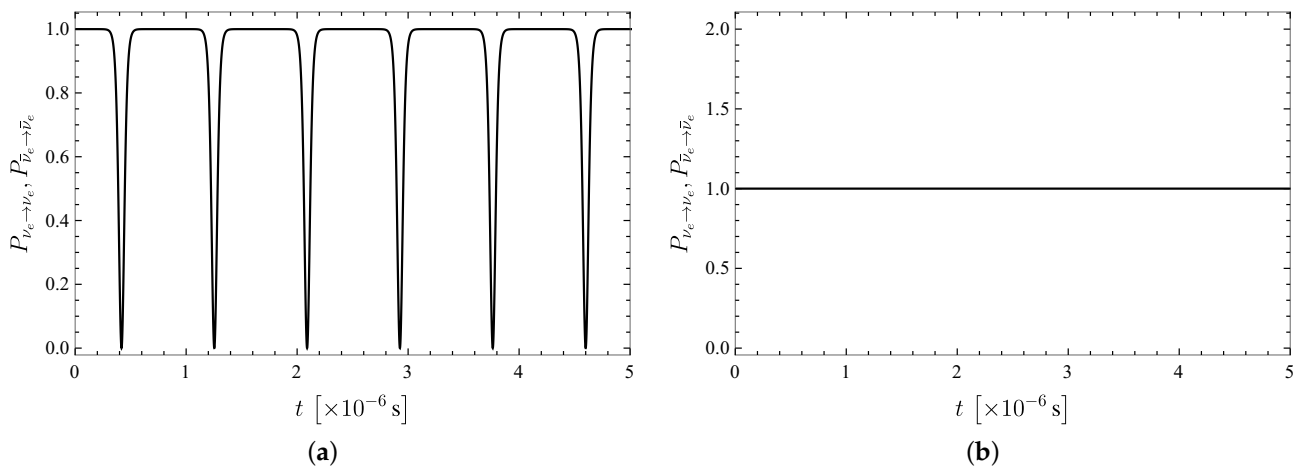


Figure 6. Survival provability for electron neutrinos and antineutrinos for the accretion disk with $\dot{M} = 0.1M_{\odot} \text{ s}^{-1}$ at $r = 10r_s$. The survival probabilities for neutrinos and antineutrinos in both plots coincide. (a) Inverted hierarchy and (b) normal hierarchy.

In Section 3.1 we proposed to calculate neutrino oscillations assuming that small neighboring regions of the disk are independent and that neutrinos can be viewed as isotropic gases in those regions. However, this cannot be considered a steady-state of the disk. To see this, consider Figure 4. The maximum value of the neutrino optical depth is in the order of 10^3 for the highest accretion rate, meaning that the time that takes neutrinos to travel a distance of one Schwarzschild inside the disk radius obeys

$$t_{r_s} \ll \text{Max}(\tau_\nu)r_s \approx 10^{-2} \text{ s}, \tag{75}$$

which is lower than the accretion time of the disk as discussed in Section 2 but higher than the oscillation time. Different sections of the disk are not independent, since they very quickly share (anti)neutrinos created with a non-vanishing momentum along the radial direction. Furthermore, the oscillation patterns between neighboring regions of the disk are not identical. In Figure 7 we show the survival probability as a function of time for different (but close) values of r for $\dot{M} = 0.1M_\odot \text{ s}^{-1}$. The superposition between neutrinos with different oscillation histories has several consequences: (1) It breaks the isotropy of the gas because close to the BH, neutrinos are more energetic and their density is higher, producing a radially directed net flux, meaning that the factor $\mathbf{v}_{q,t} \cdot \mathbf{v}_{p,t}$ does not average to zero. This implies that realistic equations of oscillations include a multi-angle term and a radially decaying neutrino flux similar to the situation in SN neutrinos. (2) It constantly changes the neutrino content at any value of r independently of the neutrino collective evolution given by the values of the oscillation potentials at that point. This picture plus the asymmetry that electron and non-electron neutrinos experience through the matter environment (electron (anti)neutrinos can interact through $n + \nu_e \rightarrow p + e^-$ and $p + \bar{\nu}_e \rightarrow n + e^+$), suggests that the disk achieves complete flavor equipartitioning (decoherence). We can identify two competing causes, namely, quantum decoherence and kinematic decoherence.

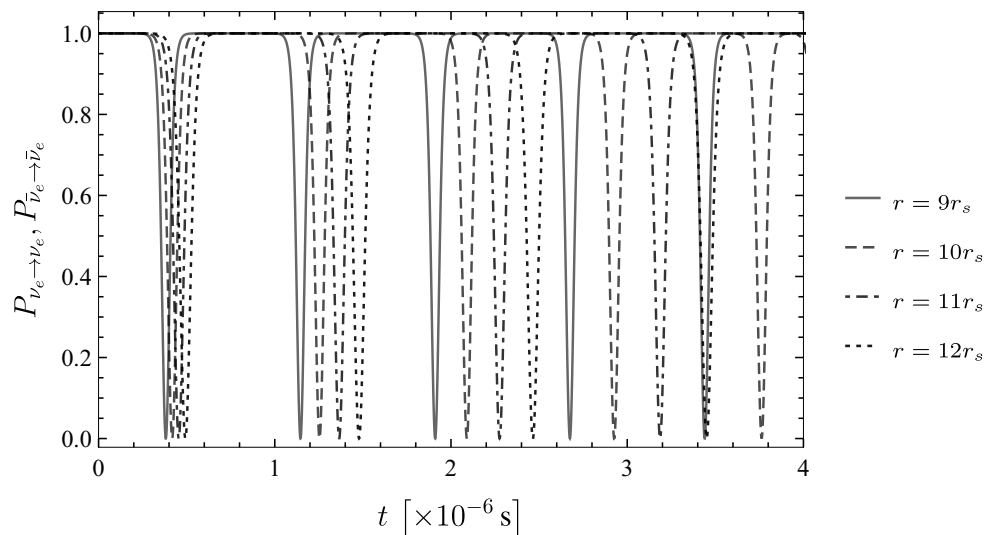


Figure 7. Survival provability for electron neutrinos and antineutrinos for the accretion disk with $\dot{M} = 0.1M_\odot \text{ s}^{-1}$ at $r = 9r_s, 10r_s, 11r_s, 12r_s$.

Quantum decoherence is the product of collisions among the neutrinos or with a thermal background medium can be understood as follows [152]. From Appendix D.2 we know that different (anti)neutrino flavors posses different cross-sections and scattering rates $\Gamma_{\nu_i, \bar{\nu}_i}$. In particular, we have $\Gamma_{\nu_x} \approx \Gamma_{\bar{\nu}_x} < \Gamma_{\bar{\nu}_e} < \Gamma_{\nu_e}$. An initial electron (anti)neutrino created at a point r will begin to oscillate into ν_x ($\bar{\nu}_x$). The probability of finding it in one of the two flavors evolves as previously discussed. However, in each interaction $n + \nu_e \rightarrow p + e^-$, the electron neutrino component of the superposition is absorbed, while the ν_x component remains unaffected. Thus, after the interaction the two flavors can no longer interfere. This allows the remaining ν_x to oscillate and develop a new coherent ν_e component which

is made incoherent in the next interaction. The process will come to equilibrium only when there are equal numbers of electronic and non-electronic neutrinos. That is, the continuous emission and absorption of electronic (anti)neutrinos generate non-electronic (anti)neutrinos with an average probability of $\langle P_{\nu_e \rightarrow \nu_e} \rangle$ in each interaction, and once the densities of flavors are equal, the oscillation dynamic stops. An initial system composed of $\nu_e, \bar{\nu}_e$ turns into an equal mixture of $\nu_e, \bar{\nu}_e$ and $\nu_x, \bar{\nu}_x$, reflected as an exponential damping of oscillations. For the particular case in which non-electronic neutrinos can be considered as sterile (do not interact with the medium), the relaxation time of this process can be approximated as [153,154]

$$t_Q = \frac{1}{2l_{\nu\bar{\nu}}\langle\omega\rangle^2 \sin^2 2\theta} + \frac{2l_{\nu\bar{\nu}}\lambda^2}{\langle\omega\rangle^2 \sin^2 2\theta'} \tag{76}$$

where $l_{\nu\bar{\nu}}$ represents the (anti)neutrino mean free path.

Kinematic decoherence is the result of a non-vanishing flux term such that at any point, (anti)neutrinos traveling in different directions do not experience the same self-interaction potential due to the multi-angle term in the integral of Equation (40). Different trajectories do not oscillate in the same way, leading to a de-phasing and a decay of the average $\langle P_{\nu \rightarrow \nu} \rangle$, and thus to the equipartitioning of the overall flavor content. The phenomenon is similar to an ensemble of spins in an inhomogeneous magnetic field. In [35] it is shown that for asymmetric $\nu\bar{\nu}$ gas, even an infinitesimal anisotropy triggers an exponential evolution towards equipartitioning, and in [36] it was shown that if the symmetry between neutrinos and antineutrinos is not broken beyond the limit of 25%, kinematic decoherence is still the main effect of neutrino oscillations. As a direct consequence of the $\nu\bar{\nu}$ symmetry present within the ignition radius of accretion disks (see Figure 3), an equipartition among different neutrino flavors is expected. This multi-angle term keeps the order of the characteristic time t_{osc} of Equation (70) unchanged, and kinematic decoherence happens within a few oscillation cycles. The oscillation time gets smaller closer to the BH due to the $1/\mu^{1/2}$ dependence. Therefore, we expect that neutrinos emitted within the ignition radius will be equally distributed among both flavors in about few microseconds. Once the neutrinos reach this maximally mixed state, no further changes are expected. We emphasize that kinematic decoherence does not mean quantum decoherence. Figures 6 and 7 clearly show the typical oscillation pattern which happens only if quantum coherence is still acting on the neutrino system. Kinematic decoherence, differently to quantum decoherence, is just the result of averaging over the neutrino intensities resulting from quick flavor conversion. Therefore, neutrinos are yet able to quantum oscillate if appropriate conditions are satisfied.

Simple inspection of Equations (70) and (76) with Figure 4 yields $t_{osc} \ll t_Q$. Clearly the equipartition time is dominated by kinematic decoherence. These two effects are independent of the neutrino mass hierarchy, and neutrino flavor equipartitioning is achieved for both hierarchies. Within the disk dynamic, this is equivalent to imposing the condition $\langle P_{\nu_e \rightarrow \nu_e} \rangle = \langle P_{\bar{\nu}_e \rightarrow \bar{\nu}_e} \rangle = 0.5$.

Figure 8 shows a comparison between disks with and without neutrino flavor equipartition for the three accretion rates considered. The roles of an equipartition are to increase the disk’s density, reduce the temperature and electron fraction and further stabilize the electron degeneracy for regions inside the ignition radius. The effect is mild for low accretion rates and very pronounced for high accretion rates. This result is in agreement with our understanding of the dynamics of the disk and can be explained in the following way. In low accretion systems the neutrino optical depth for all flavors is $\tau_{\nu\bar{\nu}} \lesssim 1$, and the differences between the cooling fluxes, as given by Equation (32) are small. Hence, when the initial (mainly electron flavor) is redistributed among both flavors, the total neutrino cooling remains virtually unchanged and the disk evolves as if equipartition had never occurred save the new emission flavor content. On the other hand, when accretion rates are high, the optical depth obeys $\tau_{\nu_x} \approx \tau_{\bar{\nu}_x} \lesssim \tau_{\bar{\nu}_e} < \tau_{\nu_e} \sim 10^3$. The ν_e cooling is heavily suppressed—the other factors, less so. When flavors are redistributed, the new ν_x particles are free to escape, enhancing the total cooling and reducing the temperature. As

the temperature decreases, so do the electron and positron densities, leading to a lower electron fraction. The net impact of a flavor equipartition is to make the disk evolution less sensitive to ν_e opacity, and thus, increase the total cooling efficiency. As a consequence, once the fluid reaches a balance between F^+ and F_ν , this state is kept without being affected by high optical depths and η_{e^-} stays at a constant value until the fluid reaches the zero torque condition close to r_{in} . Note that for every case, inside the ignition radius, we find $\tau_{\nu_x} \approx \tau_{\bar{\nu}_x} \lesssim \tau_{\bar{\nu}_e} < \tau_{\nu_e}$ so that the equipartition enhances, mainly, neutrino cooling F_ν (and not antineutrino cooling $F_{\bar{\nu}}$). The quotient between neutrino cooling with and without an equipartition can be estimated with

$$\frac{F_\nu^{\text{eq}}}{F_\nu} \approx \frac{1}{2} \left(1 + \frac{\langle E_{\nu_x} \rangle}{\langle E_{\nu_e} \rangle} \frac{1 + \tau_{\nu_e}}{1 + \tau_{\nu_x}} \right). \quad (77)$$

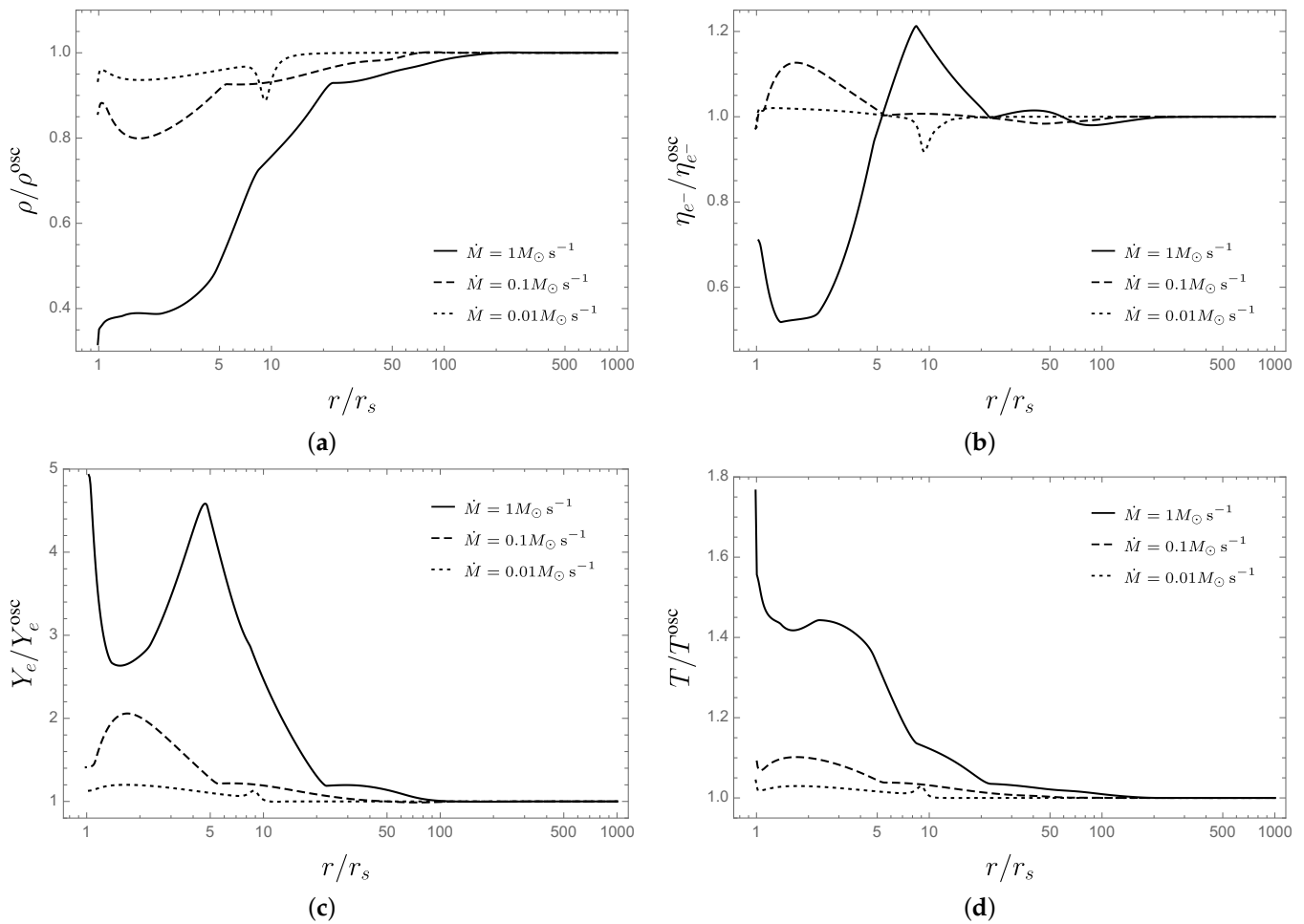


Figure 8. Comparison between the main variables describing thin disks with and without a neutrino flavor equipartition for each accretion rate considered. Here ρ^{osc} , $\eta_{e^-}^{\text{osc}}$, Y_e^{osc} , T^{osc} are the density, electron degeneracy, electron fraction and temperature of a disk with a flavor equipartition. Together with Figure 3, these plots completely describe the profile of a disk under a flavor equipartition. (a) The ratio between baryon densities. (b) The ratio between degeneracy parameters. (c) The ratio between electron fractions. (d) The ratio between temperatures.

This relation exhibits the right limits. From Figure 3 we see that $\langle E_{\nu_e} \rangle \approx \langle E_{\nu_x} \rangle$. Hence, If $1 \gg \tau_{\nu_e} > \tau_{\nu_x}$, then $F_\nu^{\text{eq}} = F_\nu$ and the equipartition is unnoticeable. However, if $1 < \tau_{\nu_x} < \tau_{\nu_e}$ then $F_\nu^{\text{eq}}/F_\nu > 1$. In our simulations, this fraction reaches values of 1.9 for $\dot{M} = 1M_\odot \text{ s}^{-1}$ to 2.5 for $\dot{M} = 0.01M_\odot \text{ s}^{-1}$.

The disk variables at each point do not change beyond a factor of order five in the most obvious case. However, these changes can be important for cumulative quantities,

e.g., the total neutrino luminosity and the total energy deposition rate into electron–positron pairs due to neutrino antineutrino annihilation. To see this we perform a Newtonian calculation of these luminosities following [99,100,112,155–158], and references therein. The neutrino luminosity is calculated by integrating the neutrino cooling flux throughout both faces of the disk:

$$L_{\nu_i} = 4\pi \int_{r_{\text{in}}}^{r_{\text{out}}} C_{\text{cap}} F_{\nu_i} r dr. \tag{78}$$

The factor $0 < C_{\text{cap}} < 1$ is a function of the radius (called capture function in [126]) that accounts for the proportion of neutrinos that are re-captured by the BH, and thus, do not contribute to the total luminosity. For a BH with $M = 3M_{\odot}$ and $a = 0.95$, the numerical value of the capture function as a function of the dimensionless distance $x = r/r_s$ is well fitted by

$$C_{\text{cap}}(x) = \left(1 + \frac{0.3348}{x^{3/2}}\right)^{-1}, \tag{79}$$

with a relative error smaller than 0.02%. To calculate the energy deposition rate, the disk is modeled as a grid of cells in the equatorial plane. Each cell k has a specific value of differential neutrino luminosity $\Delta \ell_{\nu_i}^k = F_{\nu_i}^k r_k \Delta r_k \Delta \phi_k$ and average neutrino energy $\langle E_{\nu_i} \rangle^k$. If a neutrino of flavor i is emitted from the cell k and an antineutrino is emitted from the cell k' , and before interacting at a point \mathbf{r} above the disk, each travels a distance r_k and $r_{k'}$, then their contribution to the energy deposition rate at \mathbf{r} is (see Appendix D.3 for details)

$$\begin{aligned} \Delta Q_{\nu_i \bar{\nu}_i k k'} &= A_{1,i} \frac{\Delta \ell_{\nu_i}^k}{r_k^2} \frac{\Delta \ell_{\bar{\nu}_i}^{k'}}{r_{k'}^2} \left(\langle E_{\nu_i} \rangle^k + \langle E_{\bar{\nu}_i} \rangle^{k'} \right) \left(1 - \frac{\mathbf{r}_k \cdot \mathbf{r}_{k'}}{r_k r_{k'}} \right)^2 \\ &+ A_{2,i} \frac{\Delta \ell_{\nu_i}^k}{r_k^2} \frac{\Delta \ell_{\bar{\nu}_i}^{k'}}{r_{k'}^2} \left(\frac{\langle E_{\nu_i} \rangle^k + \langle E_{\bar{\nu}_i} \rangle^{k'}}{\langle E_{\nu_i} \rangle^k \langle E_{\bar{\nu}_i} \rangle^{k'}} \right) \left(1 - \frac{\mathbf{r}_k \cdot \mathbf{r}_{k'}}{r_k r_{k'}} \right). \end{aligned} \tag{80}$$

The total neutrino annihilation luminosity is the sum over all pairs of cells integrated in space

$$L_{\nu_i \bar{\nu}_i} = 4\pi \int_{\mathcal{A}} \sum_{k,k'} \Delta Q_{\nu_i \bar{\nu}_i k k'} d^3 \mathbf{r}, \tag{81}$$

where \mathcal{A} is the entire space above (or below) the disk.

In Table 3 we show the neutrino luminosities and the neutrino annihilation luminosities for disks with and without neutrino collective effects. In each case, the flavor equipartition induces a loss in L_{ν_e} by a factor of ~ 3 , and a loss in $L_{\bar{\nu}_e}$ luminosity by a factor of ~ 2 . At the same time, L_{ν_x} and $L_{\bar{\nu}_e}$ are increased by a factor ~ 10 . This translates into a reduction of the energy deposition rate due to electron neutrino annihilation by a factor of ~ 7 , while the energy deposition rate due to non-electronic neutrinos goes from being negligible to be of the same order of the electronic energy deposition rate. The net effect is to reduce the total energy deposition rate of neutrino annihilation by a factor of ~ 3 – 5 for the accretion rates considered. In particular, we obtain factors of 3.03 and 3.66 for $\dot{M} = 1 M_{\odot} \text{ s}^{-1}$ and $\dot{M} = 0.01 M_{\odot} \text{ s}^{-1}$, respectively, and a factor of 4.73 for $\dot{M} = 0.1 M_{\odot} \text{ s}^{-1}$. The highest value corresponds to an intermediate value of the accretion rate because, for this case, there is a ν_e cooling suppression ($\tau_{\nu_e} > 1$) and the quotient $\tau_{\nu_e} / \tau_{\nu_x}$ is maximal. By Equation (77), the difference between the respective cooling terms is also maximal. In Figure 9 we show the energy deposition rate per unit volume around the BH for each flavor with accretion rates $\dot{M} = 1 M_{\odot} \text{ s}^{-1}$ and $\dot{M} = 0.1 M_{\odot} \text{ s}^{-1}$. There we can see the drastic enhancement of the non-electronic neutrino energy deposition rate and the reduction of the electronic deposition rate. Due to the double peak in the neutrino density for $\dot{M} = 0.01 M_{\odot} \text{ s}^{-1}$ case (see Figure 3), the deposition rate per unit volume also shows two peaks—one at $r_s < r < 2r_s$ and the other at $10r_s < r < 11r_s$. Even so, the behavior is similar to the other cases.

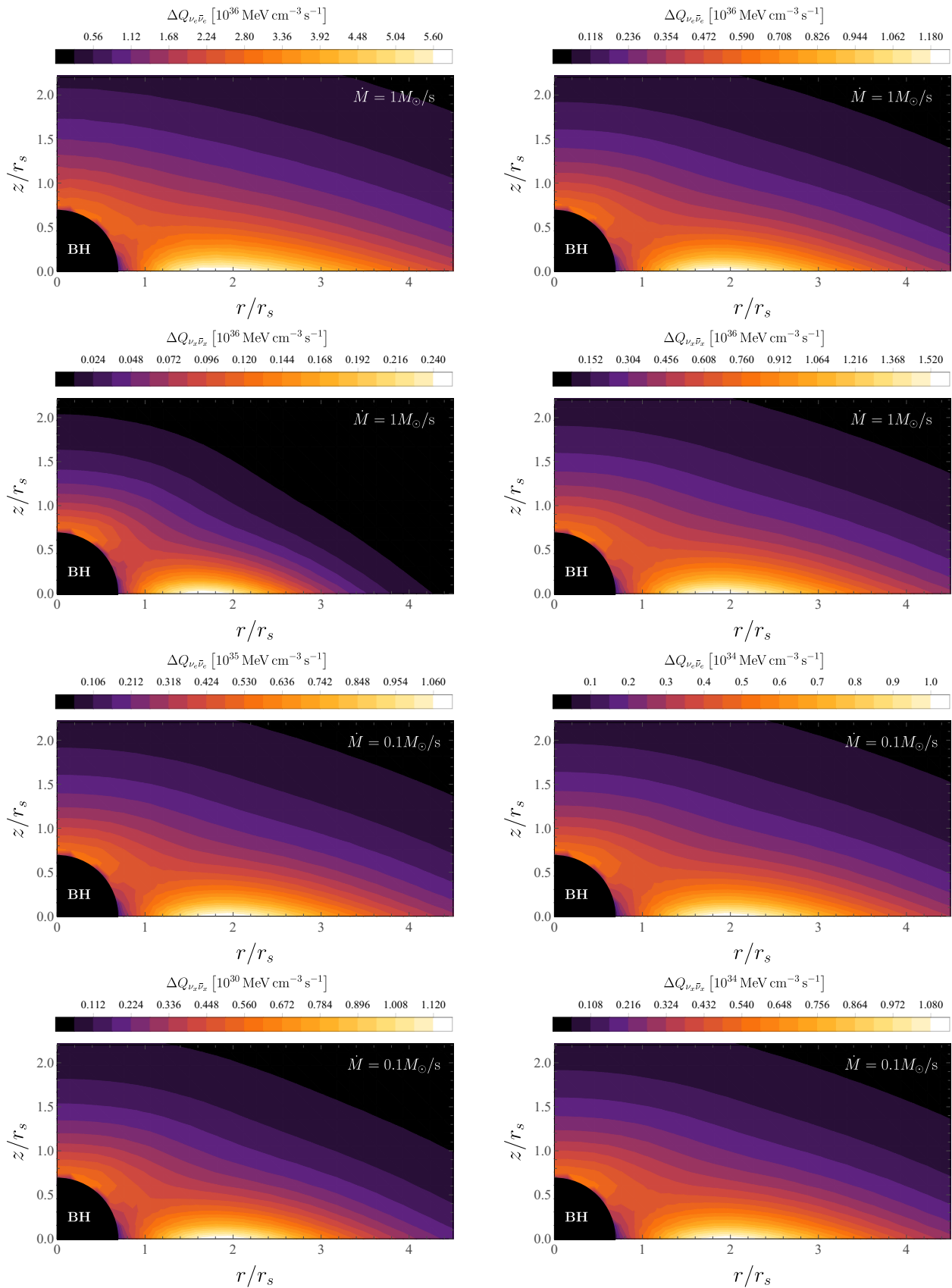


Figure 9. Comparison of the neutrino annihilation luminosity per unit volume $\Delta Q_{\nu_i \bar{\nu}_i} = \sum_{k,k'} \Delta Q_{\nu_i \bar{\nu}_i k k'}$ between disk without (left column) and with (right column) flavor equipartitioning for accretion rates $\dot{M} = 1 M_\odot \text{ s}^{-1}$ and $\dot{M} = 0.01 M_\odot \text{ s}^{-1}$.

Table 3. Comparison of total neutrino luminosities L_ν and annihilation luminosities $L_{\nu\bar{\nu}}$ between disks with and without flavor equipartitions. All luminosities are reported in MeV s^{-1} .

	Without Oscillations						With Oscillations (Flavor Equipartition)					
	$L_{\bar{\nu}_e}$	L_{ν_e}	$L_{\bar{\nu}_x}$	L_{ν_x}	$L_{\nu_e\bar{\nu}_e}$	$L_{\nu_x\bar{\nu}_x}$	$L_{\bar{\nu}_e}$	L_{ν_e}	$L_{\bar{\nu}_x}$	L_{ν_x}	$L_{\nu_e\bar{\nu}_e}$	$L_{\nu_x\bar{\nu}_x}$
$1 M_\odot \text{ s}^{-1}$	6.46×10^{58}	7.33×10^{58}	1.17×10^{58}	1.17×10^{58}	1.25×10^{57}	1.05×10^{55}	1.87×10^{58}	4.37×10^{58}	7.55×10^{58}	5.44×10^{58}	1.85×10^{56}	2.31×10^{56}
$0.1 M_\odot \text{ s}^{-1}$	9.19×10^{57}	1.08×10^{58}	8.06×10^{55}	8.06×10^{55}	1.62×10^{55}	1.27×10^{50}	2.47×10^{57}	4.89×10^{57}	7.75×10^{57}	5.27×10^{57}	1.78×10^{54}	1.64×10^{54}
$0.01 M_\odot \text{ s}^{-1}$	1.05×10^{57}	1.12×10^{57}	2.43×10^{55}	2.43×10^{55}	1.78×10^{53}	8.68×10^{48}	4.29×10^{56}	5.48×10^{56}	6.71×10^{56}	5.70×10^{56}	3.53×10^{52}	1.23×10^{52}

6. Discussion

The generation of a seed, energetic e^-e^+ plasma, seems to be a general prerequisite of GRB theoretical models for the explanation of the prompt (MeV) gamma-ray emission. The e^-e^+ pair annihilation produces photons leading to an opaque pair-photon plasma that self-accelerates, expanding to ultrarelativistic Lorentz factors in the order of 10^2 – 10^3 (see, e.g., [159–161]). The reaching of transparency of MeV-photons at large Lorentz factor and corresponding large radii is requested to solve the so-called compactness problem posed by the observed non-thermal spectrum in the prompt emission [162–164]. There is a vast literature on this subject, and we refer the reader to [165–170] and references therein for further details.

Neutrino-cooled accretion disks onto rotating BHs have been proposed as a possible way of producing the above-mentioned e^-e^+ plasma. The reason is that such disks emit a large amount of neutrino and antineutrinos that can undergo pair annihilation near the BH [100–112]. The viability of this scenario clearly depends on the energy deposition rate of neutrino-antineutrinos into e^-e^+ and so on the local (anti)neutrino density and energy.

We have here shown that, inside these hyperaccreting disks, a rich neutrino oscillation phenomenology is present due to the high neutrino density. Consequently, the neutrino/antineutrino emission and the corresponding pair annihilation process around the BH leading to electron-positron pairs, are affected by neutrino flavor conversion. Using the thin disk and α -viscosity approximations, we have built a simple stationary model of general relativistic neutrino-cooled accretion disks around a Kerr BH that takes into account not only a wide range of neutrino emission processes and nucleosynthesis, but also the dynamics of flavor oscillations. The main assumption relies on considering the neutrino oscillation behavior within small neighboring regions of the disk as independent from each other. This, albeit being a first approximation to a more detailed picture, has allowed us to set the main framework to analyze the neutrino oscillations phenomenology in inside neutrino-cooled disks.

In the absence of oscillations, a variety of neutrino-cooled accretion disks onto Kerr BHs, without neutrino flavor oscillations, have been modeled in the literature (see, e.g., [99,100,107,112,124] for a recent review). The physical setting of our disk model follows closely the ones considered in [107], but with some extensions and differences in some aspects:

1. The equation of vertical hydrostatic equilibrium, Equation (15), can be derived in several ways [124,127,131]. We followed a particular approach consistent with the assumptions in [127], in which we took the vertical average of a hydrostatic Euler equation in polar coordinates. The result is an equation that leads to smaller values of the disk pressure when compared with other models. It is expected that the pressure at the center of the disk is smaller than the average density multiplied by the local tidal acceleration at the equatorial plane. Still, the choice between the assortment of pressure relations is tantamount to the fine-tuning of the model. Within the thin disk approximation, all these approaches are equivalent, since they all assume vertical equilibrium and neglect self-gravity.
2. Following the BdHN scenario for the explanation of GRBs associated with Type Ic SNe (see Section 2), we considered a gas composed of ^{16}O at the outermost radius of the disk and followed the evolution of the ion content using the Saha equation to fix the local NSE. In [107], only ^4He is present, and in [112], ions up to ^{56}Fe are introduced.

The affinity between these cases implies that this particular model of disk accretion is insensible to the initial mass fraction distribution. This is explained by the fact that the average binding energy for most ions is very similar; hence, any cooling or heating due to a redistribution of nucleons, given by the NSE, is negligible when compared to the energy consumed by direct photodisintegration of alpha particles. Additionally, once most ions are dissociated, the main cooling mechanism is neutrino emission, which is similar for all models; the modulo includes the supplementary neutrino emission processes included in addition to electron and positron capture. However, during our numerical calculations, we noticed that the inclusion of non-electron neutrino emission processes can reduce the electron fraction by up to $\sim 8\%$. This effect was observed again during the simulation of flavor equipartition alluding to the need for detailed calculations of neutrino emissivities when establishing NSE state. We obtained similar results to [107] (see Figure 3), but by varying the accretion rate and fixing the viscosity parameter. This suggests that a more natural differentiating set of variables in the hydrodynamic equations of an α -viscosity disk is the combination of the quotient \dot{M}/α and either \dot{M} or α . This result is already evident in, for example, Figures 11 and 12 of [107], but was not mentioned there.

Concerning neutrino oscillations, we showed that for the conditions inside the ignition radius, the oscillation potentials follow the relation $\langle \omega \rangle \ll \mu \ll \lambda$, as is illustrated by Figure 5. We also showed that within this region the number densities of electron neutrinos and antineutrinos are very similar. As a consequence of this particular environment, very fast pair conversions $\nu_e \bar{\nu}_e \rightleftharpoons \nu_x \bar{\nu}_x$, induced by bipolar oscillations, are obtained for the inverted mass hierarchy case with oscillation frequencies between 10^9 s^{-1} and 10^5 s^{-1} . For the normal hierarchy case, no flavor changes were observed (see Figures 6 and 7). Bearing in mind the magnitudes of these frequencies and the low neutrino travel times through the disk, we conclude that an accretion disk under our main assumption cannot represent a steady-state. However, using numerical and algebraic results obtained in [33,35,36] and references therein, we were able to generalize our model to a more realistic picture of neutrino oscillations. The main consequence of the interactions between neighboring regions of the disk is the onset of kinematic decoherence in a timescale in the order of the oscillation times. Kinematic decoherence induces a fast flavor equipartition among electronic and non-electronic neutrinos throughout the disk. Therefore, the neutrino content emerging from the disk is very different from the one that is usually assumed (see, e.g., [113,117,171]). The comparison between disks with and without flavor equipartition is summarized in Figure 8 and Table 3. We found that the flavor equipartition, while leaving antineutrino cooling practically unchanged, it enhances neutrino cooling by allowing the energy contained (and partially trapped inside the disk due to high opacity) within the ν_e gas to escape in the form of ν_x , rendering the disk insensible to the electron neutrino opacity. We give in Equation (77) a relation to estimate the change in F_ν as a function of $\tau_{\nu_e} \tau_{\nu_x}$ that describes correctly the behavior of the disk under the flavor equipartition. The variation of the flavor content in the emission flux implies a loss in L_{ν_e} and an increase in L_{ν_x} and $L_{\bar{\nu}_e}$. As a consequence, the total energy deposition rate of the process $\nu + \bar{\nu} \rightarrow e^- + e^+$ is reduced. We showed that this reduction can be as high 80% and is maximal whenever the quotient $\tau_{\nu_e} / \tau_{\nu_x}$ is also maximal and the condition $\tau_{\nu_e} > 1$ is obtained.

At this point, we can identify several issues which must still to be investigated in view of the results we have presented:

First, throughout the accretion disk literature, several fits of the neutrino and neutrino annihilation luminosity can be found (see, e.g., [99] and references therein). However, all these fits were calculated without taking into account neutrino oscillations. Since we have shown that oscillations directly impact luminosity, these results need to be extended.

Second, the calculations of the neutrino and antineutrino annihilation luminosities we have performed ignore general relativistic effects, save for the correction given by the capture function, and the possible neutrino oscillations from the disk surface to the

annihilation point. In [172], it has been shown that general relativistic effects can enhance the neutrino annihilation luminosity in a neutron star binary merger by a factor of 10. In [100], however, it is argued that in BHs this effect has to be mild since the energy gained by falling into the gravitational potential is lost by the electron–positron pairs when they climb back up. Nonetheless, this argument ignores the bending of neutrino trajectories and neutrino capture by the BH which can be significant for $r \lesssim 10r_s$. In [173], the increment is calculated to be no more than a factor of 2 and can be less depending on the geometry of the emitting surface. However, as before, these calculations assume a purely $\nu_e\bar{\nu}_e$ emission and ignore oscillations after the emission. Simultaneously, the literature on neutrino oscillation above accretion disks (see, e.g., [113,117]) does not take into account oscillations inside the disk and assume only $\nu_e\bar{\nu}_e$ emission. A similar situation occurs in works studying the effect of neutrino emission on r-process nucleosynthesis in hot outflows (wind) ejected from the disk (see, e.g., [174]).

It is still unclear how the complete picture (oscillations inside the disk \rightarrow oscillations above the disk + relativistic effects) affects the final energy deposition. We are currently working on the numerical calculation of the annihilation energy deposition rate using a ray tracing code and including neutrino oscillations from the point of their creation until they are annihilated—i.e., within the accretion disk and after its emission from the surface of the disk and during its trajectory until reaching the annihilation point. These results and their consequences for the energy deposition annihilation rate will be the subject of a future publication.

The knowledge of the final behavior of a neutrino-dominated accretion disk with neutrino oscillations requires time-dependent, multi-dimensional, neutrino-transport simulations coupled with the evolution of the disk. These simulations are computationally costly even for systems with a high degree of symmetry, therefore a first approximation is needed to identify key theoretical and numerical features involved in the study of neutrino oscillations in neutrino-cooled accretion disks. This work serves as a platform for such a first approximation. Considering that kinematic decoherence is a general feature of anisotropic neutrino gases, with the simplified model presented here, we were able to obtain an analytical result that agrees with the physics understanding of accretion disks.

In [171] it is pointed out that for a total energy in $\bar{\nu}_e$ of 10^{52} erg and an average neutrino energy $\langle E_{\nu,\bar{\nu}} \rangle \sim 20$ MeV, the Hyper-Kamiokande neutrino-horizon is in the order of 1 Mpc. If we take a total energy carried out by $\bar{\nu}_e$ in the order of the gravitational gain by accretion ($E_g \sim 10^{52}$ – 10^{53} erg) in the more energetic case of binary-driven hypernovae and the neutrino energies in Figure 3, we should expect the neutrino-horizon distance to be also in the order of 1 Mpc. However, if we adopt the local binary-driven hypernovae rate $\sim 1 \text{ Gpc}^{-3} \text{ yr}^{-1}$ [175], it is clear that the direct detection of this neutrino signal is quite unlikely. However, we have shown that neutrino oscillation can have an effect on e^-e^+ plasma production above BHs in GRB models. Additionally, the unique conditions inside the disk and its geometry lend themselves to a variety of neutrino oscillations that can have impacts on other astrophysical phenomena, not only in plasma production, but also in r-process nucleosynthesis in disk winds. This, in particular, is the subject of a future publication. As such, this topic deserves appropriate attention, since it paves the way for new, additional astrophysical scenarios for testing neutrino physics.

Author Contributions: Conceptualization, J.D.U., E.A.B.-V. and J.A.R.; methodology, J.D.U., E.A.B.-V. and J.A.R.; software, J.D.U., E.A.B.-V. and J.A.R.; validation, J.D.U., E.A.B.-V. and J.A.R.; formal analysis, J.D.U., E.A.B.-V. and J.A.R.; investigation, J.D.U., E.A.B.-V. and J.A.R.; resources, J.D.U., E.A.B.-V. and J.A.R.; data curation, J.D.U., E.A.B.-V. and J.A.R.; writing—original draft preparation, J.D.U., E.A.B.-V. and J.A.R.; writing—review and editing, J.D.U., E.A.B.-V. and J.A.R.; visualization, J.D.U., E.A.B.-V. and J.A.R.; supervision, J.D.U., E.A.B.-V. and J.A.R.; project administration, J.D.U., E.A.B.-V. and J.A.R.; funding acquisition, J.D.U., E.A.B.-V. and J.A.R. All authors have read and agreed to the published version of the manuscript.

Funding: J.D.U. was supported by COLCIENCIAS under the program Becas Doctorados en el Exterior Convocatoria No. 728. E.A.B.-V. was supported from COLCIENCIAS under the program

Becas Doctorados Nacionales Convocatoria, number 727, the International Center for Relativistic Astrophysics Network (ICRANet), Universidad Industrial de Santander (UIS) and the International Relativistic Astrophysics Ph.D Program (IRAP-PhD).

Acknowledgments: The authors thank C. L. Fryer for insightful discussions on astrophysical consequences of neutrino flavor oscillations in accretion disks.

Conflicts of Interest: The authors declare no conflict of interest.

Abbreviations

The following abbreviations are used in this manuscript:

BdHN	Binary-Driven Hypernova
BH	Black Hole
CF	Coordinate Frame
CO _{core}	Carbon–Oxygen Star
CRF	Co-rotating Frame
GRB	Gamma-ray Burst
IGC	Induced Gravitational Collapse
ISCO	Innermost Stable Circular Orbit
LNRF	Locally Non-Rotating Frame
MSW	Mikheyev–Smirnov–Wolfenstein
NDAF	Neutrino-Dominated Accretion Flows
NS	Neutron Star
NSE	Nuclear Statistical Equilibrium
SN	Supernova

Appendix A. Transformations and Christoffel Symbols

For the sake of completeness, here we give the explicitly the transformation used in Equation (5) and the Christoffel symbols used during calculations. The coordinate transformation matrices between the CF and the LNRF on the tangent vector space is [123]

$$e_{\hat{\nu}}^{\mu} = \begin{pmatrix} \frac{1}{\sqrt{\omega^2 g_{\phi\phi} - g_{tt}}} & 0 & 0 & 0 \\ 0 & \frac{1}{\sqrt{g_{rr}}} & 0 & 0 \\ 0 & 0 & \frac{1}{\sqrt{g_{\theta\theta}}} & 0 \\ \frac{\omega}{\sqrt{\omega^2 g_{\phi\phi} - g_{tt}}} & 0 & 0 & \frac{1}{\sqrt{g_{\phi\phi}}} \end{pmatrix}, \quad e^{\hat{\nu}}_{\mu} = \begin{pmatrix} \sqrt{\omega^2 g_{\phi\phi} - g_{tt}} & 0 & 0 & 0 \\ 0 & \sqrt{g_{rr}} & 0 & 0 \\ 0 & 0 & \sqrt{g_{\theta\theta}} & 0 \\ -\omega \sqrt{g_{\phi\phi}} & 0 & 0 & \sqrt{g_{\phi\phi}} \end{pmatrix}, \quad (A1)$$

so that the basis vectors transform as $\partial_{\hat{\nu}} = e^{\mu}_{\hat{\nu}} \partial_{\mu}$, that is, with e^T . For clarity, coordinates on the LNRF have a caret ($x^{\hat{\mu}}$), coordinates on the CRF have a tilde ($x^{\tilde{\mu}}$) and coordinates on the LRF have two ($x^{\hat{\mu}}$). An observer on the LNRF sees the fluid elements move with an azimuthal velocity $\beta^{\hat{\phi}}$. This observer then can perform a Lorentz boost $L_{\beta^{\hat{\phi}}}$ to a new frame. On this new frame an observer sees the fluid elements falling radially with velocity $\beta^{\tilde{r}}$, so it can perform another Lorentz boost $L_{\beta^{\tilde{r}}}$ to the LRF. Finally, the transformation between the the LRF and the CF coordinates $x^{\mu} = e^{\mu}_{\hat{\rho}} (L_{\beta^{\hat{\phi}}})_{\tilde{\alpha}}^{\hat{\rho}} (L_{\beta^{\tilde{r}}})_{\tilde{\nu}}^{\tilde{\alpha}} x^{\tilde{\nu}} = A_{\tilde{\nu}}^{\mu} x^{\tilde{\nu}}$, where the components of A are

$$A_{\tilde{\nu}}^{\mu} = \begin{pmatrix} \gamma_{\tilde{r}} \gamma_{\hat{\phi}} \left(\sqrt{\omega^2 g_{\phi\phi} - g_{tt}} + \beta^{\hat{\phi}} \omega \sqrt{g_{\phi\phi}} \right) & -\gamma_{\tilde{r}} \beta^{\tilde{r}} \sqrt{g_{rr}} & 0 & -\gamma_{\tilde{r}} \gamma_{\hat{\phi}} \beta^{\hat{\phi}} \sqrt{g_{\phi\phi}} \\ -\gamma_{\hat{\phi}} \gamma_{\tilde{r}} \beta^{\tilde{r}} \left(\sqrt{\omega^2 g_{\phi\phi} - g_{tt}} + \beta^{\hat{\phi}} \omega \sqrt{g_{\phi\phi}} \right) & \gamma_{\tilde{r}} \sqrt{g_{rr}} & 0 & \gamma_{\tilde{r}} \gamma_{\hat{\phi}} \beta^{\tilde{r}} \beta^{\hat{\phi}} \sqrt{g_{\phi\phi}} \\ 0 & 0 & \sqrt{g_{\theta\theta}} & 0 \\ -\gamma_{\hat{\phi}} \left(\beta^{\hat{\phi}} \sqrt{\omega^2 g_{\phi\phi} - g_{tt}} + \omega \sqrt{g_{\phi\phi}} \right) & 0 & 0 & \gamma_{\hat{\phi}} \sqrt{g_{\phi\phi}} \end{pmatrix}. \quad (A2)$$

Since Lorentz transformations do not commute, the transformation A raises the question: what happens if we invert the order? In this case, we would not consider a co-rotating frame but a cofalling frame on which observers see fluid elements, not falling, but rotating. The new transformation velocities $\beta^{r'}$, $\beta^{\phi'}$ are subject to the conditions $\beta^{\phi'} = \gamma_{r'} \beta^{\hat{\phi}}$,

$\beta^{r'} = \beta^{\tilde{r}} / \gamma_{\hat{\phi}}$ and $\gamma_{r'}\gamma_{\phi'} = \gamma_{\tilde{r}}\gamma_{\hat{\phi}}$. Although both approaches are valid, considering that the radial velocity is an unknown, the first approach is clearly cleaner. To obtain the coordinate transformation between the CF and the CRF $A_{\tilde{\nu}}^{\mu}$ and $A^{\tilde{\nu}}_{\mu}$ we can simply set $\beta^{\tilde{r}} = 0$ in Equation (A2). With this, we can calculate

$$\frac{d\hat{\phi}}{d\hat{t}} = \beta^{\hat{\phi}} = \frac{u^{\mu}e^{\hat{\phi}}_{\mu}}{u^{\nu}e^{\hat{t}}_{\nu}} = \sqrt{\frac{g_{\phi\phi}}{\omega^2g_{\phi\phi} - g_{tt}}}(\Omega - \omega), \tag{A3}$$

and

$$d\tilde{r} = \sqrt{g_{rr}}dr, \quad d\tilde{t} = \frac{\gamma_{\hat{\phi}}}{\sqrt{\omega^2g_{\phi\phi} - g_{tt}}}dt = \frac{1}{\sqrt{-g_{tt} - 2\Omega g_{t\phi} - \Omega^2g_{\phi\phi}}}dt, \quad d\tilde{\theta} = \sqrt{g_{\theta\theta}}d\theta. \tag{A4}$$

The non-vanishing Christoffel symbols are

$$\begin{aligned} \Gamma^t_{tr} &= \frac{M(r^2 - M^2a^2 \cos^2 \theta)(r^2 + M^2a^2)}{\Sigma^2\Delta}, \quad \Gamma^t_{t\theta} = -\frac{M^3a^2r \sin 2\theta}{\Sigma^2}, \\ \Gamma^t_{r\phi} &= -\frac{M^2a(3r^4 + M^2a^2r^2 + M^2a^2 \cos^2 \theta(r^2 - M^2a^2)) \sin^2 \theta}{\Sigma^2\Delta}, \\ \Gamma^t_{\theta\phi} &= \frac{2M^4a^3r \cos \theta \sin^3 \theta}{\Sigma^2}, \quad \Gamma^r_{tt} = \frac{M\Delta(r^2 - M^2a^2 \cos^2 \theta)}{\Sigma^3}, \\ \Gamma^r_{t\phi} &= -\frac{M^2a\Delta(r^2 - M^2a^2 \cos^2 \theta) \sin^2 \theta}{\Sigma^3}, \\ \Gamma^r_{rr} &= \frac{r}{\Sigma} + \frac{M-r}{\Delta}, \quad \Gamma^r_{r\theta} = -\frac{M^2a^2 \sin \theta}{M^2a^2 \cos \theta + r^2 \tan \theta}, \quad \Gamma^r_{\theta\theta} = -\frac{r\Delta}{\Sigma}, \\ \Gamma^r_{\phi\phi} &= (Ma\Gamma^r_{t\phi} - \Gamma^r_{\theta\theta}) \sin^2 \theta, \quad \Gamma^{\theta}_{tt} = -\Gamma^t_{\theta\phi} \frac{\csc^2 \theta}{Ma\Sigma}, \quad \Gamma^{\theta}_{t\phi} = \frac{M^2ar(r^2 + M^2a^2) \sin 2\theta}{\Sigma^3}, \\ \Gamma^{\theta}_{rr} &= \frac{M^2a^2 \sin \theta \cos \theta}{\Sigma\Delta}, \quad \Gamma^{\theta}_{t\theta} = \frac{r}{\Sigma}, \quad \Gamma^{\theta}_{\theta\theta} = \Gamma^r_{r\theta}, \\ \Gamma^{\theta}_{\phi\phi} &= \left(\frac{\Delta}{\Sigma} + \frac{2Mr(r^2 + M^2a^2)^2}{\Sigma^3} \right) \sin \theta \cos \theta, \quad \Gamma^{\phi}_{tr} = -\frac{M^2a(r^2 - M^2a^2 \cos^2 \theta)}{\Sigma^2\Delta}, \\ \Gamma^{\phi}_{t\theta} &= -\frac{2M^2ar \cot \theta}{\Sigma^2}, \quad \Gamma^{\phi}_{r\phi} = \frac{r(\Sigma - 2Mr)}{\Sigma\Delta} + \frac{Ma\Sigma}{\Delta^2}\Gamma^r_{t\phi}, \quad \Gamma^{\phi}_{\theta\phi} = \cot \theta - \Gamma^t_{t\theta}. \end{aligned} \tag{A5}$$

Using the connection coefficients and the metric, both evaluated at the equatorial plane we can collect several equations for averaged quantities. The expansion of the fluid world lines is

$$\theta = \nabla_{\mu}u^{\mu} = \frac{2}{r}u^r + \partial_r u^r. \tag{A6}$$

There are several ways to obtain an approximate version of the shear tensor (e.g., [124,176,177]) but by far the simplest one is proposed by [127]. On the CRF the fluid four-velocity can be approximated by $u^{\tilde{\mu}} = (1, 0, 0, 0)$ by Equation (6). Both the fluid four-acceleration $a_{\nu} = u^{\mu}\nabla_{\mu}u_{\nu}$ and expansion parameter, Equation (A6), vanish so that the shear tensor reduces to $2\sigma_{\tilde{\mu}\tilde{\nu}} = \nabla_{\tilde{\mu}}u_{\tilde{\nu}} + \nabla_{\tilde{\nu}}u_{\tilde{\mu}}$. In particular, the r - ϕ component is

$$\sigma_{\tilde{r}\tilde{\phi}} = -\frac{1}{2}(\Gamma^{\tilde{t}}_{\tilde{\phi}\tilde{r}} + \Gamma^{\tilde{t}}_{\tilde{r}\tilde{\phi}}) = -\frac{1}{4}(2c_{\tilde{t}\tilde{\phi}}^{\tilde{r}} + 2c_{\tilde{t}\tilde{r}}^{\tilde{\phi}}) = \frac{1}{2}c_{\tilde{r}\tilde{t}}^{\tilde{\phi}} = \frac{\gamma_{\hat{\phi}}^2}{2} \frac{\sqrt{g_{\phi\phi}}}{\sqrt{\omega^2g_{\phi\phi} - g_{tt}\sqrt{g_{rr}}}}\partial_r\Omega, \tag{A7}$$

where $c_{\tilde{\mu}\tilde{\nu}}^{\tilde{\alpha}}$ are the commutation coefficients for the CRF. Finally, of particular interest is the $\tilde{\theta}$ component of the Riemann curvature tensor

$$R^{\tilde{\theta}}_{\tilde{t}\tilde{\theta}\tilde{r}} \Big|_{\theta=\pi/2} = \frac{M}{r^3} \frac{r^2 - 4aM^{3/2}r^{1/2} + 3M^2a^2}{r^2 - 3Mr + 2aM^{3/2}r^{1/2}}, \tag{A8}$$

which gives a measurement of the relative acceleration in the $\tilde{\theta}$ direction of nearly equatorial geodesics.

Appendix B. Stress–Energy Tensor

Here we present some equations related to the stress–energy that we used in this paper. Equation (9) for a zero bulk viscosity fluid in components is

$$T^{\mu}_{\nu} = \Pi u^{\mu} u_{\nu} + P \delta^{\mu}_{\nu} - 2\eta \sigma^{\mu}_{\nu} + q^{\mu} u_{\nu} + q_{\nu} u^{\mu}, \tag{A9}$$

whose (vanishing) covariant derivative is

$$\begin{aligned} \nabla_{\mu} T^{\mu}_{\nu} &= u^{\mu} u_{\nu} \partial_{\mu} \Pi + \Pi \theta u_{\nu} + \Pi a_{\nu} + \partial_{\nu} P - 2\eta \nabla_{\mu} \sigma^{\mu}_{\nu} + q^{\mu} \nabla_{\mu} u_{\nu} + u_{\nu} \nabla_{\mu} q^{\mu} + q_{\nu} \theta + u^{\mu} \nabla_{\mu} q_{\nu} \\ &= u^{\mu} \left[u_{\nu} \left(\partial_{\mu} \Pi - \frac{\Pi}{\rho} \partial_{\mu} \rho \right) - \frac{q_{\nu}}{\rho} \partial_{\mu} \rho \right] + \Pi a_{\nu} + \partial_{\nu} P - 2\eta \nabla_{\mu} \sigma^{\mu}_{\nu} + q^{\mu} \nabla_{\mu} u_{\nu} + u_{\nu} \nabla_{\mu} q^{\mu} + u^{\mu} \nabla_{\mu} q_{\nu}, \end{aligned} \tag{A10}$$

where baryon conservation is used $\rho \theta = -u^{\mu} \partial_{\mu} \rho$. To get an equation of motion for the fluid, we project along the direction perpendicular to u_{ν}

$$\begin{aligned} P^{\nu}_{\beta} \nabla_{\mu} T^{\mu}_{\nu} &= u^{\mu} \left[u_{\beta} \left(\partial_{\mu} \Pi - \frac{\Pi}{\rho} \partial_{\mu} \rho \right) - \frac{q_{\beta}}{\rho} \partial_{\mu} \rho \right] + \Pi a_{\beta} + \partial_{\beta} P - 2\eta \nabla_{\mu} \sigma^{\mu}_{\beta} + q^{\mu} \nabla_{\mu} u_{\beta} + u_{\beta} \nabla_{\mu} q^{\mu} \\ &+ u^{\mu} \nabla_{\mu} q_{\beta} - u^{\mu} u_{\beta} \left[\partial_{\mu} \Pi - \frac{\Pi}{\rho} \partial_{\mu} \rho \right] + u^{\nu} u_{\beta} \partial_{\nu} P - 2\eta u^{\nu} u_{\beta} \nabla_{\nu} \sigma^{\mu}_{\mu} - u_{\beta} \nabla_{\mu} q^{\mu} + u^{\nu} u_{\beta} u^{\mu} \nabla_{\mu} q_{\nu} \\ &= -\frac{q_{\beta}}{\rho} u^{\mu} \partial_{\mu} \rho + \Pi a_{\beta} + \partial_{\beta} P - 2\eta \nabla_{\mu} \sigma^{\mu}_{\beta} + q^{\mu} \nabla_{\mu} u_{\beta} + u^{\mu} \nabla_{\mu} q_{\beta} + u_{\beta} u^{\nu} \partial_{\nu} P - 2\eta u^{\nu} u_{\beta} \nabla_{\nu} \sigma^{\mu}_{\mu} + u^{\nu} u_{\beta} u^{\mu} \nabla_{\mu} q_{\nu} \\ &= -\frac{q_{\beta}}{\rho} u^{\mu} \partial_{\mu} \rho + \Pi a_{\beta} + \partial_{\beta} P - 2\eta \nabla_{\mu} \sigma^{\mu}_{\beta} + q^{\mu} \nabla_{\mu} u_{\beta} + u^{\mu} \nabla_{\mu} q_{\beta} + u_{\beta} (u^{\nu} \partial_{\nu} P + 2\eta \sigma^{\mu\nu} \sigma_{\mu\nu} - q_{\nu} a^{\nu}), \end{aligned} \tag{A11}$$

where the identities $q_{\mu} u^{\mu} = u^{\mu} a_{\mu} = \sigma^{\mu\nu} u_{\nu} = 0$, $u_{\mu} u^{\nu} = -1$, $\sigma^{\mu\nu} \sigma_{\mu\nu} = \sigma^{\mu\nu} \nabla_{\mu} u_{\nu}$ are used. Combining the Equations (A10) and (A11) we get

$$u^{\mu} \left[\partial_{\mu} U - \frac{U + P}{\rho} \partial_{\mu} \rho \right] = 2\eta \sigma^{\mu\nu} \sigma_{\mu\nu} - q_{\mu} a^{\mu} - \nabla_{\mu} q^{\mu}. \tag{A12}$$

With Equation (A6) we can obtain an equation for mass conservation

$$\begin{aligned} 0 &= \nabla_{\mu} (\rho u^{\mu}) = u^{\mu} \partial_{\mu} \rho + \rho \theta = u^{\mu} \partial_{\mu} \rho + \rho \left(\frac{2}{r} u^r + \partial_r u^r \right), \\ &\Rightarrow \partial_r (r^2 \rho u^r) + r^2 u^j \partial_j \rho = 0, \text{ for } j \in \{t, \theta, \phi\}. \end{aligned} \tag{A13}$$

Finally, we reproduce the zero torque at the innermost stable circular orbit condition that appears in [128]. Using the killing vector fields ∂_{ϕ} , ∂_t and the approximation $\Pi \approx \rho$, we can calculate

$$\begin{aligned} 0 &= \nabla \cdot (T \cdot \partial_{\phi}) = \nabla_{\mu} T^{\mu}_{\phi} = \frac{1}{\sqrt{-g}} \partial_{\mu} (\sqrt{-g} T^{\mu}_{\phi}) \approx \frac{1}{r^2} \partial_r (\rho u^r u_{\phi} r^2 - 2\eta \sigma^r_{\phi} r^2) + u_{\phi} \partial_{\theta} q^{\theta}, \\ &\Rightarrow \partial_r (\rho u^r u_{\phi} r^2 - 2\eta \sigma^r_{\phi} r^2) = -r^2 u_{\phi} \partial_{\theta} q^{\theta}, \\ &\Rightarrow \partial_r \left(\frac{\dot{M}}{2\pi} u_{\phi} + 4r H \eta \sigma^r_{\phi} \right) = 2H u_{\phi} \epsilon, \end{aligned} \tag{A14}$$

where we integrated vertically and used Equation (16). Analogously, using Equation (11) we obtain

$$\partial_r \left(\frac{\dot{M}}{2\pi} u_t - 4r H \Omega \eta \sigma^r_{\phi} \right) = 2H u_t \epsilon. \tag{A15}$$

The vertical integration of the divergence of the heat flux is as follows: Since, on average, $q = q^\theta \partial_\theta$, we have $\nabla_\mu q^\mu = \partial_\theta q^\theta$ and by Equation (A2), $q^\theta = r q^{\tilde{\theta}}$. Vertically integrating yields

$$\int_{\theta_{\min}}^{\theta_{\max}} \partial_\theta q^\theta r d\theta = r q^\theta \Big|_{\theta_{\min}}^{\theta_{\max}} = 2q^{\tilde{\theta}} = 2H\epsilon, \tag{A16}$$

where $q^{\tilde{\theta}}$ is the averaged energy flux radiating out of a face of the disk, as measured by an observer on the LRF, which we approximate as the half-thickness of the disk H times the average energy density per unit proper time ϵ lost by the disk. With the variable change $z = 8\pi r H \eta \sigma_\phi^r / \dot{M}$ and $y = 4\pi H \epsilon / \dot{M}$ the equations reduce to

$$\partial_r (u_\phi + z) = y u_\phi, \tag{A17a}$$

$$\partial_r (u_t - \Omega z) = y u_t. \tag{A17b}$$

Using the relation $\partial_r u_t = -\Omega \partial_r u_\phi$ (see Equation (10.7.29) in [178]) and $\partial_r (u_t + \Omega u_\phi) = u_\phi \partial_r \Omega$ we can combine the previous equations to obtain

$$z = -\frac{y(u_t + \Omega u_\phi)}{\partial_r \Omega}, \tag{A18a}$$

$$\partial_r (AB^2) = B \partial_r u_\phi, \tag{A18b}$$

with $A = y/\partial_r \Omega$ and $B = u_t + \Omega u_\phi$. To integrate these equations we use the zero torque condition $z(r = r^*) = 0$ where r^* is the radius of the innermost stable circular orbit, which gives the relation

$$y = \frac{\partial_r \Omega}{(u_t + \Omega u_\phi)^2} \int_{r^*}^r (u_t + \Omega u_\phi) \partial_r u_\phi dr = \frac{\partial_r \Omega}{(u_t + \Omega u_\phi)^2} \left(u_t u_\phi \Big|_{r^*}^r - 2 \int_{r^*}^r u_\phi \partial_r u_t dr \right), \tag{A19}$$

or, equivalently,

$$8\pi H r \rho v_{\text{turb}} \sigma_\phi^r \approx 8\pi H r \Pi v_{\text{turb}} \sigma_\phi^r = -\frac{\dot{M}}{(u_t + \Omega u_\phi)} \left(u_t u_\phi \Big|_{r^*}^r - 2 \int_{r^*}^r u_\phi \partial_r u_t dr \right). \tag{A20}$$

Using Equation (5), the approximation $\gamma_{\tilde{r}} \approx 1$ and the variable change $r = xM^2$ the integral can be easily evaluated by partial fractions

$$8\pi H r \rho v_{\text{turb}} \sigma_\phi^r = \dot{M} M f(x, x^*), \tag{A21a}$$

$$f(x, x^*) = \frac{x^3 + a}{x^{3/2} \sqrt{x^3 - 3x + 2a}} \left[x - x^* - \frac{3}{2} a \ln\left(\frac{x}{x^*}\right) + \frac{1}{2} \sum_{i=1}^3 \frac{ax_i^2 - 2x_i + a}{x_i^2 - 1} \ln\left(\frac{x - x_i}{x^* - x_i}\right) \right], \tag{A21b}$$

where x_1, x_2, x_3 are the roots of the polynomial $x^3 - 3x + 2a$.

Appendix C. Nuclear Statistical Equilibrium

The results in this section appear in [179]. We include them here since they are necessary to solve Equation (19). Neutrino dominated accretion disks reach densities above $\sim 10^7 \text{ g cm}^{-3}$ and temperatures above $\sim 5 \times 10^9 \text{ K}$. For these temperatures, forward and reverse nuclear reactions are balanced and the abundances in the plasma are determined by the condition $\mu_i = Z_i \mu_p + N_i \mu_n$, that is, the Nuclear Statistical Equilibrium. However, for densities above 10^6 g cm^{-3} , the electron screening of charged particle reactions can affect the nuclear reaction rates. For this reason, to obtain an accurate NSE state it is necessary to include Coulomb corrections to the ion chemical potential. The Coulomb correction to the i -th chemical potential is given by

$$\begin{aligned} \frac{\mu_i^C}{T} = & K_1 \left[\Gamma_i \sqrt{\Gamma_i + K_2} - K_2 \ln \left(\sqrt{\frac{\Gamma_i}{K_2}} + \sqrt{1 + \frac{\Gamma_i}{K_2}} \right) \right] \\ & + 2K_3 \left[\sqrt{\Gamma_i} - \arctan \sqrt{\Gamma_i} \right] + Z_1 \left[\Gamma_i - Z_2 \ln \left(1 + \frac{\Gamma_i}{Z_1} \right) \right] + \frac{Z_3}{2} \ln \left(1 + \frac{\Gamma_i^2}{Z_4} \right), \end{aligned} \quad (A22)$$

and the ion coupling parameter in terms of the electron coupling parameter is $\Gamma_i = \Gamma_e Z_i^{5/3}$ with

$$\Gamma_e = \frac{e^2}{T} \left(\frac{4\pi Y_e n_B}{3} \right)^{1/3}. \quad (A23)$$

where e is the electron charge. The parameters K_i, C_i are given in Table A1.

Table A1. Constants appearing in Equation (A22). See [179].

K_1	K_2	K_3	Z_1	Z_2	Z_3	Z_4
-0.907347	0.62849	0.278497	4.50×10^{-3}	170.0	-8.4×10^{-5}	3.70×10^{-3}

Appendix D. Neutrino Interactions and Cross-Sections

In this appendix we include the neutrino emission rates and neutrino cross-sections used in the accretion disk model. These expressions have been covered in [180–186]. We also include the expression energy emission rate for $\nu\bar{\nu}$ annihilation into electron-positron pairs. Whenever possible we write the rates in terms of generalized Fermi functions since some numerical calculations were done following [187]. We list in Table A2 some useful expressions and constants in Planck units. The numerical values can be found in [141].

Table A2. Constants used throughout this appendix to calculate emissivities and cross-sections. All quantities are reported in Planck units.

Symbol	Value	Name
M_w	6.584×10^{-18}	W boson mass
g_w	0.653	Weak coupling constant
g_a	1.26	Axial-vector coupling constant
α^*	$\frac{1}{137}$	Fine structure constant
$\sin^2 \theta_W$	0.231	Weinberg angle
$\cos^2 \theta_c$	0.947	Cabibbo angle
G_F	1.738×10^{33}	Fermi coupling constant
$C_{\nu,e}$	$2 \sin^2 \theta_W + 1/2$	Weak interaction vector constant for ν_e
$C_{a,e}$	1/2	Weak interaction axial-vector constant for ν_e
$C_{\nu,e}$	$C_{\nu,e} - 1$	Weak interaction vector constant for ν_x
$C_{a,e}$	$C_{a,e} - 1$	Weak interaction axial-vector constant for ν_x
σ_0	6.546×10^{21}	Weak interaction cross-section

Appendix D.1. Neutrino Emissivities

- Pair annihilation: $e^- + e^+ \rightarrow \nu + \bar{\nu}$

This process generates neutrinos of all flavors but around 70% are electron neutrinos [71]. This is due to the fact that the only charged leptons in the accretion systems we study are electrons and positrons, so creation of electron neutrinos occurs via either charged or neutral electroweak currents while creation of non-electronic neutrinos can only

occur through neutral currents. Using the electron or positron four-momentum $p = (E, \mathbf{p})$, the Dicus cross-section for a particular flavor i is [180]

$$\sigma_{D,i} = \frac{G_F^2}{12\pi E_{e^-} E_{e^+}} \left[C_{+,i} \left(m_e^4 + 3m_e^2 p_{e^-} \cdot p_{e^+} + 2(p_{e^-} \cdot p_{e^+})^2 \right) + 3C_{-,i} \left(m_e^4 + m_e^2 p_{e^-} \cdot p_{e^+} \right) \right]. \quad (A24)$$

The factors $C_{\pm,i}$ are written in terms of the weak interaction vector and axial-vector constants: $C_{\pm,i} = C_{v,i}^2 \pm C_{a,i}^2$ [141]. Representing the Fermi–Dirac distribution for electrons (positrons) as f_{e^-} (f_{e^+}) with η_{e^\mp} the electron (positron) degeneracy parameter including its rest mass. The number and energy emission rates can be calculated by replacing $\Lambda = 2$ and $\Lambda = E_{e^-} + E_{e^+}$ in the integral [184]:

$$\frac{4}{(2\pi)^6} \int \Lambda \sigma_D f_{e^-} f_{e^+} d^3\mathbf{p}_{e^-} d^3\mathbf{p}_{e^+}, \quad (A25)$$

giving the expressions

$$R_{\nu_i+\bar{\nu}_i} = \frac{G_F^2 m_e^8}{18\pi} [C_{+,i}(8U_1V_1 + 5U_{-1}V_{-1} + 9U_0V_0 - 2U_{-1}V_1 - 2U_1V_{-1}) + 9C_{-,i}(U_{-1}V_{-1} + U_0V_0)], \quad (A26a)$$

$$Q_{\nu_i+\bar{\nu}_i} = \frac{G_F^2 m_e^9}{36\pi} [C_{+,i}(8(U_2V_1 + U_1V_2) + 7(U_1V_0 + U_0V_1) + 5(U_{-1}V_0 + U_0V_{-1}) - 2(U_2V_{-1} + U_{-1}V_2)) + 9C_{-,i}(U_0(V_1 + V_{-1}) + V_0(U_1 + U_{-1}))]. \quad (A26b)$$

The functions U, V can be written in terms of generalized Fermi functions

$$U_j = \sqrt{2} \xi^{3/2} \sum_{k=0}^{j+1} \binom{j+1}{k} \xi^k \mathcal{F}_{k+1/2,0}(\xi, \eta_{e^-}), \quad (A27a)$$

$$V_j = \sqrt{2} \xi^{3/2} \sum_{k=0}^{j+1} \binom{j+1}{k} \xi^k \mathcal{F}_{k+1/2,0}(\xi, \eta_{e^+}). \quad (A27b)$$

It is often useful to define the functions

$$\epsilon_i^m = \frac{2G_F^2(m_e)^4}{3(2\pi)^7} \int f_{e^-} f_{e^+} (E_{e^-}^m + E_{e^+}^m) \sigma_{D,i} d^3\mathbf{p}_{e^-} d^3\mathbf{p}_{e^+}. \quad (A28)$$

For $m = 0$ and $m = 1$ Equation (A28) gives the neutrino and antineutrino number emissivity (neutrino production rate), and the neutrino and antineutrino energy emissivity (energy per unit volume per unit time) for a certain flavor i , respectively (that is, Equation (A26)). Hence, not only we are able to calculate the total number and energy emissivity, but we can also calculate the neutrino or antineutrino energy moments with

$$\langle E_{\nu_i(\bar{\nu}_i)}^m \rangle = \frac{\epsilon_i^m}{\epsilon_i^0}, \text{ for } m \geq 1. \quad (A29)$$

- Electron capture and positron capture: $p + e^- \rightarrow n + \nu_e, n + e^+ \rightarrow p + \bar{\nu}_e$ and $A + e^- \rightarrow A' + \nu_e$

Due to lepton number conservation this process generated only electron (anti)neutrinos. The number and energy emission rates for electron and positron capture by nucleons are

$$R_{\nu_e} = \frac{m_e^5 G_F^2 \cos^2 \theta_c}{\sqrt{2}\pi^3} (1 + 3g_A^2) \Delta_{np} \xi^{3/2} \left[\xi^3 \mathcal{F}_{7/2,\chi}(\xi, \eta_{e^-}) + (3 - 2\mathbb{Q})\xi^2 \mathcal{F}_{5/2,\chi}(\xi, \eta_{e^-}) + (1 - \mathbb{Q})(3 - \mathbb{Q})\xi \mathcal{F}_{3/2,\chi}(\xi, \eta_{e^-}) + (1 - \mathbb{Q})^2 \mathcal{F}_{1/2,\chi}(\xi, \eta_{e^-}) \right], \quad (\text{A30a})$$

$$Q_{\nu_e} = \frac{m_e^6 G_F^2 \cos^2 \theta_c}{\sqrt{2}\pi^3} (1 + 3g_A^2) \Delta_{np} \xi^{3/2} \left[\xi^4 \mathcal{F}_{9/2,\chi}(\xi, \eta_{e^-}) + \xi^3 (4 - 3\mathbb{Q}) \mathcal{F}_{7/2,\chi}(\xi, \eta_{e^-}) + 3(\mathbb{Q} - 1)(\mathbb{Q} - 2)\xi^2 \mathcal{F}_{5/2,\chi}(\xi, \eta_{e^-}) + (1 - \mathbb{Q})^2 (4 - \mathbb{Q}) \xi \mathcal{F}_{3/2,\chi}(\xi, \eta_{e^-}) + (1 - \mathbb{Q})^3 \mathcal{F}_{1/2,\chi}(\xi, \eta_{e^-}) \right], \quad (\text{A30b})$$

$$R_{\bar{\nu}_e} = \frac{m_e^5 G_F^2 \cos^2 \theta_c}{\sqrt{2}\pi^3} (1 + 3g_A^2) \Delta_{pn} \xi^{3/2} \left[\xi^3 \mathcal{F}_{7/2,0}(\xi, \eta_{e^+}) + (3 + 2\mathbb{Q})\xi^2 \mathcal{F}_{5/2,0}(\xi, \eta_{e^+}) + (1 + \mathbb{Q})(3 + \mathbb{Q})\xi \mathcal{F}_{3/2,0}(\xi, \eta_{e^+}) + (1 + \mathbb{Q})^2 \mathcal{F}_{1/2,0}(\xi, \eta_{e^+}) \right], \quad (\text{A30c})$$

$$Q_{\bar{\nu}_e} = \frac{m_e^6 G_F^2 \cos^2 \theta_c}{\sqrt{2}\pi^3} (1 + 3g_A^2) \Delta_{pn} \xi^{3/2} \left[\xi^4 \mathcal{F}_{9/2,0}(\xi, \eta_{e^+}) + \xi^3 (4 + 3\mathbb{Q}) \mathcal{F}_{7/2,0}(\xi, \eta_{e^+}) + 3(\mathbb{Q} + 1)(\mathbb{Q} + 2)\xi^2 \mathcal{F}_{5/2,0}(\xi, \eta_{e^+}) + (1 + \mathbb{Q})^2 (4 + \mathbb{Q}) \xi \mathcal{F}_{3/2,0}(\xi, \eta_{e^+}) + (1 + \mathbb{Q})^3 \mathcal{F}_{1/2,0}(\xi, \eta_{e^+}) \right], \quad (\text{A30d})$$

where $\Delta_{ij} = (n_i - n_j) / (\exp(\eta_i - \eta_j) - 1)$, $i, j \in \{p, n\}$ are the Fermi blocking factors in the nucleon phase spaces and $\mathbb{Q} = (m_n - m_p)m_e \approx 2.531$ is the nucleon mass difference. The number and energy emission rates for electron capture by an ion i are

$$R_{\nu_e,i} = \frac{\sqrt{2}m_e^5 G_F^2 \cos^2 \theta_c}{7\pi^3} g_A^2 n_i \kappa_{Z_i} \kappa_{N_i} \xi^{3/2} \left[\xi^3 \mathcal{F}_{7/2,\bar{\chi}}(\xi, \eta_{e^-}) + (3 - 2\mathbb{Q})\xi^2 \mathcal{F}_{5/2,\bar{\chi}}(\xi, \eta_{e^-}) + (1 - \mathbb{Q})(3 - \mathbb{Q})\xi \mathcal{F}_{3/2,\bar{\chi}}(\xi, \eta_{e^-}) + (1 - \mathbb{Q})^2 \mathcal{F}_{1/2,\bar{\chi}}(\xi, \eta_{e^-}) \right], \quad (\text{A31a})$$

$$Q_{\nu_e,i} = \frac{\sqrt{2}m_e^6 G_F^2 \cos^2 \theta_c}{7\pi^3} g_A^2 n_i \kappa_{Z_i} \kappa_{N_i} \xi^{3/2} \left[\xi^4 \mathcal{F}_{9/2,\bar{\chi}}(\xi, \eta_{e^-}) + \xi^3 (4 - 3\mathbb{Q}) \mathcal{F}_{7/2,\bar{\chi}}(\xi, \eta_{e^-}) + 3(\mathbb{Q} - 1)(\mathbb{Q} - 2)\xi^2 \mathcal{F}_{5/2,\bar{\chi}}(\xi, \eta_{e^-}) + (1 - \mathbb{Q})^2 (4 - \mathbb{Q}) \xi \mathcal{F}_{3/2,\bar{\chi}}(\xi, \eta_{e^-}) + (1 - \mathbb{Q})^3 \mathcal{F}_{1/2,\bar{\chi}}(\xi, \eta_{e^-}) \right]. \quad (\text{A31b})$$

The lower integration limits in these expressions are given by $\chi = (\mathbb{Q} - 1)/\xi$ and $\bar{\chi} = (\mu_n - \mu_p + \Delta)/T - 1/\xi$ where $\Delta \approx 2.457 \times 10^{-22}$ is the energy of the neutron $1f_{5/2}$ state above the ground state. The functions $\kappa_{Z_i}, \kappa_{N_i}$ are

$$\kappa_{Z_i} = \begin{cases} 0 & \text{if } Z_i \leq 20. \\ Z_i - 20 & \text{if } 20 < Z_i \leq 28., \\ 8 & \text{if } Z_i > 28. \end{cases}, \quad \kappa_{N_i} = \begin{cases} 6 & \text{if } N_i \leq 34. \\ 40 - N_i & \text{if } 34 < N_i \leq 40. \\ 0 & \text{if } N_i > 40. \end{cases} \quad (\text{A32})$$

- Plasmon decay: $\tilde{\gamma} \rightarrow \nu + \bar{\nu}$.

$$R_{\nu_e + \bar{\nu}_e} = \frac{C_{\nu,e} \sigma_0 T^8}{96\pi^3 m_e^2 \alpha^*} \tilde{\gamma}^6 (\tilde{\gamma} + 1) \exp(-\tilde{\gamma}), \quad (\text{A33a})$$

$$Q_{\nu_e + \bar{\nu}_e} = \frac{C_{\nu,e} \sigma_0 T^9}{192\pi^3 m_e^2 \alpha^*} \tilde{\gamma}^6 (\tilde{\gamma}^2 + 2\tilde{\gamma} + 2) \exp(-\tilde{\gamma}), \quad (\text{A33b})$$

$$R_{\nu_x + \bar{\nu}_x} = \frac{C_{\nu,x} \sigma_0 T^8}{48\pi^3 m_e^2 \alpha^*} \tilde{\gamma}^6 (\tilde{\gamma} + 1) \exp(-\tilde{\gamma}), \quad (\text{A33c})$$

$$Q_{\nu_x + \bar{\nu}_x} = \frac{C_{\nu,x} \sigma_0 T^9}{96\pi^3 m_e^2 \alpha^*} \tilde{\gamma}^6 (\tilde{\gamma}^2 + 2\tilde{\gamma} + 2) \exp(-\tilde{\gamma}), \quad (\text{A33d})$$

where $\tilde{\gamma} = \tilde{\gamma}_0 \sqrt{(\pi^2 + 3(\eta_{e^-} + 1/\xi)^2)}/3$ and $\tilde{\gamma}_0 = 2\sqrt{\frac{\alpha^*}{3\pi}} \approx 5.565 \times 10^{-2}$.

- Nucleon-nucleon bremsstrahlung $n_1 + n_2 \rightarrow n_3 + n_4 + \nu + \bar{\nu}$.

The nucleon-nucleon bremsstrahlung produces the same amount of neutrinos of all three flavors. The number and energy emission rates can be approximated by (see, e.g., [186])

$$R_{\nu_i+\bar{\nu}_i} = \left(2.59 \times 10^{13}\right) \left(X_p^2 + X_n^2 + \frac{28}{3} X_p X_n\right) n_B^2 \xi^{9/2}, \tag{A34a}$$

$$Q_{\nu_i+\bar{\nu}_i} = \left(4.71 \times 10^{-9}\right) \left(X_p^2 + X_n^2 + \frac{28}{3} X_p X_n\right) n_B^2 \xi^{10/2}. \tag{A34b}$$

Appendix D.2. Cross-Sections

We consider four interactions to describe the (anti)neutrino total cross-section.

- Neutrino annihilation: $(\nu + \bar{\nu} \rightarrow e^- + e^+)$.

$$\sigma_{\nu_e\bar{\nu}_e} = \frac{4}{3} K_{\nu_e\bar{\nu}_e} \sigma_0 \frac{\langle E_{\nu_e} \rangle \langle E_{\bar{\nu}_e} \rangle}{m_e^2} \text{ with } K_{\nu_e\bar{\nu}_e} = \frac{1 + 4 \sin^2 \theta_W + 8 \sin^4 \theta_W}{12}, \tag{A35a}$$

$$\sigma_{\nu_x\bar{\nu}_x} = \frac{4}{3} K_{\nu_x\bar{\nu}_x} \sigma_0 \frac{\langle E_{\nu_x} \rangle \langle E_{\bar{\nu}_x} \rangle}{m_e^2} \text{ with } K_{\nu_x\bar{\nu}_x} = \frac{1 - 4 \sin^2 \theta_W + 8 \sin^4 \theta_W}{12}, \tag{A35b}$$

- Electron (anti)neutrino absorption by nucleons: $(\nu_e + n \rightarrow e^- + p \text{ and } \bar{\nu}_e + p \rightarrow e^+ + n)$.

$$\sigma_{\nu_e n} = \sigma_0 \left(\frac{1 + 3g_a^2}{4}\right) \left(\frac{\langle E_{\nu_e} \rangle}{m_e} + Q\right)^2 \sqrt{1 - \frac{1}{\left(\frac{\langle E_{\nu_e} \rangle}{m_e} + Q\right)^2}}, \tag{A36a}$$

$$\sigma_{\bar{\nu}_e p} = 3.83 \times 10^{22} \left(\frac{\varphi \langle E_{\bar{\nu}_e} \rangle}{m_e} - Q\right)^2 \sqrt{1 - \frac{1}{\left(\frac{\varphi \langle E_{\bar{\nu}_e} \rangle}{m_e} - Q\right)^2}} \left(\frac{\varphi \langle E_{\bar{\nu}_e} \rangle}{m_e}\right)^{g(E_{\bar{\nu}_e})}, \tag{A36b}$$

$$g(E_{\bar{\nu}_e}) = -0.07056 + 0.02018 \ln\left(\frac{\varphi \langle E_{\bar{\nu}_e} \rangle}{m_e}\right) - 0.001953 \ln^3\left(\frac{\varphi \langle E_{\bar{\nu}_e} \rangle}{m_e}\right). \tag{A36c}$$

where $\varphi = 0.511$.

- (anti)neutrino scattering by baryons: $(\nu + A_i \rightarrow \nu + A_i \text{ and } \bar{\nu} + A_i \rightarrow \bar{\nu} + A_i)$.

$$\sigma_p = \frac{\sigma_0 \langle E \rangle^2}{4m_e^2} \left(4 \sin^4 \theta_W - 2 \sin^2 \theta_W + \frac{1 + 3g_a^2}{4}\right), \tag{A37a}$$

$$\sigma_n = \frac{\sigma_0 \langle E \rangle^2}{4m_e^2} \frac{1 + 3g_a^2}{4}, \tag{A37b}$$

$$\sigma_{A_i} = \frac{\sigma_0 A_i^2 \langle E \rangle^2}{16m_e^2} \left[\left(4 \sin^2 \theta_W - 1\right) \frac{Z_i}{A_i} + 1 - \frac{Z_i}{A_i} \right]. \tag{A37c}$$

- (anti)neutrino scattering by electrons or positrons: $(\nu + e^\pm \rightarrow \nu + e^\pm \text{ and } \bar{\nu} + e^\pm \rightarrow \bar{\nu} + e^\pm)$.

$$\sigma_e = \frac{3}{8} \sigma_0 \xi \frac{\langle E \rangle}{m_e} \left(1 + \frac{\eta_e + 1/\xi}{4}\right) \left[(C_{\nu,i} + n_\ell C_{a,i})^2 + \frac{1}{3} (C_{\nu,i} - n_\ell C_{a,i})^2 \right]. \tag{A38}$$

Here, n_ℓ is the (anti)neutrino lepton number (that is, 1 for neutrinos and -1 for antineutrinos, depending on the cross-section to be calculated), and in the last four expressions, $\langle E \rangle$ is replaced by the average (anti)neutrino energy of the corresponding flavor. With these expressions, the total opacity for neutrinos or antineutrinos is

$$\kappa_{\nu_i(\bar{\nu}_i)} = \frac{\sum_i \sigma_i n_i}{\rho}, \tag{A39}$$

where n_i is the number density of the target particle associated with the process corresponding to the cross-section σ_i . The (anti)neutrino optical depth appearing in Equation (32) can then be approximated as

$$\tau_{\nu_i(\bar{\nu}_i)} = \int \kappa_{\nu_i(\bar{\nu}_i)} \rho d\theta \approx \kappa_{\nu_i(\bar{\nu}_i)} \rho H. \tag{A40}$$

Appendix D.3. Neutrino-Antineutrino Pair Annihilation

Since the main interaction between $\nu\bar{\nu}$ is the annihilation into e^-e^+ , this process above neutrino-cooled disks has been proposed as the origin of the energetic plasma involved in the production of GRBs. Once the (anti)neutrino energy emissivity and average energies are calculated it is possible to calculate the energy deposition rate of the process $\nu_i + \bar{\nu}_i \rightarrow e^- + e^+$ for each flavor i . Ignoring Pauli blocking effects in the phase spaces of electron and positrons, the local energy deposition rate at a position \mathbf{r} by $\nu\bar{\nu}$ annihilation can be written in terms of the neutrino and antineutrino distributions $f_{\nu_i} = f_{\nu_i}(\mathbf{r}, E_{\nu_i}), f_{\bar{\nu}_i} = f_{\bar{\nu}_i}(\mathbf{r}, E_{\bar{\nu}_i})$ as [155]

$$\begin{aligned} Q_{\nu_i\bar{\nu}_i} = & A_{1,i} \int_0^\infty dE_{\nu_i} \int_0^\infty dE_{\bar{\nu}_i} E_{\nu_i}^3 E_{\bar{\nu}_i}^3 (E_{\nu_i} + E_{\bar{\nu}_i}) \int_{S_2} d\Omega_{\nu_i} \int_{S_2} d\Omega_{\bar{\nu}_i} f_{\nu_i} f_{\bar{\nu}_i} (1 - \cos \theta)^2, \\ & + A_{2,i} \int_0^\infty dE_{\nu_i} \int_0^\infty dE_{\bar{\nu}_i} E_{\nu_i}^2 E_{\bar{\nu}_i}^2 (E_{\nu_i} + E_{\bar{\nu}_i}) \int_{S_2} d\Omega_{\nu_i} \int_{S_2} d\Omega_{\bar{\nu}_i} f_{\nu_i} f_{\bar{\nu}_i} (1 - \cos \theta), \end{aligned} \tag{A41}$$

where we have introduced the constants appearing in Equation (80)

$$\begin{aligned} A_{1,i} = & \frac{\sigma_0 [(C_{\nu,i} - C_{a,i})^2 + (C_{\nu,i} + C_{a,i})^2]}{12\pi^2 m_e^2}, \\ A_{2,i} = & \frac{\sigma_0 [2C_{\nu,i}^2 - C_{a,i}^2]}{6\pi^2 m_e^2}. \end{aligned} \tag{A42}$$

In Equation (A41), θ is the angle between the neutrino and antineutrino momentum and $d\Omega$ is the differential solid angle of the incident (anti)neutrino at \mathbf{r} . The integral can be re-written in terms of the total intensity (energy integrated intensity) $I_\nu = \int E_\nu^3 f_\nu dE_\nu$ as [156]

$$\begin{aligned} Q_{\nu_i\bar{\nu}_i} = & A_{1,i} \int_{S_2} d\Omega_{\nu_i} I_{\nu_i} \int_{S_2} d\Omega_{\bar{\nu}_i} I_{\bar{\nu}_i} (\langle E_{\nu_i} \rangle + \langle E_{\bar{\nu}_i} \rangle) (1 - \cos \theta)^2 \\ & + A_{2,i} \int_{S_2} d\Omega_{\nu_i} I_{\nu_i} \int_{S_2} d\Omega_{\bar{\nu}_i} I_{\bar{\nu}_i} \frac{\langle E_{\nu_i} \rangle + \langle E_{\bar{\nu}_i} \rangle}{\langle E_{\nu_i} \rangle \langle E_{\bar{\nu}_i} \rangle} (1 - \cos \theta). \end{aligned} \tag{A43}$$

The incident radiation intensity passing through the solid differential angle $d\Omega$ at \mathbf{r} is the intensity $I_{\mathbf{r}_d,\nu}$ emitted from the point on the disk \mathbf{r}_d diluted by the inverse square distance $r_k = |\mathbf{r} - \mathbf{r}_d|$ between both points. Finally, assuming that each point \mathbf{r}_d on the disk's surface acts as a half-isotropic radiator of (anti)neutrinos, the total flux emitted at \mathbf{r}_d is $F_{\mathbf{r}_d,\nu} = \int_0^{\pi/2} \int_0^{2\pi} I_{\mathbf{r}_d,\nu} \cos \theta' \sin \theta' d\theta' d\phi' = \pi I_{\mathbf{r}_d,\nu}$, with θ', ϕ' the direction angles at \mathbf{r}_d . Collecting all obtains

$$\begin{aligned} Q_{\nu_i\bar{\nu}_i} = & A_{1,i} \int_{\mathbf{r}_{d,\nu_i} \in \text{disk}} d\mathbf{r}_{d,\nu_i} \int_{\mathbf{r}_{d,\bar{\nu}_i} \in \text{disk}} d\mathbf{r}_{d,\bar{\nu}_i} \frac{F_{\mathbf{r}_d,\nu_i}}{r_{k,\nu_i}^2} \frac{F_{\mathbf{r}_d,\bar{\nu}_i}}{r_{k,\bar{\nu}_i}^2} (\langle E_{\nu_i} \rangle + \langle E_{\bar{\nu}_i} \rangle) (1 - \cos \theta)^2 \\ & + A_{2,i} \int_{\mathbf{r}_{d,\nu_i} \in \text{disk}} d\mathbf{r}_{d,\nu_i} \int_{\mathbf{r}_{d,\bar{\nu}_i} \in \text{disk}} d\mathbf{r}_{d,\bar{\nu}_i} \frac{F_{\mathbf{r}_d,\nu_i}}{r_{k,\nu_i}^2} \frac{F_{\mathbf{r}_d,\bar{\nu}_i}}{r_{k,\bar{\nu}_i}^2} \frac{\langle E_{\nu_i} \rangle + \langle E_{\bar{\nu}_i} \rangle}{\langle E_{\nu_i} \rangle \langle E_{\bar{\nu}_i} \rangle} (1 - \cos \theta). \end{aligned} \tag{A44}$$

References

1. De Salas, P.F.; Forero, D.V.; Ternes, C.A.; Tortola, M.; Valle, J.W.F. Status of neutrino oscillations 2018: 3σ hint for normal mass ordering and improved CP sensitivity. *Phys. Lett. B* **2018**, *782*, 633–640. [[CrossRef](#)]
2. Wolfenstein, L. Neutrino Oscillations in Matter. *Phys. Rev. D* **1978**, *17*, 2369–2374. [[CrossRef](#)]
3. Mikheyev, S.P.; Smirnov, A.Y. Resonant amplification of ν oscillations in matter and solar-neutrino spectroscopy. *Il Nuovo Cimento C* **1986**, *9*, 17–26. [[CrossRef](#)]
4. Barbieri, R.; Dolgov, A. Neutrino oscillations in the early universe. *Nucl. Phys. B* **1991**, *349*, 743–753. [[CrossRef](#)]
5. Enqvist, K.; Kainulainen, K.; Maalampi, J. Refraction and Oscillations of Neutrinos in the Early Universe. *Nucl. Phys. B* **1991**, *349*, 754–790. [[CrossRef](#)]
6. Savage, M.J.; Malaney, R.A.; Fuller, G.M. Neutrino Oscillations and the Leptonic Charge of the Universe. *Astrophys. J.* **1991**, *368*, 1–11. [[CrossRef](#)]
7. Kostelecky, V.A.; Samuel, S. Neutrino oscillations in the early universe with an inverted neutrino mass hierarchy. *Phys. Lett. B* **1993**, *318*, 127–133. [[CrossRef](#)]
8. Kostelecky, V.A.; Samuel, S. Nonlinear neutrino oscillations in the expanding universe. *Phys. Rev. D* **1994**, *49*, 1740–1757. [[CrossRef](#)]
9. Kostelecký, V.; Pantaleone, J.; Samuel, S. Neutrino oscillations in the early universe. *Phys. Lett. B* **1993**, *315*, 46–50. [[CrossRef](#)]
10. McKellar, B.H.J.; Thomson, M.J. Oscillating doublet neutrinos in the early universe. *Phys. Rev. D* **1994**, *49*, 2710–2728. [[CrossRef](#)]
11. Lunardini, C.; Smirnov, A.Y. High-energy neutrino conversion and the lepton asymmetry in the universe. *Phys. Rev. D* **2001**, *64*, 73006. [[CrossRef](#)]
12. Dolgov, A.D.; Hansen, S.H.; Pastor, S.; Petcov, S.T.; Raffelt, G.G.; Semikoz, D.V. Cosmological bounds on neutrino degeneracy improved by flavor oscillations. *Nucl. Phys. B* **2002**, *632*, 363–382. [[CrossRef](#)]
13. Wong, Y.Y. Analytical treatment of neutrino asymmetry equilibration from flavor oscillations in the early universe. *Phys. Rev. D* **2002**, *66*, 25015. [[CrossRef](#)]
14. Abazajian, K.N.; Beacom, J.F.; Bell, N.F. Stringent constraints on cosmological neutrino-antineutrino asymmetries from synchronized flavor transformation. *Phys. Rev. D* **2002**, *66*, 13008. [[CrossRef](#)]
15. Kirilova, D.P. Neutrino oscillations and the early universe. *Cent. Eur. J. Phys.* **2004**, *2*, 467–491. [[CrossRef](#)]
16. Bahcall, J.N.; Concepcion Gonzalez-Garcia, M.; na-Garay, C.P. Solar Neutrinos Before and After KamLAND. *J. High Energy Phys.* **2003**, *2003*, 09. [[CrossRef](#)]
17. Balantekin, A.B.; Yuksel, H. Global Analysis of Solar Neutrino and KamLAND Data. *J. Phys. G Nucl. Part. Phys.* **2003**, *29*, 665. [[CrossRef](#)]
18. Fogli, G.L.; Lisi, E.; Marrone, A.; Montanino, D.; Palazzo, A.; Rotunno, A.M. Neutrino Oscillations: A Global Analysis. *arXiv* **2003**, arXiv:0310012.
19. de Holanda, P.C.; Smirnov, A.Y. Solar neutrinos: The SNO salt phase results and physics of conversion. *Astropart. Phys.* **2004**, *21*, 287–301. [[CrossRef](#)]
20. Giunti, C. Status of neutrino masses and mixing. *Eur. Phys. J. C* **2004**, *33*, 852–856. [[CrossRef](#)]
21. Maltoni, M.; Schwetz, T.; Tórtola, M.A.; Valle, J.W. Status of three-neutrino oscillations after the SNO-salt data. *Phys. Rev. D* **2003**, *68*, 113010. [[CrossRef](#)]
22. Dighe, A. Supernova neutrino oscillations: What do we understand? *J. Phys. Conf. Ser.* **2010**, *203*, 012015. [[CrossRef](#)]
23. Haxton, W.C.; Hamish Robertson, R.G.; Serenelli, A.M. Solar Neutrinos: Status and Prospects. *Annu. Rev. Astron. Astrophys.* **2013**, *51*, 21–61. [[CrossRef](#)]
24. Vissani, F. Solar neutrino physics on the beginning of 2017. *Nucl. Phys. At. Energy* **2017**, *18*, 5–12. [[CrossRef](#)]
25. Notzold, D.; Raffelt, G. Neutrino Dispersion at Finite Temperature and Density. *Nucl. Phys. B* **1988**, *307*, 924–936. [[CrossRef](#)]
26. Pantaleone, J. Neutrino oscillations at high densities. *Phys. Lett. B* **1992**, *287*, 128–132. [[CrossRef](#)]
27. Qian, Y.Z.; Fuller, G.M. Neutrino-neutrino scattering and matter enhanced neutrino flavor transformation in Supernovae. *Phys. Rev. D* **1995**, *51*, 1479–1494. [[CrossRef](#)] [[PubMed](#)]
28. Pastor, S.; Raffelt, G. Flavor oscillations in the supernova hot bubble region: Nonlinear effects of neutrino background. *Phys. Rev. Lett.* **2002**, *89*, 191101. [[CrossRef](#)]
29. Duan, H.; Fuller, G.M.; Qian, Y.Z. Collective neutrino flavor transformation in supernovae. *Phys. Rev. D* **2006**, *74*, 123004. [[CrossRef](#)]
30. Sawyer, R.F. Speed-up of neutrino transformations in a supernova environment. *Phys. Rev. D* **2005**, *72*, 45003. [[CrossRef](#)]
31. Fuller, G.M.; Qian, Y.Z. Simultaneous flavor transformation of neutrinos and antineutrinos with dominant potentials from neutrino-neutrino forward scattering. *Phys. Rev. D* **2006**, *73*, 23004. [[CrossRef](#)]
32. Duan, H.; Fuller, G.M.; Carlson, J.; Qian, Y.Z. Coherent Development of Neutrino Flavor in the Supernova Environment. *Phys. Rev. Lett.* **2006**, *97*, 241101. [[CrossRef](#)] [[PubMed](#)]
33. Fogli, G.L.; Lisi, E.; Marrone, A.; Mirizzi, A. Collective neutrino flavor transitions in supernovae and the role of trajectory averaging. *JCAP* **2007**, *0712*, 10. [[CrossRef](#)]
34. Duan, H.; Fuller, G.M.; Qian, Y.Z. A Simple Picture for Neutrino Flavor Transformation in Supernovae. *Phys. Rev. D* **2007**, *76*, 85013. [[CrossRef](#)]
35. Raffelt, G.G.; Sigl, G. Self-induced decoherence in dense neutrino gases. *Phys. Rev. D* **2007**, *75*, 83002. [[CrossRef](#)]
36. Esteban-Pretel, A.; Pastor, S.; Tomas, R.; Raffelt, G.G.; Sigl, G. Decoherence in supernova neutrino transformations suppressed by deleptonization. *Phys. Rev. D* **2007**, *76*, 125018. [[CrossRef](#)]

37. Esteban-Pretel, A.; Pastor, S.; Tomas, R.; Raffelt, G.G.; Sigl, G. Mu-tau neutrino refraction and collective three-flavor transformations in supernovae. *Phys. Rev. D* **2008**, *77*, 65024. [[CrossRef](#)]
38. Chakraborty, S.; Choubey, S.; Dasgupta, B.; Kar, K. Effect of Collective Flavor Oscillations on the Diffuse Supernova Neutrino Background. *JCAP* **2008**, *0809*, 13. [[CrossRef](#)]
39. Duan, H.; Fuller, G.M.; Carlson, J.; Qian, Y.Z. Flavor Evolution of the Neutronization Neutrino Burst from an O-Ne-Mg Core-Collapse Supernova. *Phys. Rev. Lett.* **2008**, *100*, 21101. [[CrossRef](#)]
40. Duan, H.; Fuller, G.M.; Carlson, J. Simulating nonlinear neutrino flavor evolution. *Comput. Sci. Dis.* **2008**, *1*, 015007. [[CrossRef](#)]
41. Dasgupta, B.; Dighe, A.; Mirizzi, A. Identifying neutrino mass hierarchy at extremely small $\theta(13)$ through Earth matter effects in a supernova signal. *Phys. Rev. Lett.* **2008**, *101*, 171801. [[CrossRef](#)] [[PubMed](#)]
42. Dasgupta, B.; Dighe, A. Collective three-flavor oscillations of supernova neutrinos. *Phys. Rev. D* **2008**, *77*, 113002. [[CrossRef](#)]
43. Sawyer, R.F. The multi-angle instability in dense neutrino systems. *Phys. Rev. D* **2009**, *79*, 105003. [[CrossRef](#)]
44. Duan, H.; Fuller, G.M.; Qian, Y.Z. Collective Neutrino Oscillations. *Ann. Rev. Nucl. Part. Sci.* **2010**, *60*, 569–594. [[CrossRef](#)]
45. Wu, M.R.; Qian, Y.Z. Resonances Driven by a Neutrino Gyroscope and Collective Neutrino Oscillations in Supernovae. *Phys. Rev. D* **2011**, *84*, 45009. [[CrossRef](#)]
46. Bilenky, S.M. Neutrino oscillations: Brief history and present status. *arXiv* **2014**, arXiv:1408.2864.
47. Kneller, J.P. The Physics Of Supernova Neutrino Oscillations. In Proceedings of the 12th Conference on the Intersections of Particle and Nuclear Physics (CIPANP 2015), Vail, CO, USA, 19–24 May 2015.
48. Volpe, C. Theoretical developments in supernova neutrino physics: Mass corrections and pairing correlators. *J. Phys. Conf. Ser.* **2016**, *718*, 62068. [[CrossRef](#)]
49. Mirizzi, A.; Tamborra, I.; Janka, H.T.; Saviano, N.; Scholberg, K.; Bollig, R.; Hüdepohl, L.; Chakraborty, S. Supernova neutrinos: production, oscillations and detection. *Nuovo Cimento Riv. Ser.* **2016**, *39*, 1–112. [[CrossRef](#)]
50. Horiuchi, S.; Kneller, J.P. What can be learned from a future supernova neutrino detection? *J. Phys. G Nucl. Phys.* **2018**, *45*, 43002. [[CrossRef](#)]
51. Zaizen, M.; Yoshida, T.; Sumiyoshi, K.; Umeda, H. Collective neutrino oscillations and detectabilities in failed supernovae. *Phys. Rev. D* **2018**, *98*, 103020. [[CrossRef](#)]
52. Zhang, B. *The Physics of Gamma-ray Bursts*; Cambridge University Press: Cambridge, UK, 2018. [[CrossRef](#)]
53. Ruffini, R.; Bernardini, M.G.; Bianco, C.L.; Vitagliano, L.; Xue, S.S.; Chardonnet, P.; Frascchetti, F.; Gurzadyan, V. Black Hole Physics and Astrophysics: The GRB-Supernova Connection and URCA-1 - URCA-2. In *The Tenth Marcel Grossmann Meeting, Proceedings of the MG10 Meeting Held at Brazilian Center for Research in Physics (CBPF), Rio de Janeiro, Brazil, 20–26 July 2003*; Novello, M., Bergliaffa, S.P., Ruffini, R., Eds.; World Scientific Publishing: Singapore, 2006; Volumes 3, p. 369. [[CrossRef](#)]
54. Ruffini, R.; Bernardini, M.G.; Bianco, C.L.; Caito, L.; Chardonnet, P.; Cherubini, C.; Dainotti, M.G.; Frascchetti, F.; Geralico, A.; Guida, R.; et al. On Gamma-ray Bursts. In *The Eleventh Marcel Grossmann Meeting On Recent Developments in Theoretical and Experimental General Relativity, Gravitation and Relativistic Field Theories*; Kleinert, H., Jantzen, R.T., Ruffini, R., Eds.; World Scientific: Singapore, 2008; pp. 368–505. [[CrossRef](#)]
55. Izzo, L.; Rueda, J.A.; Ruffini, R. GRB 090618: A candidate for a neutron star gravitational collapse onto a black hole induced by a type Ib/c supernova. *Astron. Astrophys.* **2012**, *548*, L5. [[CrossRef](#)]
56. Rueda, J.A.; Ruffini, R. On the Induced Gravitational Collapse of a Neutron Star to a Black Hole by a Type Ib/c Supernova. *Astrophys. J.* **2012**, *758*, L7. [[CrossRef](#)]
57. Fryer, C.L.; Rueda, J.A.; Ruffini, R. Hypercritical Accretion, Induced Gravitational Collapse, and Binary-Driven Hypernovae. *Astrophys. J.* **2014**, *793*, L36. [[CrossRef](#)]
58. Ruffini, R.; Wang, Y.; Enderli, M.; Muccino, M.; Kovacevic, M.; Bianco, C.L.; Penacchioni, A.V.; Pisani, G.B.; Rueda, J.A. GRB 130427A and SN 2013cq: A Multi-wavelength Analysis of An Induced Gravitational Collapse Event. *Astrophys. J.* **2015**, *798*, 10. [[CrossRef](#)]
59. Fryer, C.L.; Oliveira, F.G.; Rueda, J.A.; Ruffini, R. Neutron-Star-Black-Hole Binaries Produced by Binary-Driven Hypernovae. *Phys. Rev. Lett.* **2015**, *115*, 231102. [[CrossRef](#)]
60. Wang, Y.; Rueda, J.A.; Ruffini, R.; Becerra, L.; Bianco, C.; Becerra, L.; Li, L.; Karlica, M. Two Predictions of Supernova: GRB 130427A/SN 2013cq and GRB 180728A/SN 2018fip. *Astrophys. J.* **2019**, *874*, 39. [[CrossRef](#)]
61. Rueda, J.A.; Ruffini, R.; Karlica, M.; Moradi, R.; Wang, Y. Magnetic Fields and Afterglows of BdHNe: Inferences from GRB 130427A, GRB 160509A, GRB 160625B, GRB 180728A, and GRB 190114C. *Astrophys. J.* **2020**, *893*, 148. [[CrossRef](#)]
62. Rueda, J.A.; Ruffini, R.; Wang, Y. Induced Gravitational Collapse, Binary-Driven Hypernovae, Long Gamma-ray Bursts and Their Connection with Short Gamma-ray Bursts. *Universe* **2019**, *5*, 110. [[CrossRef](#)]
63. Becerra, L.; Bianco, C.L.; Fryer, C.L.; Rueda, J.A.; Ruffini, R. On the Induced Gravitational Collapse Scenario of Gamma-ray Bursts Associated with Supernovae. *Astrophys. J.* **2016**, *833*, 107. [[CrossRef](#)]
64. Bianco, C.L.; Ruffini, R.; Xue, S. The elementary spike produced by a pure e^+e^- pair-electromagnetic pulse from a Black Hole: The PEM Pulse. *Astron. Astrophys.* **2001**, *368*, 377–390. [[CrossRef](#)]
65. Ruffini, R.; Moradi, R.; Rueda, J.A.; Becerra, L.; Bianco, C.L.; Cherubini, C.; Filippi, S.; Chen, Y.C.; Karlica, M.; Sahakyan, N.; et al. On the GeV Emission of the Type I BdHN GRB 130427A. *Astrophys. J.* **2019**, *886*, 82. [[CrossRef](#)]
66. Ruffini, R.; Melon Fuksman, J.D.; Vereshchagin, G.V. On the Role of a Cavity in the Hypernova Ejecta of GRB 190114C. *Astrophys. J.* **2019**, *883*, 191. [[CrossRef](#)]

67. Ruffini, R.; Wang, Y.; Aimuratov, Y.; Barres de Almeida, U.; Becerra, L.; Bianco, C.L.; Chen, Y.C.; Karlica, M.; Kovacevic, M.; Li, L.; et al. Early X-ray Flares in GRBs. *Astrophys. J.* **2018**, *852*, 53. [[CrossRef](#)]
68. Ruffini, R.; Karlica, M.; Sahakyan, N.; Rueda, J.A.; Wang, Y.; Mathews, G.J.; Bianco, C.L.; Muccino, M. A GRB Afterglow Model Consistent with Hypernova Observations. *Astrophys. J.* **2018**, *869*, 101. [[CrossRef](#)]
69. Becerra, L.; Cipolletta, F.; Fryer, C.L.; Rueda, J.A.; Ruffini, R. Angular Momentum Role in the Hypercritical Accretion of Binary-driven Hypernovae. *Astrophys. J.* **2015**, *812*, 100. [[CrossRef](#)]
70. Becerra, L.; Ellinger, C.L.; Fryer, C.L.; Rueda, J.A.; Ruffini, R. SPH Simulations of the Induced Gravitational Collapse Scenario of Long Gamma-ray Bursts Associated with Supernovae. *Astrophys. J.* **2019**, *871*, 14. [[CrossRef](#)]
71. Becerra, L.; Guzzo, M.M.; Rossi-Torres, F.; Rueda, J.A.; Ruffini, R.; Uribe, J.D. Neutrino Oscillations within the Induced Gravitational Collapse Paradigm of Long Gamma-ray Bursts. *Astrophys. J.* **2018**, *852*, 120. [[CrossRef](#)]
72. Goodman, J. Are gamma-ray bursts optically thick? *Astrophys. J.* **1986**, *308*, L47–L50. [[CrossRef](#)]
73. Paczynski, B. Gamma-ray bursters at cosmological distances. *Astrophys. J.* **1986**, *308*, L43–L46. [[CrossRef](#)]
74. Eichler, D.; Livio, M.; Piran, T.; Schramm, D.N. Nucleosynthesis, neutrino bursts and gamma-rays from coalescing neutron stars. *Nature* **1989**, *340*, 126–128. [[CrossRef](#)]
75. Narayan, R.; Piran, T.; Shemi, A. Neutron star and black hole binaries in the Galaxy. *Astrophys. J.* **1991**, *379*, L17–L20. [[CrossRef](#)]
76. Balbus, S.A.; Hawley, J.F. A powerful local shear instability in weakly magnetized disks. I—Linear analysis. II—Nonlinear evolution. *Astrophys. J.* **1991**, *376*, 214–233. [[CrossRef](#)]
77. Hawley, J.F.; Balbus, S.A. A Powerful Local Shear Instability in Weakly Magnetized Disks. II. Nonlinear Evolution. *Astrophys. J.* **1991**, *376*, 223. [[CrossRef](#)]
78. Balbus, S.A.; Hawley, J.F. Instability, turbulence, and enhanced transport in accretion disks. *Rev. Mod. Phys.* **1998**, *70*, 1–53. [[CrossRef](#)]
79. Balbus, S.A. Enhanced Angular Momentum Transport in Accretion Disks. *Annu. Rev. Astron. Astrophys.* **2003**, *41*, 555–597. [[CrossRef](#)]
80. Shakura, N.I.; Sunyaev, R.A. Black holes in binary systems. Observational appearance. *Astron. Astrophys.* **1973**, *24*, 337–355.
81. King, A.R.; Pringle, J.E.; Livio, M. Accretion disc viscosity: How big is alpha? *Mon. Not. R. Astron. Soc.* **2007**, *376*, 1740–1746. [[CrossRef](#)]
82. Pessah, M.E.; Chan, C.K.; Psaltis, D. The fundamental difference between shear alpha viscosity and turbulent magnetorotational stresses. *Mon. Not. R. Astron. Soc.* **2008**, *383*, 683–690. [[CrossRef](#)]
83. King, A. Accretion disc theory since Shakura and Sunyaev. *Mem. Soc. Astron. Ital.* **2012**, *83*, 466.
84. Kotko, I.; Lasota, J.P. The viscosity parameter α and the properties of accretion disc outbursts in close binaries. *Astron. Astrophys.* **2012**, *545*, A115. [[CrossRef](#)]
85. Pringle, J.E. Accretion discs in astrophysics. *Annu. Rev. Astron. Astrophys.* **1981**, *19*, 137–162. [[CrossRef](#)]
86. Krolik, J.H. *Active Galactic Nuclei: From the Central Black Hole to the Galactic Environment*; Princeton University Press: Princeton, NJ, USA, 1999.
87. Abramowicz, M.A.; Björnsson, G.; Pringle, J.E. *Theory of Black Hole Accretion Discs*; Cambridge University Press: Cambridge, UK, 1999; p. 309.
88. Manmoto, T. Advection-dominated Accretion Flow around a Kerr Black Hole. *Astrophys. J.* **2000**, *534*, 734–746. [[CrossRef](#)]
89. Frank, J.; King, A.; Raine, D.J. *Accretion Power in Astrophysics*, 3rd ed.; Cambridge University Press: Cambridge, UK, 2002; p. 398.
90. Blaes, O.M. Course 3: Physics Fundamentals of Luminous Accretion Disks around Black Holes. In *Accretion Discs, Jets and High Energy Phenomena in Astrophysics*; Beskin, V., Henri, G., Menard, F., Pelletier, G., Dalibard, J., Eds.; Springer: Berlin/Heidelberg, Germany, 2004; pp. 137–185.
91. Narayan, R.; McClintock, J.E. Advection-dominated accretion and the black hole event horizon. *New Astron. Rev.* **2008**, *51*, 733–751. [[CrossRef](#)]
92. Kato, S.; Fukue, J.; Mineshige, S. *Black-Hole Accretion Disks—Towards a New Paradigm—*; Kyoto University Press: Kyoto, Japan, 2008.
93. Qian, L.; Abramowicz, M.A.; Fragile, P.C.; Horák, J.; Machida, M.; Straub, O. The Polish doughnuts revisited. I. The angular momentum distribution and equipressure surfaces. *Astron. Astrophys.* **2009**, *498*, 471–477. [[CrossRef](#)]
94. Montesinos, M. Review: Accretion Disk Theory. *arXiv* **2012**, arXiv:1203.6851.
95. Abramowicz, M.A.; Fragile, P.C. Foundations of Black Hole Accretion Disk Theory. *Living Rev. Relativ.* **2013**, *16*, 1. [[CrossRef](#)] [[PubMed](#)]
96. Yuan, F.; Narayan, R. Hot Accretion Flows Around Black Holes. *Annu. Rev. Astron. Astrophys.* **2014**, *52*, 529–588. [[CrossRef](#)]
97. Blaes, O. General Overview of Black Hole Accretion Theory. *Space Sci. Rev.* **2014**, *183*, 21–41. [[CrossRef](#)]
98. Lasota, J.P. Black Hole Accretion Discs. *Astrophysics of Black Holes: From Fundamental Aspects to Latest Developments*; Bambi, C., Ed.; Astrophysics and Space Science Library; Springer: Berlin/Heidelberg, Germany, 2016; Volume 440, p. 1. [[CrossRef](#)]
99. Liu, T.; Gu, W.M.; Zhang, B. Neutrino-dominated accretion flows as the central engine of gamma-ray bursts. *New Astron. Rev.* **2017**, *79*, 1–25. [[CrossRef](#)]
100. Popham, R.; Woosley, S.E.; Fryer, C. Hyperaccreting Black Holes and Gamma-ray Bursts. *Astrophys. J.* **1999**, *518*, 356–374. [[CrossRef](#)]
101. Narayan, R.; Piran, T.; Kumar, P. Accretion Models of Gamma-ray Bursts. *Astrophys. J.* **2001**, *557*, 949–957. [[CrossRef](#)]

102. Kohri, K.; Mineshige, S. Can Neutrino-cooled Accretion Disks Be an Origin of Gamma-ray Bursts? *Astrophys. J.* **2002**, *577*, 311–321. [[CrossRef](#)]
103. Di Matteo, T.; Perna, R.; Narayan, R. Neutrino Trapping and Accretion Models for Gamma-ray Bursts. *Astrophys. J.* **2002**, *579*, 706–715. [[CrossRef](#)]
104. Kohri, K.; Narayan, R.; Piran, T. Neutrino-dominated Accretion and Supernovae. *Astrophys. J.* **2005**, *629*, 341–361. [[CrossRef](#)]
105. Lee, W.H.; Ramirez-Ruiz, E.; Page, D. Dynamical Evolution of Neutrino-cooled Accretion Disks: Detailed Microphysics, Lepton-driven Convection, and Global Energetics. *Astrophys. J.* **2005**, *632*, 421–437. [[CrossRef](#)]
106. Gu, W.M.; Liu, T.; Lu, J.F. Neutrino-dominated Accretion Models for Gamma-ray Bursts: Effects of General Relativity and Neutrino Opacity. *Astrophys. J.* **2006**, *643*, L87–L90. [[CrossRef](#)]
107. Chen, W.X.; Beloborodov, A.M. Neutrino-cooled Accretion Disks around Spinning Black Holes. *Astrophys. J.* **2007**, *657*, 383–399. [[CrossRef](#)]
108. Kawanaka, N.; Mineshige, S. Neutrino-cooled Accretion Disk and Its Stability. *Astrophys. J.* **2007**, *662*, 1156–1166. [[CrossRef](#)]
109. Janiuk, A.; Yuan, Y.F. The role of black hole spin and magnetic field threading the unstable neutrino disk in gamma ray bursts. *Astron. Astrophys.* **2010**, *509*, A55. [[CrossRef](#)]
110. Kawanaka, N.; Piran, T.; Krolik, J.H. Jet Luminosity from Neutrino-dominated Accretion Flows in Gamma-ray Bursts. *Astrophys. J.* **2013**, *766*, 31. [[CrossRef](#)]
111. Luo, S.; Yuan, F. Global neutrino heating in hyperaccretion flows. *Mon. Not. R. Astron. Soc.* **2013**, *431*, 2362–2370. [[CrossRef](#)]
112. Xue, L.; Liu, T.; Gu, W.M.; Lu, J.F. Relativistic Global Solutions of Neutrino-dominated Accretion Flows. *Astrophys. J. Suppl. Ser.* **2013**, *207*, 23. [[CrossRef](#)]
113. Malkus, A.; Kneller, J.P.; McLaughlin, G.C.; Surman, R. Neutrino oscillations above black hole accretion disks: Disks with electron-flavor emission. *Phys. Rev. D* **2012**, *86*, 85015. [[CrossRef](#)]
114. Frensel, M.; Wu, M.R.; Volpe, C.; Perego, A. Neutrino flavor evolution in binary neutron star merger remnants. *Phys. Rev. D* **2017**, *95*, 23011. [[CrossRef](#)]
115. Tian, J.Y.; Patwardhan, A.V.; Fuller, G.M. Neutrino flavor evolution in neutron star mergers. *Phys. Rev. D* **2017**, *96*, 43001. [[CrossRef](#)]
116. Wu, M.R.; Tamborra, I. Fast neutrino conversions: Ubiquitous in compact binary merger remnants. *Phys. Rev. D* **2017**, *95*, 103007. [[CrossRef](#)]
117. Padilla-Gay, I.; Shalgar, S.; Tamborra, I. Multi-Dimensional Solution of Fast Neutrino Conversions in Binary Neutron Star Merger Remnants. *arXiv* **2020**, arXiv:2009.01843.
118. Janiuk, A.; Mioduszewski, P.; Moscibrodzka, M. Accretion and outflow from a magnetized, neutrino cooled torus around the gamma-ray burst central engine. *Astrophys. J.* **2013**, *776*, 105. [[CrossRef](#)]
119. Janiuk, A. Microphysics in the Gamma-ray Burst Central Engine. *Astrophys. J.* **2017**, *837*, 39. [[CrossRef](#)]
120. Janiuk, A.; Sapountzis, K.; Mortier, J.; Janiuk, I. Numerical Simulations of Black Hole Accretion Flows. *arXiv* **2018**, arXiv:1805.11305.
121. Janiuk, A. The r-process Nucleosynthesis in the Outflows from Short GRB Accretion Disks. *Astrophys. J.* **2019**, *882*, 163. [[CrossRef](#)]
122. Bardeen, J.M. A Variational Principle for Rotating Stars in General Relativity. *Astrophys. J.* **1970**, *162*, 71. [[CrossRef](#)]
123. Bardeen, J.M.; Press, W.H.; Teukolsky, S.A. Rotating Black Holes: Locally Nonrotating Frames, Energy Extraction, and Scalar Synchrotron Radiation. *Astrophys. J.* **1972**, *178*, 347–370. [[CrossRef](#)]
124. Gammie, C.F.; Popham, R. Advection-dominated Accretion Flows in the Kerr Metric. I. Basic Equations. *Astrophys. J.* **1998**, *498*, 313–326. [[CrossRef](#)]
125. Bardeen, J.M. Kerr Metric Black Holes. *Nature* **1970**, *226*, 64–65. [[CrossRef](#)]
126. Thorne, K.S. Disk-Accretion onto a Black Hole. II. Evolution of the Hole. *Astrophys. J.* **1974**, *191*, 507–520. [[CrossRef](#)]
127. Novikov, I.D.; Thorne, K.S. Astrophysics of black holes. In *Black Holes (Les Astres Occlus)*; Dewitt, C., Dewitt, B.S., Eds.; Gordon and Breach Science Publishers Inc.: New York, NY, USA, 1973; pp. 343–450.
128. Page, D.N.; Thorne, K.S. Disk-Accretion onto a Black Hole. Time-Averaged Structure of Accretion Disk. *Astrophys. J.* **1974**, *191*, 499–506. [[CrossRef](#)]
129. Landau, L.D.; Lifshitz, E.M. *Fluid Mechanics*; Pergamon Press: Oxford, UK, 1959.
130. Abramowicz, M.A.; Chen, X.M.; Granath, M.; Lasota, J.P. Advection-Dominated Accretion Flows Around Kerr Black Holes. *Astrophys. J.* **1996**, *471*, 762–773. [[CrossRef](#)]
131. Abramowicz, M.A.; Lanza, A.; Percival, M.J. Accretion Disks around Kerr Black Holes: Vertical Equilibrium Revisited. *Astrophys. J.* **1997**, *479*, 179–183. [[CrossRef](#)]
132. Misner, C.W.; Thorne, K.S.; Wheeler, J.A. *Gravitation*; Princeton University Press: Princeton, NJ, USA, 1973.
133. Mihalas, D.; Mihalas, B.W. *Foundations of Radiation Hydrodynamics*; Oxford University Press: Oxford, UK, 1984.
134. Clifford, F.E.; Tayler, R.J. The equilibrium distribution of nuclides in matter at high temperatures. *Mon. Not. R. Astron. Soc.* **1965**, *69*, 21. [[CrossRef](#)]
135. Calder, A.C.; Townsley, D.M.; Seitzzahl, I.R.; Peng, F.; Messer, O.E.B.; Vladimirova, N.; Brown, E.F.; Truran, J.W.; Lamb, D.Q. Capturing the Fire: Flame Energetics and Neutronization for Type Ia Supernova Simulations. *Astrophys. J.* **2007**, *656*, 313–332. [[CrossRef](#)]

136. Mavrodiev, S.C.; Deliyergiyev, M.A. Modification of the nuclear landscape in the inverse problem framework using the generalized Bethe-Weizsäcker mass formula. *Int. J. Mod. Phys. E* **2018**, *27*, 1850015. [[CrossRef](#)]
137. Rauscher, T.; Thielemann, F.K. Astrophysical Reaction Rates From Statistical Model Calculations. *At. Data Nucl. Data Tables* **2000**, *75*, 1–351.
138. Rauscher, T. Nuclear Partition Functions at Temperatures Exceeding 10^{10} K. *Astrophys. J. Suppl. Ser.* **2003**, *147*, 403–408. [[CrossRef](#)]
139. Vincenti, W.G.; Kruger, C.H. *Introduction to Physical Gas Dynamics*; Krieger Pub Co (June 1, 1975); John Wiley & Sons: Hoboken, NJ, USA, 1965.
140. Buresti, G. A note on Stokes' hypothesis. *Acta Mech.* **2015**, *226*, 3555–3559. [[CrossRef](#)]
141. Particle Data Group. Review of Particle Physics. *Phys. Rev. D* **2018**, *98*, 30001. [[CrossRef](#)]
142. Dolgov, A.D. Neutrinos in the Early Universe. *Sov. J. Nucl. Phys.* **1981**, *33*, 700–706.
143. Sigl, G.; Raffelt, G. General kinetic description of relativistic mixed neutrinos. *Nucl. Phys. B* **1993**, *406*, 423–451. [[CrossRef](#)]
144. Hannestad, S.; Raffelt, G.G.; Sigl, G.; Wong, Y.Y.Y. Self-induced conversion in dense neutrino gases: Pendulum in flavour space. *Phys. Rev. D* **2006**, *74*, 105010. Erratum in **2007**, *76*, 029901, doi:10.1103/PhysRevD.76.029901. [[CrossRef](#)]
145. Cardall, C.Y. Liouville equations for neutrino distribution matrices. *Phys. Rev. D* **2008**, *78*, 85017. [[CrossRef](#)]
146. Strack, P.; Burrows, A. Generalized Boltzmann formalism for oscillating neutrinos. *Phys. Rev. D* **2005**, *71*, 93004. [[CrossRef](#)]
147. Dasgupta, B.; Dighe, A.; Mirizzi, A.; Raffelt, G.G. Collective neutrino oscillations in non-spherical geometry. *Phys. Rev. D* **2008**, *78*, 33014. [[CrossRef](#)]
148. Tolman, R.C. *Relativity, Thermodynamics, and Cosmology*; Clarendon Press: Oxford, UK, 1934.
149. Klein, O. On the statistical derivation of the laws of chemical equilibrium. *Il Nuovo Cimento (1943–1954)* **1949**, *6*, 171–180. [[CrossRef](#)]
150. Klein, O. On the Thermodynamical Equilibrium of Fluids in Gravitational Fields. *Rev. Mod. Phys.* **1949**, *21*, 531–533. [[CrossRef](#)]
151. Paczynski, B. A model of selfgravitating accretion disk. *Acta Astron.* **1978**, *28*, 91–109.
152. Raffelt, G.G. *Stars as Laboratories for Fundamental Physics*; University of Chicago Press: Chicago, IL, USA, 1996.
153. Harris, R.A.; Stodolsky, L. Two state systems in media and “Turing's paradox”. *Phys. Lett. B* **1982**, *116*, 464–468. [[CrossRef](#)]
154. Stodolsky, L. Treatment of neutrino oscillations in a thermal environment. *Phys. Rev. D* **1987**, *36*, 2273–2277. [[CrossRef](#)] [[PubMed](#)]
155. Janka, H.T. Implications of detailed neutrino transport for the heating by neutrino-antineutrino annihilation in supernova explosions. *Astron. Astrophys.* **1991**, *244*, 378–382.
156. Ruffert, M.; Janka, H.T.; Takahashi, K.; Schaefer, G. Coalescing neutron stars - a step towards physical models. II. Neutrino emission, neutron tori, and gamma-ray bursts. *Astron. Astrophys.* **1997**, *319*, 122–153.
157. Rosswog, S.; Ramirez-Ruiz, E.; Davies, M.B. High-resolution calculations of merging neutron stars—III. Gamma-ray bursts. *Mon. Not. R. Astron. Soc.* **2003**, *345*, 1077–1090. [[CrossRef](#)]
158. Kawanaka, N.; Kohri, K. A possible origin of the rapid variability of gamma-ray bursts due to convective energy transfer in hyperaccretion discs. *Mon. Not. R. Astron. Soc.* **2012**, *419*, 713–717. [[CrossRef](#)]
159. Preparata, G.; Ruffini, R.; Xue, S.S. The dyadosphere of black holes and gamma-ray bursts. *Astron. Astrophys.* **1998**, *338*, L87–L90.
160. Ruffini, R.; Salmonson, J.D.; Wilson, J.R.; Xue, S.S. On evolution of the pair-electromagnetic pulse of a charged black hole. *A&AS* **1999**, *138*, 511–512. [[CrossRef](#)]
161. Ruffini, R.; Salmonson, J.D.; Wilson, J.R.; Xue, S.S. On the pair-electromagnetic pulse from an electromagnetic black hole surrounded by a baryonic remnant. *Astron. Astrophys.* **2000**, *359*, 855–864.
162. Shemi, A.; Piran, T. The appearance of cosmic fireballs. *Astrophys. J.* **1990**, *365*, L55–L58. [[CrossRef](#)]
163. Piran, T.; Shemi, A.; Narayan, R. Hydrodynamics of Relativistic Fireballs. *Mon. Not. R. Astron. Soc.* **1993**, *263*, 861. [[CrossRef](#)]
164. Meszaros, P.; Laguna, P.; Rees, M.J. Gasdynamics of relativistically expanding gamma-ray burst sources - Kinematics, energetics, magnetic fields, and efficiency. *Astrophys. J.* **1993**, *415*, 181–190. [[CrossRef](#)]
165. Piran, T. Gamma-ray bursts and the fireball model. *Phys. Rep.* **1999**, *314*, 575–667. [[CrossRef](#)]
166. Piran, T. The physics of gamma-ray bursts. *Rev. Mod. Phys.* **2004**, *76*, 1143–1210. [[CrossRef](#)]
167. Mészáros, P. Theories of Gamma-ray Bursts. *Annu. Rev. Astron. Astrophys.* **2002**, *40*, 137. [[CrossRef](#)]
168. Mészáros, P. Gamma-ray bursts. *Rep. Prog. Phys.* **2006**, *69*, 2259–2321. [[CrossRef](#)]
169. Berger, E. Short-Duration Gamma-ray Bursts. *Annu. Rev. Astron. Astrophys.* **2014**, *52*, 43–105. [[CrossRef](#)]
170. Kumar, P.; Zhang, B. The physics of gamma-ray bursts and relativistic jets. *Phys. Rep.* **2015**, *561*, 1–109. [[CrossRef](#)]
171. Liu, T.; Zhang, B.; Li, Y.; Ma, R.Y.; Xue, L. Detectable MeV neutrinos from black hole neutrino-dominated accretion flows. *Phys. Rev. D* **2016**, *93*, 123004. [[CrossRef](#)]
172. Salmonson, J.D.; Wilson, J.R. General Relativistic Augmentation of Neutrino Pair Annihilation Energy Deposition near Neutron Stars. *Astrophys. J.* **1999**, *517*, 859–865. [[CrossRef](#)]
173. Birkel, R.; Aloy, M.A.; Janka, H.T.; Müller, E. Neutrino pair annihilation near accreting, stellar-mass black holes. *Astron. Astrophys.* **2007**, *463*, 51–67. [[CrossRef](#)]
174. Caballero, O.L.; McLaughlin, G.C.; Surman, R. Neutrino Spectra from Accretion Disks: Neutrino General Relativistic Effects and the Consequences for Nucleosynthesis. *Astrophys. J.* **2012**, *745*, 170. [[CrossRef](#)]
175. Ruffini, R.; Rueda, J.A.; Muccino, M.; Aimuratov, Y.; Becerra, L.M.; Bianco, C.L.; Kovacevic, M.; Moradi, R.; Oliveira, F.G.; Pisani, G.B.; Wang, Y. On the Classification of GRBs and Their Occurrence Rates. *Astrophys. J.* **2016**, *832*, 136. [[CrossRef](#)]

176. Moghaddas, M.; Ghanbari, J.; Ghodsi, A. Shear Tensor and Dynamics of Relativistic Accretion Disks around Rotating Black Holes. *Publ. Astron. Soc. Jpn.* **2012**, *64*. [[CrossRef](#)]
177. Moeen, M. Calculation of the relativistic bulk tensor and shear tensor of relativistic accretion flows in the Kerr metric. *Iran. J. Astron. Astrophys.* **2017**, *4*, 205–221. [[CrossRef](#)]
178. Zeldovich, Y.B.; Novikov, I.D. *Relativistic Astrophysics. Volume 1: Stars and Relativity*; University of Chicago Press: Chicago, IL, USA, 1971.
179. Potekhin, A.Y.; Chabrier, G. Equation of state of fully ionized electron-ion plasmas. II. Extension to relativistic densities and to the solid phase. *Phys. Rev. E* **2000**, *62*, 8554–8563. [[CrossRef](#)] [[PubMed](#)]
180. Dicus, D.A. Stellar energy-loss rates in a convergent theory of weak and electromagnetic interactions. *Phys. Rev. D* **1972**, *6*, 941–949. [[CrossRef](#)]
181. Tubbs, D.L.; Schramm, D.N. Neutrino Opacities at High Temperatures and Densities. *Astrophys. J.* **1975**, *201*, 467–488. [[CrossRef](#)]
182. Bruenn, S.W. Stellar core collapse—Numerical model and infall epoch. *Astrophys. J. Suppl. Ser.* **1985**, *58*, 771–841. [[CrossRef](#)]
183. Ruffert, M.; Janka, H.T.; Schaefer, G. Coalescing neutron stars—A step towards physical models. I. Hydrodynamic evolution and gravitational-wave emission. *Astron. Astrophys.* **1996**, *311*, 532–566.
184. Yakovlev, D.G.; Kaminker, A.D.; Gnedin, O.Y.; Haensel, P. Neutrino emission from neutron stars. *Phys. Rep.* **2001**, *354*, 1–155. [[CrossRef](#)]
185. Burrows, A.; Thompson, T.A. *Neutrino-Matter Interaction Rates in Supernovae*; Fryer, C.L., Ed.; Astrophysics and Space Science Library; Springer: Dordrecht, The Netherlands, 2004; Volume 302, pp. 133–174. [[CrossRef](#)]
186. Burrows, A.; Reddy, S.; Thompson, T.A. Neutrino opacities in nuclear matter. *Nucl. Phys. A* **2006**, *777*, 356–394. [[CrossRef](#)]
187. Aparicio, J.M. A Simple and Accurate Method for the Calculation of Generalized Fermi Functions. *Astrophys. J. Suppl. Ser.* **1998**, *117*, 627–632. [[CrossRef](#)]

